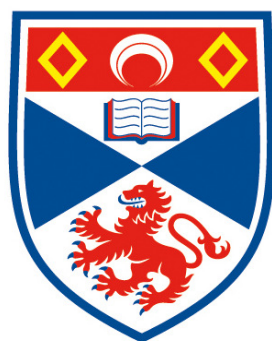


Chemical control of the polymorphic phase
boundaries in doped barium titanate



University of
St Andrews

600
YEARS

Sarah Ann Turp MChem

This thesis is submitted in application for the degree of

Doctor of Philosophy

at the faculty of Science, University of St Andrews

April 2013

Abstract

Barium titanate (BaTiO_3), a known ferroelectric material, is of great interest as a future lead-free piezoelectric if appropriately doped to tailor the electric properties for specific applications. This work focuses on the study and rationalisation of the dielectric properties of a series of A-site/B-site co-doped compositions: SrZrO_3 - BaTiO_3 , CaZrO_3 - BaTiO_3 , LaScO_3 - BaTiO_3 and GdScO_3 - BaTiO_3 .

The effect of sintering conditions and microstructure on ceramics is shown to have a significant impact on the physical properties of these materials. Pellet inhomogeneity, air sensitivity in pre-calcined powders and the presence of parasitic grain boundary capacitances are all shown to have adverse effects on properties, including the magnitudes of relative permittivity and T_C calculated from total capacitance data. These can be overcome by careful control of synthesis conditions.

Dielectric spectroscopy measurements on the optimised materials show that increasing addition of SrZrO_3 , CaZrO_3 or LaScO_3 causes the phase transitions between the various polymorphs of BaTiO_3 to coalesce. In each case T_C is reduced whilst each of the other phase transitions is shifted to higher temperatures, until the coalescence temperature is reached. When doped with GdScO_3 T_C is observed to fall, but so too are the rhombohedral/orthorhombic and orthorhombic/tetragonal transitions, resulting in a stabilisation of the tetragonal polymorphic phase. This is suggested to result from an antipolar displacement of small Gd^{3+} ions, resulting in 8-coordinate ion and stabilisation of the tetragonal polymorph.

The addition of dopant species is shown to result in two different high temperature conduction regimes. Both mechanisms are observed within single compositions over different temperature ranges. It is suggested that this is due to a change between n- and p-type electronic conduction processes or mixed ionic/electronic processes.

Finally, it is shown that trends observed in changes to T_C cannot be accounted for by simple and widely used size-based arguments alone, but requires consideration of cation size variance and charge dilution effects in order to fully understand the impact on T_C of dopant addition.

Declaration

1. Candidate's declarations:

I, Sarah A. Turp hereby certify that this thesis, which is approximately 45000 words in length, has been written by me, that it is the record of work carried out by me and that it has not been submitted in any previous application for a higher degree.

I was admitted as a research student in October 2009 and as a candidate for the degree of PhD in September 2010; the higher study for which this is a record was carried out in the University of St Andrews between 2009 and 2013.

Date Signature of candidate

2. Supervisor's declaration:

I hereby certify that the candidate has fulfilled the conditions of the Resolution and Regulations appropriate for the degree of PhD in the University of St Andrews and that the candidate is qualified to submit this thesis in application for that degree.

Date Signature of supervisor

3. Permission for electronic publication:

In submitting this thesis to the University of St Andrews I understand that I am giving permission for it to be made available for use in accordance with the regulations of the University Library for the time being in force, subject to any copyright vested in the work not being affected thereby. I also understand that the title and the abstract will be published, and that a copy of the work may be made and supplied to any bona fide library or research worker, that my thesis will be electronically accessible for personal or research use unless exempt by award of an embargo as requested below, and that the library has the right to migrate my thesis into new electronic forms as required to ensure continued access to the thesis. I have obtained any third-party copyright permissions that may be required in order to allow such access and migration, or have requested the appropriate embargo below.

The following is an agreed request by candidate and supervisor regarding the electronic publication of this thesis:

Embargo on both all of printed copy and electronic copy for the same fixed period of 2 years on the following grounds:

publication would preclude future publication;

Date Signature of candidate Signature of supervisor

Acknowledgements

First off, I would like to thank my supervisor Dr Finlay Morrison for all the support and guidance he has given me during the course of this PhD. Thanks also to Donna for getting me started in the lab and answering all those annoying questions that new PhD students inevitably seem to have.

I am very grateful to Professor Chiu Tang and Dr Stephen Thompson at Diamond and also Sandra who showed me the ropes on Ill and for letting me program the robot. I would also like to thank Sandy Cochran, Christine and Zhen for all their help at IMSaT.

Thanks to Chris for lots of laughter and help round the lab, especially where computers were involved. I shall always remember your thesis writing advice, “Keep calm & drink tea”, though I still think it needs the addition of “...and eat lots of chocolate!” Thanks also to the rest of the group who have put up with me over the years and with whom I have had a lot of fun.

Thanks to all those funding guys at Scottish Funding Council who paid for me to be here doing what I love, and cheers also to all my friends in St Andrews, especially Katie, Judith and Nick, who have made this time so enjoyable.

I shower huge thanks upon my family, especially my Mum and Dad for putting up with me during three-and-a-half more years of student life, and for completing a 1200 mile round trip to get me to my graduation on time when I broke my leg! And also for Mum’s amazing knowledge of all things grammatical, without which I would still be searching the internet for the correct use of a semi-colon!

Finally thanks to my brother Craig and his wonderful fiancé Sharon, whose wedding has made the perfect deadline to get me to finish this on time.

Contents

Chapter 1: Introduction.....	1
1.1: Electronic functional materials.....	1
1.1.1: Dielectric materials.....	1
1.1.2: Piezoelectricity	2
1.1.3: Pyroelectricity.....	3
1.1.4: Ferroelectricity	4
1.2: The perovskite structure	5
1.3: Piezoelectric materials.....	6
1.4: Perovskite-based piezoelectric materials.....	7
1.4.1: Lead zirconate titanate, PZT.....	8
1.4.1.1: Morphotropic phase boundaries	9
1.4.2: Alkali metal niobates.....	11
1.4.3: Barium titanate	12
1.4.4: Doped barium titanate	15
1.4.4.1: Isovalent doping	16
1.4.4.2: Aliovalent doping	19
1.4.4.3: Kröger Vink notation.....	20
1.4.4.4: Size effects of dopants.....	21
1.4.4.5: Strain effects of dopants	22
1.4.4.6: Barium zirconium titanate - barium calcium titanate, BZT-BCT	24
1.5: Crystalline ceramic materials	27
1.5.1: Grain growth.....	28
1.5.2: Grain size effects	29
1.6: The scope of this project.....	31
References	34
Chapter 2: Electrical theory and dielectric materials.....	41
2.1: Polarisation	41
2.2: Capacitors	43
2.3: Complex dielectric permittivity.....	46
2.4: Immittance spectroscopy	47
2.4.1: Immittance formalisms.....	49
2.4.2: Brick layer model	49
2.5: Polarisation field hysteresis measurements	54
2.6: Piezoelectric operation modes.....	55

References	57
Chapter 3: Experimental methods	58
3.1: Ceramic synthesis	58
3.2: Electrodes	59
3.2.1 Sputter-coater	59
3.2.2: Painted electrodes	59
3.3: Powder X-ray diffraction	60
3.3.1: In-House Data Collection	60
3.3.1.1: Reflection mode	60
3.3.1.2: Transmission mode	61
3.3.2: Synchrotron Data Collection	63
3.4: Rietveld Refinement	65
3.5: Scanning Electron Microscopy	66
3.6: Immittance Spectroscopy	67
3.6.1: Isothermal measurements	67
3.6.2: Curie-Weiss analysis	68
3.6.3: Arrhenius behaviour	69
3.6.4: Temperature controlled sweeps	69
3.7: Theoretical Density Calculations	70
3.8: Hysteresis Measurements	71
References	73
Chapter 4: The effects of ceramic processing	74
4.1: Introduction	74
4.2: Case Study 1: 50% $[\text{Ba}(\text{Ti}_{0.8}\text{Zr}_{0.2})\text{O}_3]$ -50% $[(\text{Ba}_{0.7}\text{Ca}_{0.3})\text{TiO}_3]$ – Parasitic grain boundary contributions	74
4.2.1: Synthesis	75
4.2.2: Pellet densities	75
4.2.3: Dielectric properties	79
4.2.4: X-ray data	81
4.2.5: Capping of the permittivity maxima	82
4.2.6: High temperature immittance data	86
4.2.7: Conductivity data	93
4.3: Case study 2: 95% (BaTiO_3) -5% (LaScO_3) – Air sensitivity	95
4.4: Case study 3: 95% (BaTiO_3) -5% (GdScO_3) – Inhomogeneity	103
4.5: Conclusions	106
References	108
Chapter 5: The effects of dopants on the phase transitions of BaTiO_3	110

5.1: Dopant ions selection	111
5.2: The effects of CaZrO_3 dopant addition to BaTiO_3	113
5.2.1: Synthesis	113
5.2.2: Dielectric spectroscopy	115
5.2.3: Synchrotron powder X-ray diffraction data analysis	119
5.2.4: CaZrO_3 – BaTiO_3 Phase diagram	123
5.3: The effects of SrZrO_3 dopant addition to BaTiO_3	124
5.3.1: Synthesis	125
5.3.2: Dielectric spectroscopy	125
5.3.3: Synchrotron powder X-ray diffraction data analysis	128
5.3.4: SrZrO_3 – BaTiO_3 phase diagram	129
5.4: The effects of LaScO_3 dopant addition to BaTiO_3	130
5.4.1: Synthesis	130
5.4.2: Dielectric spectroscopy	131
5.4.3: Synchrotron powder X-ray diffraction analysis	133
5.4.4: LaScO_3 – BaTiO_3 Phase diagram	134
5.5: The effects of GdScO_3 dopant addition to BaTiO_3	135
5.5.1: Synthesis	135
5.5.2: Dielectric spectroscopy	136
5.5.3: Synchrotron powder X-ray diffraction analysis	138
5.5.4: GdScO_3 – BaTiO_3 Phase diagram	143
5.6: Trends as a result of dopant addition to BaTiO_3	144
5.6.1: Trends in T_C	144
5.6.2: Trends in $T_{R/O}$ and $T_{O/T}$	149
5.6.3: Tetragonal stabilisation in GdScO_3 -doped BaTiO_3	150
5.6.4: Variable temperature X-ray data of coalesced peaks	153
5.6.4.1: 12% CaZrO_3	154
5.6.4.2: 5% LaScO_3	160
5.7: Hysteresis	161
5.8: Conclusions	166
References	169
Chapter 6: Microstructural analysis and high temperature immittance spectroscopy	172
6.1: High temperature immittance spectroscopy	172
6.1.1: SrZrO_3 –doped BaTiO_3	173
6.1.2: CaZrO_3 –doped BaTiO_3	184
6.1.3: GdScO_3 –doped BaTiO_3	187
6.1.4: LaScO_3 –doped BaTiO_3	190

6.2: Discussion.....	192
6.2.1: Changes in activation energies	192
6.2.2: Anomalous tail feature present in LaScO ₃ doped BaTiO ₃	197
6.3: Conclusions	197
References	200
Chapter 7: Quantification of size, strain and charge effects.....	202
7.1: Separation of size, strain and charge effects on T _C	202
7.2: Quantifying size, strain and charge effects.....	203
7.3: Discussion.....	214
7.4: Conclusions	216
References	218
Chapter 8: Conclusions and future work	219
8.1: Conclusions	219
8.2: Further Work	223
References	225
Appendix	I
Appendix chapter 2.....	I
Appendix chapter 3.....	III
Appendix chapter 4.....	III
Appendix chapter 5.....	V
Appendix chapter 7.....	XIV

Chapter 1: Introduction

The content of this thesis is focused on the structure and properties of some lead-free ferroelectrics, namely doped barium titanates. Particular attention is focused on how local and long range strain and electrostatics affect both structure and properties. This introduction will include a brief look at electronic functional materials, their history and current uses as well as the desired move away from lead-based materials. There will be some discussion on different piezoelectric compounds currently known and their relative merits, before moving on to look more closely at BaTiO_3 and at the known dopant effects on BaTiO_3 -based materials on which this work builds.

1.1: Electronic functional materials

Electrical ordering on an atomic scale gives rise to a variety of electronic functionality in materials^[1], causing characteristic behaviours when exposed to electric fields, the precise behaviour being dependent upon the specific electronic ordering type within the material. These characteristic behaviours fall into the categories of piezoelectric, pyroelectric and ferroelectric behaviour. Due to an ever increasing reliance on electronics, materials which exhibit piezo-, pyro- or ferroelectricity are in great demand for device applications^[2-5], with much research being done on furthering our knowledge of these families of materials and how they might be tailored to specific electronic applications, as well as researching new materials that may exhibit such properties.

1.1.1: Dielectric materials

Dielectrics are materials which are electrically insulating and remain so, even when subjected to high voltages, i.e. they have high dielectric strength, where this is defined as the applied voltage per millimetre of material required to result in its breakdown^[6]. This is the point at which large numbers of electrons are excited to the conduction band, resulting in significant current through the material, often

associated with an irreversible deformation or degradation of the material. Typical dielectric strengths for dielectric materials range from $\sim 1 - 50 \text{ V mm}^{-1}$, with ceramic titanates having typical values of $1.2\text{-}7.6 \text{ V mm}^{-1}$ [7]. A good dielectric should also have a low dielectric loss; where dielectric loss is defined as being the amount of energy of an alternating field lost as heat energy per cycle of the applied field. Dielectric materials may also be piezo-, pyro- or ferro- electric.

1.1.2: Piezoelectricity

By definition, a piezoelectric material is a non-centrosymmetric material which becomes electrically polarised upon the application of a mechanical force^[8], hence the name piezoelectric, which is derived from the Greek word *piezen*, which means to press^[9]. This effect is both linear and reversible, thus the magnitude of the polarisation is directly related to the magnitude of the stress applied, with the sign being dependant on the direction of stress (tensile or compressive). All compounds with a non-centrosymmetric crystal class except 432 are piezoelectric, figure 1.1.

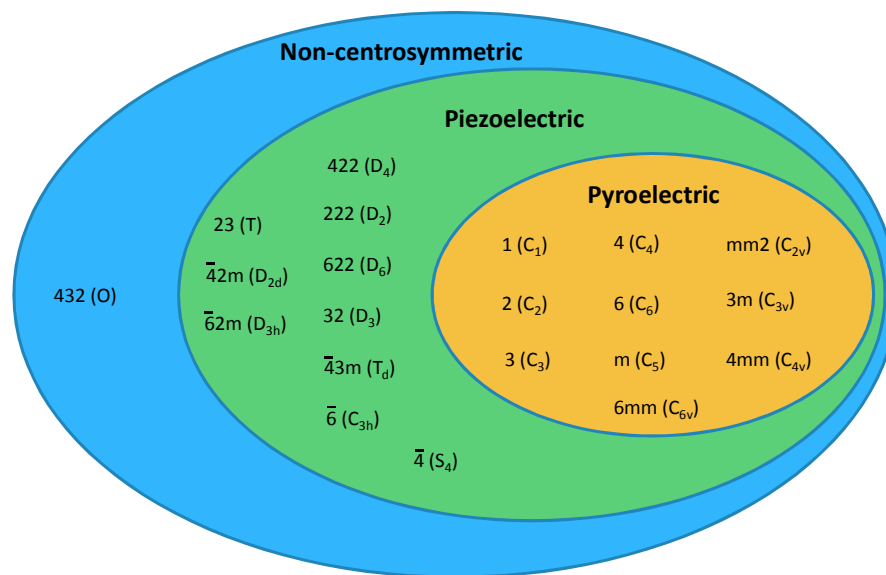


Figure 1.1: Diagram showing the relationship between physical properties and crystal class for dielectric materials

The fact that polarisation and stress are correlated, as described above, gives rise to two formal definitions of piezoelectricity, known as the direct and converse piezoelectric effects. The direct piezoelectric effect is the observation that the

physical deformation of, or applied stress to, a piezoelectric material induces a polarisation and corresponding surface charge in the material. The converse piezoelectric effect describes the application of an applied electric field to a piezoelectric material resulting in a physical deformation (strain). These two effects can be described mathematically by equations 1.1 and 1.2^[10]:

$$\vec{D} = d_{ab} \vec{E} + \epsilon^T \vec{E} \quad \text{Direct Effect} \quad \text{Equation 1.1}$$

$$\vec{S} = d_{ab} \vec{E} + s^E \vec{T} \quad \text{Converse Effect} \quad \text{Equation 1.2}$$

Where \vec{D} is the electric displacement, directly related to the polarisation of the material, \vec{T} is the stress, \vec{E} is the electric field, \vec{S} is the strain, d is the piezoelectric coefficient relating the applied field along axis a to the resultant strain along axis b , s is the material compliance, (also the inverse of the modulus of the elasticity of the material) and ϵ is the dielectric constant, also known as its permittivity. The use of superscripts indicates any quantity held constant, *i.e.* s^E implies the material compliance at constant electric field.

1.1.3: Pyroelectricity

Pyroelectric materials form a sub-group of piezoelectrics. Unlike piezoelectric materials where the polarisation is only necessarily present whilst stress is applied, in pyroelectric materials the polarisation is spontaneous, forming permanent dipoles, the modulus of which is temperature and stress dependant. Pyroelectric materials have a unique polar axis in addition to being non-centrosymmetric and, as with piezoelectrics, a material can be determined to be pyroelectric based on the knowledge of its crystal class alone, figure 1.1. The name pyroelectric stems from the Greek *pur* or *purus*, meaning heat or fire^[11], and was assigned to this group of materials due to the fact that the spontaneous polarisation, and associated physical properties, vary as a function of temperature.

1.1.4: Ferroelectricity

Ferroelectric materials are in turn a subgroup of pyroelectric materials, whose spontaneous polarisation can be switched upon the application of a suitable applied electric field. As a result, when the electrical polarisation of the material is plotted against a changing field, a hysteresis loop is observed (see chapter 2.5). An example loop is shown in figure 1.2.

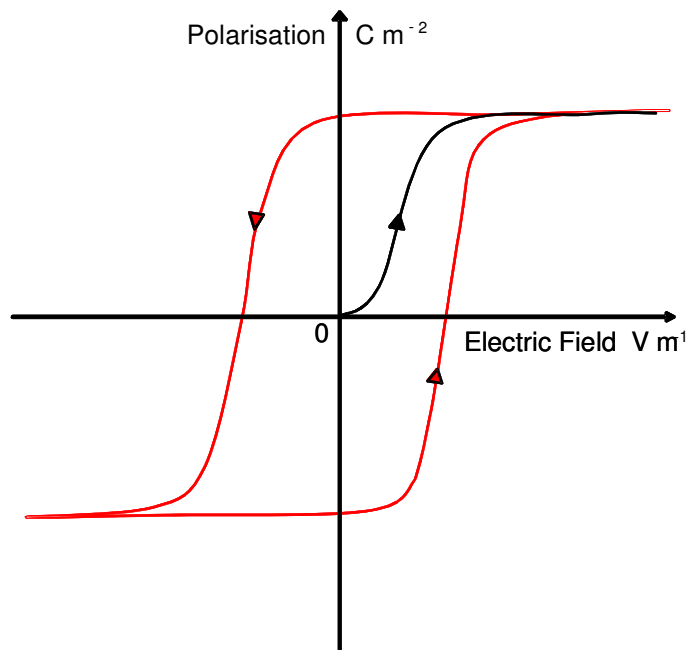


Figure 1.2: Ferroelectric hysteresis loop

Unlike piezoelectric and pyroelectric materials, it is not possible to determine whether a material will exhibit ferroelectric properties by knowledge of the crystal class alone. Instead, experimental evidence must be gathered, such as the presence of a ferroelectric hysteresis loop, which confirms the presence of 2 or more orientational states, which the material can be made to convert between by the application of an electric field.

In each of these types of electronically functional materials, it is the non-centrosymmetric nature of the crystal class of the material that allows for the physical properties of interest. As the environment of the material; temperature, atmosphere and pressure, is changed, it is common for the crystal structure of the material to alter. Thus, it is generally found that materials are only piezo- pyro- or

ferroelectric over certain temperature ranges. The temperature at which the spontaneous polarisation falls to zero is known as the Curie temperature, T_C , and is often accompanied by a polymorphic phase change to a centrosymmetric crystal class.

1.2: The perovskite structure

Many of the piezoelectric materials currently in use are based on the perovskite structure, named after the mineral perovskite, CaTiO_3 . The structure of an ideal perovskite, consists of a cubic $Pm\bar{3}m$ unit cell with an A-site species located at $[\frac{1}{2}, \frac{1}{2}, \frac{1}{2}]$, B-site species at $[0,0,0]$ and oxygen located at $[\frac{1}{2}, 0, 0]$ resulting in the B-site species forming a sub-lattice of 6-coordinate, vertex-sharing octahedra and A-site species forming a sub-lattice of 12-coordinate face-sharing cuboctahedra, figure 1.3.

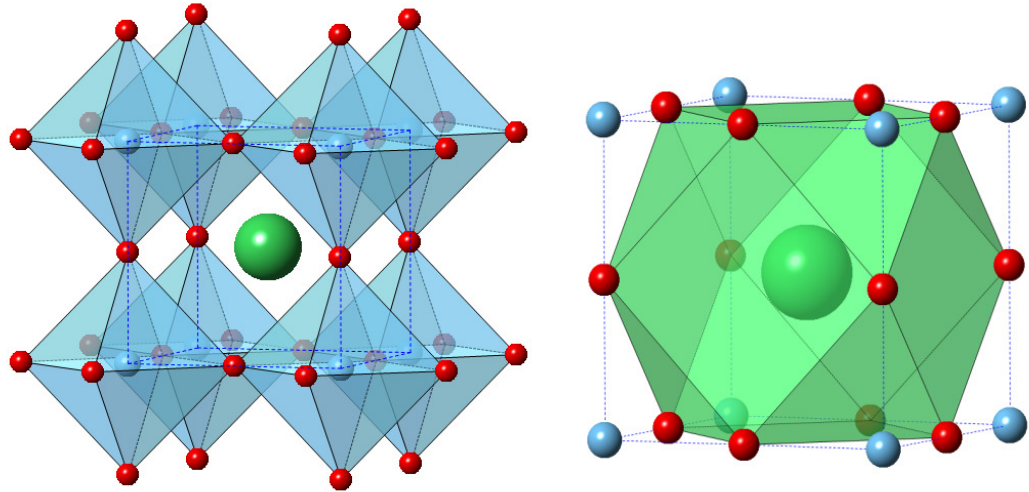


Figure 1.3: Perovskite unit cell showing B-site octahedra (left) and A-site cuboctahedra (right)

In 1926 V. M. Goldschmidt established an empirical model for determining the stability of the ideal perovskite structure^[12]. This was based on the system being purely ionic, with hard spheres, where each cation would be surrounded by as many anions as could touch it, but no more, and where anions must touch the cations, such that the cation-anion distance would be the sum of their radii. This provided the following ideal relation between the cation and anion ionic radii.

$$r_A + r_O = \sqrt{2}(r_B + r_O) \quad \text{Equation 1.3}$$

However, for actual crystal systems, this equation will not generally hold true. As a result the system becomes distorted from the ideal cubic structure, often having tilted octahedra, and resulting in tetragonal, rhombohedral, orthorhombic or monoclinic structures^[13-16].

The Goldschmidt tolerance factor, t (equation 1.4), can be used to predict the distortion with a value of 1 being expected for the undistorted cubic perovskite. When $0.75 < t < 0.90$, tilting giving rise to an orthorhombic distortion is usually observed. If $0.9 < t < 0.98$ a rhombohedral distortion is most common and where $t > 1$ a tetragonal distortion generally occurs.

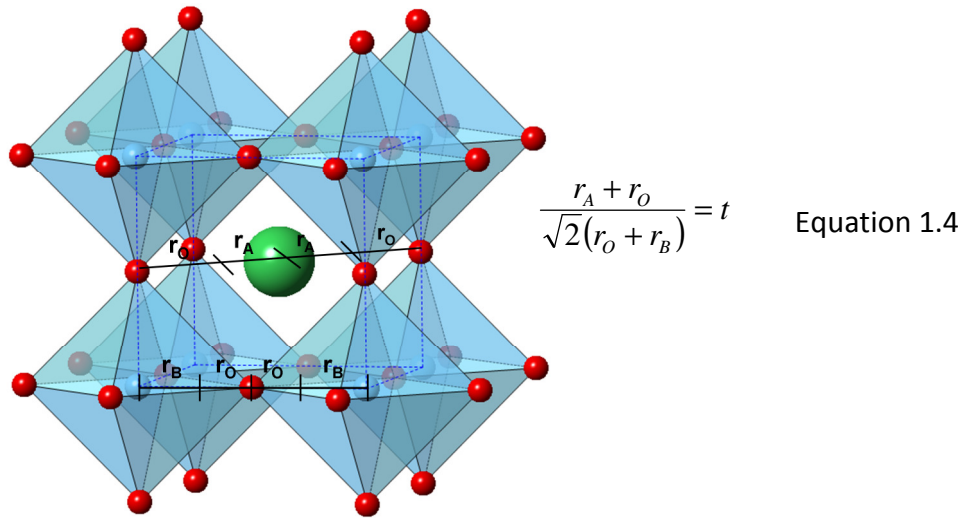


Figure 1.4: Diagram showing the mathematical reasoning behind the tolerance factor, equation 1.4

1.3: Piezoelectric materials

Though the first synthetic piezoelectric material was formed as early as 1665 by Elie Seignete in La Rochelle when studying sodium potassium tartrate, “Rochelle salt”^[17], it was over 200 years later that its piezo- and pyroelectric responses were discovered. The phenomenon of piezoelectricity in materials was first discovered by Jacques and Pierre Curie in 1880^[18] and has since found applications in a vast array of devices including quartz resonators in watches^[19], medical imaging devices^[3, 5], actuators, electromechanical transducers^[20] and sensors^[21]. There has also been more recent interest in the use of piezoelectric materials as energy harvesters, utilizing piezoelectric properties to convert wasted kinetic energy into electrical

energy^[22-26]. Many of the best piezoelectric materials are actually poled ferroelectrics^[27]. These are materials which exhibit ferroelectric behaviour, and have been subjected to a large electric field whilst they are cooled below T_C . This causes the domains to be aligned when in a more fluxional state around T_C , becoming fixed in this aligned state as the thermal energy of the system is lowered, resulting in a larger spontaneous polarisation than would be otherwise achieved in a ceramic material.

The temperature range over which a material may exhibit piezoelectricity is dependent on the composition and has huge implications on the practicality of the material being used in devices. For many devices wide operating temperature ranges are required in order that the material, often a poled ferroelectric, does not undergo a polymorphic phase change to a non-piezoelectric crystal class or thermally depole during its working life. This generally requires that the material remains piezoelectric to temperatures well above room temperature *i.e.* $T_C \gg 300K$.

Practical applications of piezoelectric materials also require that the piezoelectric effect observed is great enough to be able to convert electrical power into a useful amount of mechanical power and vice-versa, *i.e.* that the deformation caused by the application of a voltage, or that the polarisation observed as the result of an applied stress to the material is sizeable. To be commercially viable the process also needs to be efficient, *i.e.* have small losses, be stable, reproducible, reliable and the material must be cheap to make.

1.4: Perovskite-based piezoelectric materials

Many of the piezoelectric materials that are extensively studied or used are poled ferroelectric perovskite ceramics. The piezoelectric properties in these materials arise due to a non-symmetric Jahn-Teller like distortion of the B-site octahedra resulting in a cooperative shift of the cationic species relative to the oxygen anion lattice (Figure 1.5), creating a polarisation. This requires that the unit cell distorts from its ideal cubic perovskite structure. The application of an electric field to the material can further promote the off-centring, or hamper it, depending on the

direction of the applied field relative to the off-centring ions. This results in a physical deformation of the material. Conversely, if the ceramic is compressed or put under tensile strain, the unit cell distortion is either enhanced or reduced, along with the ion off-centring, resulting in a change in the polarisation.

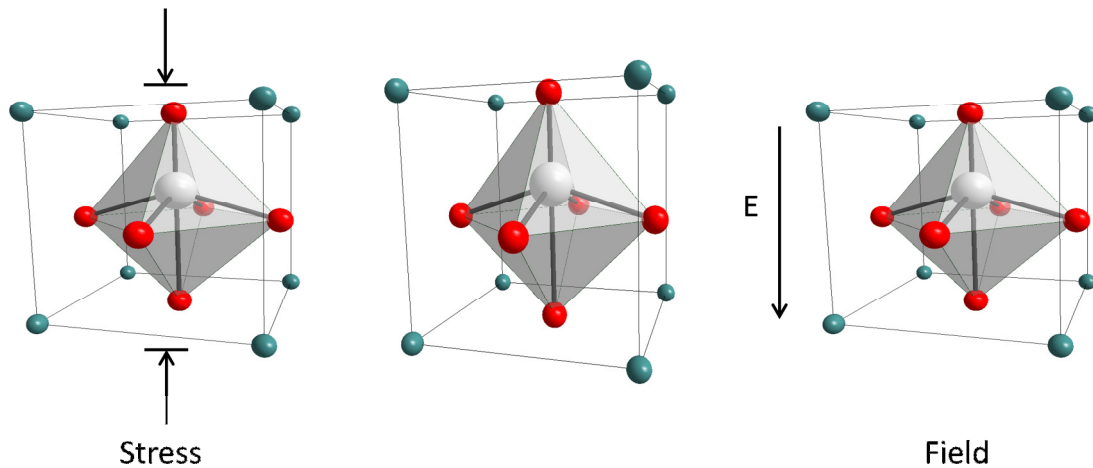


Figure 1.5: Distortion of a piezoelectric perovskite by an stress (left) and applied electric field (right), causing deformation and changing the polarisation

Perovskites are of significant scientific interest due to the flexibility of the perovskite structure allowing it to adopt a range of geometries from cubic to rhombohedral^[13-16, 28] forming stable compositions with a wide range of species. In order to be used commercially, most piezoelectrics are tailored to specific purposes by means of doping; this involves the partial substitution of one of more species with another. The effect of this is to alter the physical properties of the composition, ideally without causing a significant change to the crystal structure.

1.4.1: Lead zirconate titanate, PZT

Most of the piezoelectric devices in use today are based on lead zirconate titanate compounds of the form $\text{PbZr}_x\text{Ti}_{1-x}\text{O}_3$ (PZT), $a\%[\text{Pb}(\text{Mg}_x\text{Nb}_y)\text{O}_3] - b\%[\text{PbTiO}_3]$ (PMN-PT) or lead titanate, PbTiO_3 , due to their favourable piezoelectric properties including high T_c values, typically $>750\text{ K}$ with polarisations $>70\text{ }\mu\text{C cm}^{-2}$ ^[29] and piezoelectric coefficient, (d_{33}), values of up to 590 pC N^{-1} (PZT-5H[†])^[30]. However, these sorts of compositions are undesirable due to the toxicity of lead along with its high

[†] PZT-5H is a particular commercial form of PZT known to be soft in nature and possessing a high d_{33} coefficient.

atomic weight resulting in very heavy ceramics. The official Journal of the European Union - DIRECTIVE 2002/95/EC OF THE EUROPEAN PARLIAMENT AND OF THE COUNCIL of 27 January 2003 on the restriction of the use of certain hazardous substances in electrical and electronic equipment^[31] states that *Member States shall ensure that, from 1 July 2006, new electrical and electronic equipment put on the market does not contain lead, mercury, cadmium, hexavalent chromium, polybrominated biphenyls (PBB) or polybrominated diphenyl ethers (PBDE)*, due to the health and environmental risks associated with the toxicity of these elements and their compounds. Exemptions to this clause allow for the use of the above chemical species in certain situations. Included in the list of exemptions is the use of *lead in electronic ceramic parts (e.g. piezoelectronic devices)*^[31]. However it is required that any exception to a policy is reviewed every four years, at which point the exemption may no longer be deemed appropriate. Consequently much research has been done in recent years to develop lead-free alternatives to such materials.

1.4.1.1: Morphotropic phase boundaries

Lead zirconate titanate based compounds are widely used due to the presence of a morphotropic phase boundary, MPB, which exists in these materials. A morphotropic phase boundary is defined as being *an abrupt change in the structure of a solid solution with variation in composition*^[32]. At such a phase boundary two or more different structures with different polarisabilities but with similar free energies may co-exist and there will be a fluxional nature between the two states. Each of the different structures will have different possible axes of polarisation; thus when an electric field is applied there are more different axes which may be in alignment with the applied field, giving rise to enhanced piezoelectric properties. The structure changes tend to be virtually independent of temperature, thus it is possible for an MPB to exist in a material over a wide range of temperatures giving enhanced piezoelectric properties over a large temperature range.

In PZT an MPB exists at the composition $\text{PbZr}_{0.46}\text{Ti}_{0.54}\text{O}_3$ ^[8], with the material adopting either the rhombohedral or tetragonal structure. At this point there is a total of 14

axes of polarisation that may be able to align with an applied electric field, 6 from the tetragonal phase and 8 from the rhombohedral phase. (fig 1.6)

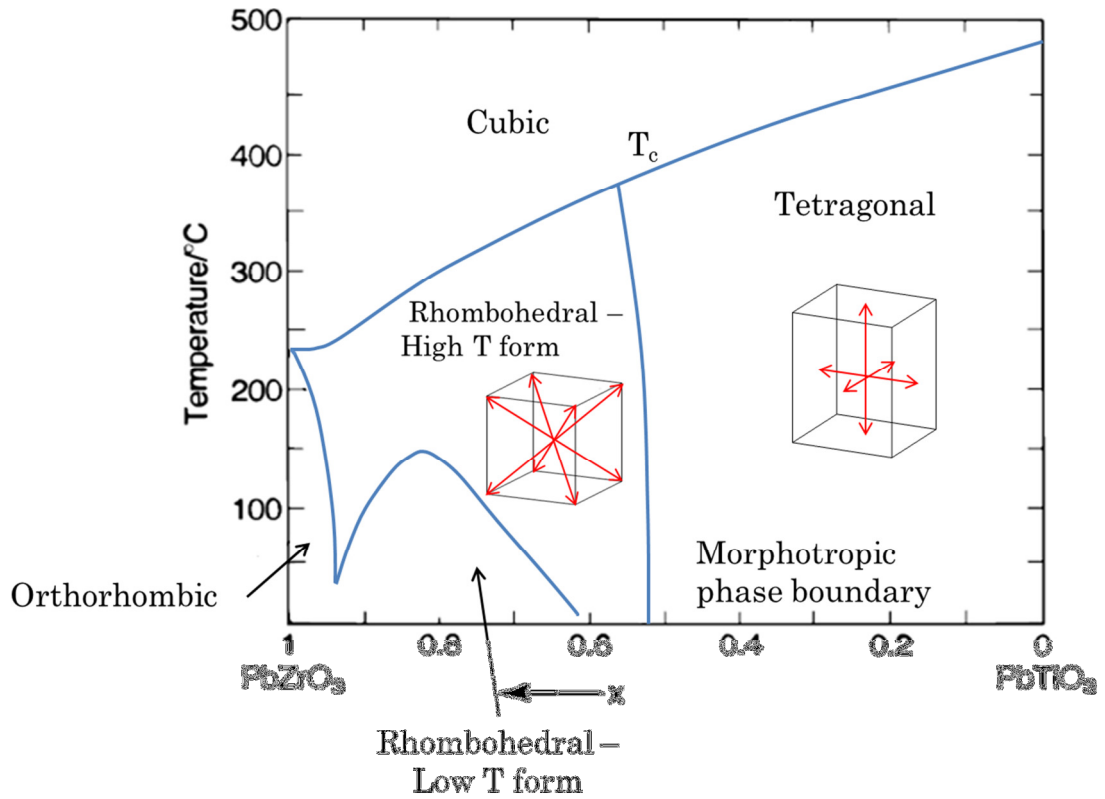


Figure 1.6: Phase diagram for lead zirconate titanate adapted from^[8]

Properties such as the relative permittivity, ϵ_r , which is the ratio of the amount of electrical energy stored in a material by an applied voltage relative to a vacuum, and coupling coefficient, k_p , which is a measure of the efficiency with which electrical energy is converted to mechanical energy (or vice versa), are some of the properties which are found to be greatly enhanced at morphotropic phase boundaries, an example of which can be seen in figure 1.7, which depicts the variations of these two parameters for various PZT compositions about its MPB.

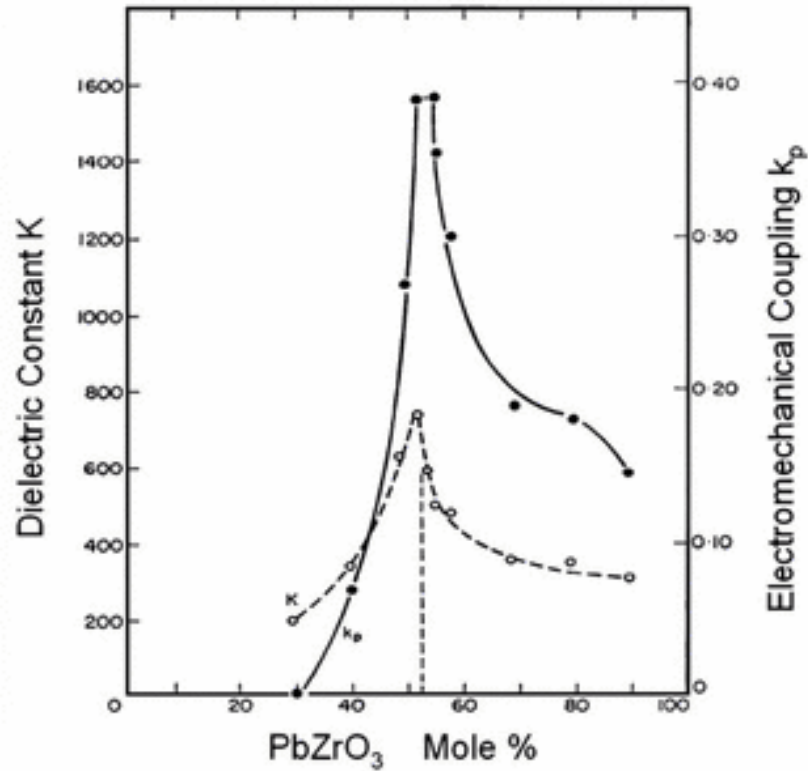


Figure 1.7: Enhanced dielectric and piezoelectric properties shown in PZT around the MPB[8, 33]

1.4.2: Alkali metal niobates

Alkali metal niobates have been extensively studied as a class of lead-free compounds known to exhibit piezoelectric characteristics. They have a perovskite structure $M\text{NbO}_3$, where M may be an alkali metal species or a mixture of two or more alkali metal species. Three of the most commonly studied alkali metal niobates are KNbO_3 , NaNbO_3 and $\text{K}_{0.5}\text{Na}_{0.5}\text{NbO}_3$.

In 1959 it was reported that $\text{K}_{0.5}\text{Na}_{0.5}\text{NbO}_3$ had an MPB between two different orthorhombic ferroelectric phases^[34]. This resulted in high Curie temperatures, ($\sim 420^\circ\text{C}$ ^[35]) and good piezoelectric coefficients, ($d_{33} \sim 160 \text{ pC N}^{-1}$) and led to much work being done both on $\text{K}_{0.5}\text{Na}_{0.5}\text{NbO}_3$, as well as other variations of the composition. However, the synthesis of alkali metal niobates is often hindered due to the volatile nature of the alkali metal species resulting in products with somewhat undetermined stoichiometry, lowering the green density and causing cation vacancies which lead to a disruption of the electrical properties of the materials.

In addition to issues surrounding the volatility of some of the ions in these compounds, these compositions also tend to be hygroscopic. This can make the processing of these materials into devices a much more challenging and costly task.

1.4.3: Barium titanate

Barium titanate has a perovskite structure with Ba^{2+} on the A-site and Ti^{4+} on the B-site. It was discovered in 1941 amid the secrecy that surrounded many scientific developments during the war era, and thus was worked on by many scientists including Thurnauer, Wainer and Salomon^[10]. Due to the war, it was not until the mid-1940s that patents and papers started to be published^[36-39], with the material being developed as a high- ϵ capacitor. In 1945 it was first used as a piezoelectric transducer^[20] when Robert B. Gray discovered that applying an external electric field of a suitable strength would cause the domains of certain ceramics, including barium titanate, to align and give rise to the electrical properties of ferroelectric single crystals. This electrical field became known as the poling field and is unique to each ferroelectric ceramic material, though in some cases the field required is prohibitively large for the material to be of use in bulk form.

Barium titanate has a room temperature permittivity $\epsilon' \approx 1000\text{-}5000$ ^[40] and a T_c of 130 °C. This value of T_c is lower than the corresponding values for PZT^[41], but significantly higher than any other materials known about at the time of its discovery. This led to it being of great commercial use in the 1950's, particularly in capacitors where it replaced TiO_2 , which had a room temperature permittivity of $\approx 80\text{-}90$ ^[6].

The structure of barium titanate varies with temperature, but is based on one of two systems: a non-ferroelectric hexagonal structure or a cubic close packed structure which may be ferroelectric. The hexagonal form exists at temperatures above 1460 °C^[8]. Below this the cubic close packed perovskite is more stable. The perovskite formed can itself take on a variety of different symmetries at various temperatures, three of which, the rhombohedral, orthorhombic and tetragonal, are ferroelectric. These forms exist at much lower temperatures, giving a T_c of 130 °C.

At each phase boundary, many of the electronic properties including dielectric permittivity, capacitance and piezoelectric operation modes are all enhanced, just as in the MPB region of PZT.

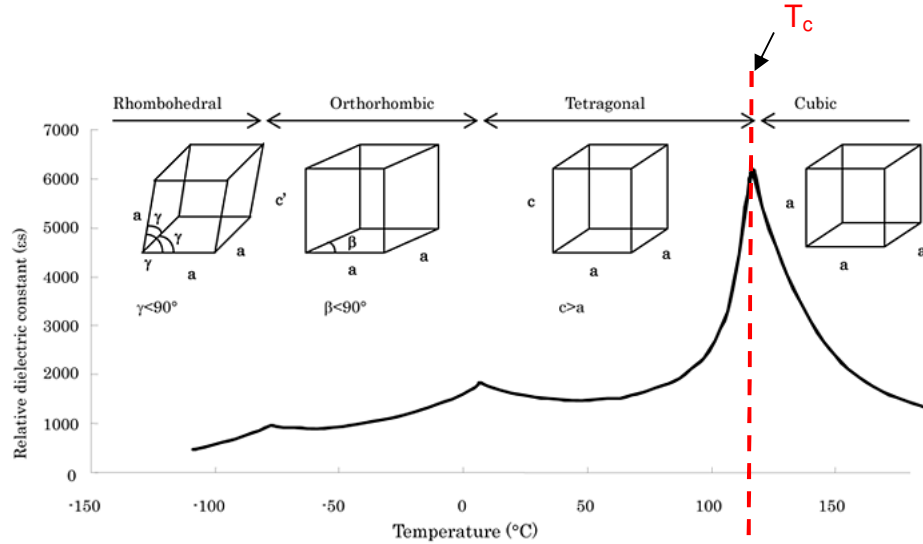


Figure 1.8: Cubic closed packed perovskite forms of BaTiO_3 showing transition temperatures, the direction of distortion accompanying each phase transition and accompanying peaks in the dielectric constant adapted from^[8]

The low temperature tetragonal, orthorhombic and rhombohedral ferroelectric polymorphs of barium titanate are typical piezoelectric perovskites of the type discussed in section 1.4. In the tetragonal form the Ti^{4+} ions are displaced along the c -axis. Depending on the orientation of the unit cell in any given domain, this gives rise to 6 possible axes of polarisation, figure 1.9^[8, 21].

In the orthorhombic unit cell the polarisation occurs along the face diagonal, giving rise to 12 axes of polarisation, whilst in the rhombohedral polymorph the polarisation occurs along the body diagonal. This gives rise to 8 possible axes of polarisation^[8, 21].

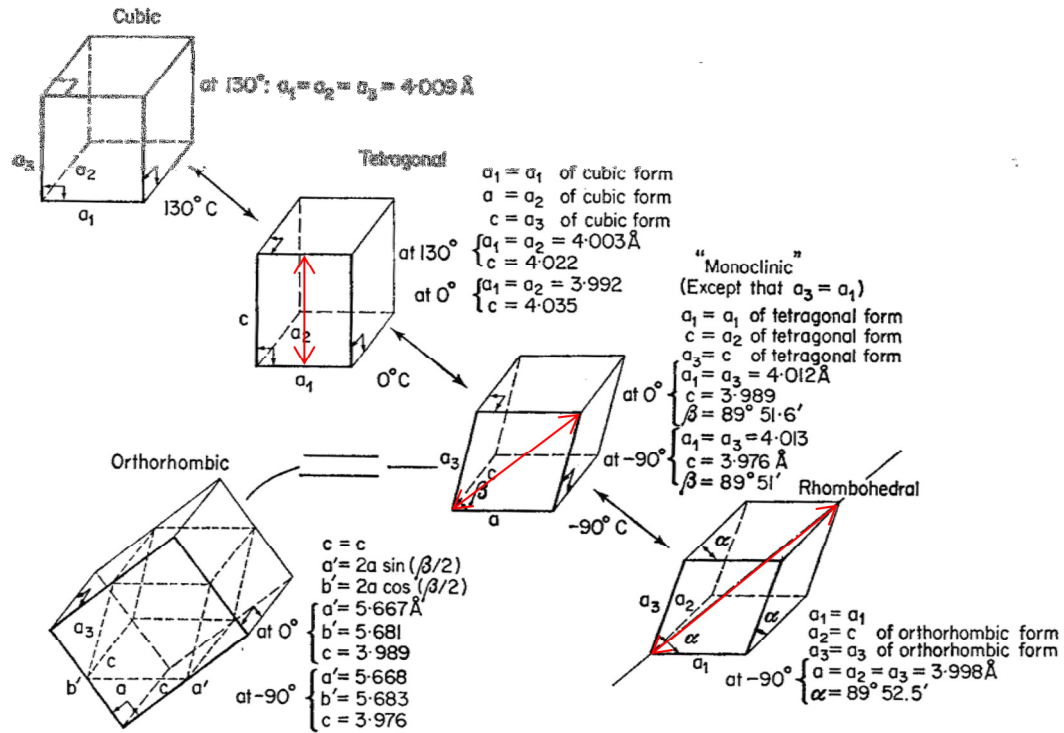


Figure 1.9: Unit cell distortions for each of the cubic close packed perovskite forms with the orientation of polarisation shown in red, adapted from [8]

The presence of different possible polarisation axes within a polymorphic phase gives rise to a complex domain structure in barium titanate and barium titanate based compositions. Each domain exists as a region of unit cells, all of which have the same axis of polarisation. Each domain is surrounded by other domains which have a different polarisation axis. The result of this is for the overall polarisation of the ceramic to be negligible due to the cancelling effects of the competing random domains. The application of an electric field to ferroelectric perovskites, such as BaTiO_3 , especially at temperatures above or near the Curie temperature, can lead to domains that are in alignment with the field growing at the expense of other domains resulting in a ceramic with a larger resultant polarisation. When barium titanate is cooled in such a field the domains become "locked" and the material is said to be poled. If the system is heated up once more to temperatures approaching that of T_c the thermal energy starts to become sufficient to allow for the re-randomisation of the orientation of the domains, a process known as depoling.

As well as thermal depoling, domains can become reoriented by the application of high compressive stresses. When applied in the direction of the polarisation, this can result in re-randomisation of the domain orientations^[42]. In un-doped BaTiO_3 the

domain walls are found to be fairly rigid with less than 10 % of 90° domains generally being re-orientated by the application of pressure, compared to up to 50 % of such domains in other materials, such as PZT^[6]. This means that BaTiO₃ and doped variations of it can be of particular use in applications such as high power acoustics, where high compressive stresses can lead to depoling.

The angles at which the adjacent domains form relative to each other are dependant on the 3-dimensional form of the unit cell, and thus vary with the polymorphic phase. In tetragonal BaTiO₃ the domains form at 90° and 180° to each other^[42]. In the orthorhombic phase domains also exist at 60° and 120°, whilst in the rhombohedral phase domain exist at ~ 70°, ~ 110° and 180° angles^[8, 42].

1.4.4: Doped barium titanate

As a perovskite material, barium titanate is able to accommodate many different dopants, both cationic and anionic. The majority of doped BaTiO₃ compositions, including the dopants studied in this thesis, are focused on cationic dopant substitution and thus this discussion will be limited to the effects of cationic dopants. Doping allows the physical properties of barium titanate, including T_C and its relative permittivity, to be tailored to a wide range of uses. Dopants can be added to shift T_C , often to lower temperatures such that the higher permittivities that occur near T_C occur closer to the working temperature of the device, generally around room temperature^[43-45]. Dopants can also cause T_C to be suppressed and the permittivity peak broadened, resulting in a flatter relative permittivity-temperature profile^[43, 46]. This can be used for capacitor type devices which do not require huge relative permittivities, but do require a more stable temperature profile and often a wider temperature range of operation.

Doping generally takes one of three forms. The first of these is isovalent doping which involves the substitution with a dopant species of the same charge as the species which it replaces. The second is acceptor doping which involves the partial substitution of cationic species with cations of a lower charge. The third type is donor doping which involves partial cation substitution with more highly charged

cations. Both the second and third types of doping involve partial substitution with a differently charged species than the original and are thus said to be aliovalent.

In order to maintain overall charge neutrality of the composition, it is a requirement that the system is charge compensated when any aliovalent doping occurs. This may arise through a number of mechanisms, including the creation of anion or cation vacancies or the addition of more than one dopant in such a ratio so as to result in an overall balancing of charge^[47], a mechanism known as self-compensation.

1.4.4.1: Isovalent doping

Isovalent doping can take the form of A-site doping with a 2+ cation such as Sr^{2+} , Ca^{2+} or Pb^{2+} , B-site doping with ions such as Zr^{4+} , Sn^{4+} or Hf^{4+} , or a combination of the two. In isolation, each of the dopants has been studied, figure 1.10, with SrTiO_3 addition causing a steady decrease in T_C of 3.7 °C for every per cent of dopant added and PbTiO_3 causing a steady 3.7 °C increase in T_C for each per cent of dopant addition. The addition of CaTiO_3 initially causes a slight increase in T_C with dopant levels of up to 8 %, before causing T_C to fall with further dopant addition^[8, 48].

The addition of these dopants also has an effect on the lower temperature phase transitions, tetragonal/orthorhombic and orthorhombic/rhombohedral, with each of the dopants causing a reduction in these transition temperatures. The exception to this is the effect of SrTiO_3 doping on the orthorhombic/rhombohedral transition which is negligible. These effects are summarised in table 1.1.

The addition of an isovalent B-site species, Zr^{4+} , Sn^{4+} and Hf^{4+} , also brings about a reduction in T_C , but in each case is accompanied by an increase in the transition temperatures of both of the two lower temperature transitions^[45, 49, 50]. This can lead to the phases coming together so as to form a triple point of the phases, which can be described as a polymorphic phase boundary, PPB[†]. Unlike MPB's which are compositional based and extend over a wide range in temperature, PPB's are limited

[†] There is a lot of ambiguity over the use of MPB and PPB in the literature with the two phrases often used interchangeably. In this study a phase boundary will be said to morphotropic if the boundary exists between two different polymorphs and exists over a wide temperature range. The term polymorphic phase boundary will be used to define a phase boundary that exists between 3 or more polymorphs over a relatively narrow temperature range.

to relatively narrow temperature windows, however, like MPB's there is a similar enhancement of the piezoelectric properties at the boundary. At the PPB a single broad peak in the dielectric constant is observed, with the dielectric constant being maximised but T_c lowered.

Figure 1.10 shows the effect of single isovalent dopants on the phase transitions of BaTiO_3 , with numerical values given in table 1.1. The presence of a PPB region with Zr^{4+} dopant addition can be observed at a dopant concentration of about 15-18 %^[8].

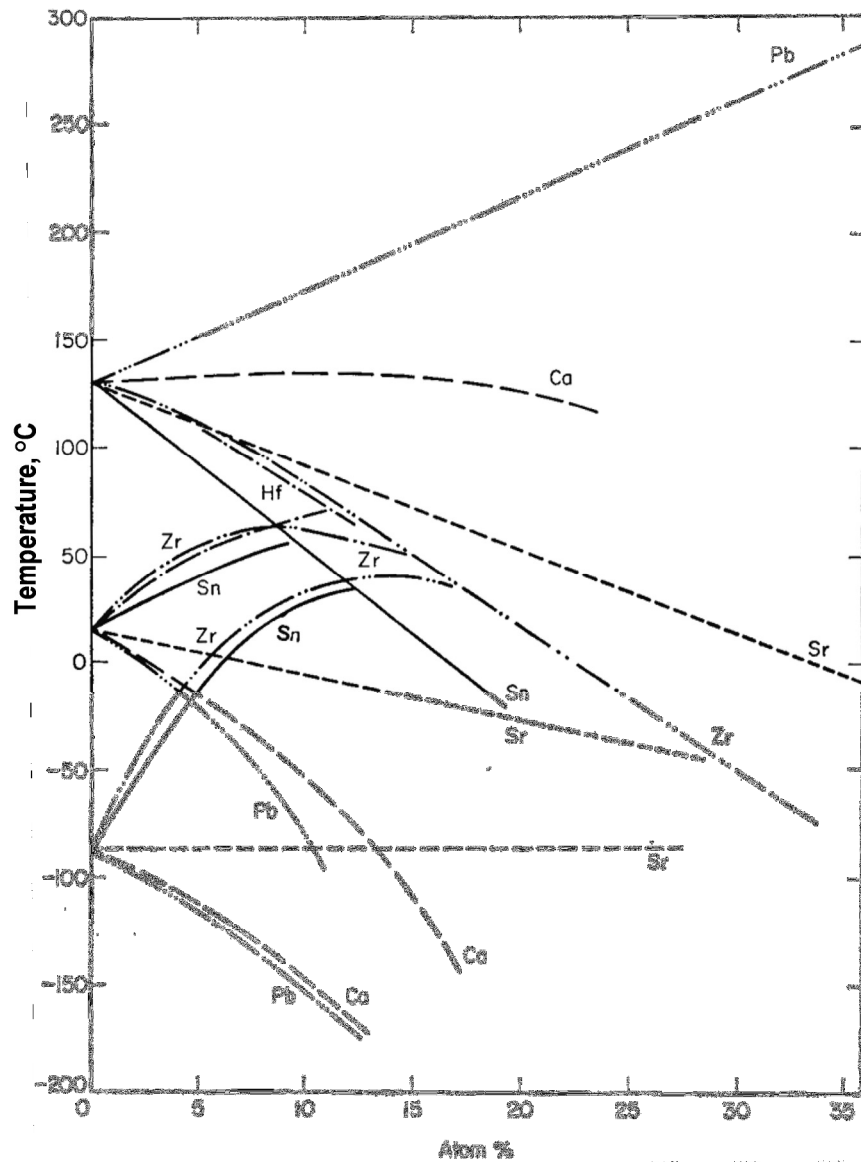


Figure 1.10: The effects of single ion doping with isovalent species on the phase transition temperatures of the various polymorphs of un-doped BaTiO_3 . Image reproduced from^[8]

Table 1.1: Effect of isovalent substitution on the phase transition temperatures of un-doped BaTiO₃, with data taken from^[8]

Dopant	ΔT_c (°C)	Orthorhombic/ tetragonal transition, $T_{O/T}$ (°C)	Rhombohedral/ orthorhombic transition, $T_{R/O}$ (°C)
PbTiO₃	+3.7	-9.5	-6.0
SrTiO₃	-3.7	-2	0
CaTiO₃	Non-linear	-6.7	-6.0
BaZrO₃	-5.3	-7	+18
BaSnO₃	-8	+5	+16
BaHfO₃	-5.0	+7	+16

As well as shifting the phase boundaries, the addition of dopants can also cause a change in the type of ferroelectric behaviour from that of a typical ferroelectric to a relaxor ferroelectric^[51], RFE, or ferroelectric with a diffuse phase transition, DPT. There is some discussion over the terminology with RFE generally being used where the ϵ'_{\max} and T_c are both frequency dependent, whilst DPT is used to describe systems with a frequency dependent ϵ'_{\max} which has a well-defined T_c . However the two terms are sometimes used interchangeably and it can be argued that a DPT is just a RFE with a minimal dispersion in T_c with frequency.

Relaxor materials are commercially important for devices including sensors, high permittivity capacitors, transducers and electromechanical actuators, due to the presence of a large broadened peak in the dielectric giving relatively large temperature ranges over which a high permittivity can be achieved. This is a feature which is common in BaTiO₃ based materials which have a PPB as a result of either isovalent or aliovalent doping.

Simultaneous isovalent substitution of both the A and B-site is generally considered to be a cumulative effect of each of the separate dopant species. The most extensively studied of these is CaZrO₃ addition, which shall be discussed further in section 1.4.4.6.

1.4.4.2: Aliovalent doping

Aliovalent doping can take the form of acceptor and donor doping, where the former involves the partial substitution of an original cationic species with a cationic species of lower positive charge, whilst donor doping involves cation replacement with a more highly charged ion. In both cases the dopant species can be accommodated on the A- or B-site as well as a mixture of both, depending on the size of the dopant ion species.

Acceptor doping with a single dopant species such as Fe^{3+} , Mg^{2+} or Mn^{2+} in place of Ti^{4+} generally have a limited solubility in the lattice and are accommodated by the formation of oxygen vacancies^[41, 52]. These materials often exhibit significant aging of the ferroelectric properties which can be observed by the presence of a double hysteresis loop^[53]. The addition of donor species such as La^{3+} in place of Ba^{2+} or Nb^{5+} in place of Ti^{4+} is often accompanied by B-site vacancies^[54, 55]. Their addition often results in a marked decrease in the resistance of the material, with n-type semi-conduction being possible in many donor doped systems at low dopant concentrations^[41, 56].

The addition of donor species generally results in the formation of cation vacancies in the lattice in order to compensate for the higher charge of the donor ion. Donor ions most commonly take the form of a +3 ion substituting for Ba^{2+} or a +5 ion substituting for Ti^{4+} . Initially it was thought that doping with a +3 cation would result in A-site vacancies, however it was later shown that the vacancies formed on the B-site^[54, 57]. In addition to the B-site vacancies oxygen is lost from the lattice resulting in anion vacancies which can result in semi-conductor properties. The addition of a +5 cation such as Nb also creates Ti (B-site) vacancies in order to compensate for the Nb^{5+} charge^[55]. The oxygen vacancies formed when BaTiO_3 is doped with a donor species are often able to be either partially or fully filled by heating the material in an oxygen enriched atmosphere or by slow cooling, resulting in more insulating pellets. Thus the synthesis conditions for these materials can play a large part in determining the properties of the materials.

The addition of donor dopants such as niobium has also been shown to be able to produce materials which exhibit a positive temperature coefficient of resistance, PCTR^[58]. Above T_C there is a large increase in the resistivity, with a change in gradient observed at T_C . Explanations for this are varied, but are generally based on grain boundary effects^[58].

The addition of a donor or acceptor aliovalent species can significantly alter the resistance of the material and can result in ceramics ranging from highly insulating dielectrics to semi-conductors and PTCRs. This is due to a change in the conduction mechanisms of the materials shifting from a p-type mechanism in un-doped or acceptor doped BaTiO₃ to n-type in acceptor doped materials. This will be discussed in more detail in chapter 6.

The addition of two aliovalent species that self-compensate has the advantage of allowing for the manipulation of T_C without the added complications of cation/anion vacancies or other charge compensation routes, whilst allowing for a greater range of compounds to be studied than the rather limited choice of available 2+ and 4+ cations of the appropriate size.

Several such +3/+3 self-compensating aliovalent systems have been studied^[59-63], as well as a large number of compositions which incorporate multiple different dopant species on each site^[64-67]. This has led to a range of diverse properties including relaxor ferroelectrics, high piezoelectric coefficients and positive temperature coefficients of resistivity with a wide variation in the temperature ranges and magnitudes of these properties. As such, the scope of barium titanate-based perovskites for forming novel materials with piezo-, pyro- or ferroelectric properties is extensive. Accordingly, this work shall focus on judiciously chosen co-dopant pairs, either isovalent with BaTiO₃, or aliovalent +3/+3 charge compensated pairs, which shall allow for comparisons to be made between the differently doped compositions.

1.4.4.3: Kröger Vink notation

Kröger Vink notation^[68] is used to describe point defects, to concisely show what dopant or impurity is present in a material, as well as its location and the effect it

causes with regards to ion vacancies, changes in the oxidation state of a site, release of electrons or formation of electron holes. Each component species represented in Kroger Vink notation takes the form M_S^C , where M can be an elemental species denoted by the appropriate chemical symbol, a vacancy, denoted as V, an electron, e, or an electron hole, h. The superscript C gives information on the change in charge relative to the un-doped lattice caused by the species with x used to denote no change, • a positive charge and ' a negative charge. The subscript S indicates the lattice site occupied by the species.

Thus Gd_{Ba}^{\bullet} would indicated a gadolinium species occupying the barium site with a charge of +1 greater than expected of the Ba site, *i.e.* Gd^{3+} on a Ba^{2+} site.

1.4.4.4: Size effects of dopants

The effect of introducing dopant species of a different size to the perovskite lattice is to alter the tolerance factor of the material. This has an effect on the stability of the various polymorphic phases, cubic, tetragonal, orthorhombic and rhombohedral. $BaTiO_3$ is known to have a tetragonal room temperature phase and has a tolerance factor greater than 1^[8]. If a smaller A-site cation species is added the tolerance factor will be reduced. This would give a tolerance factor closer to 1 and hence stabilises the cubic phase to lower temperatures, reducing T_C . Similarly a smaller B-site species would be expected to increase T_C .

Vergard's law^[69] predicts that the change in the lattice constant upon dopant addition will be linearly dependant on the concentration of the dopant species added, assuming that the temperature of the system is maintained as a constant. This law is based on the assumption that the ions present can be treated as hard spheres which are being packed together. Thus a relationship between the lattice constants and dopant concentration as a function of size difference between the ion species can be established.

This linear change in the lattice constants as a result of increasing dopant addition results in a linear change in the Curie temperature of the material, with smaller lattices resulting in lower T_C 's as shown in table 1.1. This size-only argument is only

valid where there are no other significant contributions to T_C such as a change in the charge of the dopant species, a change from the perovskite structure due to a vastly different sized cation dopant, or significant strain contributions.

However, for many species, including Ca^{2+} , these sorts of size-effect based arguments do not appear to fit with the observed data^[70, 71] suggesting more subtle effects are also having an impact in many cases.

1.4.4.5: Strain effects of dopants

Initially established by Attfield et al.^[72] when studying magnetic transition temperatures (T_m) in magnetoresistive manganese perovskites, it was noted that the cation size variance as well as average cation size can have a significant effect on T_m , where the variance is a measure of size-mismatch between differing A-site cations, equation 1.5. By synthesising a range of compositions of the form $\text{Ln}_{0.7}\text{M}_{0.3}\text{MnO}_3$, where Ln was a mixture of one or more of La, Pr and Nd and M was a mixture of one or more of Ca, Sr and Ba such that the overall average cation radius $\langle r_A \rangle$ was constant ($\langle r_A \rangle = 1.23 \text{ \AA}$), it was possible to isolate the effect of variance, σ^2 , on T_m . It was found that changing the variance led to systematic trends in bond angles and lengths, though with the overall cell volume remaining approximately constant, as well as a linear decrease in T_m with increasing variance. The concept of variance was then studied in ferroelectric perovskites by Sinclair and Attfield^[71], where it was shown that T_C increased linearly with A-cation size variance in ATiO_3 perovskites for a series of (Ba, Sr, Ca) TiO_3 compositions, figure 1.11.

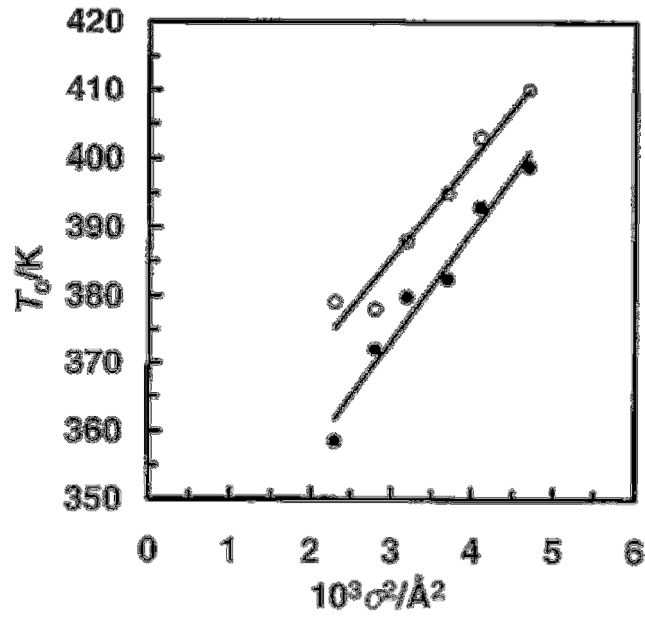


Figure 1.11: Variation in T_c with σ^2 , open and filled circles correspond to data obtained from permittivity and DSC measurements respectively, taken from^[71]

Cation size variance in doped perovskites can be described as a size mismatch between cations located on the same site, creating a strain on the lattice. This strain can be mathematically modelled by equation 1.5, where r_A is the mean ionic radii of the A-site species.

$$\sigma^2 = \langle r_A^2 \rangle - \langle r_A \rangle^2 \quad \text{Equation 1.5}$$

Ca dopant addition to BaTiO_3 was known to cause changes to T_c that could not be explained by simple size-only rules. Work by Attfield et al.^[71], was able to show that the effect of strain may be integral in determining the shifts observed in T_c when certain dopant species are added to the perovskite lattice, such as Ca. They were able to show that the increase in T_c observed at low Ca doping levels could be reduced to a linear decrease if the strain effect at each dopant concentration was calculated and subtracted from the raw data, figure 1.12.

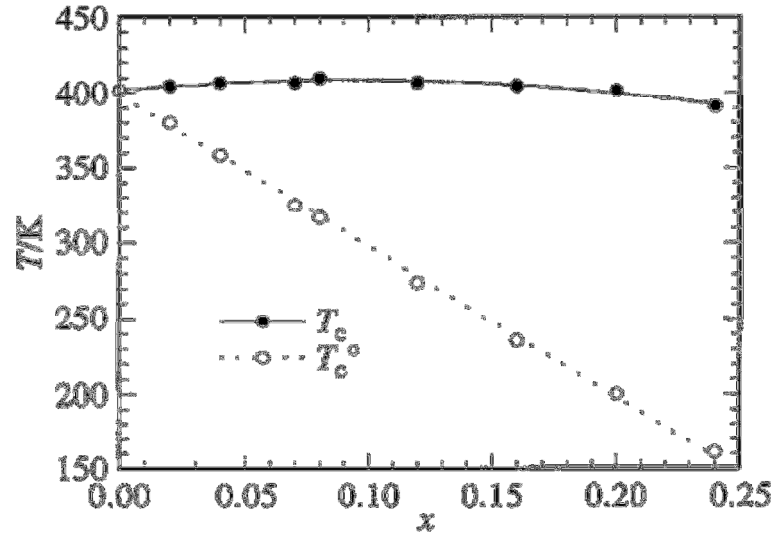


Figure 1.12: The variation in T_C for $\text{Ba}_{1-x}\text{Ca}_x\text{TiO}_3$ taken from^[48] and corrected for strain^[71], image taken from^[71]

This suggests that in most systems T_C is affected by both average cation size effects and a strain effect caused by the A-cation size variance. The effect on T_C due to size and strain is additive, with decreasing $\langle r_A \rangle$ lowering T_C due to long-range size effects, but also resulting in higher σ^2 which raises T_C due to increased strain. These two competing effects both need to be taken into account when looking at the effects of dopant addition on the Curie temperature of a material.

1.4.4.6: Barium zirconium titanate - barium calcium titanate, BZT-BCT

The combination of adding both CaTiO_3 and BaZrO_3 isovalent dopants to BaTiO_3 has been of considerable study since the late 1950s with the aim of improving various aspects of BaTiO_3 including its piezoelectric properties, T_C , poling fields and ferroelectric aging, although initially the compositions studied were generally doped with a range of A-site and B-site dopants alongside Ca and Zr^[73-75]. More recently compositions containing only Ca and Zr dopants have been closely studied with the aim of creating a lead-free piezoelectric with high d_{33} coefficients whilst maintaining a high T_C ^[76-79]. This takes advantage of the effect of calcium dopant ions in keeping T_C high whilst using zirconium to bring up the temperatures of the two lower temperature transitions forming a PPB with enhanced properties, figure 1.13.

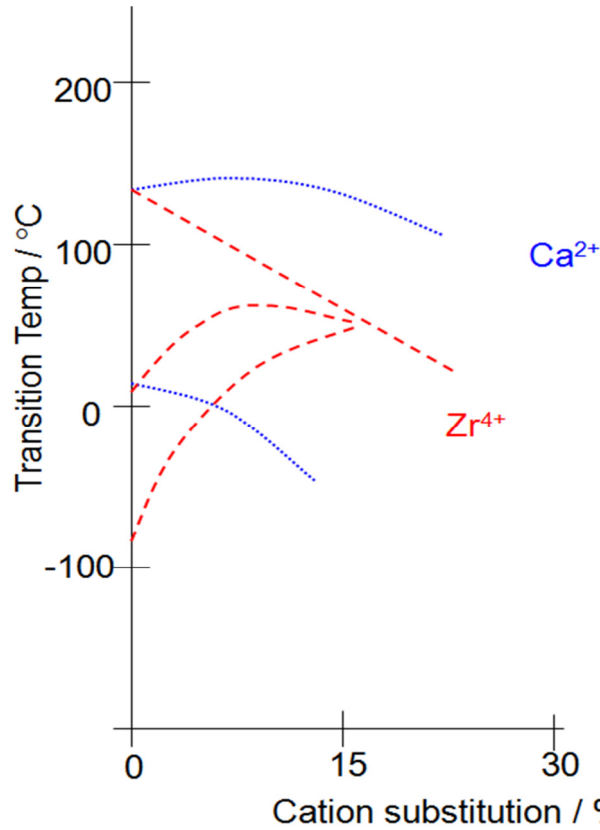


Figure 1.13: Representation of the effects of doping BaTiO₃ with Ca²⁺ and Zr⁴⁺, adapted from [8].

In 2008 Ren et al. synthesised a series of compositions of the form Ba(Ti_{0.8}Zr_{0.2})O₃ – $\delta\%$ [(Ba_{0.7}Ca_{0.3})TiO₃], some of which exhibited very high dielectric coefficients: $d_{33} = 584 \text{ pC N}^{-1}$ ^[30, 80] as shown in figure 1.14. This anomalously high value was found to exist for the $\delta = 50$ composition, with substantially lower d_{33} values occurring for slightly varying compositions. The maximum value is comparable to the best values obtained for PZT based ceramics, (PZT-5H, $d_{33} = 590 \text{ pC N}^{-1}$ ^[30] shown in figure 1.15-e, and was assigned as being resultant of an MPB (PPB) between the rhombohedral and tetragonal phase over the composition range [Ba(Ti_{0.8}Zr_{0.2})O₃] – $\delta\%$ [(Ba_{0.7}Ca_{0.3})TiO₃] where $\delta = 40 - 60 \%$ ^[30], figure 1.15-a-d. This was based on the fact that Ba(Ti_xZr_{1-x})O₃ adopts a rhombohedral structure at room temperature for $0.1 < x < 0.5$ whereas (Ba_{1-y}Ca_y)TiO₃ adopts a tetragonal structure at room temperature for compositions where $0.1 < y < 0.7$, and the absence of any noticeable orthorhombic phase, along with the enhanced piezoelectric properties.

As well as piezoelectric factors of the same magnitude as the best PZT based compositions and significantly higher than many other lead-free systems, figure

1.15×10^{-4} , plus exceptionally high electrostriction, figure 1.15-f, BZT – δ % BCT compounds did not suffer volatilisation or hygroscopic problems of the sort expected in KNN based composition. It also has relatively low production costs compared to Na or Ta based compositions^[30], and is lead-free.

Other compositions based on $\text{Ba}(\text{Ti}_{0.85}\text{Zr}_{0.15})\text{O}_3 - \delta \%[(\text{Ba}_{0.8}\text{Ca}_{0.2})\text{TiO}_3]$ have also been synthesised and have been found to show similar behaviour, with a maximum d_{33} value of 450 pC/N ^[81].

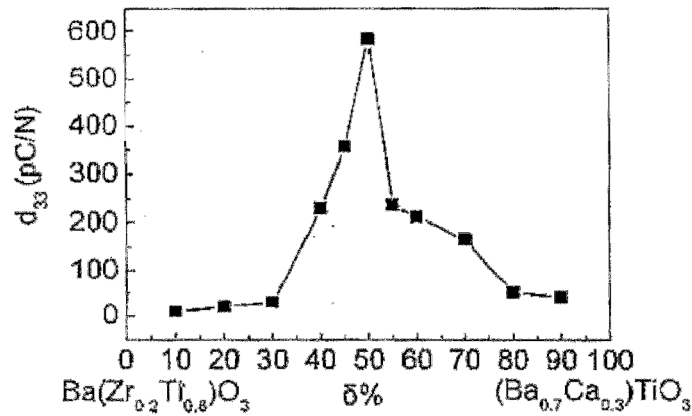


Figure 1.14: Dramatic increase observed in the piezoelectric coefficient d_{33} in 50 % $[\text{Ba}(\text{Ti}_{0.8}\text{Zr}_{0.2})\text{O}_3] - 50 \%[(\text{Ba}_{0.7}\text{Ca}_{0.3})\text{TiO}_3]$ ^[30]

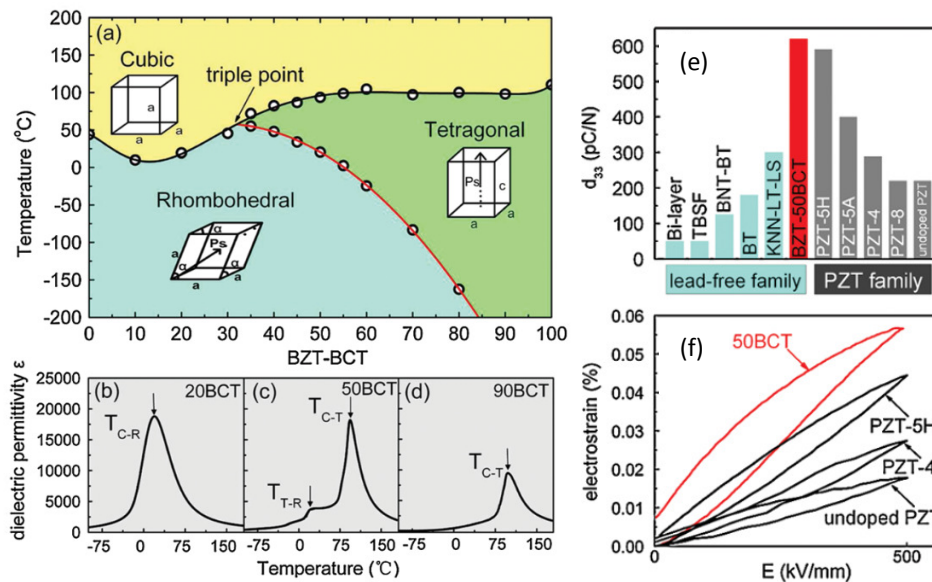


Figure 1.15: Structural phase diagram and enhanced properties of 50 % $[\text{Ba}(\text{Ti}_{0.8}\text{Zr}_{0.2})\text{O}_3] - 50 \%[(\text{Ba}_{0.7}\text{Ca}_{0.3})\text{TiO}_3]$ ^[80] compared to other piezo- and ferroelectric materials.

[†] Bi-layer = Bismuth based Aurivillius phases, e.g. $\text{Bi}_4\text{Ti}_3\text{O}_{12}$, $\text{SrBi}_2\text{Nb}_2\text{O}_9$ or $\text{SrBi}_2\text{Ta}_2\text{O}_9$.

TBSF = Tetragonal tungsten bronze structured ferroelectrics, e.g. $\text{Sr}_{0.5}\text{Ba}_{0.5}\text{Nb}_2\text{O}_6$

BNT-BT = $\text{Bi}_{0.5}\text{Na}_{0.5}\text{TiO}_3 - \text{BaTiO}_3$

BT = BaTiO_3

KNN-LT-LS = $(\text{K}, \text{Na})\text{NbO}_3 - \text{LiTaO}_3 - \text{LiSbO}_3$

It has subsequently been shown that the presence of an orthorhombic phase does exist over this compositional range, though with only over a very limited temperature range^[82] with the new structural phase diagram shown in figure 1.16. This diagram also shows that the orthorhombic region should be present at lower Ca and Zr dopant concentrations, such as in the composition $\text{Ba}(\text{Ti}_{0.85}\text{Zr}_{0.15})\text{O}_3 - \delta$ $\%[(\text{Ba}_{0.8}\text{Ca}_{0.2})\text{TiO}_3]$ ^[81] which also show anomalously high d_{33} values, originally explained as due to an MPB between the rhombohedral and tetragonal phase.

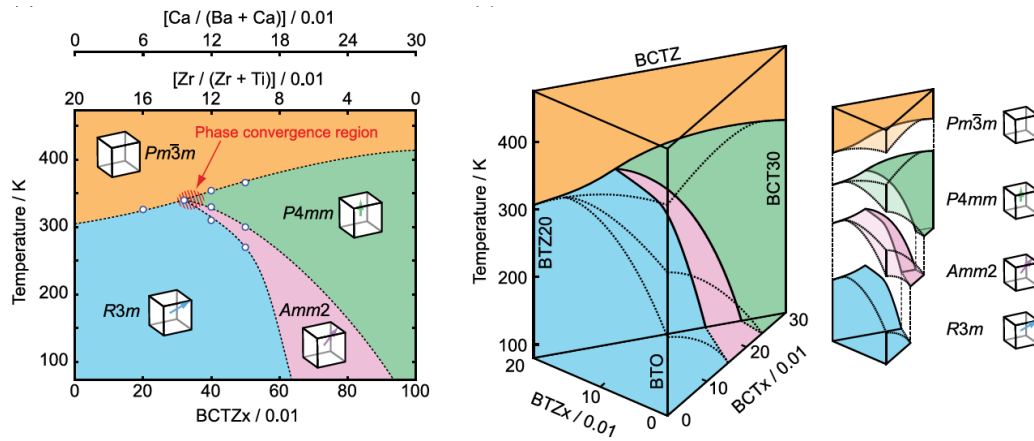


Figure 1.16: Revised phase diagram for 50 % $[\text{Ba}(\text{Ti}_{0.8}\text{Zr}_{0.2})\text{O}_3] - 50 \%[(\text{Ba}_{0.7}\text{Ca}_{0.3})\text{TiO}_3]$ showing the presence of an orthorhombic region^[82]

The presence of an orthorhombic phase means that an MPB (PPB) between the rhombohedral and tetragonal phases cannot exist and thus can't be the cause of the heightened properties. However, the narrow temperature region over which the orthorhombic phase is stable does suggest that around the temperature of convergence all four phases would have similar energies, and thus a PPB between all four phases may be the cause of the increased piezoelectric responses.

This is likely to be the case in a whole variety of compositions doped with varying amounts of Ca and Zr which exhibit heightened piezoelectric properties and stabilised T_C 's^[78, 79, 81, 83-85].

1.5: Crystalline ceramic materials

The materials made and studied in this report are all ceramic materials; inorganic compounds which have been sintered to produce dense, polycrystalline pellets. Each

pellet is made up of a series of grains connected by grain boundaries (figure 1.17), and hence their properties are resultant of both the grain boundary and bulk contributions. The grains are of large enough size and homogeneous enough nature for the materials to be considered crystalline for X-ray purposes, i.e. that the material has a lattice and motif that repeats without variation over distances consistent with many unit cells, such that each individual unit cell can be said to be in an identical environment.

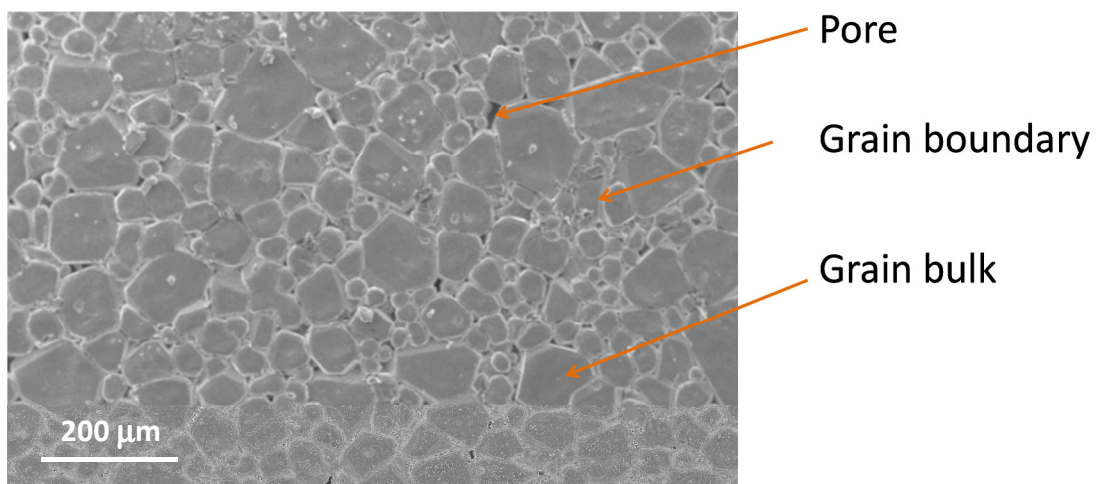


Figure 1.17: Pellet surface showing the presence of a series of grains surrounded by regions of grain boundaries and isolated pores

1.5.1: Grain growth

The synthesis of ceramic monoliths generally uses finely ground particles of pre-reacted or calcined starting reagents which are then firmly pressed into the desired pellet shape, often using a uniaxial or oil press to apply greater forces and thus maximise the resulting pellet density, in a process which is described in section 3.1. During the sintering process “necks” form along the touching edges of neighbouring particles, with a grain boundary forming along each neck. The interstice between particles becomes a pore. As the sintering progresses the pores become more rounded and shrink as the material becomes denser. Atomic diffusion from the bulk to the neck allows for grain growth with neighbouring grains starting to coalesce into larger grains surrounding by well-defined boundary regions. The driving force for the

sintering process is reduction in the surface area of the particles/grains due to the higher energies associated with the surface than the grain boundary or bulk. The grain growth process is depicted in figure 1.18.

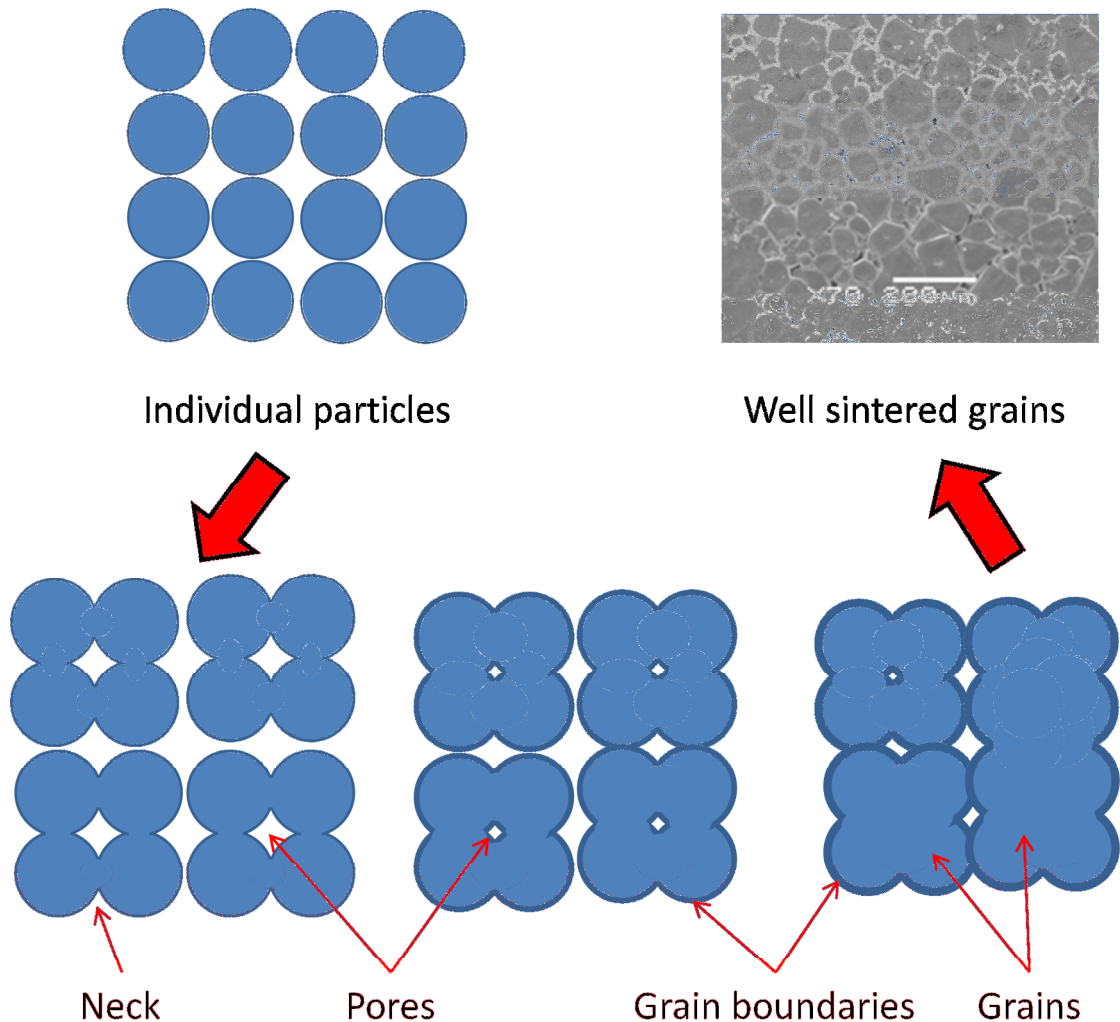


Figure 1.18: Grain growth in ceramics, “showing necking”, the formation of pores, grains and grain boundaries

Grain growth is highly dependent on the sintering temperature, dwell time, heating and cooling ramp rates, impurity levels and composition, and thus is impossible to fully control or predict. However, careful control of the sintering conditions can lead to reasonably reproducible microstructures, and hence reproducible properties.

1.5.2: Grain size effects

Unlike in single crystals where precise values can be established for the various piezoelectric response and permittivity for each composition, this is not possible for ceramics. The microstructure of the material inevitably varies with each individual

ceramic synthesised. Each has a different domain structure, which itself can vary over the lifetime of the ceramic when exposed to heat, electric fields or stress. In addition, all ceramics will possess some level of impurities and defects which can have an impact of the pellet's physical properties. This results in subtly different properties in each pellet.

The grain size can have a significant effect on the properties of the material, impacting alignment of domains and their reorientation. Although it is possible to try and control the grain size by careful selection of heating temperatures and times, it cannot be fully controlled, particularly where there are large numbers of variables between samples, such as different levels of dopants or different types of dopants. Thus it is not always possible to compare sample of like grain sizes.

In un-doped BaTiO_3 it is found that the dielectric constant increases with decreasing grain sizes when in a ferroelectric phase, particularly the lower temperature phases, but has little dependency when in a paraelectric state^[86, 87], figure 1.19.

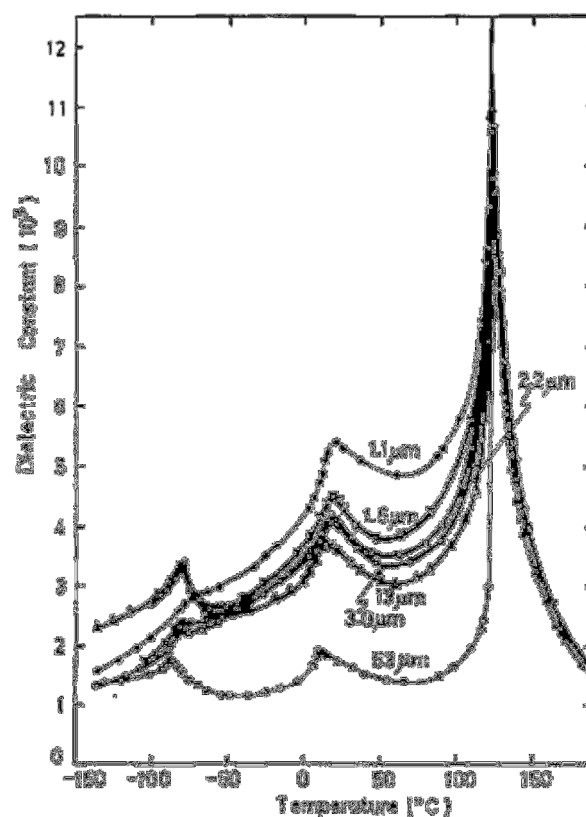


Figure 1.19: The effect of grain size on the dielectric constant of high-purity BaTiO_3 ^[86]

1.6: The scope of this project

The aim of this research is to study novel lead-free piezoelectric materials which, through careful dopant selection, have polymorphic phase boundaries. The research focuses on three sub-aims. Firstly to synthesis some new lead-free materials which have T_C 's suitable for device applications, such as medical ultrasound or underwater sonar. This will require T_C to be not lower than ~ 70 °C. The second aim is to understand the properties of these materials, particularly with regards to the intrinsic properties of the materials and also properties that arise as a result of the microstructure of the material, with work carried out to try and optimise the microstructure so as to get the best possible properties, including pellet reproducibility, ϵ' and T_C for each composition. This is something of great importance to industry, but which is commonly overlooked in more academic studies to some extent. Thirdly this work aims to gain some insight as to the differing contributions to changes in T_C as a result of average size effects, strain (variance) and charge. Some simple size based arguments are already known and can be utilised for the prediction of changes to T_C at a qualitative level. Work by Sinclair et al.^[71] have introduced strain effects which can be calculated as variance and added to the size-only effects. This work also incorporates the effect of changes in cation charges on the A and B site and hopes to show the relative magnitudes of the effects on T_C from each contribution: size, strain and charge. This may be useful when choosing other complex groups of dopants for future studies into BaTiO₃-based compositions.

This work will focus on materials which are doped simultaneously with an A-site and B-site dopant. This dopant pairs will consist of ions with either +2/+4 charges or +3/+3 charges, such that the systems are charge-compensating. In each case the same amount of A-site and B-site dopant species will be added. This will allow for comparisons to be made between the +2/+4 and +3/+3 doped systems.

Four series of dopant pairs are to be studied in this project:

- Sr^{2+} and Zr^{4+}
- Ca^{2+} and Zr^{4+}
- La^{3+} and Sc^{3+}
- Gd^{3+} and Sc^{3+}

These pairs have been carefully selected based on the individual cation ionic radii, the combined A-site and B-site change to the cation radii and the ion charges. Ions were selected with the requirement that they did not easily form compositions with mixed valence. They were also selected to result in a tolerance factor conducive to forming a perovskite material.

Chapter 4 focuses on the influence of processing and the microstructure of the pellets on the electrical properties, aiming to show how the properties can be studied to determine whether the microstructure is causing any significant detriment of the electrical properties. In particular the effects of different types of porosity and cracking, the impact of grain boundary contributions to the electronic responses of the materials and the optimisation of the processing conditions will be shown and discussed.

Optical and scanning electronic microscopy apparatus were used to study both pellet cracking and grain growth of materials having been formed using differing synthesis conditions. Analysis of dielectric data will be utilised to show the effects of capping by regions of “parasitic” capacitance including the grain boundary microstructure, with high temperature immittance data being used to confirm the relative levels of grain boundary presence in the materials. The effects of changing atmosphere will be briefly looked at, focusing on materials which exhibit some air-sensitivity. Finally the chapter will look at irregular peaks in the dielectric data, which can arise due to inhomogeneity of the pellet as opposed to being inherent of the composition, and will show how careful data analysis and synthesis can be used to remove such inhomogeneity and yield pellets with electrical properties which are resultant of the desired stoichiometry.

Chapter 5 discusses the effects of each of the dopant pairs on the phase transitions. The transition temperatures were established by analysis of dielectric spectroscopy

data, with variable temperature X-ray diffraction data used to confirm the crystal classes associated with each event observed in the dielectric data. Trends in T_C are discussed, considering both the level of dopant addition as well as the dopant species, with particular emphasis on the differences in size, strain and charge of the doped compositions. There is also discussion on the formation of materials that exhibit a PPB, with some analysis on the structure of these materials at the point of phase coalescence and beyond. Some analysis of the effects of dopant addition on the ferroelectric properties of these materials as a function of temperature is also presented, as studied by the use of variable temperature hysteresis measurements.

Chapter 6 is a study of the high temperature immittance data of these materials. This yields information on the bulk and grain boundary contributions to each pellet, with SEM used to confirm the presence of either well sintered ceramics, or poorly sintered, “necked” ceramics. This chapter focuses on the activation energies on the bulk component of each composition. Evidence of two conduction mechanisms is presented with some explanation given as to the methods of conduction in these materials as well as offering an explanation for the observed change between conduction mechanisms.

Chapter 7 is a brief study into the size, strain-variance and charge-dilution effects on T_C . It aims to show how the cumulative result of these components to T_C can be deconvoluted to some extent. This enables the relative magnitudes that each component has on T_C to be approximated. This is based on simple models, utilising the sizes, strains and charges of the different dopant pairs studied, which can approximate: size-only; size and strain-variance; and size, strain-variance and charge-dilution based systems.

Final conclusions of the project are then presented along with some ideas for future work on this topic.

References

1. Newnham, R.E., *Phase transformations in smart materials*. Acta Cryst. A, 1998. **54**: p. 729-737.
2. Wolny, W.W., *Application driven industrial development of piezoceramics*. J. Eur. Ceram. Soc., 2005. **25**(12): p. 1971-1976.
3. Chen, Q.X., et al., *A new laser-ultrasound transducer for medical applications*. Ultrasonics, 1994. **32**(4): p. 309-313.
4. Moynihan, E.R., P.A. Hoisington, and D.W. Gailus, *Perovskite thin-film ink jet transducer*. 1997: US: 5500988.
5. Nudelman, I. and A. Rybyanets, *Piezoelectric transducer for medical application such as ultrasound imaging, has piezoelectric structure and electrically conductive layers that are arranged to form several separate series-connected transducer elements*. 2009, Ultrashape LTD (ULTR-Non-standard): US: 7709997.
6. Moulson, A.J. and J.M. Herbert, *Electroceramics*. 1997: Chapman & Hall.
7. Callister Jr, W.D., *Materials Science and Engineering, An Introduction*. 7th ed. 2007: Wiley.
8. Jaffe, B., W.R. Cook, and H. Jaffe, *Piezoelectric Ceramics*. 1971: Academic Press London.
9. Kutz, M., *Handbook of materials*. 2002, John Wiley & Sons. p. 403.
10. Haertling, G.H., *Ferroelectric Ceramics: History and Technology*. J. Am. Ceram. Soc., 1999. **82**(4): p. 797-818.
11. *Merriam-Webster's Collegiate Dictionary*. 11th ed. 2004. p. 1014.
12. Goldschmidt, V.M., *Die Gesetze der Krystallochemie*. Die Naturwissenschaften, 1926. **21**: p. 477-487.
13. Cohen, R.E., *Origin of ferroelectricity in perovskite oxides*. Nature, 1992. **358**(6382): p. 136-138.
14. Lin, D.M. and K.W. Kwok, *Dielectric and piezoelectric properties of $(\text{Bi}_{1-x-y}\text{Nd}_x\text{Na}_{1-y})(0.5)\text{Ba}_y\text{TiO}_3$ lead-free ceramics*. Curr. Appl. Phys. **10**(2): p. 422-427.
15. Ye, F., et al., *Incommensurate magnetic structure in the orthorhombic perovskite ErMnO_3* . Phys. Rev. B, 2007. **76**.

16. Wong-Ng, W., et al., *Crystal structure of the monoclinic perovskite $Sr_{3.94}Ca_{1.31}Bi_{2.70}O_{12}$* . Powder Diffr., 2000. **15**(4): p. 227-233.
17. Buchanan, R.C., *Ceramic Materials for electronics*. 3rd Edition ed. Mater. Eng. S. 2004: Marcel Dekker. 676.
18. Curie, J. and P. Curie, *Développement, par pression, de l'électricité polaire dans les cristaux hémihédres à faces inclinées*. Bull. Soc. Min De France, 1880. **3**(90): p. 294-295.
19. Marrison, W.A., *The Evolution of the Quartz Crystal Clock*. The Bell System Technical Journal, 1948. **Vol. XXVII**: p. 510-588.
20. Gray, R.B., *Transducer and method making the same*. 1949: US: 2486560.
21. Heywang, W., K. Lubitz, and W. Wersing, eds. *Piezoelectricity : Evolution and Future of a Technology*. Springer Series Mate. 2008, Springer.
22. Alexe, M., et al., *Energy Harvesting Using Nanowires? (vol 317,pg 780, 2007)*. Advanced Materials, 2008. **20**(24): p. 4624-4624.
23. Wang, X.D., et al., *Direct-current nanogenerator driven by ultrasonic waves*. Science, 2007. **316**(5821): p. 102-105.
24. Granstrom, J., et al., *Energy harvesting from a backpack instrumented with piezoelectric shoulder straps*. Smart Mater. Struct., 2007. **16**(5): p. 1810-1820.
25. Arnold, D.P. and T. Nishida, *Dual-Mode Piezoelectric/Magnetic Vibrational Energy Harvester*. 2011, University of Florida Research Foundation Inc. : US: 0215590.
26. Lee, S.K. and Y.S. Yang, *Apparatus for harvesting and storing piezoelectric energy and manufacturing method thereof*. 2013, Electronics and Telecommunications Research Institute, S. Korea . US: 0049539A1.
27. Prewitt, A.D. and J.L. Jones, *Effects of the Poling Process on Piezoelectric Properties in Lead Zirconate Titanate Ceramics*. Ferroelectrics, 2011. **49**(1).
28. Maunders, C., et al., *Electron diffraction and microscopy study of the structure and microstructure of the hexagonal perovskite $Ba_3Ti_2MnO_9$* . Acta Cryst. B, 2007. **63**: p. 390-395.
29. Baettig, P., et al., *Theoretical prediction of new high-performance lead-free piezoelectrics*. Chem. Mater., 2005. **17**(6): p. 1376-1380.

30. Ren, X. and W. Lui, *Non-Lead-Type piezoelectric Material*, N.I.f.M.S. [JP], Editor. 2009: Japan: 054540.
31. *Directive 2002/95/EC of the European parliament and of the council of 27 January 2003 on the restriction of the use of certain hazardous substances in electrical and electronic equipment*. 2003: Brussels.
32. (1997) *IUPAC Compendium of Chemical Terminology*,.
33. Zhang, S.J., R. Xia, and T.R. Shrout, *Lead-free piezoelectric ceramics vs. PZT?* J. Electroceram., 2007. **19**(4): p. 251-257.
34. Egerton, L. and D.M. Dillon, *Piezoelectric and dielectric properties of ceramics in the system potassium sodium niobate*. J. Am. Ceram. Soc., 1959. **42**(9): p. 438-42.
35. Lin, D.M., et al., *Structure, piezoelectric and ferroelectric properties of Li- and Sb-modified $K_{0.5}Na_{0.5}NbO_3$ lead-free ceramics*. J. Phys. D. Appl. Phys., 2007. **40**(11): p. 3500-3505.
36. Wainer, E. and A.N. Salomon, *High Dielectric Constant Ceramics*, T.A.M. Company, Editor. 1943: US: 2377910.
37. Wainer, E. and A.N. Salomon, *Ceramics of high-dielectric constant*. 1945, Titanium Alloy Mfg. Co. : US: 1943-489382.
38. Thurnauer, H. and J. Deaderick, *Insulating material*. 1947, American Lava Corp.: US: 2429588.
39. Wainer, E., *High-dielectric material*. 1946, The Titanium Alloy Manufacturing Company US: 2402515.
40. Zhao, Z., et al., *Grain-size effects on the ferroelectric behavior of dense nanocrystalline $BaTiO_3$ ceramics*. Phys. Rev. B, 2004. **70**(2): p. 8.
41. Moulson, A.J. and J.M. Herbert, *Electroceramics*. 2 ed. 2003: Wiley.
42. Lines, M.E. and A.M. Glass, *Principles and Applications of Ferroelectrics and Related Materials*. Oxford Classic Texts in the Physical Sciences. 2001: Oxford University Press Inc., New York.
43. Yun, S. and X. Wang, *Dielectric properties of $(Ba_{1-2x}Sr_xCa_x)TiO_3$ ferroelectric ceramics*. J. Electroceram., 2008. **21**(1-4): p. 585-588.

44. Reddy, S.B., K.P. Rao, and M.S.R. Rao, *Structural and dielectric characterization of Sr substituted Ba(Zr,Ti)O₃ based functional materials*. Appl. Phys. A-Mater., 2007. **89**(4): p. 1011-1015.
45. Dong, L., D.S. Stone, and R.S. Lakes, *Enhanced dielectric and piezoelectric properties of xBaZrO₃-(1-x)BaTiO₃ ceramics*. J. Appl. Phys., 2012. **111**(8).
46. Qi, J.Q., et al., *Dielectric properties of barium zirconate titanate (BZT) ceramics tailored by different donors for high voltage applications*. Solid State Sciences, 2012. **14**(10): p. 1520-1524.
47. Datta, K. and P.A. Thomas, *Structural investigation of a novel perovskite-based lead-free ceramics: xBiScO₃-(1-x)BaTiO₃*. J. Appl. Phys., 2009. **107**(4): p. 1-5.
48. Mitsui, T. and W.B. Westphal, *Dielectric and X-ray studies of Ca_xBa_{1-x}TiO₃ and Ca_xSr_{1-x}TiO₃*. Phys. Rev., 1961. **124**(5): p. 1354.
49. Wei, X. and X. Yao, *Preparation, structure and dielectric property of barium stannate titanate ceramics*. Mater. Sci. Eng. B, 2007. **137**(1-3): p. 184-188.
50. Chen, J., et al., *Microstructures, dielectric and ferroelectric properties of BaHf_xTi_{1-x}O₃ ceramics*. J. Alloy. Comp., 2012. **544**(0): p. 82-86.
51. Shvartsman, V.V., W. Kleeman, and J. Dec, *Diffuse phase transition in BaTi_{1-x}Sn_xO₃ ceramics: An intermediate state between ferroelectric and relaxor behavior*. J. Appl. Phys., 2006. **99**(124111).
52. Jeong, J. and Y.H. Han, *Electrical Properties of Acceptor Doped BaTiO₃*. J. Electroceram., 2004. **13**: p. 549-553.
53. Zhang, L., et al., *Mn dopant on the "domain stabilization" effect of aged BaTiO₃ and PbTiO₃-based piezoelectrics*. Appl. Phys. Lett., 2012. **101**(242903).
54. Morrison, F.D., D.C. Sinclair, and A.R. West, *Electrical and structural characteristics of lanthanum-doped barium titanate ceramics*. J. Appl. Phys., 1999. **86**(11): p. 6355-6366.
55. Maso, N., et al., *Synthesis and electrical properties of Nb-doped BaTiO₃*. J. Mater. Chem., 2006. **16**: p. 3114-3119.
56. Villegas, M., et al., *Factors affecting the electrical conductivity of donor-doped Bi₄Ti₃O₁₂ piezoelectric ceramics*. J. Am. Ceram. Soc., 1999. **82**(9): p. 2411-2416.

57. Jonker, G.H. and E.E. Havinga, *The influence of foreign ions on the crystal lattice of barium titanate*. Mater. Res. Bull., 1982. **17**: p. 345-350.
58. Gillot, C., et al., *Microscopic origin of the PTC effect in niobium-doped barium titanate*. J. Am. Ceram. Soc., 1997. **80**(4): p. 1043-1046.
59. Gulwade, D. and P. Gopalan, *Diffuse phase transition in La and Ga doped barium titanate*. Solid State Communications, 2008. **146**(7-8): p. 340-344.
60. Feteira, A., D.C. Sinclair, and J. Kreisel, *Average and Local Structure of $(1-x)\text{BaTiO}_3\text{-}x\text{LaYO}_3$ ($0 \leq x \leq 0.50$) Ceramics*. J. Am. Ceram. Soc., 2010. **93**(12): p. 4174-4181.
61. Skapin, S., D. Kolar, and D. Suvorov, *Chemical reactions and dielectric properties of the $\text{BaTiO}_3\text{-LaAlO}_3$ and $\text{BaTiO}_3\text{-LaAlO}_3\text{-LaTi}_{3/4}\text{O}_3$ systems*. J. Solid State Chem., 1997. **129**(2): p. 223-230.
62. Parkash, O.M., C.D. Prasad, and D. Kumar, *Preparation and characterization on the system $\text{Ba}_{1-x}\text{La}_x\text{Ti}_{1-x}\text{Co}_x\text{O}_3$ (X less-than-or-equal-to 0.50)*. J. Mater. Sci. Lett., 1989. **8**(4): p. 475-476.
63. Feteira, A., et al., *Synthesis and characterisation of $\text{La}_{0.4}\text{Ba}_{0.6}\text{Ti}_{0.6}\text{RE}_{0.4}\text{O}_3$ (where RE = Y, Yb) ceramics*. J. Eur. Ceram. Soc., 2006. **26**(10-11): p. 1947-1951.
64. Li, M., A. Feteira, and D.C. Sinclair, *Origin of the high permittivity in $(\text{La}_{0.4}\text{Ba}_{0.4}\text{Ca}_{0.2})(\text{Mn}_{0.4}\text{Ti}_{0.6})\text{O}_3$ ceramics*. J. Appl. Phys., 2005. **98**(8).
65. Li, G., et al., *The structural and electric properties of the perovskite system $\text{BaTiO}_3\text{-Ba}(\text{Fe}_{1/2}\text{Ta}_{1/2})\text{O}_3$* . J. Solid State Chem., 2003. **177**: p. 1695-1703.
66. Tian, H.Y., et al., *Diffusion phase transition and dielectric characteristics of $\text{Bi}_{0.5}\text{Na}_{0.5}\text{TiO}_3\text{-Ba}(\text{Hf,Ti})\text{O}_3$ lead-free ceramics*. Solid State Communications, 2007. **142**(1-2): p. 10-14.
67. Zhou, C., et al., *Remarkably high-temperature stable piezoelectric properties of $\text{Bi}(\text{Mg}_{0.5}\text{Ti}_{0.5})\text{O}_3$ modified $\text{BiFeO}_3\text{-BaTiO}_3$ ceramics*. Appl. Phys. Lett., 2012. **101**(3).
68. Kröger, F.A. and H.J. Vink, *Relations between the Concentrations of Imperfections in Crystalline Solids*. Solid State Physics, 1956. **3**: p. 307-435.
69. A. R. Denton and N.W. Ashcroft, *Vegard's Law*. Phys. Rev. A, 1991. **43**(6).

70. Zheng, R.K., et al., *Effects of Ca doping on the Curie temperature, structural, dielectric, and elastic properties of $Ba_{0.4}Sr_{0.6-x}Ca_xTiO_3$ ($0 \leq x \leq 0.3$) perovskites*. J. Appl. Phys., 2005. **98**(8).
71. Sinclair, D.C. and J.P. Attfield, *The influence of A-cation disorder on the Curie temperature of ferroelectric $ATiO_3$ perovskites*. Chem. Commun., 1999(16): p. 1497-1498.
72. Rodriguez-Martinez, L.M. and J.P. Attfield, *Structural Effects of Cation Size Variance in Magnetoresistive Manganese Oxide Perovskites*. Chem. Mater., 1999. **11**: p. 1504-1509.
73. Miller, W.S., *Plastic titanate piezoelectric compositions*. 1961, American Bosch Arma Corp.: US: 2989481.
74. Miller, W.S., *Ceramic titanate piezoelectric composition and method for preparing the same*. 1961, American Bosch Arma Corp.: US: 2989482.
75. *Modified barium titanate dielectrics*. 1964, Telegraph Condenser Co. Ltd.: GB: 964726.
76. Li, W., et al., *High piezoelectric d_{33} coefficient in $(Ba_{1-x}Ca_x)(Ti_{0.98}Zr_{0.02})O_3$ lead-free ceramics with relative high Curie temperature*. Mater. Lett., 2010. **64**(21): p. 2325-2327.
77. Gao, J.H., et al., *Microstructure basis for strong piezoelectricity in Pb-free $Ba(Zr_{0.2}Ti_{0.8})O_3$ - $(Ba_{0.7}Ca_{0.3})TiO_3$ ceramics*. Appl. Phys. Lett., 2011. **99**(9).
78. Wu, J., et al., *Sintering Temperature - Induced Electrical properties of $(Ba_{0.90}Ca_{0.10})(Ti_{0.85}Zr_{0.15})O_3$ Lead-free Ceramics*. Mater. Res. Bull., 2010.
79. Hao, J., et al., *Correlation Between the Microstructure and Electrical Properties in High-Performance $(Ba_{0.85}Ca_{0.15})(Zr_{0.1}Ti_{0.9})O_3$ Lead-Free Piezoelectric Ceramics*. J. Am. Ceram. Soc., 2012. **95**(6): p. 1998-2006.
80. Liu, W. and X. Ren, *Large piezoelectric effect in Pb-free ceramics*. Phys. Rev. Lett., 2009. **103**(25): p. 257602.
81. Bao, H.X., et al., *A modified lead-free piezoelectric BZT-xBCT system with higher T-C*. J. Phys. D: Appl. Phys., 2010. **43**(46): p. 1-4.
82. Keeble, D.S., et al., *Revised structural phase diagram of $(Ba_{0.7}Ca_{0.3}TiO_3)$ - $(BaZr_{0.2}Ti_{0.8}O_3)$* . Appl. Phys. Lett., 2013. **102**(092903).

83. Su-Wei Zhang, H.Z., Bo-Ping Zhang, Sui Yang, *Phase transition behavior and piezoelectric properties of lead-free $(\text{Ba}_{0.95}\text{Ca}_{0.05})(\text{Ti}_{1-x}\text{Zr}_x)\text{O}_3$ ceramics*. 2010.
84. Li, W., et al., *Polymorphic phase transition and piezoelectric properties of $(\text{Ba}_{1-x}\text{Ca}_x)(\text{Ti}_{0.9}\text{Zr}_{0.1})\text{O}_3$ lead-free ceramics*. Physica B-Condensed Matter, 2010. **405**(21): p. 4513-4516.
85. Favarim, H.R., et al., *Phase-transition studies of $\text{Ba}_{0.90}\text{Ca}_{0.10}(\text{Ti}_{1-x}\text{Zr}_x)\text{O}_3$ ferroelectric ceramic compounds*. Phys. Status Solidi A, 2010. **207**(11): p. 2570-2577.
86. Kinoshita, K.Y., Akihiko *Grain-size effects on dielectric properties in barium titanate ceramics* J. Appl. Phys., 1976. **47**: p. 371.
87. Zheng, P., et al., *Grain-size effects on dielectric and piezoelectric properties of poled BaTiO_3 ceramics*. Acta Materialia, 2012. **60**(13-14): p. 5022-5030.

Chapter 2: Electrical theory and dielectric materials

2.1: Polarisation

The permanent or induced polarisation of a material by the application of an electric field causes changes in the electronic distribution of a material and can often give rise to interesting and useful electronic properties.

The total polarisation of a material is a vector quantity which is the sum of up to four types of polarisation: electronic, ionic, orientational (or dipole) and space charge.

$$\vec{P} = \sum \vec{P}_x = \vec{P}_e + \vec{P}_i + \vec{P}_o + \vec{P}_s \quad \text{Equation 2.1}$$

Electronic polarisation, \vec{P}_e , is a spontaneous process that occurs with all atoms when placed in an electric field and arises as a result of a shift of the electron cloud relative to the positively charged nucleus of the atom, figure 2.1. The polarisation direction is dependent on that of the applied field and the effect is reversible, only being present whilst the field is applied. This type of polarisation operates at high frequencies as shown in figure 2.2.

Ionic polarisation, \vec{P}_i , can only be observed in materials with ionic character and arises as a result of the energetic stability that can be achieved by the displacement of the anionic and cationic species in opposite directions due to the application of an electric field, giving rise to a net dipole moment, figure 2.1. The magnitude of the dipole moment, \vec{P}_i , for an ionic pair is equal to the product of the magnitude of the charge, Q , on each ion and the displacement, d_i .

$$\vec{P}_i = Qd_i \quad \text{Equation 2.2}$$

Polarisation as a result of orientation, \vec{P}_o , is only observed in materials which exhibit a permanent dipole moment. In such cases, when an electric field is applied the dipoles align with the field in order to stabilize the system, figure 2.1. The effect of increasing the temperature of the system is to supply thermal energy, which, when

greater than the stabilisation energy, can allow for the re-randomisation of the dipoles. Thus orientational polarisation is temperature dependant and decreases with increasing temperature.

Space charge, \vec{P}_s , polarisation occurs when an applied electric field causes charge carriers to move small distances in a material before getting trapped, often at lattice defects, resulting in the formation of localised charges and therefore dipole moments, figure 2.1. Whilst the magnitude of the space charge polarisation is the highest, it only operates at low frequencies due to the relative length scales of the charge displacement as shown in figure 2.2.

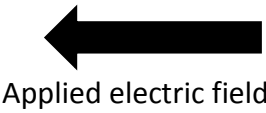


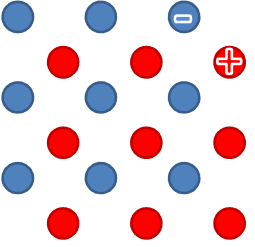
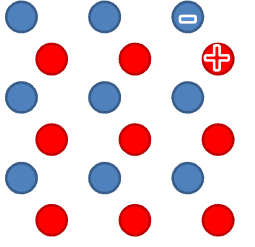
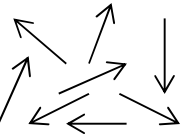
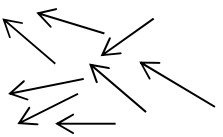
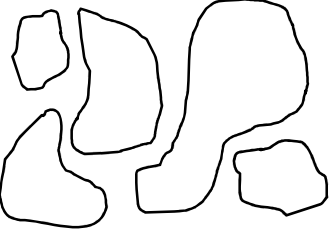
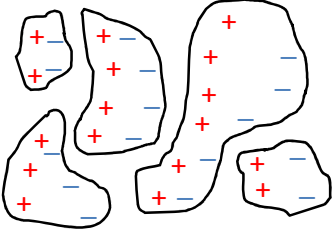
Polarisation		
\vec{P}_e		
\vec{P}_i		
\vec{P}_o		
\vec{P}_s		

Figure 2.1: Representations of the different polarisation types; Electronic polarisation, \vec{P}_e , ionic polarisation, \vec{P}_i , orientational polarisation, \vec{P}_o and space charge polarisation, \vec{P}_s .

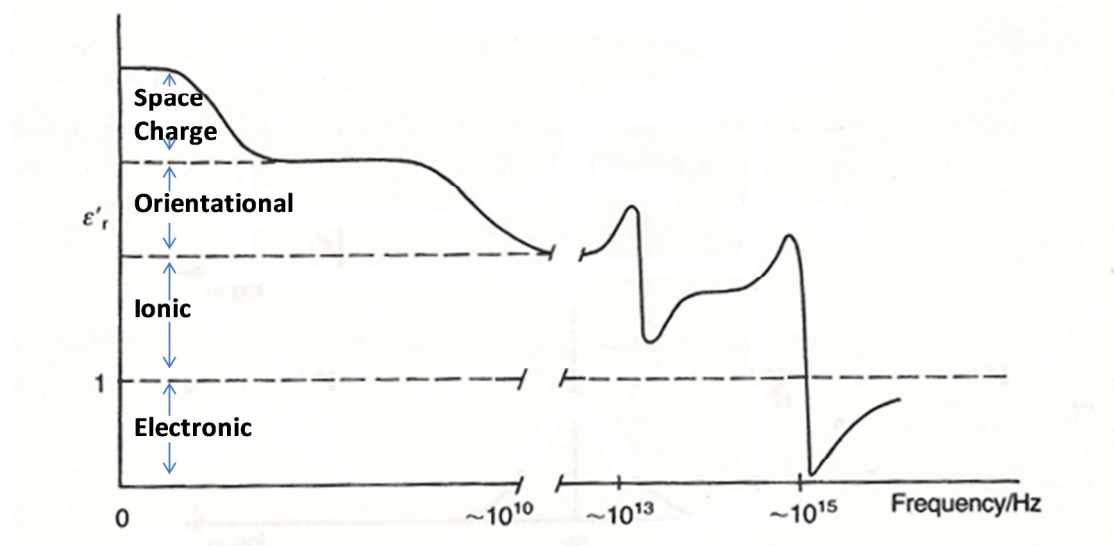


Figure 2.2: Relative magnitudes of polarisation responses and operating frequencies, adapted from^[1]

A dielectric material is an electrical insulator which exhibits an electrical dipole^[2] as a result of an applied electric field, strain or heat. When a voltage is applied across a dielectric material, the material acts as a capacitor with parallel faces becoming equally but oppositely charged. The resultant material is then said to be polarised, with the polarisation being calculated by equation 2.2. Technically this polarisation is a sum of many local dipole moments, \vec{p} , giving rise to the macroscopic polarisation, \vec{P} , which is measured as the surface charge of the material.

2.2: Capacitors

A capacitor is a device which is able to store energy by means of separated charges. The most simplistic example of a capacitor would be that of a circuit consisting of a power supply and two plate electrodes separated by a vacuum, (figure 2.3-a). For a capacitor such as this, the electric field, \vec{E} , between the two plates, created by the charge separation can be calculated by dividing the applied voltage by the separation of the parallel plates. Using Gauss's theorem^[3], the surface charge density can be calculated (Equation 2.3).

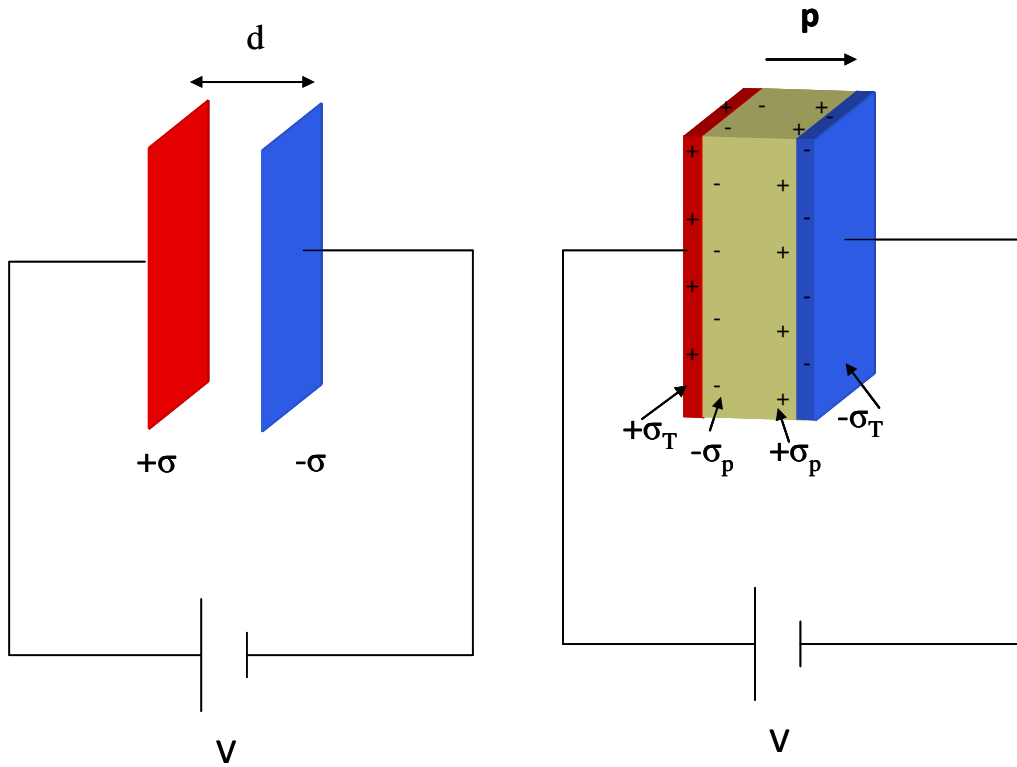


Figure 2.3: a) a vacuum parallel plate capacitor (left) and a b) a dielectric material capacitor (right)

$$\vec{E} = \frac{V}{d} = \frac{\sigma}{\epsilon_0} \quad \text{Equation 2.3}$$

\vec{E} = Electric field

V = Voltage

d = Plate separation

σ = Surface charge density

ϵ_0 = Permittivity of free space

As capacitance, C , of the material is a measure of how much charge can be stored for a given voltage, for a vacuum parallel plate capacitor, C_0 is given by equation 2.4. It is related to the area of the parallel plates and the distance between them, by a constant, ϵ_0 , the permittivity of free space.

$$C_0 = \frac{Q}{V} = \epsilon_0 \frac{A}{d} \quad A = \text{Area of plates} \quad \text{Equation 2.4}$$

When a dielectric material is placed between the parallel plates, (figure 2.3-b) the electric field can be calculated as before. If the applied voltage and separating distance is the same then \vec{E} will also remain constant, implying that the surface

charge density must also be unchanged. However, the charge density is now split as polarisation charge density is found on the dielectric material parallel faces, thus the effective charge density which gives rise to the electric field, \vec{E} , is reduced (equation 2.5).

$$\vec{E} = \frac{V}{d} = \frac{\sigma_T - \sigma_p}{\epsilon_0} \quad \text{Equations 2.5}$$

where σ_T is equal to the total surface charge density and σ_p is equal to the polarisation charge density. The total charge density, σ_T , is also known as the charge displacement vector \vec{D} , which is a function of the electric field and the polarisation vector, \vec{P} .

$$\vec{D} = \epsilon_0 \vec{E} + \vec{P} \quad \text{Equation 2.6}$$

For most materials the polarisation is directly proportional to the electric field and the dielectric is said to be linear. When this is true, the polarisation can be expressed in terms of the electric field using a dimensionless constant, χ_e . This is the electrical susceptibility of the dielectric and is unique to each material.

$$\vec{P} = \chi_e \epsilon_0 \vec{E} \quad \text{Equation 2.7}$$

Using equations 2.5, 2.6 and 2.7 along with the fact that $\vec{D} = \sigma_T$, where the surface charge density is the total charge, Q , divided by the surface area, A , the following transformations can be made.

$$\begin{aligned} \vec{D} &= \epsilon_0 \vec{E} + \chi_e \epsilon_0 \vec{E} \\ \hookrightarrow \vec{D} &= (1 + \chi_e) \epsilon_0 \vec{E} \\ \hookrightarrow \frac{Q_T}{A} &= (1 + \chi_e) \epsilon_0 \frac{V}{d} \end{aligned} \quad \text{Equation 2.8}$$

As capacitance is equal to the total charge stored by two plates divided by the applied voltage used to separate the charges, capacitance can then be defined as follow.

$$C = \frac{Q_T}{V} = (1 + \chi_e) \epsilon_0 \frac{A}{d} \quad \text{Equation 2.9}$$

The increase in capacitance that arises from having a dielectric material between a parallel plate capacitor, as opposed to a vacuum is therefore $1 + \chi_e$, which is the relative permittivity, ϵ_r , of the material. Thus for a parallel plate capacitor separated by a dielectric material, equation 2.10 can be applied[†].

$$C = \epsilon_r \epsilon_0 \frac{A}{d} \quad \text{Equation 2.10}$$

Just as the capacitance arising from having a dielectric material as our capacitor varies compared to that of a vacuum, so too does the permittivity. Whilst the permittivity of a vacuum is frequency independent, this is not generally the case for materials. When considering how the polarisation of the material changes when a field is applied, it is easily understood that any change in the polarisation will not be instantaneous and thus if an alternating field were to be applied, the polarisation response would have a phase difference to the applied field and would therefore be frequency dependant.

2.3: Complex dielectric permittivity

The permittivity of the material must instead be considered as a complex function with an angular frequency, $\epsilon \rightarrow \hat{\epsilon}(\omega)$. This can then be separated into its real and imaginary parts (equation 2.11) as shown in figure 2.4.

$$\hat{\epsilon}(\omega) = \epsilon'(\omega) + i\epsilon''(\omega) = \frac{D_0}{E_0} (\cos \delta + i \sin \delta) \quad \text{Equation 2.11}$$

[†] Where the capacitance has been corrected for pellet geometry, C has units of Farads per centimetre (F cm^{-1}), as opposed to F, for the capacitance that has not been corrected for geometry. Resistances which have been corrected for geometry are technically resistivities, but generally still referred to as resistances. Unless stated otherwise, all capacitances and resistances given in this thesis will be corrected for pellet geometries.

Where ϵ' is the real part of the permittivity, often called the dielectric constant, which is a measure of the stored energy per cycle of a.c. field. ϵ'' is the imaginary part which relates to the energy dissipation per cycle and is referred to as the dielectric loss.

More commonly, a normalised loss is used, equation 2.12. This is a measure of the displacement of the material. All losses referred to in this project will be normalised losses, unless otherwise stated.

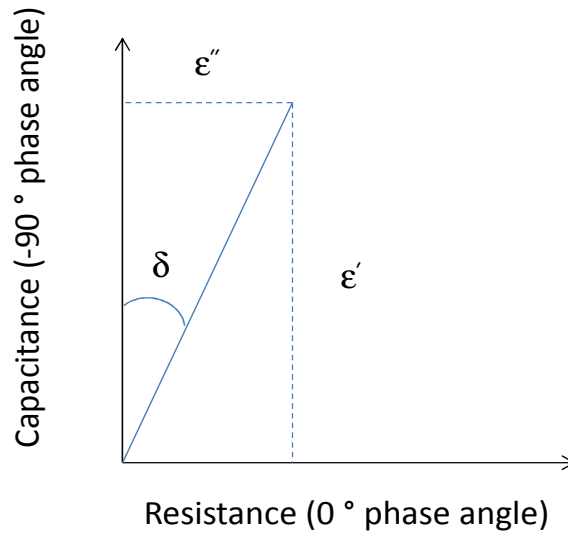


Figure 2.4: Graphical representation of the normalisation of the dielectric loss[†]

$$D = \tan \delta = \frac{\epsilon''}{\epsilon'}$$

Equation 2.12

2.4: Immittance spectroscopy

Impedance spectroscopy is a technique which measures the electrical properties of materials as a function of frequency and can be used as a technique to study the internal electrical microstructure of a material, on which the macroscopic electrical properties will be highly dependent.

[†] See appendix 2.1 for justification of phase angles.

Electrical impedance, Z^* , is the ability of a material to restrict the flow of electricity in an a.c. field. It can be expressed by the summation of a real and imaginary part, corresponding to the resistive and capacitive properties of the material respectively.

$$Z^* = Z' - jZ'' \quad \text{Equation 2.13}$$

Z' = Resistance

$\omega = 2\pi f$ where f is the frequency

$$Z'' = \frac{1}{\omega C}$$

C = Capacitance

The capacitor-like behaviour is an elastic phenomenon corresponding to the polarisation i.e., an off-centring of ions due to an electric field. The resistive part is inelastic and corresponds to the long range migration of electrons through the lattice, which is opposed by “friction”. Thus the electrical nature of an ideal material can be expressed in terms of a capacitor and a resistor connected in parallel with each other.

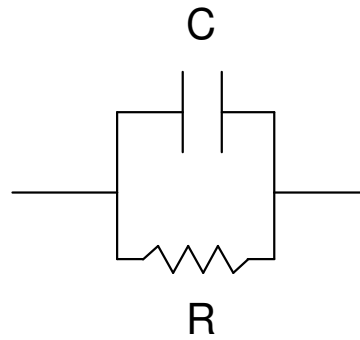


Figure 2.5: Electrical behaviour of a dielectric material described in terms of a parallel resistor and capacitor, known as a parallel RC element

In anything other than a perfect crystal, the total macroscopic electrical response observed is comprised of the responses due to several different components, corresponding to different electroactive regions within the material's microstructure. This can include bulk regions, grain boundaries, surface interactions, electrode interfaces and regions with different concentrations of the relative ionic species of the composition. Each of these component regions can be described by a sub-circuit of the form shown in figure 2.5, generally referred to as a parallel RC element. From the parallel RC element a time constant, τ , can be calculated as shown in equation 2.14. Generally the time constants will be markedly different for

each of the major components allowing for contributions to the electrical response of a material due to different regions to be separated out in the frequency domain.

$$\tau = RC$$

Equation 2.14

2.4.1: Immittance formalisms

There are four interrelated immittance formalisms, Z^* , M^* , Y^* and ε^* (impedance, electrical modulus, admittance and dielectric permittivity respectively). Data collected as a function of frequency for any of the above at various temperatures can then be converted to the related formalisms as required^[4].

Impedance

$$Z^* = Z' - jZ''$$

Z' = Resistance
 $Z'' = 1/\omega C$ = Reactance
 $\omega = 2\pi f$
 C = Capacitance

Admittance

$$Y^* = Y' + jY'' = \frac{1}{Z^*}$$

Y' = Conductance, σ
 Y'' = Susceptance $\propto 1/C$

Electric Modulus

$$M^* = M' + jM'' = \frac{1}{\varepsilon^*}$$

$$M^* = j\omega C_0 Z^{*\dagger}$$

$j = \sqrt{-1}$
 $C_0 = \varepsilon_0 A d^{-1}$
 A = Pellet area
 d = Pellet thickness

Complex Permittivity

$$\varepsilon^* = \varepsilon' - j\varepsilon'' = \frac{1}{M^*}$$

$$\varepsilon^* = (j\omega C_0 Z^*)^{-1}$$

ε' = Dielectric constant
 ε'' = Dielectric loss

2.4.2: Brick layer model

The brick layer model^[5] is used to deconvolute the macroscopic electrical properties of a material into various components, such as the bulk response and grain boundary effects. This technique models the material as a series of “bricks” of conductive

[†] If a geometric correction factor, A/d , is included in the Z^* term, then C_0 becomes ε_0

material portraying the bulk material, surrounded by an insulating “mortar” of resistive material, representing the grain boundaries.

This enables us to consider our constituent components as an equivalent circuit comprising of parallel RC elements connected in series, where each parallel RC element represents one component region, i.e. bulk, grain boundary, electrode interface etc. Thus for a simple grain boundary/ bulk system, the equivalent circuit would be as shown in figure 2.6.

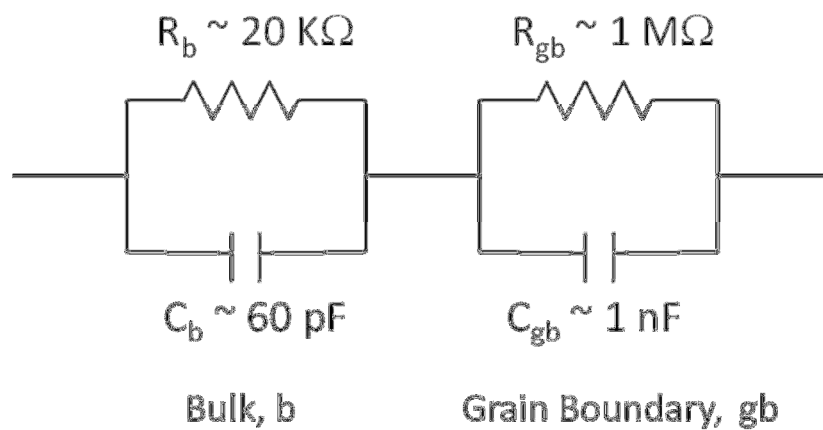


Figure 2.6: Equivalent circuit for a material with only bulk and grain boundary components; R_b = bulk resistance, C_b = bulk capacitance, R_{gb} = grain boundary resistance, C_{gb} = grain boundary capacitance

The measured capacitance for each of the RC parallel measurements is related to their geometry by equation 2.10, thus provided the boundary of the grain has a significantly larger A/d term, which is generally the case for well sintered pellets with thin well-defined grain boundary regions, there is often a significant difference in the electrical properties of the electro-active regions, despite their having a very similar compositional makeup.

Where the time constants, τ , for each of these components are orders of magnitude different it is then possible to separate out the electrical responses of each using the immittance formalisms defined in section 2.4.1.

Each parallel RC element results in a semi-circular arc in the complex plane impedance, Z^* , and complex plane modulus plots, M^* . The complex plane impedance plot generally shows the grain boundary electrical response most clearly and the complex plane electrical modulus plot generally shows the bulk electrical properties

most clearly, figures 2.7 and 2.8, respectively. This is due to the large area of the grain boundary, but narrow thickness resulting in a large recorded capacitance, and thus small $1/C$ value in the complex plane modulus plot, as well as generally higher resistances in the grain boundary regions compared to the bulk resulting in a large presence in the complex impedance plane plot.

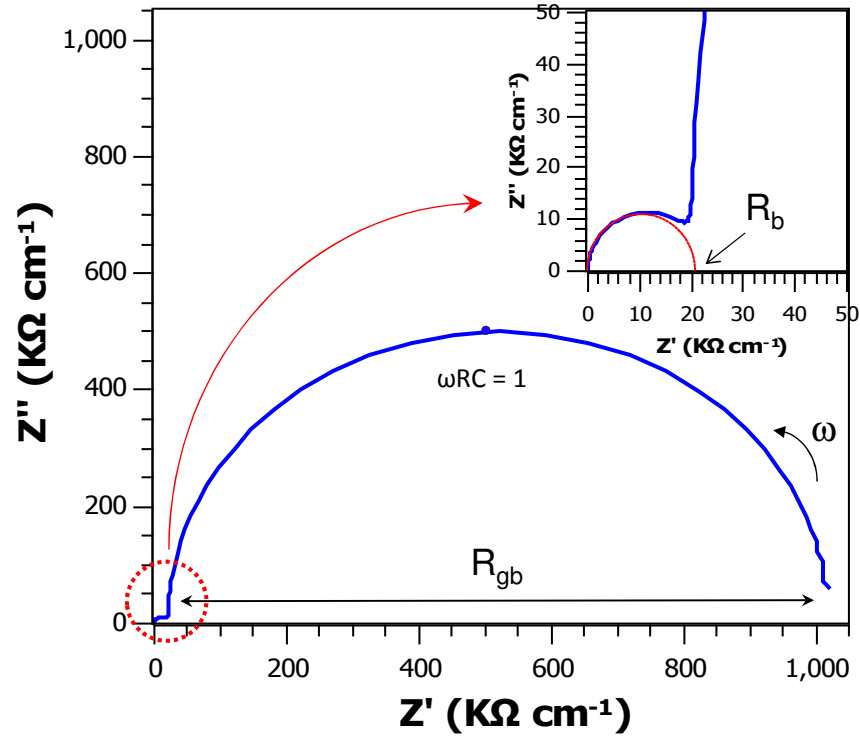


Figure 2.7: Complex impedance plane plot of an ideal dielectric ceramic with typical values for grain boundary and bulk regions (as expressed in figure 2.6) with no other electrically active regions

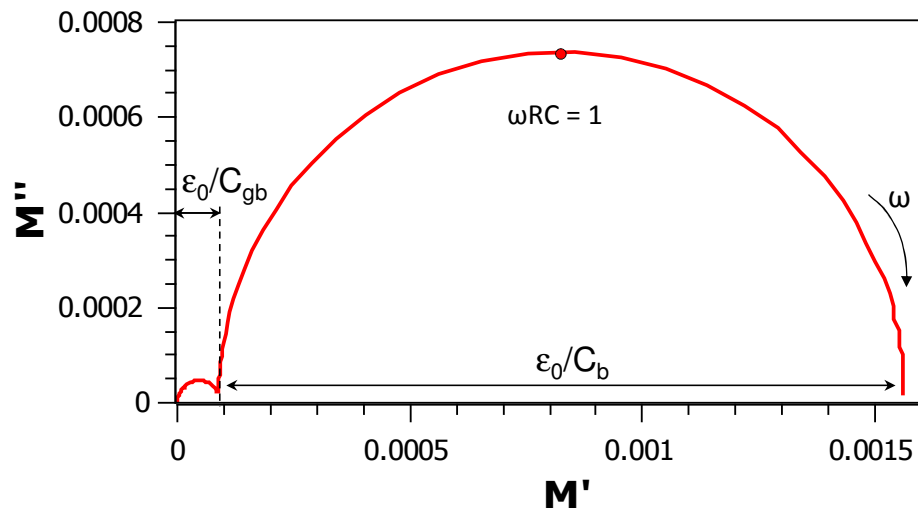


Figure 2.8: Complex modulus plane plot of an ideal dielectric ceramic with typical values for grain boundary and bulk regions (as expressed in figure 2.6) with no other electrically active regions

$$\omega_{max} = 2\pi f_{max} = (RC)^{-1} = \tau^{-1} \quad \text{Equation 2.15}$$

The diameters of the resolved semi-circles in the complex plane impedance plot are equal to the resistance of the region it represents i.e. R_g , R_{gb} . The frequency at the semi-circular arc maximum is given by equation 2.15 and can be used to calculate the capacitance of the region as well as the time constant.

In the plot of complex electrical modulus, the diameter of each resolved semi-circle corresponds to C^{-1} of the related region, with equation 2.15 allowing for the resistance and time constant to be calculated.

Ideal data would result in a series of clearly separated, perfect semi-circular arcs, one present for each electro-active region, such as bulk, boundary, non-ohmic electrode contacts etc. However the semi-circular arcs are often found to appear somewhat depressed, asymmetric and/or poorly resolved. These issues arise when two or more component regions have similar time constants and where the capacitance or resistance of one or more components is many orders of magnitude different to another, causing some components to be masked.

The semicircle maxima in the complex plane plots correspond to maxima in imaginary components. When plotted against the log of the frequency, this gives rise to Debye peaks, figure 2.9. Assuming ideal semicircles, the peak heights are given by equations 2.16 and 2.17 respectively.

$$Z'' = R \left[\frac{\omega RC}{1+(\omega RC)^2} \right] \quad \text{Equation 2.16}$$

$$M'' = \frac{\varepsilon_0}{C} \left[\frac{\omega RC}{1+(\omega RC)^2} \right] \quad \text{Equation 2.17}$$

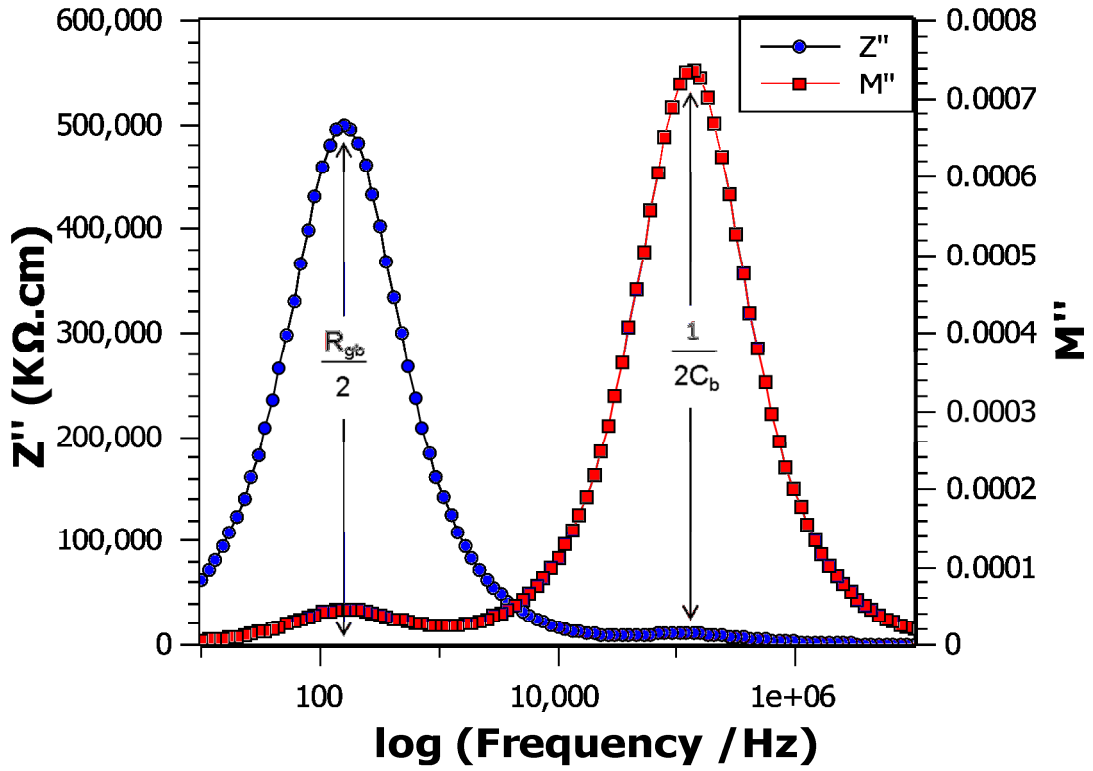


Figure 2.9: Spectroscopic Debye plots of the imaginary components of impedance and electric modulus.

As with the complex plots, the frequency of each maxima, f_{max} , for circuits shown in figure 2.7 are related to the time constant of a particular component of the material, such as grain boundary or bulk, and can be described by equation 2.15 allowing for both the resistance and the capacitance to be calculated from both peaks. Again, similarly to the complex plane plots, the main modulus Debye peak generally corresponds to the bulk response, and is given by equation 2.18, whilst the main impedance Debye peak tends to correspond to the grain boundary response, following equation 2.19.

$$M''_{max} : f_{max} = \frac{\epsilon_0}{2C} \quad \text{Equation 2.18}$$

$$Z''_{max} : f_{max} = \frac{R}{2} \quad \text{Equation 2.19}$$

It is the fact that the Z'' Debye peak scales with R and the M'' Debye peak scales with C^{-1} that results in the impedance Debye plot being dominated by the grain boundary response and the modulus Debye plot being dominated by the bulk response, as the

resistance of a material is generally orders of magnitude higher in the grain boundary regions than the bulk and similarly the capacitance of the bulk is lower than that of the grain boundary.

The number of Debye peaks present in each of the impedance and modulus Debye plots with different characteristic f_{\max} 's can be used as an indication of the number of electroactive regions present in the material.

Where the time constants are separated by at least two orders of magnitude and there are no other significant regions such as impurities or electrode/ceramic interfaces, the values obtained from the complex plane and spectroscopic plots should be complimentary. However this is often not the case and it is frequently easier to get a more accurate value from one or other of the plots as a result of non-ideal material micro-structure, thus both types of plot will be interpreted for materials synthesized in this project.

2.5: Polarisation field hysteresis measurements

A ferroelectric material is defined as being a polar material, the electric dipole of which can be reversibly re-orientated by the application of an electric field^[6].

When an electric field, greater than that of the coercive field of the material, is applied to a ferroelectric material a polarisation of the material is observed, the magnitude of which will be dependent on the electric field strength. Hysteresis data are collected by measuring the polarisation of a sample in an applied electric field. Data are collected as the field is cycled through from a large "positive" field through to a large "negative" field and back. In a ferroelectric material the domains in the material will align themselves with a strong field resulting in a large polarisation. As the field strength is lowered and ultimately switches sign, the polarisation flips to realign with the new field direction. The field required for the dipoles to "flip" is greater than would be required to align randomised domains due to the extra stability that arises from the aligned state. This results in an open hysteresis loop, figure 2.10.

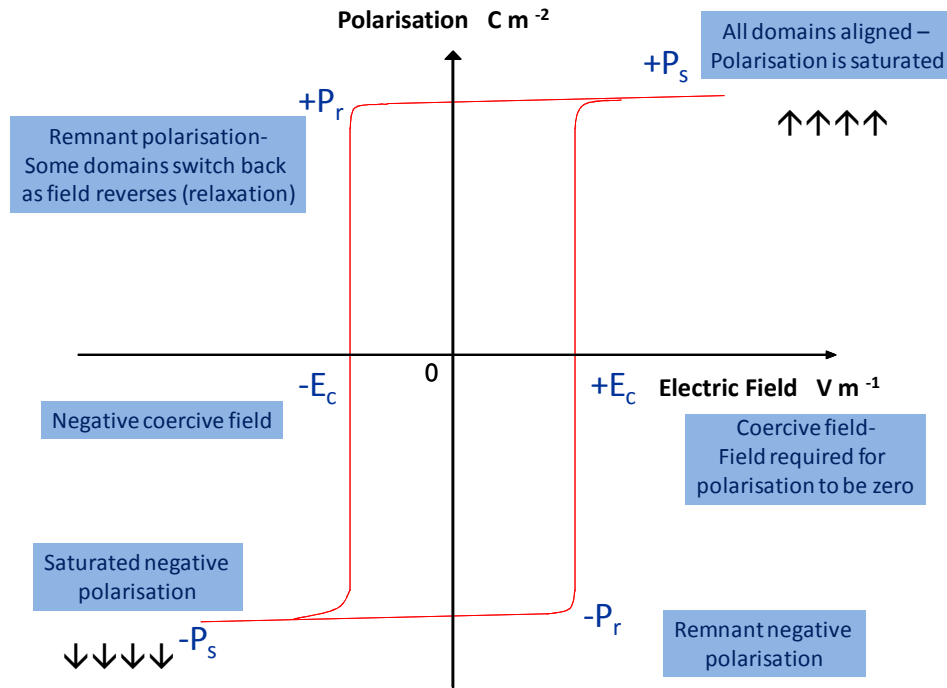


Figure 2.10: Hysteresis loop for an ideal ferroelectric, showing the remnant polarisation, $\pm P_r$, coercive fields, $\pm E_c$, and saturated polarisations, $\pm P_s$

The presence of defects in the ceramic can cause the field strength required to achieve the maximum polarisation to be increased as they can cause domain wall pinning in hard ferroelectric ceramics^[7], resulting in broad square loops. A soft ferroelectric gives rise to slimmer, canted loops^[8,9]. By contrast, poor dielectrics with large leakage currents result in hysteresis loops with a “rugby-ball” shape where an increase in the polarisation is observed between the remnant and saturated polarisations^[10].

2.6: Piezoelectric operation modes

Coupling between mechanical and electrical domains in piezoelectric ceramics gives rise to various operation modes, longitudinal, transverse, shear and hydrostatic. Each of these four modes can be applied in various directions with regards to both the axis of deformation and the electric field. Each operation mode is symbolised with a lower case d, followed by two subscript numbers, the first relating to the relative direction of the electrical field (displacement) and the second relating to the

mechanical response (strain or stress). The exception to this is the hydrostatic mode which is symbolised d_h .

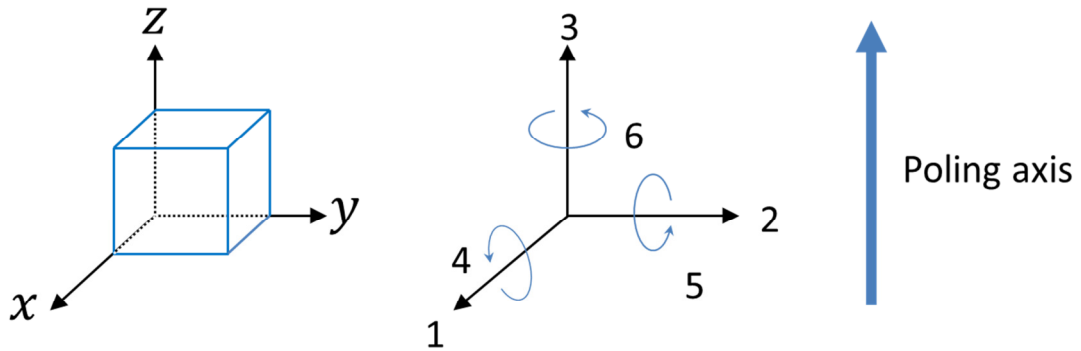


Figure 2.11: Piezoelectric coefficients reference axes^[11] relating to the direction of displacements, stresses and strains

The d_{33} (longitudinal operation) mode, along with the d_{31} (transverse operation) mode, are two of the most commonly quoted and calculated values for piezoelectric materials. d_{33} has both the electric field and deformation parallel to the polarisation., whilst d_{31} has the electric field parallel to the axis of polarisation, but the relevant deformation perpendicular to this.

References

1. Moulson, A.J. and J.M. Herbert, *Electroceramics*. 2 ed. 2003: Wiley.
2. Callister Jr, W.D., *Materials Science and Engineering, An Introduction*. 7th ed. 2007: Wiley.
3. Sabinine, G., *Sur le reste de la formule de Gauss*. Matematiceskii Sbornik, 1867. **2**(1): p. 52-70.
4. Hirose, N. and A.R. West, *Impedance spectroscopy of undoped BaTiO₃ ceramics*. J. Am. Ceram. Soc., 1996. **79**(6): p. 1633-1641.
5. Mason, T.O., N.H. Perry, and N.J. Kidner, *The Brick Layer Model Revisited: Introducing the Nano-Grain Composite Model*. J. Am. Ceram. Soc., 2008. **91**(6): p. 1733-1746.
6. Jaffe, B., W.R. Cook, and H. Jaffe, *Piezoelectric Ceramics*. 1971: Academic Press London.
7. Li, W., et al., *Collective domain-wall pinning of oxygen vacancies in bismuth titanate ceramics*. J. Appl. Phys., 2005. **98**(2): p. 5.
8. Wongdamnern, N., et al., *Comparative studies of dynamic hysteresis responses in hard and soft PZT ceramics*. Ceram. Int., 2008. **34**(4): p. 731-734.
9. Garcia, J.E., et al., *Evidence of temperature dependent domain wall dynamics in hard lead zirconate titanate piezoceramics*. J. Appl. Phys., 2012. **112**(1).
10. Bose, S. and S.B. Krupanidhi, *Improved ferroelectric and leakage properties in symmetric BiFeO₃/SrTiO₃ superlattice*. Appl. Phys. Lett., 2007. **90**.
11. Jordan, T.L. and Z. Ounaies, *Piezoelectric Ceramics Characterization*. 2001, ICASE NASA Langley Research Center.

Chapter 3: Experimental methods

3.1: Ceramic synthesis

A ceramic synthesis route was used to prepare samples. Reagents, (oxides and carbonates), were first dried at an appropriate temperature, 1000 °C for oxides and 180 °C for carbonates, for a period of at least two hours to remove any absorbed moisture or carbon dioxide. Stoichiometric ratios appropriate to the desired composition were then weighed and ground in an agate mortar and pestle until a homogeneous mixture was formed. This mixture was then placed in an open, platinum-lined, alumina crucible and heated to 1000°C in air overnight in order to decompose any carbonates.

The resulting powders were then ball-milled as an ethanol slurry at 600 revolutions per minute until a fine, homogeneous powder was achieved, before being dried over a hot-plate at 80°C until all the ethanol had evaporated. The powder was then re-ground and pressed into pellets 1-2 mm thick using a 10 mm pellet die and a uniaxial press, applying a pressure of 1000 psi. An isostatic press was then used to subject the pellets to 30000 psi of pressure (figure 3.1).

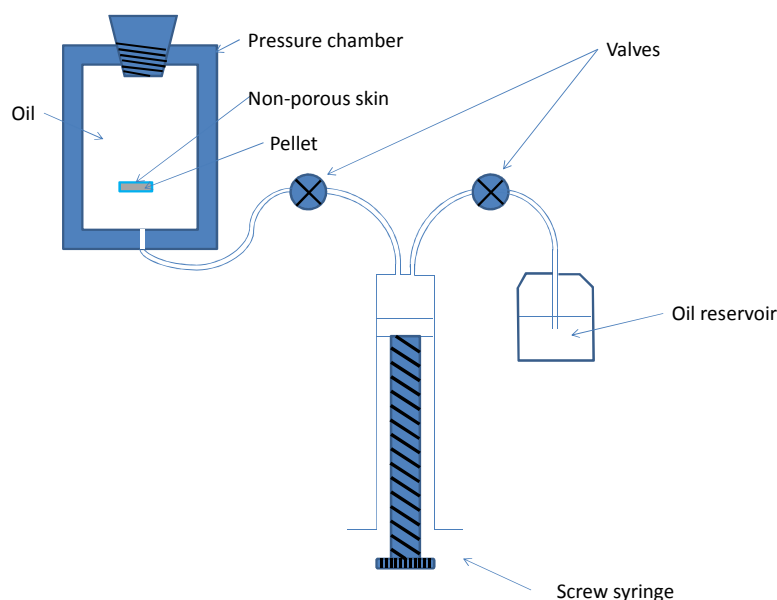


Figure 3.1: Diagram showing the set-up of the isostatic oil press

The pellets were placed on platinum foil in an alumina crucible and heated in a tube or muffle furnace in the temperature range of 1250 – 1500 °C for a period of 12-30 hours; specific details of which can be found in each results chapter. Formation of the desired product was then verified by the analysis of in-house powder X-ray diffraction data.

3.2: Electrodes

3.2.1 Sputter-coater

Platinum electrodes were applied to pellets using an EMITECH K550X sputter-coater. Prior to deposition, pellet faces were smoothed using fine-grained polishing paper. The circumference of the pellet was masked with tape leaving the polished surfaces exposed. The pellets were placed in the coating chamber which was then evacuated to a pressure of less than 1×10^{-1} mbar. A coating current of 35 mA was applied for a period of 4 minutes. This process was repeated until the electrode surface was thick enough to give a sheet resistance, measured across the face of the pellet, of less than 10 Ohms. This process was then repeated for the opposite face.

3.2.2: Painted electrodes

For pellets of a chalkier or less robust nature which were deemed likely to be damaged by the removal of tape required for sputter-coated electrodes, painted electrodes were applied. This was done either using platinum electrode paste or silver conductive paint.

The platinum electrode paste has the advantage of being stable for high temperature studies, however they require firing at 1000 °C which is not suitable for all compositions. The silver paint has a much lower firing temperature, but has a maximum operating temperature of 260 °C.

To apply the silver conductive paint, pellets faces were smoothed with fine-grained polishing paper and washed with acetone to remove any oils or greases present. One face was then painted with the silver paint and then placed painted side up on a

clean piece of aluminium foil over a hot plate at 120 °C for 10 minutes. The other side was then similarly treated, with the pellet finally left at 120 °C for 30 minutes to ensure the complete removal of any organic species from the paint to leave a conductive surface

Platinum electrodes were applied to similarly prepared pellet faces. The paste was applied using the back of a metal spatula to give a smooth layer of approximately equal thickness over the complete face before being dried over a hot plate at 120 °C for a period of 15 minutes. The other side was then painted and dried in the same manner. After drying the pellets were placed on a clean piece of platinum foil and put in a muffle furnace at 600 °C for a period of 15 minutes before being heated to 1000 °C at a rate of 10 K min⁻¹. The tiered heating process tended to produce a more stable electrode which was less prone to flaking off. The pellets were held at temperature for 30 minutes before being removed from the furnace.

3.3: Powder X-ray diffraction

3.3.1: In-House Data Collection

In-house X-ray diffraction was carried out using either a STOE Stadi P powder diffractometer (transmission mode) or a PANalytical EMPYREAN diffractometer (transmission and reflection mode).

3.3.1.1: Reflection mode

Powder X-ray diffraction data were collected on samples using a PANalytical EMPYREAN powder X-ray diffractometer in reflection mode. Samples were ground to give a smooth, fine powder which was then loaded in to the sample holder such that the powder was densely packed and level with the surface of the sample holder, figure 3.2. In situations where it was not preferable to break the pellet and grind it for powder X-ray analysis, the sample holder was instead filled with silicon powder, on top of which the pellet was set before being pushed down, using a clean glass slide, until it was flush with the top of the sample holder. Pellets to be studied in this

way were first sanded using a fine polishing paper to ensure a flat surface and cleaned with acetone to remove any dirt, dust or oil impurities on the surface. The powder X-ray diffraction patterns carried out on the whole pellets show peaks as a result of the silicon packing powder. In order to be able to exclude these peaks from subsequent analysis of the data, data was collected on a sample of the silicon packing powder (see appendix 3), with sharp peaks being found at 28.45, 47.30, 56.12, 69.13, 76.38, 88.04 and 94.96 ° 2 θ . These peaks were then assigned as silicon peaks in X-ray patterns from other pellets and masked from refinements.



Figure 3.2: Powder X-ray diffraction reflection mode sample holder

The PANalytical EMPYREAN X-ray diffractometer uses a Ge crystal monochromator to select only the $K\alpha_1$ (1.540598Å) radiation from a generating tube which operates at a current of 40mA, with a voltage of 45kV using a Cu anode. The mounted sample was spun in the beam at 1.0 revolution per second to prevent either uneven surface coverage or preferred orientation causing any distortion of the observed intensities.

Data were collected over a range of $10^\circ \leq 2\theta \leq 100^\circ$ with a step size of 0.0167°, with data typically collected over a one hour period.

3.3.1.2: Transmission mode

In instances where there was insufficient powder to fill the sample holder used in reflection mode, transmission powder X-ray diffraction was carried out. This requires considerably less sample to be used, however the sample used is irrecoverable, unlike in reflection mode. Also, the transmission mode diffraction results in

considerably lower peak intensity, giving lower resolution over a given data collection time frame.

Data collected on the PANalytical EMPYREAN X-ray diffractometer had the same operating voltages, currents and wavelengths, but samples were mounted between two non-diffracting thin films with a thin layer of non-diffracting grease applied to the inside faces of the films to ensure that the powder did not move as the sample holder was rotated, figure 3.3-a. Data were again collected over a range of $10^\circ \leq 2\theta \leq 100^\circ$ with a step size of 0.0167° , however, data were collected over a period of two hours to give better peak intensity.

Data were also collected on ground samples using a STOE Stadi P powder diffractometer which uses a germanium monochromator with a copper source to select $\text{CuK}\alpha_1$ ($\lambda=1.5406 \text{ \AA}$) radiation from a generating tube that operates at 35mA with a voltage of 40 kV. Samples were mounted between two non-diffracting thin films using non-diffracting grease and rotated throughout data collection in order to average the effects that can occur as a result of preferred orientation and powder packing inhomogeneity, figure 3.3-b.

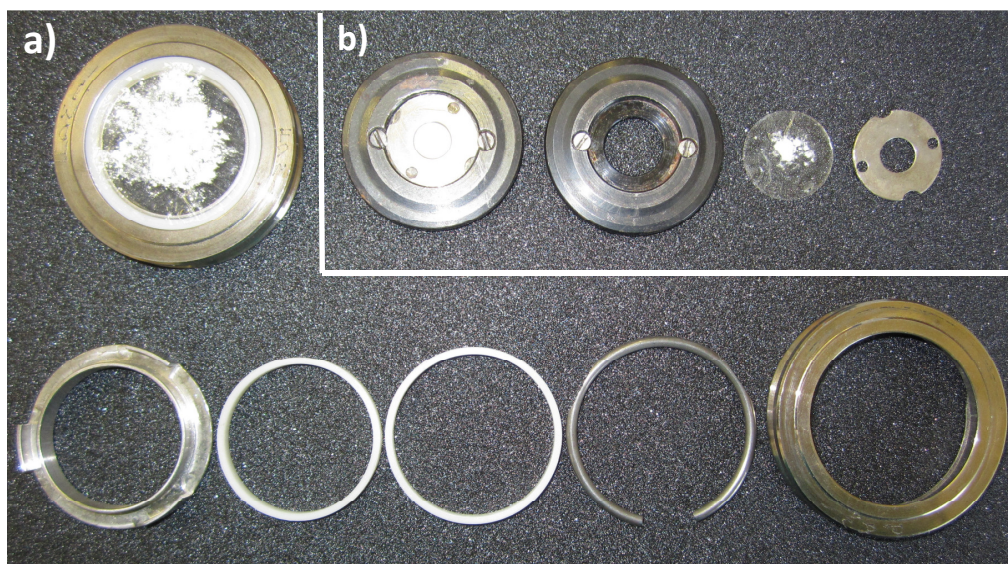


Figure 3.3: Powder X-ray diffraction transmission mode sample holders for the a) PANalytical EMPYREAN and b) STOE Stadi P powder diffractometers

Data collected were compared to the ICSD database^[1] of known phases in order to show up the presence of any known impurities or remaining starting materials.

Where no starting materials or known phases were found to be present, models were created using the general structure analysis system, GSAS^[2, 3], which were then refined against the collected data by the Rietveld refinement method.

3.3.2: Synchrotron Data Collection

The Diamond III high resolution powder diffraction beamline at the Rutherford Appleton Laboratory in Oxford was used to collect high resolution powder X-ray diffraction data on each composition studied in this project, with a series of data sets collected over a temperature range encompassing a series of phase transitions in several samples.

The Diamond Light Source uses an electron gun to create a stream of electrons which are then focused and accelerated by a magnetic field around a 561.6 m ring to energies of 3 Giga electron Volts (GeV). The “beam” then is channelled to a second ring which uses magnets to maintain the travelling speeds and also to excite the electrons causing the release of X-ray radiation. This X-ray beam is then split off to the many separate beamlines including III.

A series of 5 multi-analyser crystal (MAC) detectors, each comprising of 9 Si 111 crystals and 9 detectors is used to collect data over 2theta range of 0.01 ° - 149 °, figure 3.4.

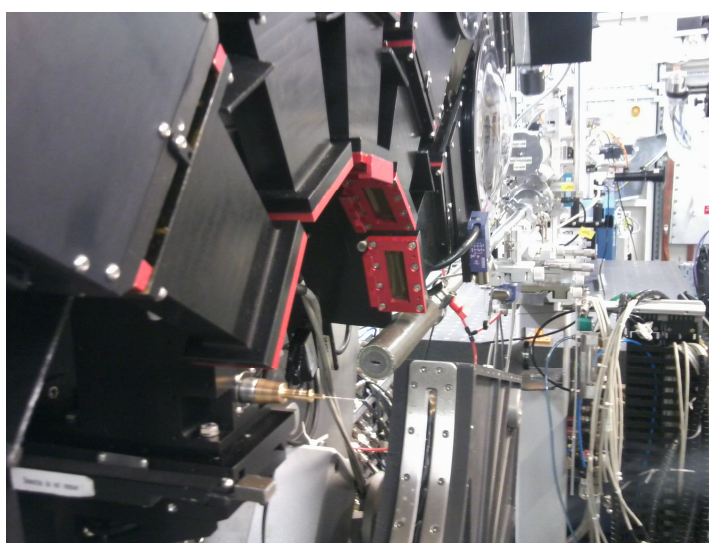


Figure 3.4: III high resolution powder X-ray diffractometer

Samples were mounted in borosilicate glass capillaries with a 0.5 mm internal diameter and heat sealed before being mounted in a brass base, with care taken to ensure that the capillary was held perpendicular to the base plate, such that when it is mounted and spun it would be centred in the beam. This could then be attached to the diffractometer by the base through the presence of magnets.

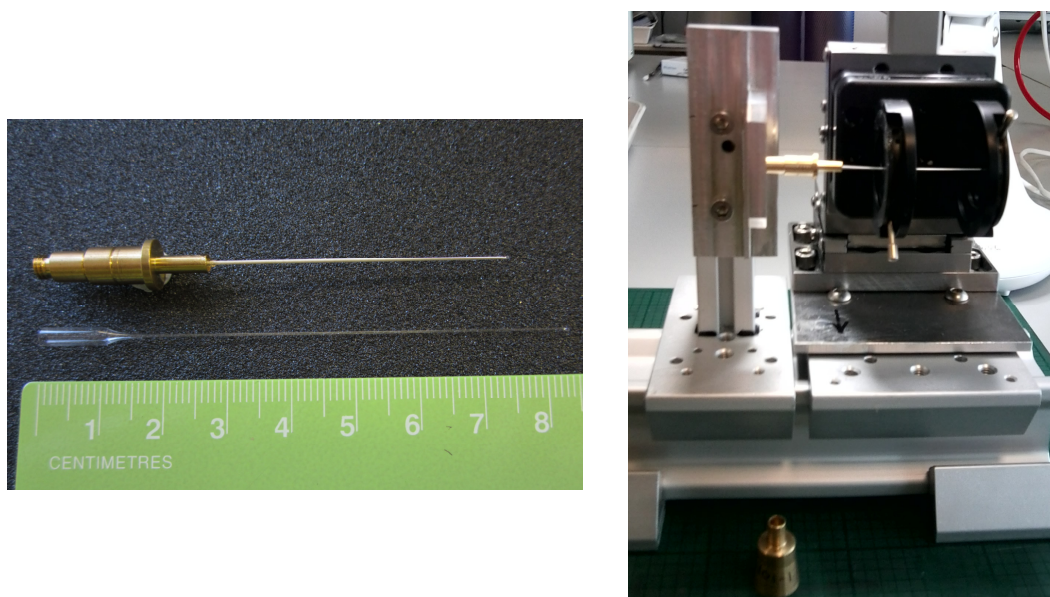


Figure 3.5: Loaded capillary and mounting procedure to ensure the capillary rotates perpendicular to the X-ray beam

Data were collected on samples at room temperature for a period of 1200 s, over a 2θ range of $0 - 149^\circ$, with the samples spinning to prevent any artificial peak distortions such as broadening or intensity changes as a result of inhomogeneous packing of the capillaries. For several samples a Cryostream Plus was used to collect data from temperatures as low as 95 K and as high as 470 K in order to observe the sample in polymorphic different phases. In each instance data were collected at temperature for a period of 900 s with the sample rotating, before being ramped to the next temperature and then undergoing a dwell period of 300 s in order that the sample reach thermal equilibrium with the thermocouple, before the next data set was collected. Depending on the location of the phase boundaries, which were approximately known before the high resolution diffraction studies were initiated, data were collected at 10, 20, 25 or 50 K intervals.

3.4: Rietveld Refinement

Powder X-ray diffraction data gives information on a 3-dimensional crystal lattice, but displays this information in 1-dimension. As a result of this, some of the information can become hidden as a result of peaks overlapping and combining their intensities. The Rietveld method calculates a mathematical model for a theoretical lattice and a motif of ions contained within, taking into account any peaks which overlap. This model can then be refined against collected powder X-ray diffraction data by way of a “least squares fit” to find the minimum difference between the theoretical model and the experimental data. This is done using the following equations:-

$$S = \sum w_i [y_i(obs) - y_i(calc)]^2$$

w_i = weighting factor (equation 3.2)
 $y_i(obs)$ = Observed intensity at i
 $y_i(calc)$ = Calculated intensity at i Equation 3.1

The weighting factor, w_i , is used to ensure that low intensity peaks and background are fitted as well as the higher intensity peaks.

$$w_i^{-1} = \sigma_i^2 = \sigma_i^2(statistical) - \sigma_i^2(background)$$

Equation 3.2

GSAS^[2, 3] is used to minimise the function S by refining parameters such as atomic positions, site occupancy, lattice parameters, background coefficients and peak profile. The quality of the fit can be monitored by the R_p (profile factor), and wR_p (weighted profile factor), whilst the goodness of fit is indicated by the χ^2 value, which is optimal when $\chi^2 = 1$, representing an ideal match between experimental and theoretical data.

$$R_p = \frac{\sum y_i(obs) - y_i(calc)}{\sum y_i(obs)}$$

Equation 3.3

$$wRp = \left(\frac{\sum w_i (y_i(obs) - y_i(calc))^2}{\sum w_i y_i(obs)^2} \right) = \left(\frac{s}{\sum w_i y_i(obs)^2} \right)^{1/2} \quad \text{Equation 3.4}$$

$$\chi^2 = \frac{\sum w_i [y_i(obs) - y_i(calc)]^2}{N - V + C} = \frac{S}{N - V + C} \quad \text{Equation 3.5}$$

N = Number of observables

V = Number of variables

C = Number of constraints

3.5: Scanning Electron Microscopy

A Jeol JSM 5600 scanning electron microscope (SEM) was used to gain insight into the ceramic microstructure of sample pellets, giving information on the grain sizes, homogeneity and packing in the samples after sintering.

Samples were cracked to expose interior faces which were then mounted perpendicular to the beam in the sample chamber which was then evacuated. A tungsten filament was used as a source to create a high energy beam of electrons which were accelerated through a voltage of 5 kV, with this beam being focused onto the sample surface, allowing for up to 300000 times magnification of the surface.

Increasing the accelerating voltage to 30 kV increases the number of back scattered electrons with the intensity of the back-scattered electrons related to the atomic number of an element. This allowed for a qualitative analysis of the sample, indicating the presence of possible impurities and giving information on the homogeneity of the sample.

3.6: Immittance Spectroscopy

3.6.1: Isothermal measurements

Immittance spectroscopy was used to study the electrical properties of the samples made. When properly analysed, immittance data is able to give information on the electrical microstructure of the pellets as described in chapter 2.

Immittance data were collected on electroded pellets using an HP 4192A Impedance analyser. Samples were mounted in a horizontal jig, (figure 3.6), which could be mounted in a Carbolite 301 furnace. A thermocouple was held in a fixed position in close proximity to the pellet in order to establish the pellet temperature. A series of data sets were recorded at increasing temperature, with time given for the pellet and its surrounding environment to equilibrate before each data set was collected. A geometric factor, d/A , was applied to the collected data so as to take into account sample geometry.

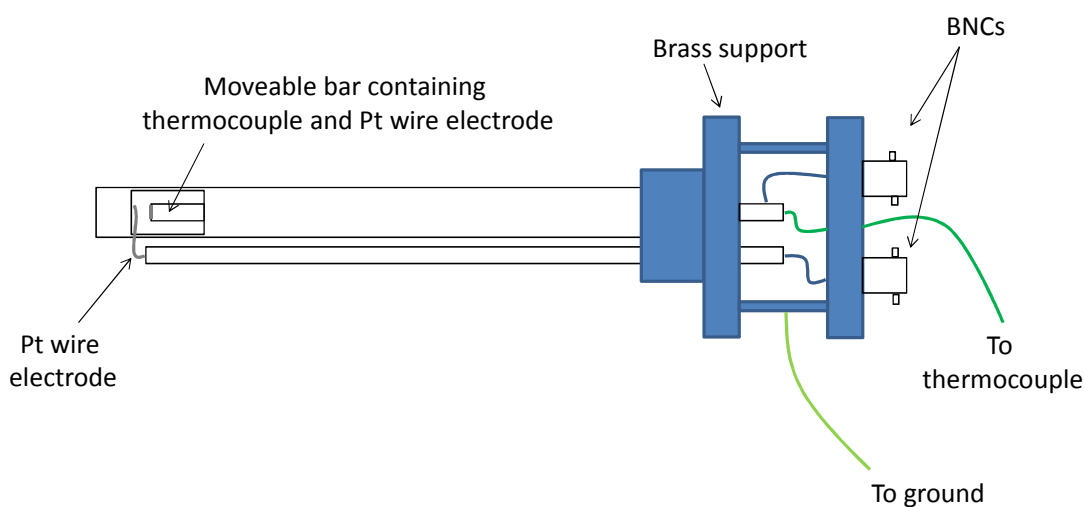


Figure 3.6: Horizontal sample jig.

ZView Version 2.9c was used to process and plot the collected data as a series of complex plane and spectroscopic plots, including those discussed in section 2.3, as well as capacitance and loss spectroscopic plots. Analysis of this data was able to yield values including R_b , R_{gb} , C_b , C_{gb} , ϵ' , ϵ'' and conductivities.

3.6.2: Curie-Weiss analysis

As well as referring to the temperature at which a ferro- or ferri-magnetic material becomes paramagnetic; the Curie temperature, T_C , refers to the temperature at which spontaneous polarisation is lost in ferroelectric materials and the material becomes effectively non-polar dielectric or “paraelectric”^[4] due to thermal randomisation of dipoles. Above this temperature the electrical susceptibility, and therefore the relative permittivity, of the material follows the Curie Weiss law.

$$\epsilon_r = \frac{C_w}{T - T_0} \quad \text{Equation 3.6}$$

In this equation C_w is the Curie constant of the material, T_0 is the Curie-Weiss temperature and ϵ_r is the relative permittivity.

The value of T_0 when compared to the value of T_C , can be used to determine something of the nature of the phase transitions, with phase transitions with $T_0 \approx T_C$ being second order and phase transitions where $T_0 < T_C$ bring first order^[5].

The magnitude of the Curie-Weiss constant can also be used to establish the type of ferroelectric, based on the phase transition at the Curie temperature, with three methods of generating ferroelectric behaviour having been distinguished between by the magnitude to the Curie temperature^[6]. These are

- Group I; Displacive ferroelectrics: Spontaneous polarisation as a result of displacement of ions from their thermal equilibrium position below T_C . (e.g. BaTiO_3)
- Group II; Order-disorder ferroelectrics: Ordering of rotatable permanent dipoles below T_C . (e.g. Rochelle salt)
- Group III: Coupled order-disorder ferroelectrics; Ordering of strongly coupled dipoles below the T_C . (e.g. $(\text{NH}_4)_2\text{SO}_4$)

Group I ferroelectrics generally have Curie-Weiss constants of the order of magnitude $\sim 10^5$, compared to $\sim 10^3$ for group II and $\sim 10^1$ for group III^[6].

3.6.3: Arrhenius behaviour

As the materials studied in these thesis are wide band gap semi-conductors and conductance is generally thermally activated and thus should exhibit Arrhenius behaviour. The conductivity of the bulk material can be calculated as resistance⁻¹, the log of this can then be plotted against temperature⁻¹ to give a linear Arrhenius plot, equation 3.7. The gradient of this plot corresponds to the band gap of the electrons in the material, the magnitude of which can be used to make inferences as to the type of any conduction in the pellets, such as through oxygen vacancy routes.

$$\sigma = \sigma_0 \exp\left(\frac{-E_a}{kT}\right) \quad \text{Equation 3.7}$$

In this equation σ is the conductivity, σ_0 is a pre-exponential factor, E_a is the activation energy, k is the Boltzman constant and T is the temperature in Kelvin.

3.6.4: Temperature controlled sweeps

Capacitance and loss data as a function of frequency were also collected at both above and sub-ambient temperatures, by means of automated sweeps. Data were collected at room temperature and above using a Wayne-Kerr 6500B impedance analyser connected to a horizontal sample jig, figure 3.6, mounted in a Carbolite 301 furnace. Sub-ambient temperature measurements were recorded using an Agilent 4294A precision impedance analyser connected to a closed-cycle cryostat, which had a working temperature range of 50-320 K.

Automated sweep programs were used to collect data over the frequency range of $1-1 \times 10^6$ Hz at 2 degree intervals; this gave a more accurate profile of the dielectric constant in order to establish the T_c and maximum dielectric constant.

In order to collect the sub-ambient temperature the electrode sample was mounted next to a thermocouple and the chamber sealed and evacuated to a pressure no greater than 6.0×10^{-2} mbar. The sample chamber was heated to 320K in order to give some overlap between the cryostat and furnace data set, such that the two data sets could be combined, and left for a period of at least 30 minutes to equilibrate. Data

was then collected on cooling at 2 degree intervals over the frequency range of $1-1 \times 10^6$ Hz, with a cooling rate of 2 Kmin^{-1} , just as with the above ambient temperature data.

3.7: Theoretical Density Calculations

The theoretical density of a ceramic consisting of a matrix of small crystallites can be calculated using equation 3.8 which takes into account the size of the unit cell as well as the structure type and mass of the atomic species. This equation assumes that the composition of the solid is free from the presence of impurities or defects and relies on accurate, well defined X-ray diffraction data and analysis in order to calculate the unit cell volume.

$$\text{Theoretical Density} = \frac{n \cdot M_r}{V_c \cdot N_A} \quad \text{Equation 3.8}$$

n = Number of formula units per unit cell

M_r = Mass of formula in g mol^{-1}

V_c = Volume of unit cell in cm^{-3}

N_A = Avogadro's number,
 $6.023 \times 10^{23} \text{ mol}^{-1}$

Thus for a perovskite unit cell, ABO_3 , $n=1$, as shown in figure 3.7, M_r can be calculated from the atomic masses of the involved ionic species, Avogadro's constant is known and the volume, V_c , can be determined from X-ray diffraction data analysis.

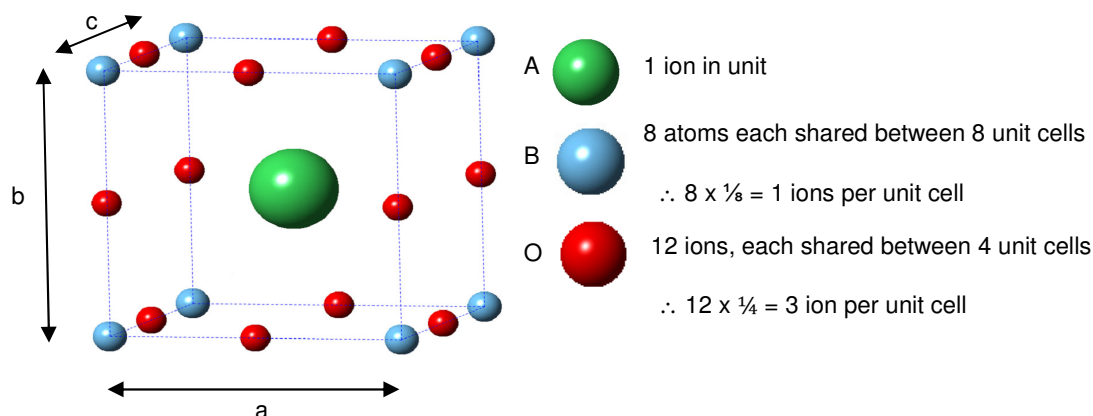


Figure 3.7: Showing the number of formula units, ABO_3 , in the perovskite unit cell

3.8: Hysteresis Measurements

An aixACCT TF 2000 analyser was used to carry out ferroelectric hysteresis measurements on electroded pellets. Samples were mounted between two contacts in an oil bath to prevent arcing. The presence of the electric field causes a distortion of the unit cell dimensions of the ferroelectric material, and thus the changing field can result in any weaknesses in the pellets due to the presence of pores, impurities and other pinning points, becoming catastrophic weaknesses in the sample such as cracks and holes. In order to prevent this from occurring, data were collected on each pellet several times at increasing voltages and decreasing frequencies, with the data studied in between runs in order to look for any irregularities in the data that might suggest that the pellet was starting to break down. A voltage of 2000 V was applied to pellets approximately 1 mm thick, resulting in fields of around 20000 V cm^{-1} . These fields could generally be applied at a frequency of 1 Hz without damaging the pellets.

As well as recording the remnant polarisations, saturation polarisations and coercive fields, the geometry of the pellet, area and thickness, were taken into account, allowing for the calculation of capacitance and loss which could then be compared to values obtained by the use of other analytical techniques.

In each instance a series of 3 loops were obtained by the application of three bipolar excitation fields each separated by a relaxation period. A prepolarisation pulse results in the formation of $P_{\text{rrel-}}$ (relaxed remnant polarisation state in the negative

field direction) which is where the first loop starts; as the voltage is increased, this traces up to $P_{\max+}$ which is the saturated polarisation in the positive field direction. The magnitude of the voltage is then reduced to 0 V, at which point the resulting polarisation is the remnant polarisation, P_{r+} in the positive direction. As the field is then increased in the alternate direction, $P_{\max-}$, the saturated polarisation in the negative field direction is reached. As the field is then reduced back to zero the remnant polarisation, P_{r-} , in the negative direction is achieved. This is generally greater in magnitude than P_{rrel-} due to polarisation losses with time. The second loop then takes the sample to P_{r+} without collecting data, with the third loop then starting at P_{rrel+} which is then driven to $P_{\max-}$. The voltage is then reduced until P_{r-} is reached and the sample is then driven up to $P_{\max+}$ before ending at P_{r+} , with the repetition in $P_{\max+}$ and $P_{\max-}$ being used to balance the loops.

The points at which the x-axis is crossed, i.e. at zero polarisation, are termed the coercive fields, E_{c-} and E_{c+} . The closed loop is created by a combination of parts of each of the first and third loop. All of the pulses applied during the hysteresis measurements use triangular voltage excitations.

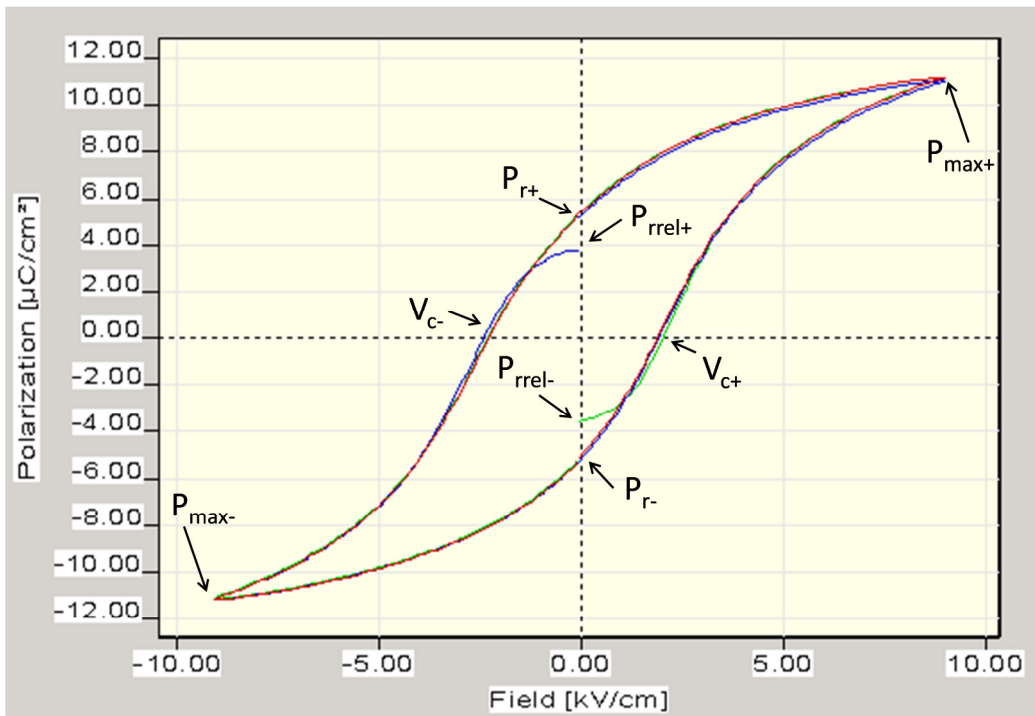


Figure 3.8: Characteristic parameters determined from a dynamic hysteresis measurement.

References

1. Fletcher, D.A., McMeeking, R.F., Parkin, D., J. , *The United Kingdom Chemical Database Service*, in *Chem. Inf. Comput. Sci.* 1996. p. 746-749.
2. A.C. Larson and R.B. Von Dreele, *General Structure Analysis System (GSAS)*. 2000: Los Alamos National Laboratory Report LAUR 86-748.
3. B. H. Toby, *EXPGUI, a graphical user interface for GSAS*. *J. Appl. Cryst.*, 2001. **34**: p. 210-213.
4. Trainer, M., *Ferroelectrics and the Curie-Weiss law*. *Eur. J. Phys.*, 2000. **21**(5): p. 459-464.
5. Jaffe, B., W.R. Cook, and H. Jaffe, *Piezoelectric Ceramics*. 1971: Academic Press London.
6. Nakamura, E., T. Mitsui, and J. Furuichi, *A Note on the Classification of Ferroelectrics*. *J. Phys. Soc. Jpn.*, 1963. **18**(10): p. 1477-1481.

Chapter 4: The effects of ceramic processing

4.1: Introduction

When working with ceramics as opposed to single crystals, the properties of the samples are highly dependent on the microstructure, which is in turn partially dependant on the precise conditions under which the material was prepared.^[1-6] Properties such as the impedance, capacitance and hence the relative permittivity all have both grain boundary and bulk contributions and may also be affected by the presence of porosity in the ceramics, as well as the presence of impurities and defects.

The extent to which grains grow during the sintering process depends on both the temperature and atmospheric sintering conditions, as well as the pressure to which the pellet compacts have been exposed to prior to sintering, and the sintering dwell time^[5, 7, 8]. Grain growth can also be affected by the treatment of the powder pre-pressing, including the number of times it has been heated and the conditions of those heating cycles.

The particle size of the powders, both initial oxides and carbonates as well as partially reacted compositions, can also have an effect on the grain growth during sintering. Particle size may also influence the homogeneity of the material and can impact on the packing of the green body, which, along with pressures applied pre-sintering, can affect the final density of the pellet, which in turn can affect its electrical characteristics,

4.2: Case Study 1: 50% $[\text{Ba}(\text{Ti}_{0.8}\text{Zr}_{0.2})\text{O}_3]$ -50% $[(\text{Ba}_{0.7}\text{Ca}_{0.3})\text{TiO}_3]$ – Parasitic grain boundary contributions

The composition 50% $[\text{Ba}(\text{Ti}_{0.8}\text{Zr}_{0.2})\text{O}_3]$ -50% $[(\text{Ba}_{0.7}\text{Ca}_{0.3})\text{TiO}_3]$, 50:50 BZT-BCT, was first synthesised by Ren et al.^[9, 10] and was found to have a very high dielectric constant

of around 19000 at $\sim 80\text{ }^{\circ}\text{C}$ as well as a Piezoelectric coefficient (d_{33}) value of $\sim 620\text{ pC N}^{-1}$ which is comparable to many PZT-based compositions^[11].

Several pellets of 50:50 BZT-BCT were synthesised for study in this project, with the aim of doing a more comprehensive study on these materials. This included the investigation of the frequency dependencies of the electrical properties and the reproducibility of the microstructure, as well as going on to compare these materials to other doped compositions.

4.2.1: Synthesis

Samples were formed using the ceramic synthesis techniques described in chapter 3.1. Appropriate stoichiometric ratios of BaCO_3 (purity $>99\%$), CaCO_3 ($>99\%$), TiO_2 ($>99.9\%$) and ZrO_2 ($>99\%$) were used. The first batch of pellets were formed by pressing the calcined powder into pellets, applying 30000 psi of pressure by means of an isostatic oil press, and then subjecting the pellets to sintering at a temperature of $1350\text{ }^{\circ}\text{C}$ for a period of 30 hours in air, with ramping rates of 20 K min^{-1} . Another batch of pellets was made in the same manner, but with a sintering temperature of $1450\text{ }^{\circ}\text{C}$.

The properties of these pellets were compared to that of un-doped BaTiO_3 which had been prepared in exactly the same manner as the $1450\text{ }^{\circ}\text{C}$ sintered 50:50 BZT-BCT pellets.

4.2.2: Pellet densities

After measuring and weighing the pellet, in order to establish their geometries and density, it was found that the pellets sintered at the lower temperature of $1350\text{ }^{\circ}\text{C}$ were denser than those sintered at $1450\text{ }^{\circ}\text{C}$, 89 % compared to 84 %. A 91 % average density was achieved for un-doped barium titanate.

Dense pellets are generally expected to have more desirable properties due to the fact that low densities commonly arise as a result of pores being present in the material. This porosity can take the form of isolated pores or continuous propagating cracks.

Ceramic materials are inherently prone to weakness in the form of cracking^[12]. This can commonly occur during the sintering process caused by thermal gradients in the pellet and differences in shrinkage rates between the pellet surface and exterior. Slow heating and cooling rates, along with isothermal dwell periods, are often used in order to prevent or limit this form of cracking^[13, 14]. It is often found with ceramics that fracturing is more likely to occur than plastic deformation when tensile strain is applied, and even in the case of a compressive stress, the irregularity of the grains can give rise to fault lines which can form cracks upon the relief of the load^[15]. This cracking normally propagates itself along an axis perpendicular to the applied force and can be either trans- or inter-granular in nature^[16].

One of the most common types of crack found is often formed during the uniaxial pressing of the pellet and is a “mushroom” shape crack that can expand over the whole cross section of the pellet, figure 4.1. This sort of cracking renders the pellet unsuitable for any electrical measurements due to the presence of an air layer throughout the whole face, or large sections of the face of the pellet. The presence of these cracks in between the two electrode surfaces significantly reduces the capacitance.

These cracks often form during the pellet formation process when a uniaxial force is applied to loose powder in a pellet press in order to form the desired pellet geometry. By pressing the powder into very loosely formed compacts using an uniaxial press and then using an isostatic press at higher pressures to achieve good pellet densities, the prevalence of this type of crack can be greatly reduced as a result of lower strain gradients in the pressed pellet pre-sintering.

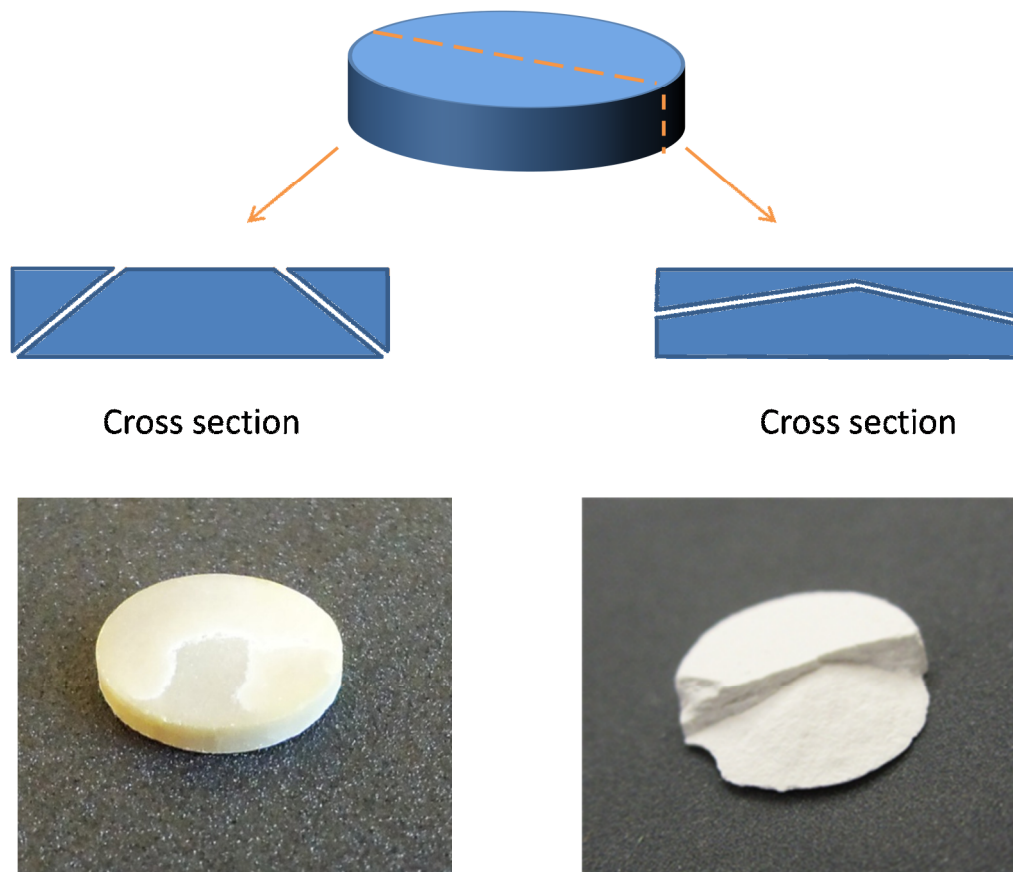


Figure 4.1: Brittle fracturing of pellets yielding them unsuitable for electrical measurements

By contrast, the presence of isolated pores in the material has only a minor effect on the properties of the pellet.

SEM images of pellets of un-doped BaTiO_3 shows the presence of large grains averaging between 25 and 75 microns in diameter, including some considerably larger, as well as a few isolated pores, figure 4.2. Though the grains were not found to be particularly uniform in their size, they were found to be densely packed throughout, with no evidence of any cracks or localised areas of high porosity. The grain boundaries also appear to be narrow and well defined.

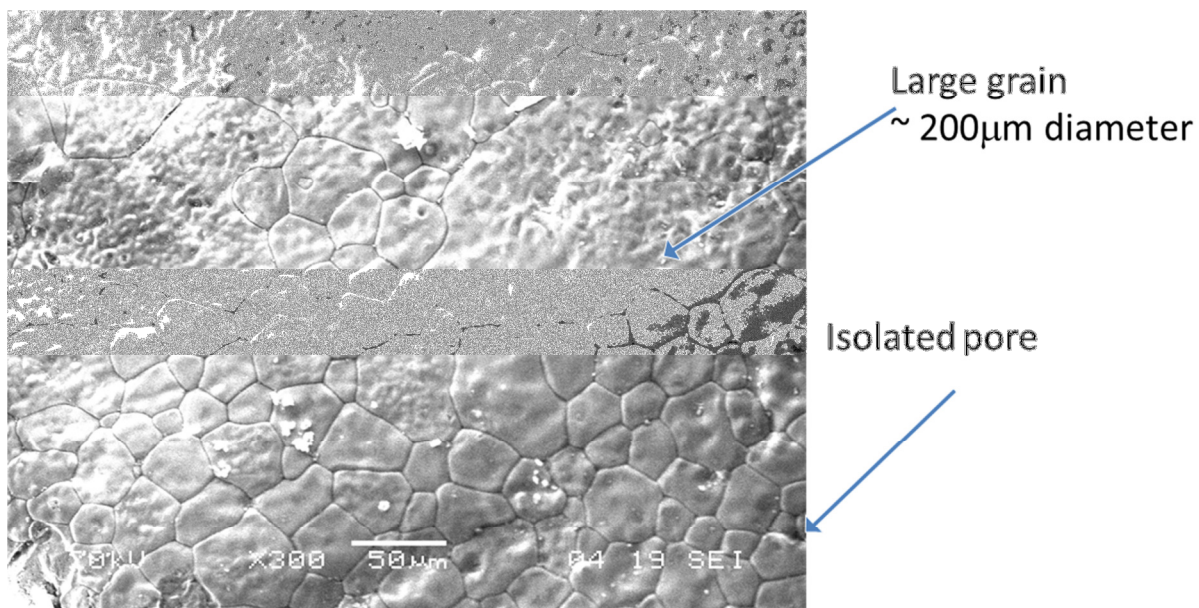


Figure 4.2: SEM image of un-doped BaTiO₃ sintered at 1450°C

The SEM images obtained for the 50:50 BZT-BCT pellets sintered at 1450°C show a similar profile of large grain sizes around 25 microns in diameter with isolated pores, although the grain sizes in and around the pores appear to be somewhat smaller, figure 4.3. Again, the grain boundaries appear distinct and no evidence of fracturing was observed.

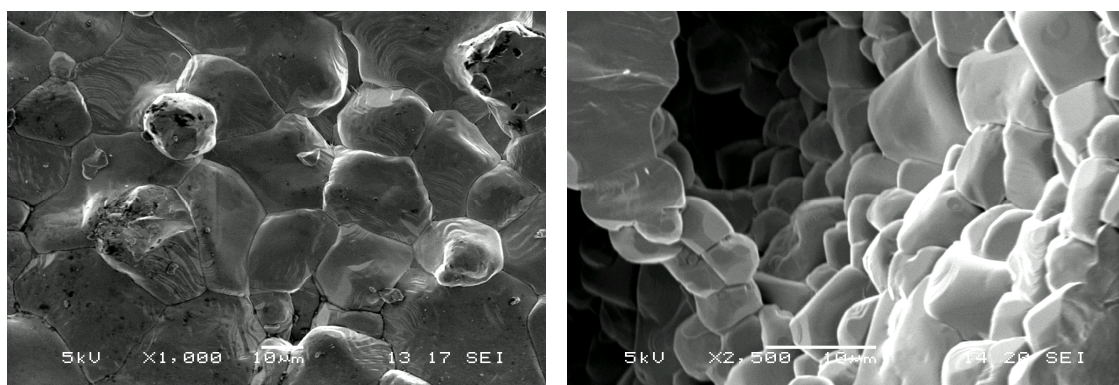


Figure 4.3: SEM images of 50:50 BZT-BCT sintered at 1450 °C showing a) a pellet surface and b) the interior of an isolated pore

By contrast, SEM images collected on a sample of 50:50 BZT-BCT sintered at 1350 °C show the presence of small grains (< 5 µm) which are poorly formed and difficult to distinguish from grain boundary regions, figure 4.4. This suggests that unlike both the un-doped BaTiO₃ and 1450 °C sintered 50:50 BZT-BCT compositions which showed the presence of clearly defined, (relatively) large grains with thin, well-defined grain boundaries, the 1350 °C sintered pellet appears to have much thicker

grain boundaries with smaller grains. This would result in a greater volume fraction of grain boundary material. Again only isolated pores are observed with no evidence of cracks being present.

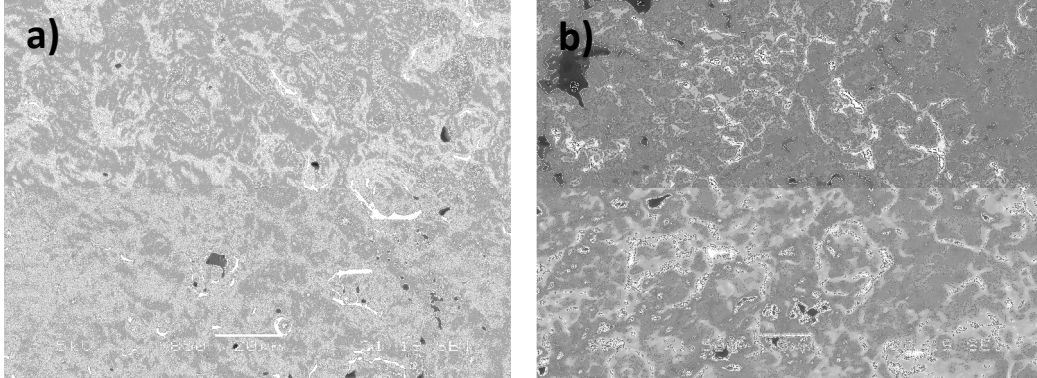


Figure 4.4: SEM images of 50:50 BZT-BCT sintered at 1350 °C showing a) isolated pores and b) small, poorly defined grains with thick grain boundaries

4.2.3: Dielectric properties

The capacitance of each of the pellets was measured as a function of both temperature and frequency, and was adjusted to account for pellet geometry and the permittivity of free space in order to give the relative permittivity as a function of temperature as described in section 2.2. The data collected from each sample at a frequency of 100 kHz are shown in figure 4.5.

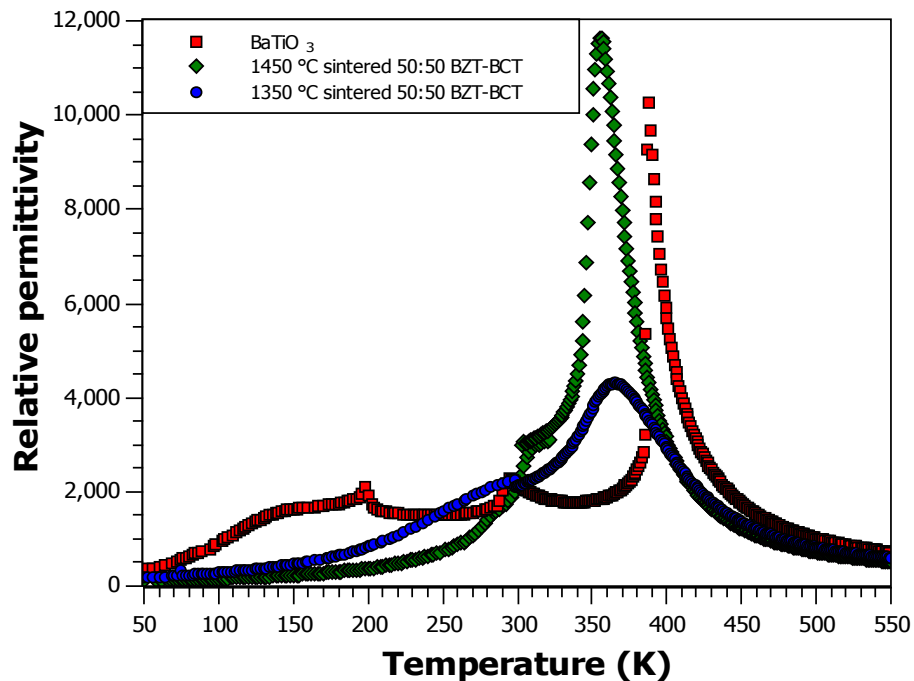


Figure 4.5: Relative permittivities of BaTiO₃, 1350 °C sintered 50:50 BZT-BCT and 1450 °C sintered BZT-BCT

For pellets sintered at 1450 °C, the addition of the calcium and zirconium dopants was found to cause an increase in the dielectric constant with respect to the un-doped BaTiO₃, along with a bringing together of the phase transitions, although all three were still visibly present. This is in agreement with the sorts of responses reported by Ren et al^[9]. However, the pellets sintered at 1350 °C were found to exhibit a relative permittivity maximum which was severely depressed compared to both the un-doped barium titanate and 50:50 BZT-BCT pellets sintered at 1450 °C, although with a marginally higher T_C. In addition to this, the lower temperature peaks, which in un-doped BaTiO₃ can be assigned to the rhombohedral/orthorhombic and orthorhombic/tetragonal phase transitions, were observed to be coalesced into one broadened peak in data collected from the pellets sintered at 1350 °C.

Plotting the loss data ($\tan \delta$) as a function of temperature, figure 4.6, also showed a correspondingly depressed maximum in the loss for the lower temperature sintered pellet compared to both the 1450 °C sintered pellet and un-doped BaTiO₃. The temperature at which this maximum occurred was also found to be depressed compared to the 1450 °C pellet, contrary to that of the relative permittivity data. Good agreement between the temperature of the peaks in the relative permittivity and loss data was observed for both un-doped BaTiO₃ and the 1450 °C sintered 50:50 BZT-BCT. However, the 1350 °C sintered 50:50 BZT-BCT pellet showed the peak in $\tan \delta$ to be depressed by ~11 °C relative to the relative permittivity maximum (see appendix chapter 4, figures A4.1-3). In addition to this, it was found that for both of the doped materials, the number of peaks observed in the loss data was fewer than that of the un-doped BaTiO₃, with two peaks being observed in data collected on both the 1350 °C and 1450 °C sintered pellet, compared to 3 peaks in the un-doped BaTiO₃. However, both the BZT-BCT pellets show the presence of a broad region of increasing loss between 50 -175 K, figure 4.6.

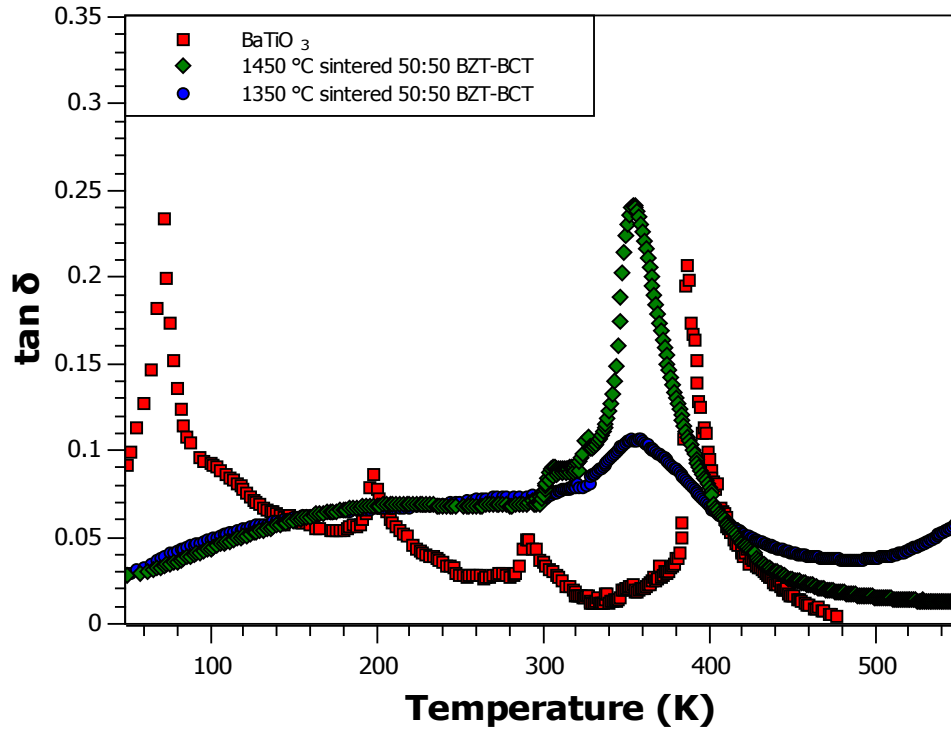


Figure 4.6: Temperature dependence of the loss data for BaTiO₃ and 50:50 BZT-BCT sintered at 1350 °C & 1450 °C collected at 100 KHz

Slight discrepancies in the data sets at around 300 K arise due to the fact that two separate apparatus were used to collect the data (see section 3.6), one for sub-ambient temperature readings and one for above-ambient readings, resulting in slightly shifted traces which were then corrected, such that the two traces were aligned.

4.2.4: X-ray data

In-house powder X-ray diffraction data were collected on each of the pellets. Samples were mounted in a bed of Si powder as described in chapter 3, section 3, resulting in the presence of Si peaks in each of the patterns, figure 4.7. A reference sample of Si is shown alongside the experimental data for comparison.

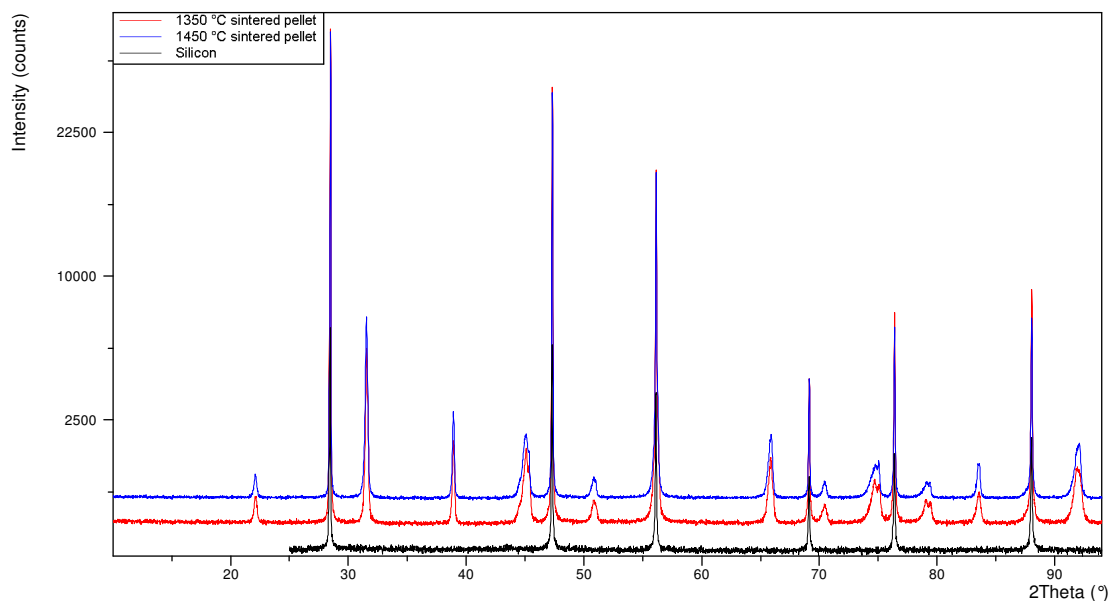


Figure 4.7: In-house powder X-ray diffraction data collected on samples of 1350 °C and 1450 °C sintered BZT:BCT mounted in silicon with a Si reference shown in black. *N.b.* data has been off-set in the on the y-axis

This data shows that despite clear differences in density, grain growth and dielectric spectroscopy data, the samples are virtually indistinguishable by in-house powder X-ray diffraction analysis. Diffraction data from each sample is consistent with a perovskite structure with no additional or un-indexed peaks, save for those shown to be due to the Si mount. This is consistent with the samples being single phase with no appreciable crystalline impurities or unreacted starting reagents. Several of the peaks are asymmetric suggesting a non-cubic perovskite; however the resolution of the data is too low to accurately determine peak splitting and thus crystal symmetry.

This shows that X-ray diffraction as an analysis tool is not a suitable technique for determining whether a doped BaTiO₃ ceramic is optimally processed and that a more in-depth analysis of each pellet is required.

4.2.5: Capping of the permittivity maxima

The lowering of the magnitude of the relative permittivity of the 1350 °C sintered pellet, but with a lack of evidence to suggest a multiphase state, leads to capping being the most likely reason for the observations. Capping arises as a result of any parasitic capacitances such as a large grain boundary contribution to the total

sample capacitance. As described in chapter 2, section 4, the most common equivalent circuit used to describe the electrical response of a polycrystalline ceramic is based on the brick layer model and consists of two parallel RC elements placed in series, figure 4.8. The parallel RC elements represent the responses of the bulk and grain boundary regions. The impedance, modulus, admittance and complex permittivities are comprised of a contribution from both RC elements.

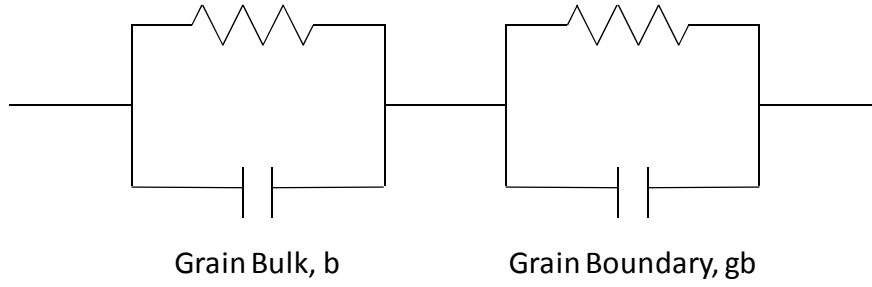


Figure 4.8: Equivalent circuit for a ceramic comprising of bulk and grain boundary regions

In an uncapped pellet, the contribution to the overall capacitance of the pellet is almost entirely that of the bulk material, with little to no contribution from either the grain boundary or other parasitic components such as the electrodes or measuring leads. However, when large volume fractions of grain boundary are present, either due to small grain sizes or thick, poorly defined grain boundary regions, this is no longer the case^[17]. As a thin layer region the grain boundary generally has a capacitance many orders of magnitude greater than that of the bulk^[18]. The effective capacitance of the sample, C' , is comprised of both the bulk and grain boundary contributions, and is also dependent on the measuring frequency. The circuit in figure 4.8 results in a C' vs frequency spectra with two plateaus separated by a dispersion, figure 4.9. This is due to the difference in the time constants of the two RC elements. For the equivalent circuit shown in figure 4.8, at low frequency C' is given by equation 4.1

$$C'_{lf} = \frac{R_b^2 C_b + R_{gb}^2 C_{gb}}{(R_b + R_{gb})^2} \quad \text{Equation 4.1}$$

where R_{gb} is the resistance of the grain boundary, R_b is the bulk resistance, C_{gb} is the grain boundary capacitance and C_b is the bulk capacitance. Thus at low frequency, if $R_{gb} \gg R_b$ and $C_{gb} \gg C_b$; then

$$C'_{lf} = \frac{R_b^2 C_b + R_{gb}^2 C_{gb}}{(R_b + R_{gb})^2} \cong \frac{R_{gb}^2 C_{gb}}{(R_{gb})^2} \cong C_{gb} \quad \text{Equation 4.2}$$

At high frequency C' is given by

$$C'_{hf} = \frac{1}{(C_b)^{-1} + (C_{gb})^{-1}} \quad \text{Equation 4.3}$$

If $C_{gb} \gg C_b$, this equation can be simplified to

$$C'_{hf} = \frac{1}{(C_b)^{-1} + (C_{gb})^{-1}} \cong \frac{1}{(C_b)^{-1}} \cong C_b \quad \text{Equation 4.4}$$

Thus, provided that $R_{gb} \gg R_b$ and $C_{gb} \gg C_b$ the capacitance of a ceramic should tend to two plateaus where the capacitance at high frequency is $\cong C_b$ and the capacitance at low frequency is $\cong C_{gb}$. As the difference in magnitude between the grain boundary and bulk R and C values falls, some mixing occurs, altering the capacitances such $C'_{hf} \neq C_b$ and $C'_{lf} \neq C_{gb}$.

Using R_{gb} , R_b and C_b data of the order of magnitude observed for BaTiO_3 -based ceramics and by varying C_{gb} we can show the impact of grain boundary capacitance on the overall C' spectra, figure 4.9. The magnitudes of R_{gb} , R_b , C_{gb} and C_b used are shown in table 4.1.

Table 4.1: Model bulk and grain boundary capacitances and resistances to be plotted as a function of frequency in figure 4.9

Scenario	Bulk		Grain boundary	
	Capacitance (F)	Resistance (Ω)	Capacitance (F)	Resistance (Ω)
1	1×10^{-11}	5×10^4	1×10^{-11}	2.5×10^5
2	1×10^{-11}	5×10^4	1×10^{-10}	2.5×10^5
3	1×10^{-11}	5×10^4	1×10^{-9}	2.5×10^5
4	1×10^{-11}	5×10^4	1×10^{-8}	2.5×10^5

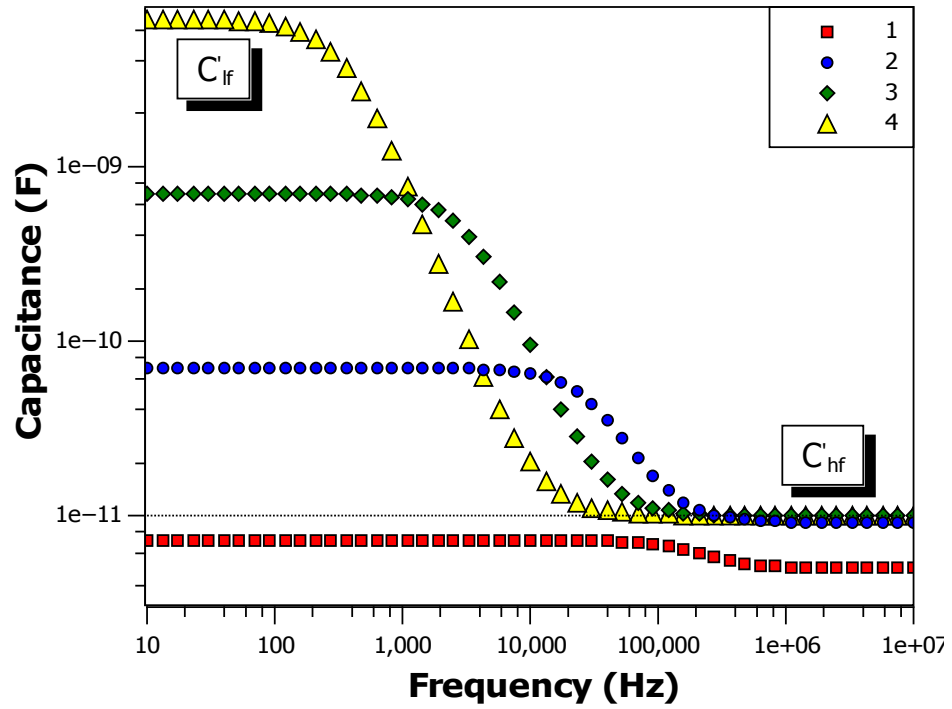


Figure 4.9: Capacitance as a function of frequency for scenarios 1-4 listed in table 4.1, with C_b shown as a dotted black line

This clearly shows how the capacitance of the high frequency plateau is lowered by the presence of grain boundary with a similar capacitance to the bulk region. At very high grain boundary capacitances ($\geq 1 \times 10^{-9}$ F for the scenarios listed in table 4.1) $C'_{hf} \cong C_b$ as shown by figure 4.10 and table 4.2.

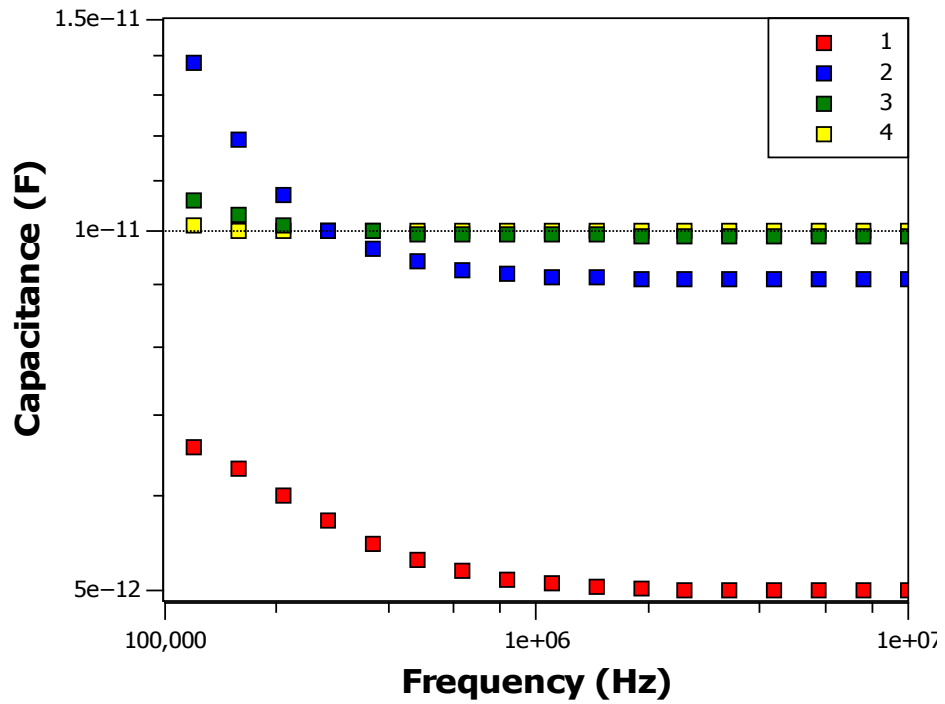


Figure 4.10: Capacitance as a function of frequency for scenarios 1-4 listed in table 4.1, with C_b shown as a dotted black line

Table 4.2: Magnitudes of C'_{hf} calculated using data sets shown in table 4.8

Scenario	C_b (F)	C_{gb} (F)	C'_{hf} (F)
1	1×10^{-11}	1×10^{-11}	0.50×10^{-11}
2	1×10^{-11}	1×10^{-10}	0.909×10^{-11}
3	1×10^{-11}	1×10^{-9}	0.99×10^{-11}
4	1×10^{-11}	1×10^{-8}	1.00×10^{-11}

Altering the magnitude of C_{gb} also acts to shift the frequency range of each curve as it affects the time constant, τ . This can also be shifted by varying the temperature at which the capacitance is measured, thus it is possible to alter which part of the profile is observed over the frequency range accessible by the apparatus used to study the pellets electrical responses^[17]. At higher temperatures the C'_{lf} plateau shifts to higher frequencies. As a result, the impact of the grain boundary response to the overall capacitance becomes more easily observed in both the complex impedance and modulus plots as well as the spectroscopic plots of Z'' and M'' . Thus by collecting data over a wide temperature range it is possible to obtain data from both the high and low frequency plateaus and establish the impact that the grain boundary electro-active region has on the effective capacitance of the material.

4.2.6: High temperature immittance data

Immittance spectroscopy measurements were collected on each of the 1350 °C and 1450 °C sintered 50:50 BZT-BCT compositions, with data being collected from room temperature to 543 °C and 650 °C, respectively. When comparing the complex impedance plots for the two samples (figures 4.11 and 4.12) collected at 513 °C and 518 °C, respectively, it was observed that whilst for each of the pellets the trace could be approximated as two semi-circular arcs, consistent with two distinct electro-active regions, the relative magnitudes of the two arcs varied greatly between the two pellets.

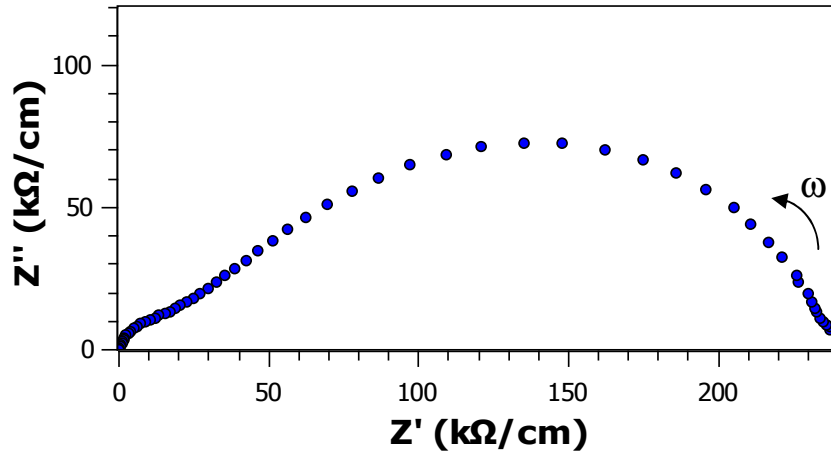


Figure 4.11: Complex impedance data from 1350 °C sintered pellet, collected at 513 °C

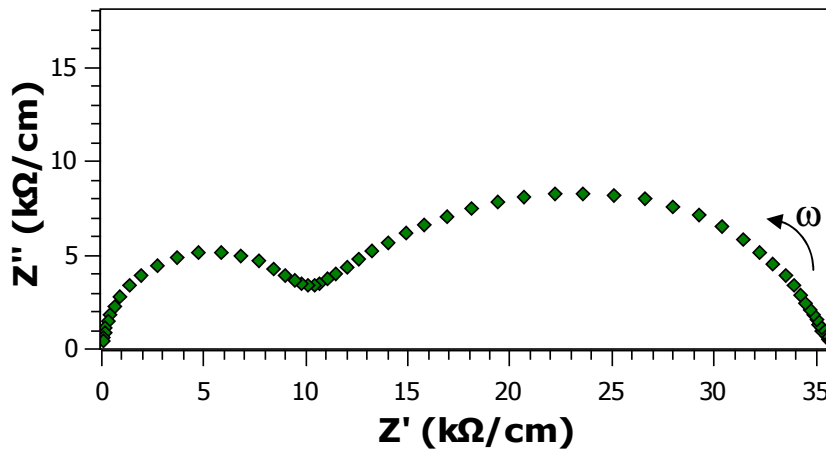


Figure 4.12: Complex impedance data from 1450 °C sintered pellet, collected at 518 °C

Whilst the high frequency arc of each composition was found to be of similar magnitude, the low frequency arc was found to be considerably larger in the data set collected on the lower temperature sintered pellet. This is consistent with the low frequency arc of the 1350 °C sintered composition having a significantly greater resistance than the 1450 °C sintered pellet.

The complex modulus plots for both the 1350 °C and 1450 °C sintered pellets are shown in figures 4.13 and 4.14, respectively. Data collected on the 1350 °C sintered sample shows the presence of an asymmetry of the main semi-circular arc at low frequency. A considerably smaller deviation is observed in the low frequency data collected on the 1450 °C sintered pellet. The dominant semi-circular arc observed in in data set collected from the 1350 °C sintered pellet was also found to be considerably more depressed than the dominant arc observed in the data collected on the pellets sintered at 1450 °C.

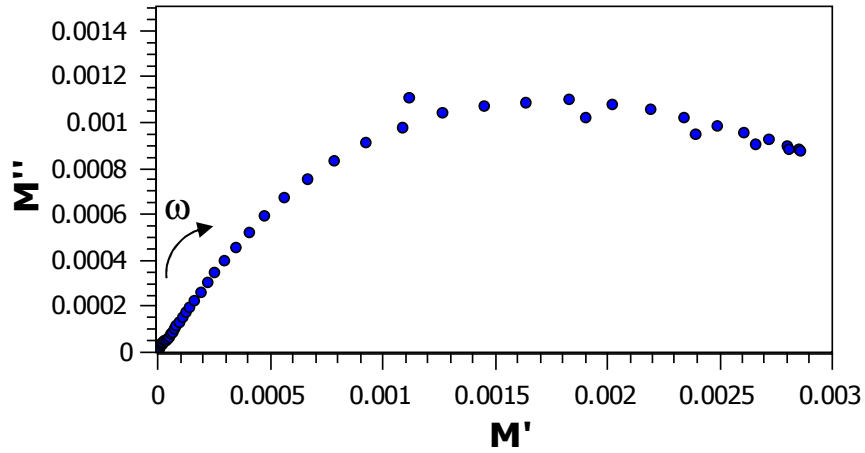


Figure 4.13: Complex modulus plot from 1350 °C sintered pellet, collected at 513 °C

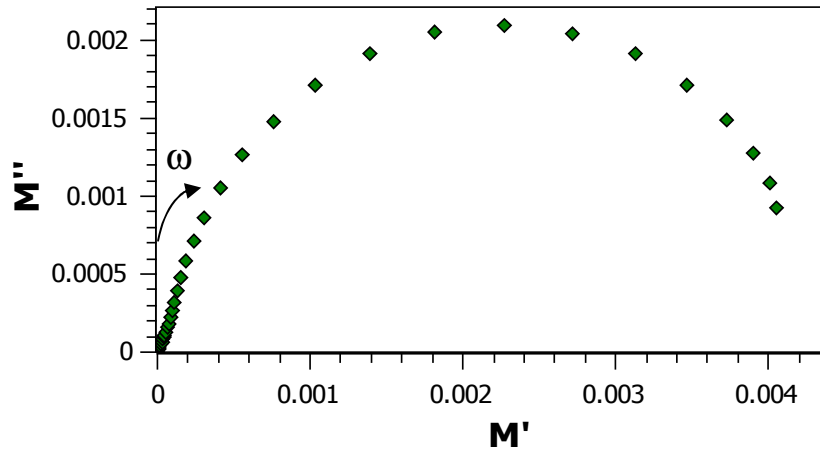


Figure 4.14: Complex modulus plot from 1450 °C sintered pellet, collected at 518 °C

As described in chapter 2, section 4, it is most commonly the case that dominant arcs in complex plane impedance plots are resultant of grain boundary electro-active regions, whilst the dominant arcs in complex plane modulus plots correspond to bulk responses. This can be confirmed by establishing the capacitance associated with each arc in the complex plane plots. Responses that arise due to bulk components in BaTiO₃-based ceramics would be expected to have a capacitance of the order of $\sim 1 \times 10^{-11} - 1 \times 10^{-12}$ F, whilst the grain boundary capacitance is generally much greater, $\sim 1 \times 10^{-8} - 1 \times 10^{-11}$ F^[18].

Using the frequency at the semi-circular arc maxima, along with the diameter of each arc in the complex plane plots it is possible to calculate an associated capacitance, and from the magnitude of that capacitance assign each arc as being either a grain boundary or bulk response (equation 2.15). The dominant arcs in the impedance data are found to be resultant of grain boundary electro-active regions,

whilst the minor arcs are that of the bulk response. The opposite is true for the M^* data in which the dominant arcs are found to correspond to bulk regions. This is consistent with the bulk capacitances being of the same order of magnitude for both pellets.

Plotting Z'' and M'' as a function of frequency, figure 4.15, for both pellets confirms that each pellet has two distinct electro-active regions. In each case the high frequency peak in the impedance data is coincident with the dominant peak in the M'' data, confirming that the two responses are resultant of the same electro-active region of the pellet, known to be the bulk response by virtue of the magnitude of the associated capacitances.

The data clearly shows that the lower temperature sintered pellet has a much larger low frequency, grain boundary peak, whilst the higher temperature sintered pellet has a substantially higher bulk contribution. It is also observed that the 1450 °C sintered pellet gives rise to more symmetric Debye peaks, most clearly observed in the M'' data sets. This implies a more ideal, electrically homogeneous sample.

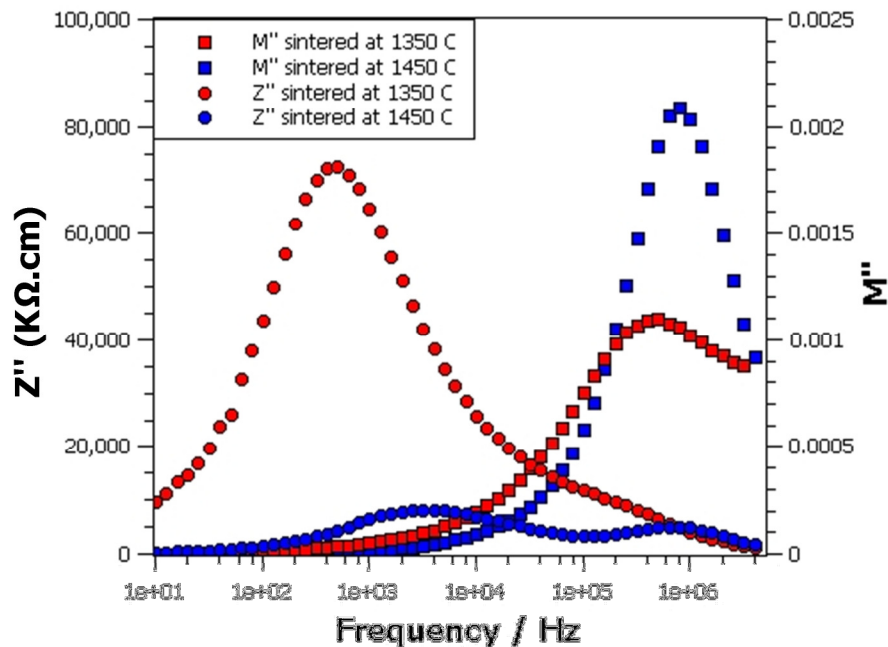


Figure 4.15: Spectroscopic plots of Z'' and M'' data collected on samples of 50:50 BZT-BCT sintered at 1350 ° and 1450 °C; data collected at 513 and 518 °C, respectively

Fitting each of the dominant semi-circular arcs in the complex plane impedance and modulus plots allowed for the calculation of the bulk and grain boundary resistivities

and capacitances over a range of temperatures. The values of each of these were then plotted alongside the total capacitance as a function of temperature, shown in figures 4.16 and 4.17 for the 1350 °C and 1450 °C sintered pellets respectively, with capacitance data plotted both on a linear and logarithmic capacitance.

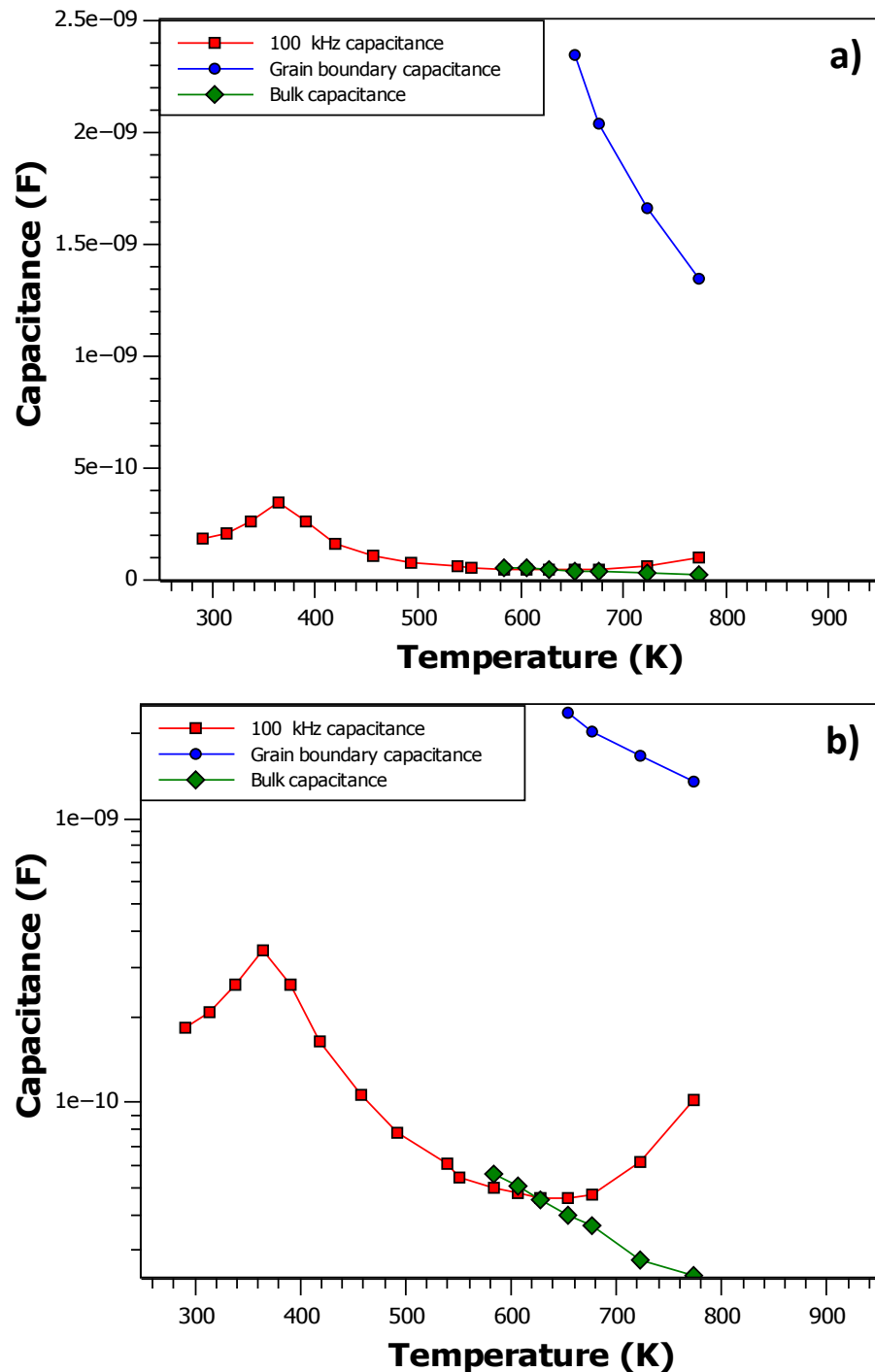


Figure 4.16: Bulk, grain boundary and total capacitance (at 100 KHz) data as a function of temperature for 1350 °C sintered pellet. Data is plotted on both a) linear and b) logarithmic scales

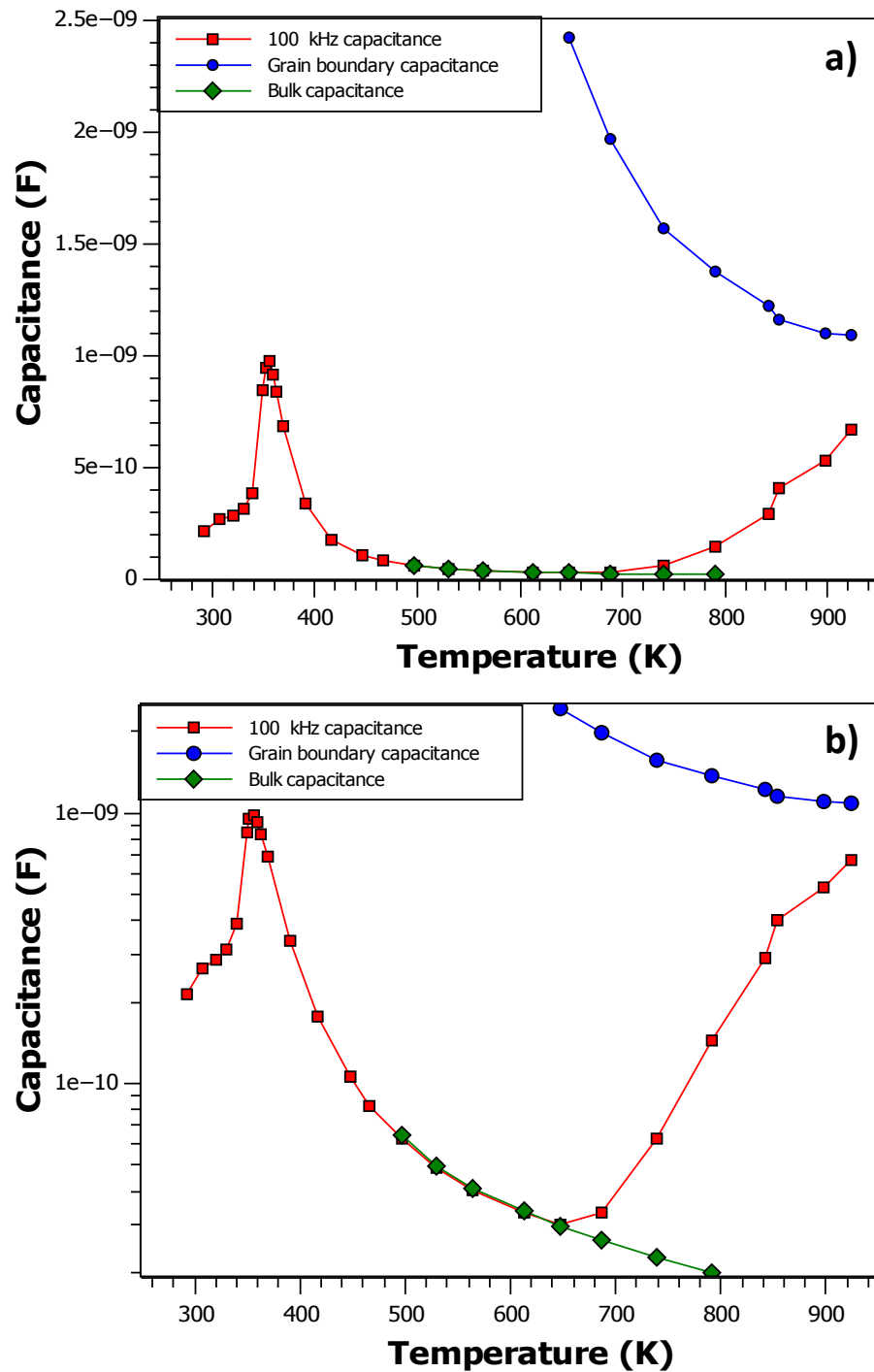


Figure 4.17: Bulk, grain boundary and total capacitance (at 100 KHz) data as a function of temperature for 1450 °C sintered pellet. Data is plotted on both a) linear and b) logarithmic scales

As well as showing the relative magnitude of the various component contributions to the total capacitance, this data clearly shows a good match between the bulk capacitance and total capacitance for the 1450 °C sintered pellet. Whilst for the 1350 °C sintered pellet, the linear capacitance plot of figure 4.16-a) shows a good agreement between the bulk and total capacitance magnitudes at high temperature,

the logarithmic scale shows that there is actually significant deviation between the two data sets[†].

In order to get a better appreciation for the fit, a Curie-Weiss representation of the data was plotted for the 1350 °C and 1450 °C sintered pellets, figures 4.18 and 4.19, respectively.

In the plot showing data from the 1450 °C sintered pellet there is a clear overlap between the total capacitance recorded at 100 KHz and that of the bulk capacitance. This shows that the magnitude of the overall capacitance is almost entirely that the bulk, with very little contribution from the grain boundary component. Thus this system can be said to be uncapped by grain boundary contributions.

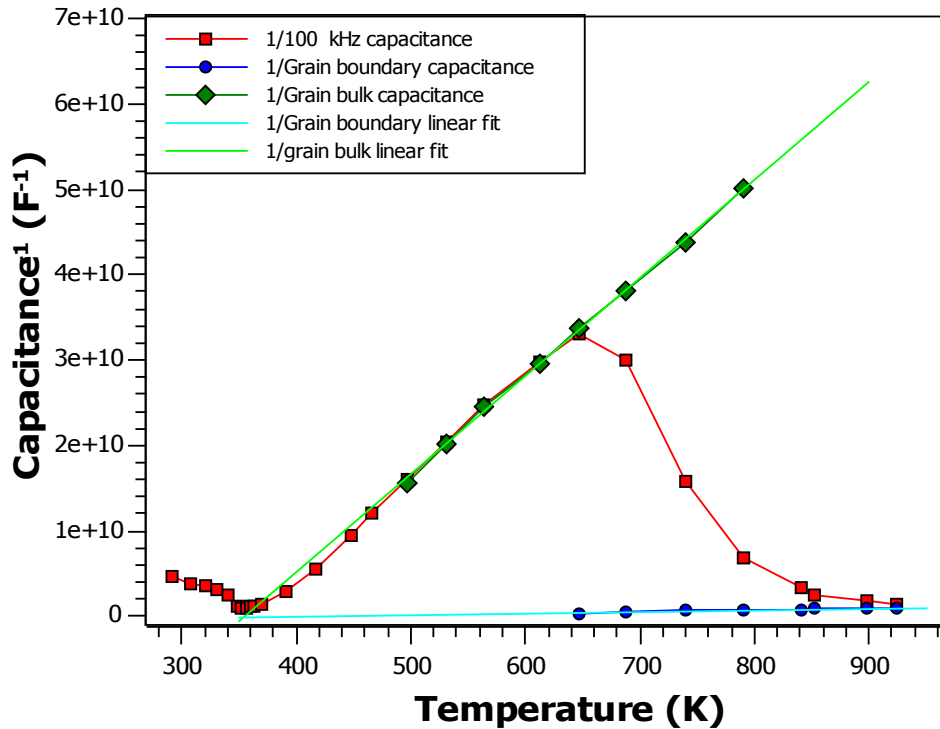


Figure 4.18: Curie-Weiss plot for 50:50 BZT-BCT sintered at 1450 °C

By contrast, the data obtained from the 1350 °C sintered pellet shows a clear deviation of the total capacitance measured at 100 KHz from that of the bulk, figure

[†] It should be noted that the total capacitance, for both compositions is seen to increase at high temperatures. This is due to increasing temperature shifting the capacitance plateaus shown in figure 4.9 to the right. As a result the dispersions between the two plateaus shifts into the measuring frequency range of the apparatus.

4.19. Thus, the total capacitance measured at 100 KHz is not dominated by the bulk capacitance. This data shows clear evidence of grain boundary capping of the capacitance of the pellet, where presence of a significant amount of parasitic grain boundary causes the total capacitance to be severely depressed. This results in the poor relative permittivity of the material which was observed in figure 4.4. Thus the properties arising due to the microstructure of the pellet has been shown to have a significant impact on the physical properties of the pellet.

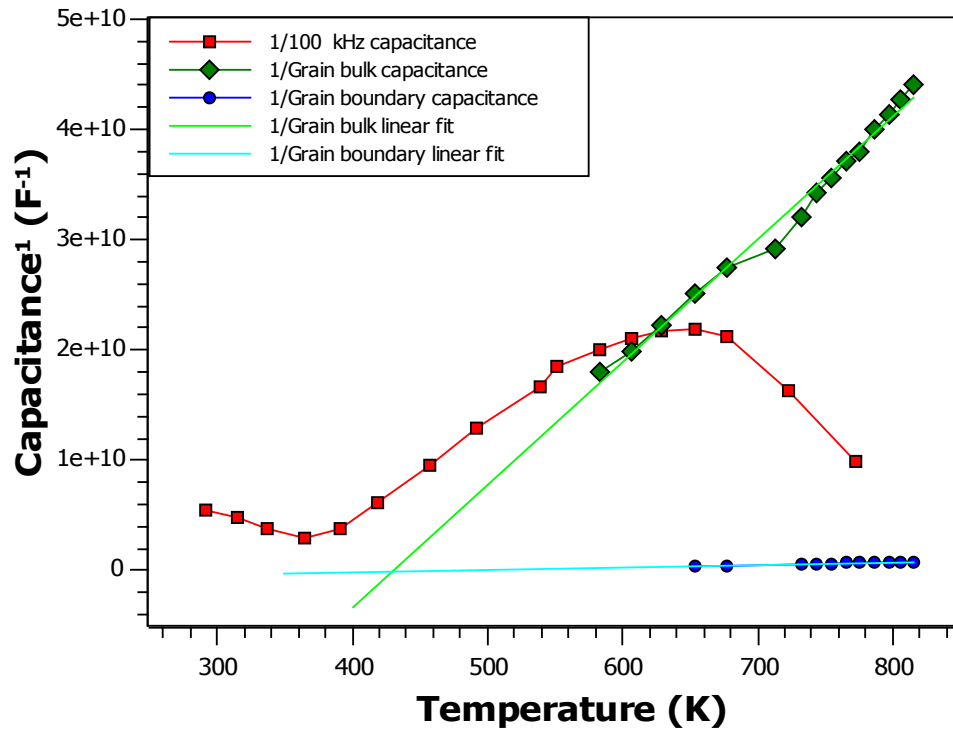


Figure 4.19: Curie-Weiss plot for 50:50 BZT-BCT sintered at 1350 °C

4.2.7: Conductivity data

The conductivity of each pellet was calculated as a function of temperature by taking the reciprocal of the resistance extracted from the Z^* plots, and plotted according to the Arrhenius expression. For both compositions, the bulk and grain boundary responses gave a linear response, figure 4.20. The activation energy to conduction was then calculated as shown in chapter 3, section 6. The calculated values are given in table 4.3.

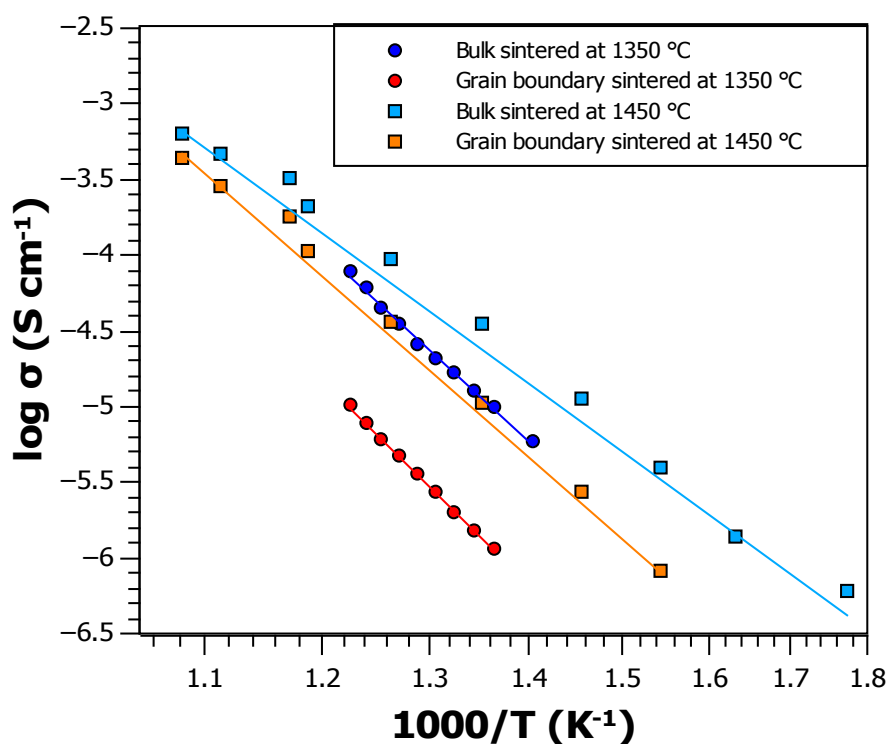


Figure 4.20: Bulk and grain boundary conductivities for pellets sintered at 1350 and 1450 °C

Table 4.3: Bulk and grain boundary activation energies for 50:50 BZT-BCT sintered at 1350 and 1450 °C

Sample sintering temperature (°C)	E_a (eV) Bulk	E_a (eV) Grain boundary
1350	1.244 ± 0.032	1.348 ± 0.016
1450	0.917 ± 0.026	1.190 ± 0.026

In each case the activation energy of the grain boundary was found to be higher than that of the bulk, but all the values are consistent with the sorts of values expected for conduction occurring as a result of anion vacancies^[19, 20]. This will be discussed in more detail in chapter 6.

4.3: Case study 2: 95%(BaTiO₃)-5%(LaScO₃) – Air sensitivity

A series of lanthanum scandate doped barium titanate compositions were synthesised for study within this project. Several synthesis routes were utilized in order to achieve the formation of pellets with reproducible properties, deemed to be characteristic of the composition of the material, as opposed to inherent of the pellet microstructure as a result of the synthesis conditions.

Initial pellets were synthesised by the ceramic synthesis route described in chapter 3.1. Appropriate stoichiometric ratios of BaCO₃ (>99%), TiO₂ (>99.9%), La₂O₃ (>99.99%) and Sc₂O₃ (>99.99%) were ground together and decomposed at 1000 °C before being reground and pressed isostatically to a pressure of 30000 psi. The pellets were then sintered at 1400 °C for 18 hrs. The pellets were found to be chalky to the touch and had an average density of 3.7 gcm⁻³. This was calculated to be equivalent to approximately 61% of the theoretical density of the material based on the unit cell as determined by analysis of powder X-ray diffraction data. Pellets were re-sintered at higher temperatures and were found to give less chalky pellets, but the density remained low. SEM images (see appendix chapter 4, A4.4) showed a lack of grain growth with a high number of small pores distributed randomly throughout the pellet.

A second set of pellets were synthesised from the same starting reagents, but were subjected to heating as a loose powder for 30 hours at 1425 °C prior to sintering as pellets for 30 hours, also at 1425 °C. This yielded pellets with substantially improved densities, averaging 5.2 gcm⁻³ or ~ 86% of the theoretical density. Accounting for pellet geometry, the relative permittivity maximum for this pellet was found to be at 282K and had a magnitude of ~ 3600, figure 4.21.

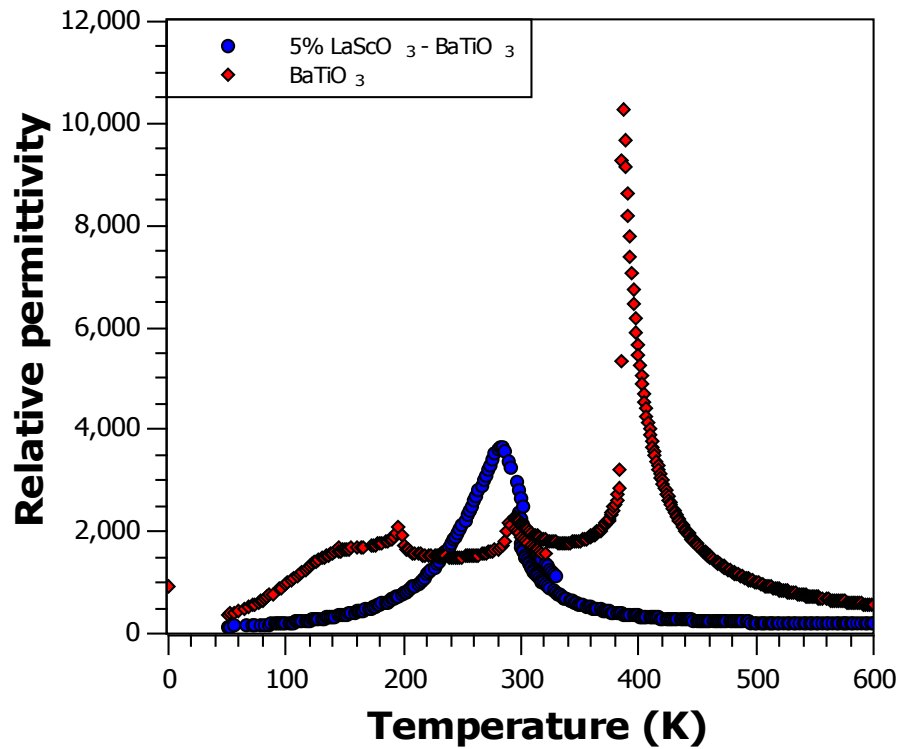


Figure 4.21: Relative permittivity of 5%LaScO₃ doped BaTiO₃ in comparison with un-doped BaTiO₃

As well a significant reduction in the magnitude of the relative permittivity compared to that of the un-doped BaTiO₃, it is found that the presence of a series of distinct peaks in the magnitude of the relative permittivity, assigned as polymorphic phase transitions, are no longer seen in the 5% LaScO₃ doped BaTiO₃.

High temperature immittance measurements carried out on a sample of this material shows the presence of only one clear component in the complex impedance plot along with two features in the complex modulus plot, figures 4.22 and 4.23, respectively.

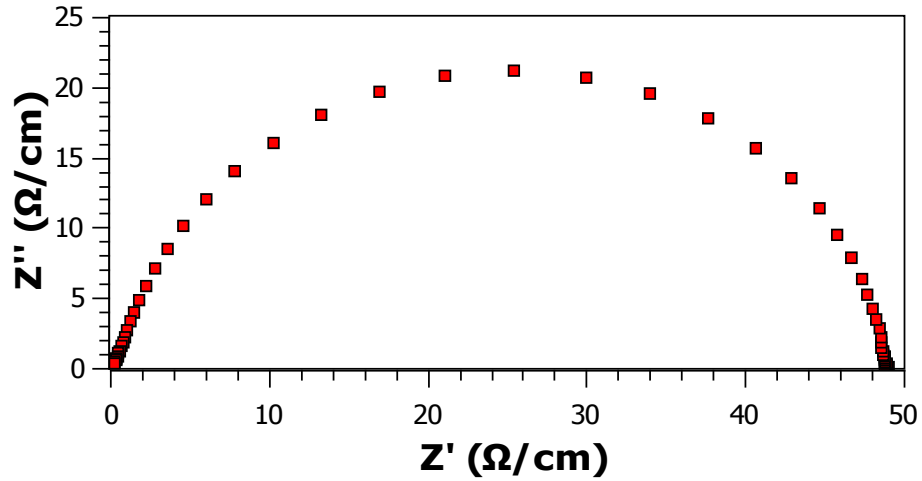


Figure 4.22: Complex impedance plot of data collected on a sample of 5%LaScO₃-BaTiO₃ at 602 °C

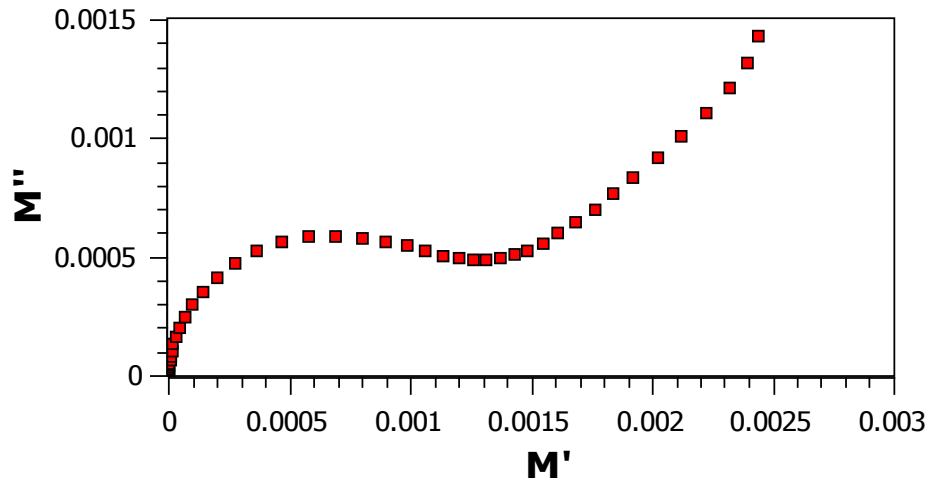


Figure 4.23: Complex modulus plot of data collected on a sample of 5%LaScO₃-BaTiO₃ at 602 °C

The capacitance of the M^* arc is calculated to be $\sim 7 \times 10^{-11}$ F which is consistent with this being a bulk type response. The capacitance of the Z^* arc is $\sim 8 \times 10^{-11}$ F, suggesting that the pellet has no discernible distinct grain boundary response.

As well as a semi-circular arc consistent with a bulk region, the M^* plot also shows the presence of a “tail” at high frequency. When data is collected at several temperatures the curvature of this tail alters such that it may be interpreted that the “tail” is in fact the start of a very large semi-circular feature, although the precise nature of the tail is unclear, and shall be discussed further in chapter 6. The spectroscopic plot of the Z'' and M'' data, figure 4.24, confirms that the Z^* arc and the resolved M^* arc are coincident in frequency, and thus correspond to the same electro-active region.

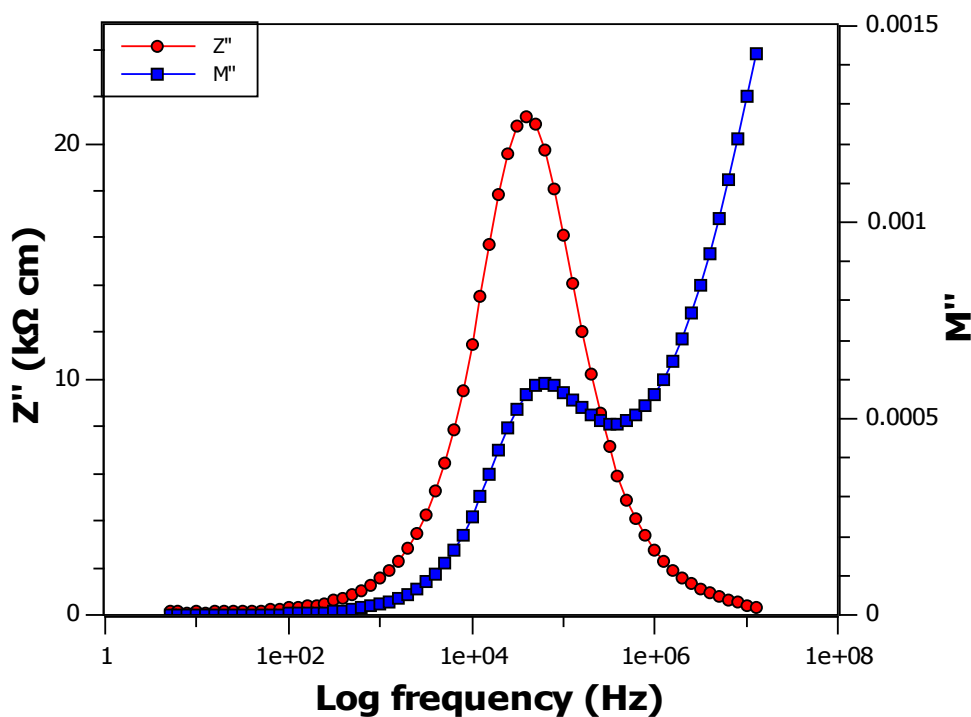


Figure 4.24: Spectroscopic plot showing the presence of one electro-active region in the Z'' data and one clear electro-active region, as well as a “tail” feature, in the M'' data

SEM images of the interior surface of the pellet, figure 4.25, show regions of high porosity and cracks, as well as average grain sizes of $\sim 1 \mu\text{m}$ diameter. This is consistent with the high temperature impedance data, suggesting very small grains in which there is little distinction between the grain boundary and the core bulk region of the grain.

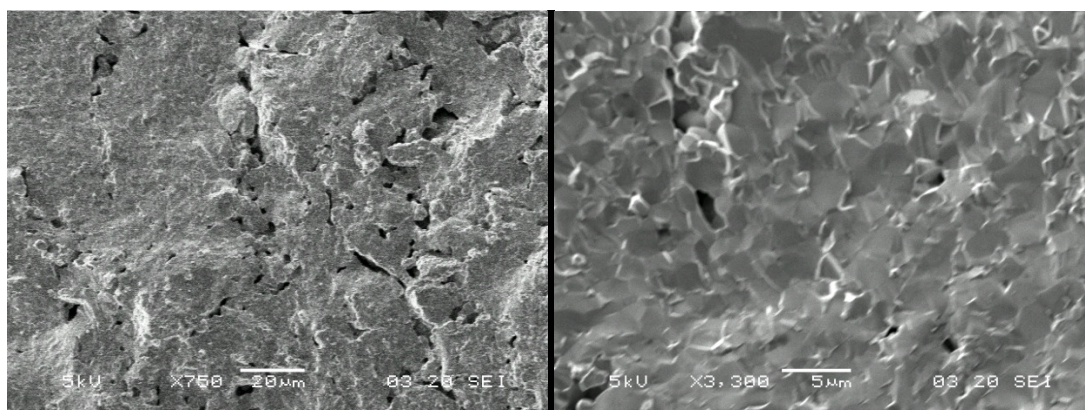


Figure 4.25: Areas of high porosity and cracks present in a sample of 5%LaScO₃ doped BaTiO₃

Further work with these materials led to the discovery that, when higher percentages of LaScO_3 were doped into the BaTiO_3 , the decomposed powder appeared to be air sensitive. In the case of a 50% LaScO_3 – BaTiO_3 sample, when the decomposed powder was pressed into pellets with a 10 mm die, the pellets expanded to a diameter >10.4 mm before disintegrating, suggesting air (CO_2) or moisture sensitivity.

New synthesis routes were attempted in order to overcome the issues surrounding the air-sensitivity of the pre-calcined pellets. This included the use of pre-reacted LaScO_3 , in place of La_2O_3 and Sc_2O_3 , using $\text{La}(\text{NO}_3)_3 \cdot 6\text{H}_2\text{O}$ in place of La_2O_3 and carrying out the sintering of pellets made from the oxides in an O_2 -enriched atmosphere.

The use of pre-reacted LaScO_3 resulted in dense pellets $\sim 91\%$ of theoretical density, with a maximum in the relative permittivity of ~ 5400 , however the temperature of the maximum was found to exhibit a slight frequency dependency, varying by 6°C over a frequency range of 1×10^2 – 13×10^6 Hz. The magnitude of the relative permittivity was also found to vary systematically over this frequency range, by as much as $\sim 18\%$ of the maximum magnitude, figure 4.26.

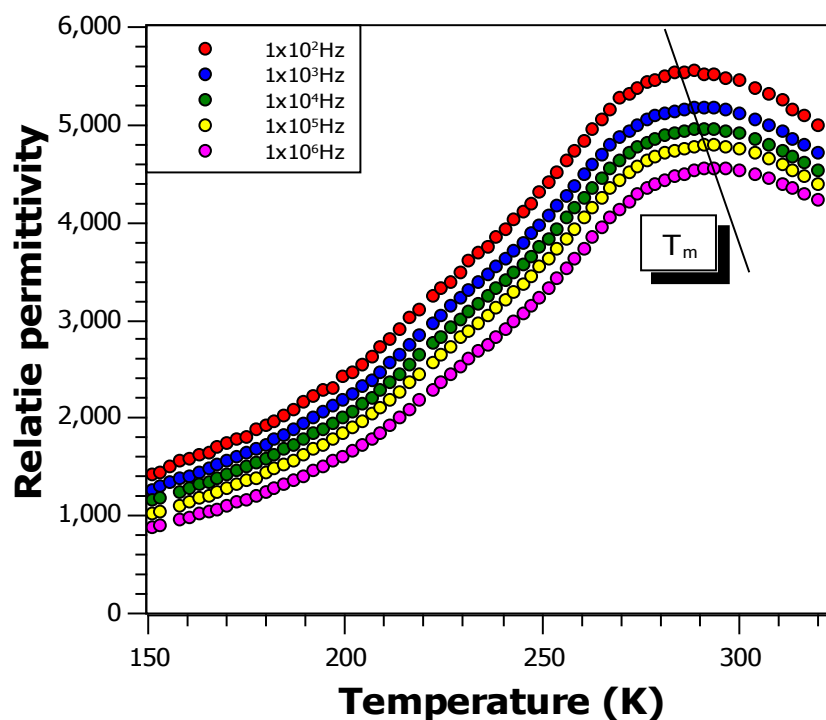


Figure 4.26: Frequency dependence of the relative permittivity maximum in a sample of 5% LaScO_3 doped BaTiO_3

Materials which exhibit a frequency dependant temperature of the maximum in the relative permittivity, where that frequency dependency is such that the temperature of the peak shifts to higher temperatures as the frequency is increased, are generally considered to be relaxor ferroelectrics^[21], RFE's. However, the microstructure of the material may give rise to unusual frequency dependencies, and as a result may yield data that are consistent with that of a relaxor ferroelectric, where that behaviour is inherent of the microstructure and not of the composition.

Synthesis of the 5%LaScO₃-BaTiO₃ composition using lanthanum nitrate as a starting material yielded pellets of lower density of $\sim 4.6 \text{ gcm}^{-3}$, equating to $\sim 76\%$ of the theoretical density. The pellets were also found to be speckled in appearance, as can be seen in appendix chapter 4, A4.5. This suggests a high degree on inhomogeneity within the pellets. This inhomogeneity could not be removed by subsequent reheating of the pellets to higher temperatures, or, by re-starting the synthesis procedure using different heating times or temperatures.

Analysis of high temperature immittance spectroscopy data showed the presence of depressed, non-ideal “semi-circle” consistent with multiple grain boundary and bulk phases overlapping, figure 4.27. This often arises where there is a non-uniform level of doping throughout the pellet, suggesting that this synthesis route is not capable of consistently forming dense, homogeneous, reproducible materials.

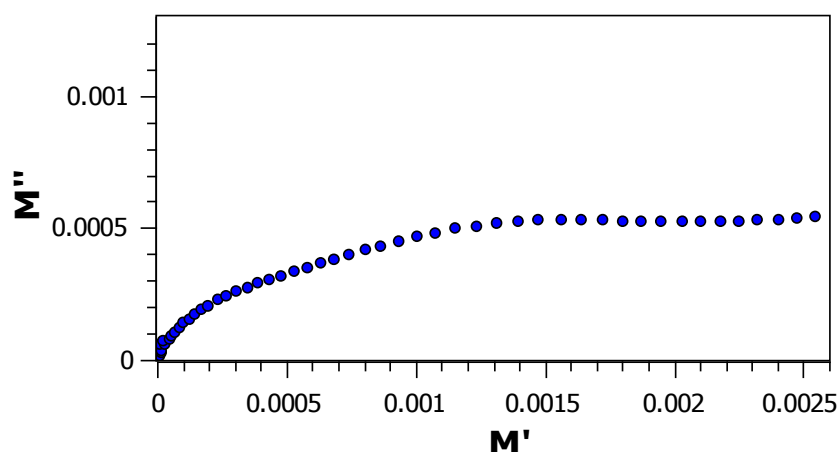


Figure 4.27: Complex modulus plot from a sample of 5%LaScO₃-BaTiO₃ synthesised using (LaNO₃)₃-6H₂O as a starting reagent

Synthesis by the standard route, but using an oxygen enriched atmosphere was able to yield the best overall pellets. Whilst the density achieved was not the greatest for

this composition, and average density of $\sim 5.0 \text{ gcm}^{-3}$ was achieved, corresponding to approximately 80% of the theoretical density. Although density was low, analysis of SEM images showed good grain growth, with grain sizes commonly in excess of $40 \mu\text{m}$ diameter, with odd isolated large pores, shown in figure 4.28.

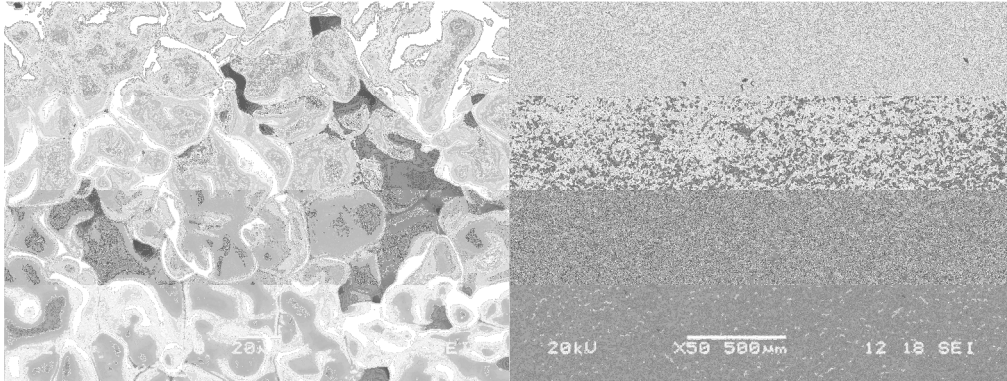


Figure 4.28: Presence of large grains in a sample of 5%LaScO₃-BaTiO₃ sintered in an oxygen enriched atmosphere

The relative permittivity as a function of temperature for this material was found to have a significantly greater magnitude than for the same composition synthesised by other routes, as shown in figure 4.29, with no frequency variation in the temperature of the maximum in the relative permittivity.

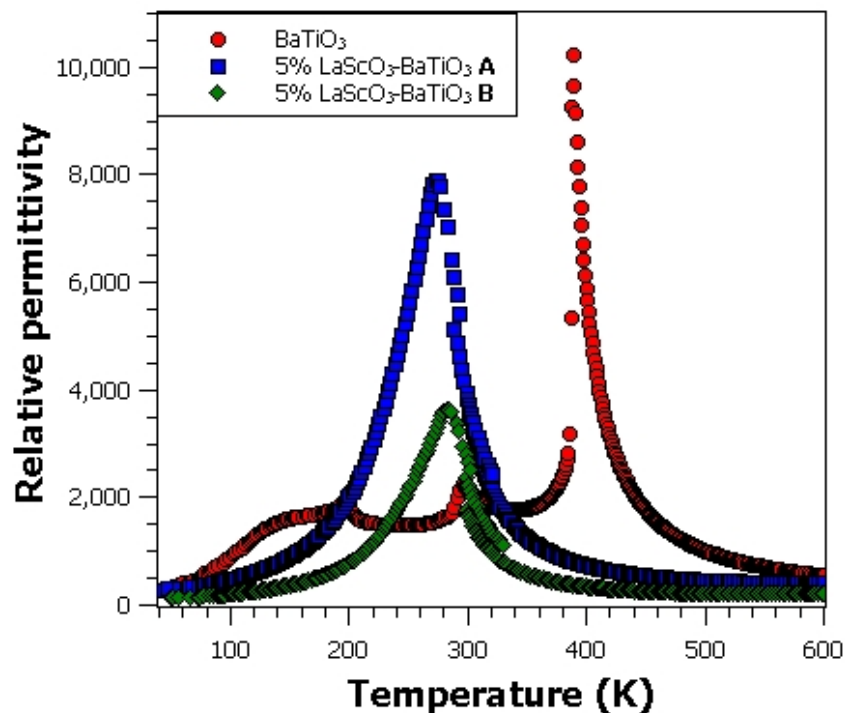


Figure 4.29: Relative permittivities of 5%LaScO₃-BaTiO₃ sintered in an oxygen enriched atmosphere (A), air atmosphere (B) and un-doped BaTiO₃

The magnitude of the maximum in the relative permittivity, though suppressed compared to un-doped BaTiO₃, is substantially higher than observed in pellets formed using different synthesis techniques. The maximum peak magnitude and T_m are also much more reproducible. The high peak height suggests little capping of the peak maximum due to grain boundary contributions.

Complex plane plots taken from high temperature electrical immittance data show the presence of both grain boundary and bulk components in both the Z^* and M^* plots, figures 4.30 and 4.31. The M^* plot also shows the presence of a “tail” feature, common to all the LaScO₃-doped BaTiO₃ compositions studied in this project. The presence of this tail feature does not appear to have a significant impact on the physical properties of the materials and will be discussed further in chapter 6.

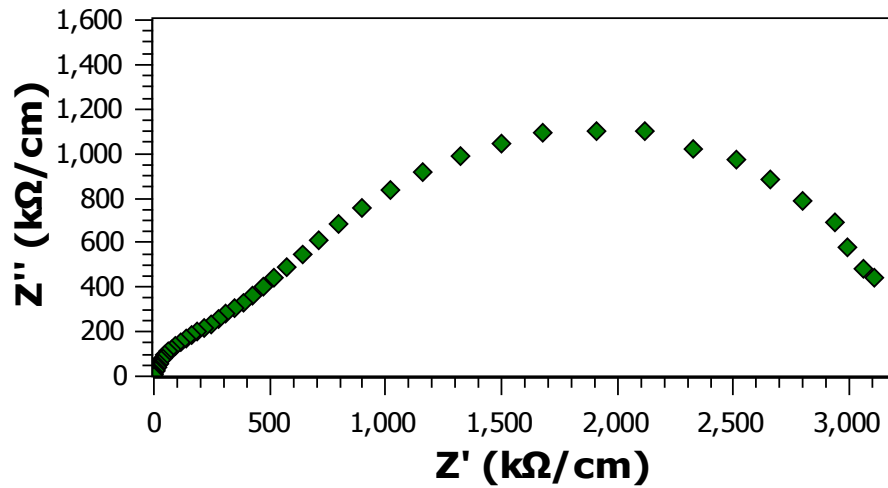


Figure 4.30: Complex impedance data collected from a sample of 5%LaScO₃-BaTiO₃ sintered in an oxygen enriched atmosphere at 602 °C

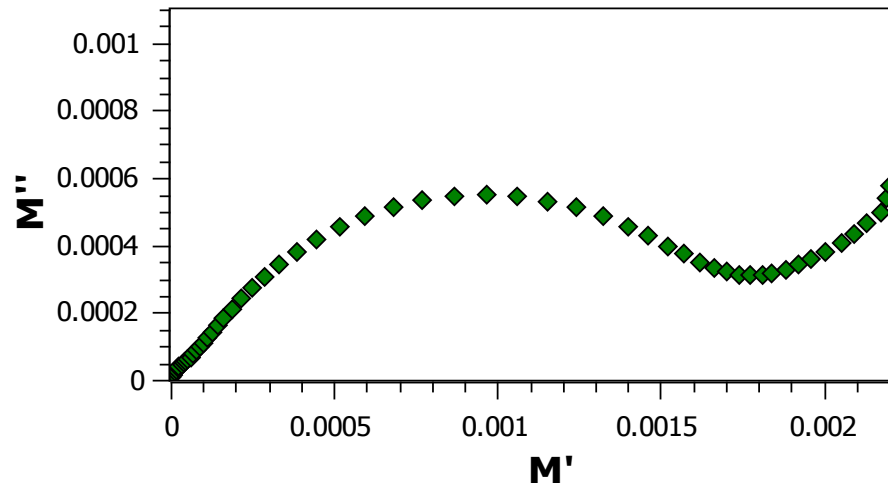


Figure 4.31: Complex modulus data collected from a sample of 5%LaScO₃-BaTiO₃ sintered in an oxygen enriched atmosphere at 602 °C

4.4: Case study 3: 95% (BaTiO₃)-5% (GdScO₃) – Inhomogeneity

Pellets of 5% gadolinium scandate doped barium titanate were initially formed by the method described in section 3.1, being heated loose at 1450 °C for a period of 15 hours, before being reground and pressed isostatically to 30000 psi before heating under the same conditions.

The capacitance and $\tan \delta$ of the pellets was recorded as a function of temperature between room temperature and 400 °C. These were then corrected for pellet geometry and the permittivity of free space, as described in chapter 2, section 2, allowing for the calculation of the relative permittivity of the pellet as a function of temperature, shown in figure 4.32.

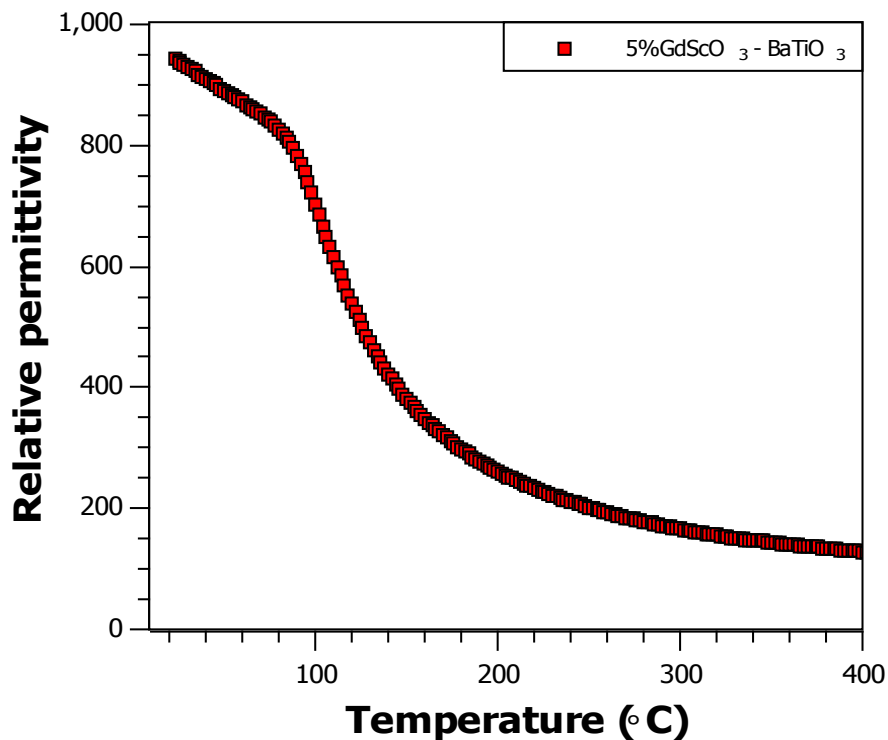


Figure 4.32: Relative permittivity of 5%GdScO₃-BaTiO₃ sintered at 1450 °C for 15 hours , showing the presence of an anomalous feature at ~ 90 °C

A clear feature is observed at ~ 90 °C, however the profile shape is not consistent with that of a simple phase change, where the expected profile would be a sharp peak in the relative permittivity. Though the peak might be expected to be broadened due to the addition of dopant species, a significant increase in the relative permittivity of the material would still be expected at the phase transition.

Analysis of powder X-ray diffraction data showed a single phase composition with no starting reagent or other impurities. However, the broad nature of the peaks, along with the similarity of peak positions arising from similar perovskites with slight variation in dopant levels, could mean that the presence of other similar phases has been masked.

By re-grinding and re-heating the pellets, any inhomogeneity in the composition would be expected to be reduced. Thus, in order to determine whether the feature observed was due to an impurity phase, the pellet was re-ground, ball-milled and pressed isostatically as before, before being sintered at 1475 °C for a period of 15 hours. This yielded a pellet with 97% theoretical density, which was even in colour.

The relative permittivity as a function of temperature is plotted alongside the initial data obtained for comparison, figure 4.33.

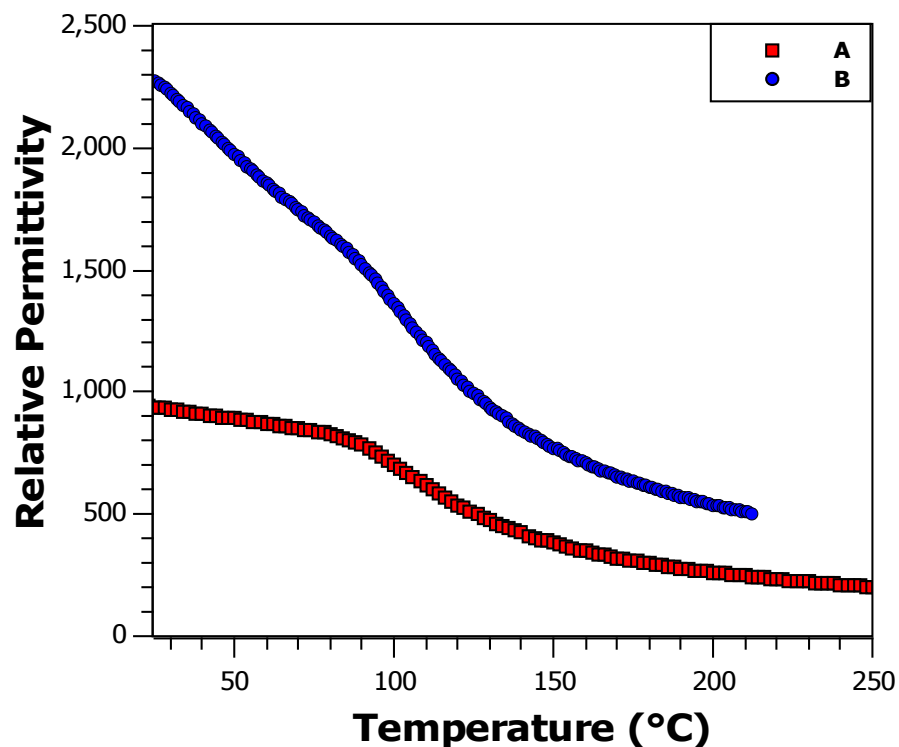


Figure 4.33: Relative permittivity of 5%GdScO₃-BaTiO₃ sintered at 1450 °C for 30 hours (A), and for a further 15 hours at 1475 °C (B)

Clearly the feature is still present after the extra steps, however its intensity relative to the “background” slope was reduced by the second grinding and heating cycle. This suggests that it is resultant of a phase transition in a second phase of the

material within the pellet, the percentage of which is reduced by the second heating phase. The temperature of the event is $\sim 90^\circ\text{C}$, which is slightly lower than that of the tetragonal to cubic phase transition in un-doped barium titanate^[22]. Coupled with the lack of any other clear phase shown in powder X-ray diffraction data analysis, the hypothesis that this feature is due to a region of the barium titanate with a very low concentration of the dopant species seems most likely.

In order to remove the feature completely the pellet was initially subjected to a further grinding and heating steps at 1500°C for a period of 15 hours, with this being repeated until the feature disappeared, figure 4.34. Full details of the sintering steps are listed in table 4.3, *N.b.* Heating temperatures and times are cumulative within each scenario.

Table 4.3: Sintering conditions for 5% GdScO₃-doped BaTiO₃

Scenario	Sintering temperature ($^\circ\text{C}$)	Heating time (hrs)
A	1450	30
B	1450	30
	1475	15
C	1450	30
	1475	15
	1500	15
D	1450	30
	1475	15
	1500	15
	1500	15

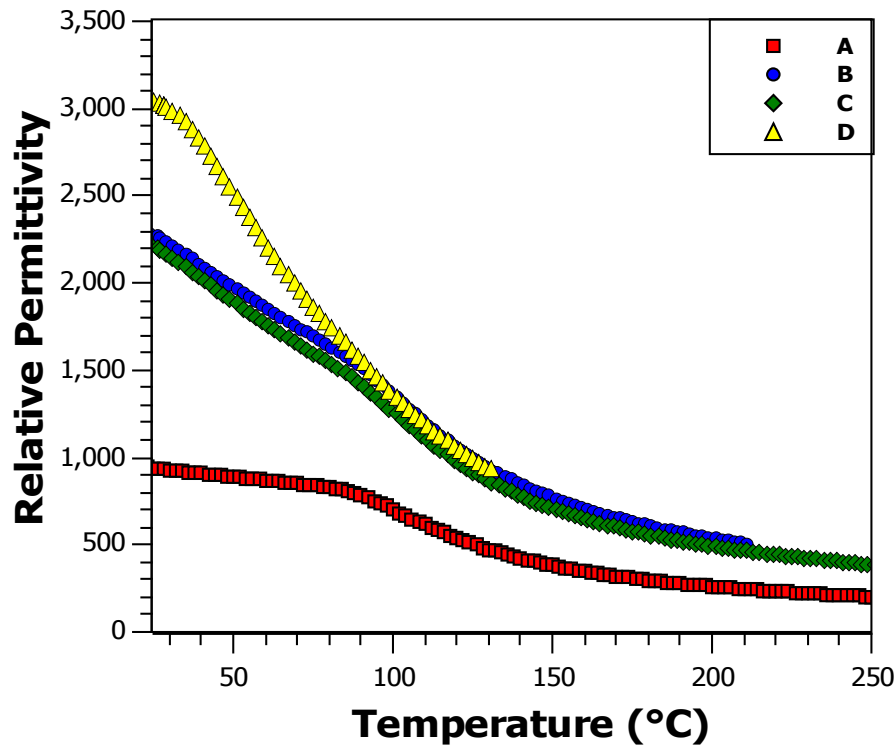


Figure 4.34: Relative permittivity of 5%GdScO₃-BaTiO₃ sintered using the conditions listed in table 4.2 for scenarios A-D

The lack of any discernible feature in trace D, along with high temperature immittance data and variable temperature synchrotron powder X-ray diffraction data analysis, both of which will be discussed in subsequent chapters, led to the conclusion that the pellet was single phase and chemically homogeneous. It is also noted that the removal of the impurity phase resulted in enhancing the magnitude of the relative permittivity of the material. This is consistent with forming more of the phase associated with the dominant peak in the relative permittivity.

This form of capping of the relative permittivity by pellet inhomogeneity is utilised in the formation of MLCC (multi-layer ceramic capacitor) devices. These often utilize dopants to create a core-shell consisting of an un-doped or low-level doped BaTiO₃ core with a significantly doped shell, resulting in a significant suppression and broadening of the relative permittivity peaks^[23-25].

4.5: Conclusions

The processing route by which pellets are formed can have a significant impact of the properties of the pellet. This is often as a result of the pellet microstructure,

inhomogeneity or air-sensitivity and, as a result, cannot be seen by analysis of low resolution (in-house) room temperature powder X-ray diffraction data.

A series of techniques is required in order to establish the type of microstructure present in a given ceramic pellet and to understand any effects this has on the physical properties of the pellet. Capping by the presence of parasitic grain boundary contributions or chemical inhomogeneity causes a significant reduction in the relative permittivity maxima of a material, as well as causing broadening of the peak. By varying the sintering temperature and dwell times it is possible to improve the homogeneity of the ceramics as well as improved the grain growth, such that under optimal synthesis conditions it is generally possible to form ceramics with large grains and narrow, well-defined grain boundaries which account for low fractions of the pellet volume.

The effect of inhomogeneity as a result of air or moisture sensitivity can be a cause of relaxor ferroelectric (RFE) -like behaviour in doped-BaTiO₃ compositions. However, this dependency can be removed by altering the synthesis route. Thus, the frequency dependency can be considered to be resultant of the pellet microstructure and not representative of the elementary composition of the pellet. Hence the material is not considered to be a true RFE. Whilst RFE's are of considerable interest for devices such as multi-layer ceramic capacitors and actuators^[21, 26], electrical properties that vary with exposure to air or moisture are unsuitable for the manufacturing of devices and would not result in materials with reproducible properties.

References

1. Kinoshita, K.Y., Akihiko *Grain-size effects on dielectric properties in barium titanate ceramics* J. Appl. Phys., 1976. **47**: p. 371.
2. Lanfredi, S., L. Dessemond, and A.C.M. Rodrigues, *Dense ceramics of NaNbO_3 produced from powders prepared by a new chemical route*. J. Eur. Ceram. Soc., 2000. **20**(7): p. 983-990.
3. Tang, X.G., et al., *Effects of grain size on the dielectric properties and tunabilities of sol-gel derived $\text{Ba}(\text{Zr}_{0.2}\text{Ti}_{0.8})\text{O}_3$ ceramics*. Solid State Communications, 2004. **131**(3-4): p. 163-168.
4. Wang, C.H., S.J. Chang, and P.C. Chang, *Effect of sintering conditions on characteristics of PbTiO_3 - PbZrO_3 - $\text{Pb}(\text{Mg}_{1/3}\text{Nb}_{2/3})\text{O}_3$ - $\text{Pb}(\text{Zn}_{1/3}\text{Nb}_{2/3})\text{O}_3$* . Mater. Sci. Eng. B-Solid., 2004. **111**(2-3): p. 124-130.
5. Zheng, P., et al., *Grain-size effects on dielectric and piezoelectric properties of poled BaTiO_3 ceramics*. Acta Materialia, 2012. **60**(13-14): p. 5022-5030.
6. Jha, P.A. and A.K. Jha, *Influence of processing conditions on the grain growth and electrical properties of barium zirconate titanate ferroelectric ceramics*. J. Alloy. Comp., 2012. **513**: p. 580-585.
7. Lee, H.Y. and L.C. Burton. *Effect of grain size on the grain boundary resistance of undoped barium titanate ceramics*. in *Applications of Ferroelectrics, 1992. ISAF '92., Proceedings of the Eighth IEEE International Symposium on*. 1992.
8. Lee, B.K., et al., *Method for making BaTiO_3 -based dielectric*. 2002, Korea Advanced Institute of Science and Technology: USA.
9. Ren, X. and W. Lui, *Non-Lead-Type piezoelectric Material*, N.I.f.M.S. [JP], Editor. 2009: Japan: 054540.
10. Liu, W. and X. Ren, *Large piezoelectric effect in Pb-free ceramics*. Phys. Rev. Lett., 2009. **103**(25): p. 257602.
11. Baettig, P., et al., *Theoretical prediction of new high-performance lead-free piezoelectrics*. Chem. Mater., 2005. **17**(6): p. 1376-1380.
12. Suo, Z., et al., *Fracture-mechanics for piezoelectric ceramics*. J. Mech. Phys. Solids, 1992. **40**(4): p. 739-765.
13. Nishinoiri, S. and M. Enoki, *Development of in-situ monitoring system fo sintering of ceramics using laser AE technique*. Journal of Acoustic Emission, 2005. **23**.

14. Salamon, D., K. Maca, and Z. Shen, *Rapid sintering of crack-free zirconia ceramics by pressure-less spark plasma sintering*. Scripta Mater., 2012. **66**: p. 899-902.
15. Callister Jr, W.D., *Materials Science and Engineering, An Introduction*. 7th ed. 2007: Wiley.
16. Guillon, O., et al., *New considerations about the fracture mode of PZT ceramics*. J. Eur. Ceram. Soc., 2005. **25**(12): p. 2421-2424.
17. Hirose, N. and A.R. West, *Impedance spectroscopy of undoped BaTiO₃ ceramics*. J. Am. Ceram. Soc., 1996. **79**(6): p. 1633-1641.
18. Irvine, T.S., D.C. Sinclair, and A.R. West, *Electroceramics: Characterization by Impedance Spectroscopy*. Advanced Materials, 1990. **2**(3).
19. Islam, M.S., *Ionic transport in ABO₃ perovskite oxides: a computer modelling tour*. J. Mater. Chem., 2000. **10**(5): p. 1027-1038.
20. Cherry, M., M.S. Islam, and C.R.A. Catlow, *Oxygen-ion migration in perovskite-type oxides*. J. Solid State Chem., 1995. **118**(1): p. 125-132.
21. Cross, L.E., *Piezoelectricity*, in *Springer Series Mate*. 2008. p. 131-155.
22. Jaffe, B., W.R. Cook, and H. Jaffe, *Piezoelectric Ceramics*. 1971: Academic Press London.
23. Ming-Jen, P. and C.A. Randall, *A brief introduction to ceramic capacitors*, in *Electrical Insulation Magazine, IEEE*. 2010. p. 44-50.
24. Chang-Hoon, K., et al. *Formation of core-shell structure of BaTiO₃ grains in MLCC*. in *Applications of Ferroelectrics, 2007. ISAF 2007. Sixteenth IEEE International Symposium on*. 2007.
25. Park, Y. and H.G. Kim, *The microstructure analysis of cerium-modified barium titanate having core-shell structured grains*. Ceram. Int., 1997. **23**(4): p. 329-336.
26. Wei, X.Y., Y.J. Feng, and X. Yao, *Dielectric relaxation behavior in barium stannate titanate ferroelectric ceramics with diffused phase transition*. Appl. Phys. Lett., 2003. **83**(10): p. 2031-2033.

Chapter 5: The effects of dopants on the phase transitions of BaTiO₃

Barium titanate is a ferroelectric material with a perovskite structure^[1] (Chapter 1, Section 6). It can take the form of five different polymorphs, hexagonal, cubic, tetragonal, orthorhombic and rhombohedral, with the latter three phases being ferroelectric. The generally accepted space groups associated with BaTiO₃ are $P6_3mm$ (hexagonal), $Pm\bar{3}m$ (cubic), $P4mm$ (tetragonal), $Amm2$ (orthorhombic) and $R3m$ (rhombohedral). However, these space groups were determined in the 1950s^[2, 3] and there has been some more recent debate as to the precise space groups^[1, 4].

The dielectric properties are dependent on the polymorphic phase, which is in turn temperature dependant, figure 5.1. For many applications it is important to understand the root causes of these phase changes and the temperatures at which they occur. It may also be advantageous to shift the temperatures of the transitions, such that the operating temperatures over which the device can work efficiently and reproducibly are altered.

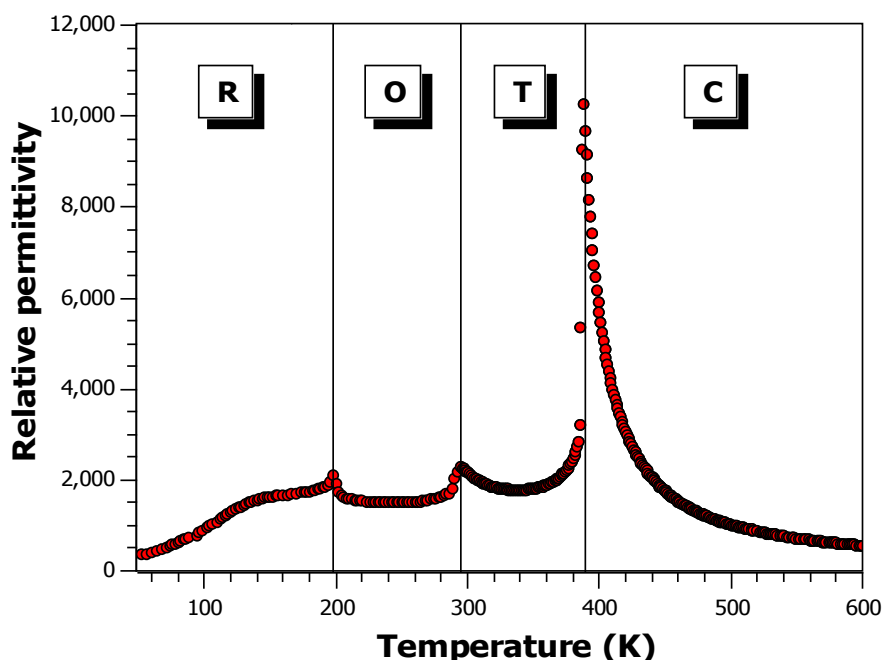


Figure 5.1: Relative permittivity of BaTiO₃ as a function of temperature, showing the presence of a peak in the relative permittivity at each phase boundary, rhombohedral/orthorhombic, (R/O), orthorhombic/tetragonal (O/T) and tetragonal/cubic (T/C)

The addition of dopant species results in a shift in the temperatures of the phase transitions^[5-10]. However, the movement of the phase transitions is often complex.

Various doped barium titanate compounds have been synthesised and studied^[11-13], with lead and calcium doping proving to be of particular interest as both result in an increase in T_C . Whilst for lead the increase scales linearly with dopant addition, with calcium, there is found to be a slight increase in T_C , reaching a maximum at 8 % doping^[14] before falling with increasing dopant addition. Work by Ren et al.^[15] has also shown how morphotropic phase boundary, MPB, like compositions can be achieved using calcium and zirconium, resulting in enhanced piezoelectric properties.

In this chapter, data will be presented showing the effects of adding certain dopants, as well as giving some justification of the causes of the effects with the aim of improving the understanding of how different dopant species may affect the phase temperature and hence the properties of BaTiO₃-based materials.

5.1: Dopant ions selection

All the dopants studied were added in charge balancing pairs, either $2^+/4^+$ or $3^+/3^+$, such that an equal amount of two dopant species, one A-site and one B-site, were always added, with the resultant perovskite being charge neutral.

As well as selecting dopants based on their charge, particular attention was also paid to the ionic radii of the dopant species. It is known that the average sizes of the A-site and B-site species relative to that of the anionic species affects the crystal class adopted by the perovskite structure^[16], (chapter 1, section 2). Previous work suggests that the T_C for ferroelectric perovskites is dependent on the tolerance factor of the composition^[17], with higher tolerance factors favouring the tetragonal state and so resulting in an increase in the Curie temperature. There is also some evidence to show that the localised strain caused by a variance in the size of neighbouring same-site species can result in an increase in T_C ^[18].

Pairs were chosen where a size difference between the A-site and its smaller dopant was partially offset by having a larger dopant species on the B-site, shown to scale in figure 5.2. Sr^{2+} and Ca^{2+} dopants were studied, with both being co-doped with Zr^{4+} . Pairs were also chosen where the off-centring B-site species was of lower charge than the Ti^{4+} species it replaced, with a counter balancing A-site species of higher charge than the Ba^{2+} used to maintain overall charge neutrality, without the requirement for other charge compensation mechanisms, such as anion vacancies. It was also important that the B-site dopant chosen was a d^0 species in order to avoid any electronic effects. These ions were also chosen for their relative sizes in order to study long range size effects and localised strain. The pairs chosen for study were $\text{La}^{3+}/\text{Sc}^{3+}$ and $\text{Gd}^{3+}/\text{Sc}^{3+}$.

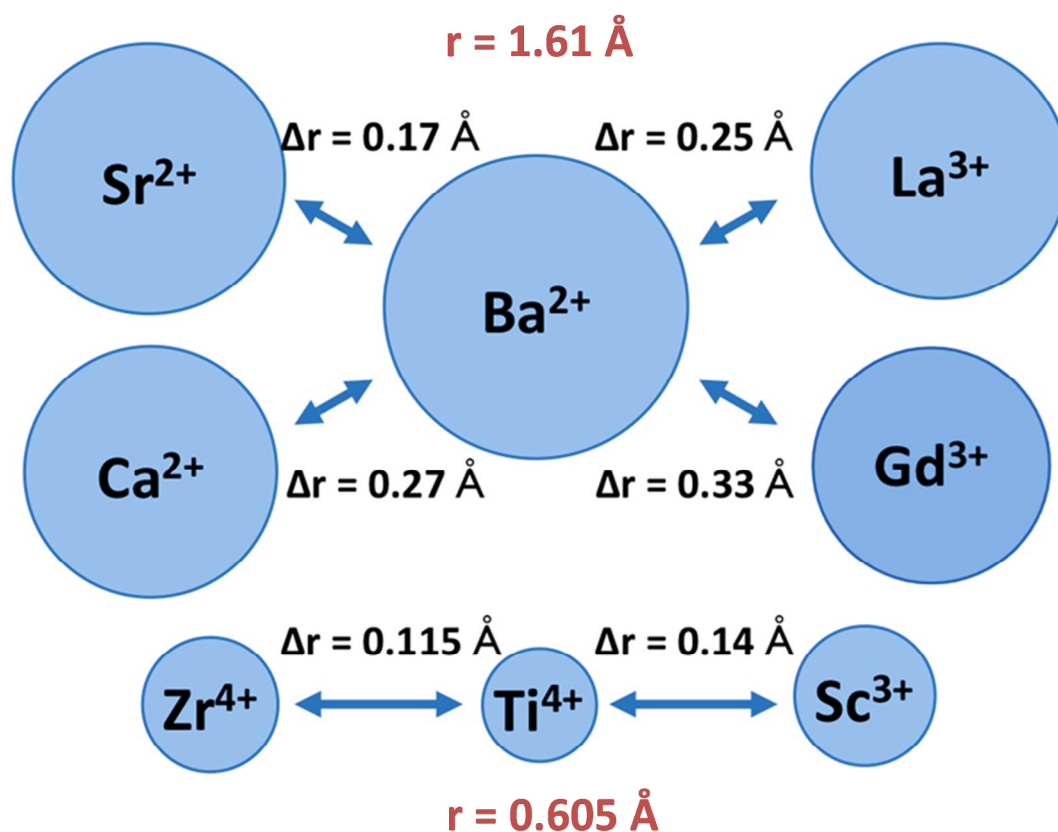


Figure 5.2: Relative sizes of Ba^{2+} and Ti^{4+} cations, accompanied by the various A and B site dopants species studied with corresponding difference in radii. All ions depicted are shown drawn to relative scale, using ionic radii taken from Shannon et al. ^[19]

5.2: The effects of CaZrO_3 dopant addition to BaTiO_3

5.2.1: Synthesis

Samples containing 2, 5, 8, and 12 % CaZrO_3 -doped into barium titanate were synthesised by the methods summarised in section 3.1, using starting reagents of BaCO_3 (>99 %), CaCO_3 (>99 %), TiO_2 (>99.9 %) and ZrO_2 (>99 %). Pellets were heated for between 18 and 30 hours at a variety of temperatures in order to establish the conditions needed to produce dense, single phase pellets with a microstructure conducive to good dielectric properties. The optimised conditions for each composition are shown in table 5.1 below.

Table 5.1: Synthesis conditions for CaZrO_3 -doped BaTiO_3

Composition	Furnace temperature (°C)	Heating time (hours)
2% CaZrO_3 – 98% BaTiO_3	1350	18
5% CaZrO_3 – 95% BaTiO_3	1400	18
8% CaZrO_3 – 92% BaTiO_3	1375	30
12% CaZrO_3 – 88% BaTiO_3	1375	18

Analysis of in-house power X-ray diffraction data obtained at room temperature, showed each of the samples to be of a single phase, consistent with that of the perovskite structure, and was able to yield some information as to the polymorph of the material, figure 5.4. Figure 5.3 below shows powder X-ray diffraction patterns for each sample. It is noted that there is negligible change in the lattice parameters at room temperature with increasing dopant concentration. This is likely to be due to the fact that the Ca^{2+} species is smaller than the Ba^{2+} species it replaces, but that the Zr^{4+} species is larger than Ti^{4+} , resulting in little overall change in the average lattice parameters.

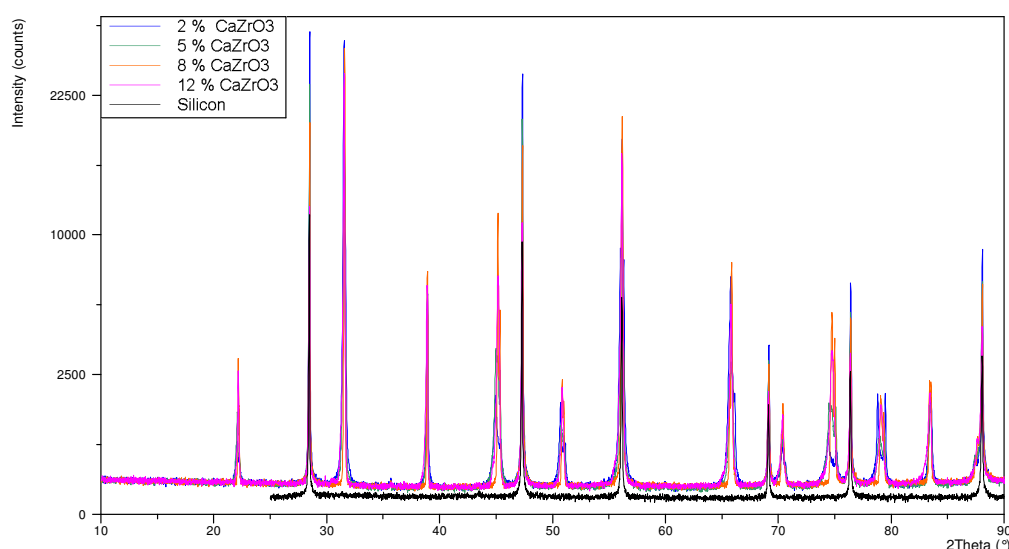


Figure 5.3: In-house powder X-ray diffraction data for 2, 5, 8 and 12 % CaZrO_3 -doped BaTiO_3 , along with that of a Si standard, showing phase purity of each composition and negligible change in lattice parameters

Although very similar in appearance at low angles, increased peak splitting that arise at higher angles allowed for differences in the X-ray diffraction data to be observed as dopant concentration was increased. This showed that as the dopant concentration was increased, the split peak present at $74.8^\circ 2\theta$, associated with a tetragonal phase at room temperature in un-doped BaTiO_3 ^[20], got successively narrower before coalescing into a single peak. This would be consistent with a reduction in tetragonality with increasing dopant concentration, before becoming cubic or pseudo-cubic at 12% dopant addition, figure 5.4.

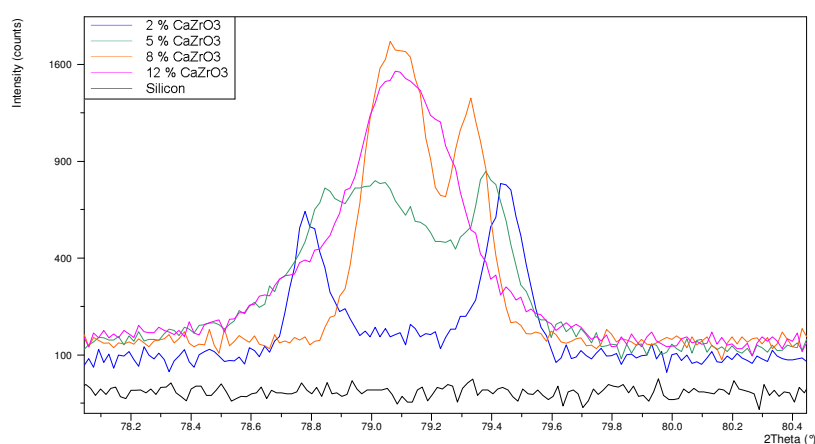


Figure 5.4: In-house powder X-ray diffraction data showing a change in the polymorphic phase as the dopant level is increased from 2 – 12% CaZrO_3 in BaTiO_3

5.2.2: Dielectric spectroscopy

Dielectric data were collected on pellets of each composition over a temperature range of 50 – 650 K at a rate 2 K min⁻¹ using both a cryostat and furnace as described in section 3.6.4. Data from the 2 % sample showed the presence of three peaks in the relative permittivity of the material as a function of T, figure 5.5. The heights of the peaks relative to each other, along with the temperatures of the occurrence of the peaks, are similar to the trace observed for un-doped BaTiO₃^[20], (figure 5.1) suggesting that the peaks correspond to the same polymorphic phase changes.

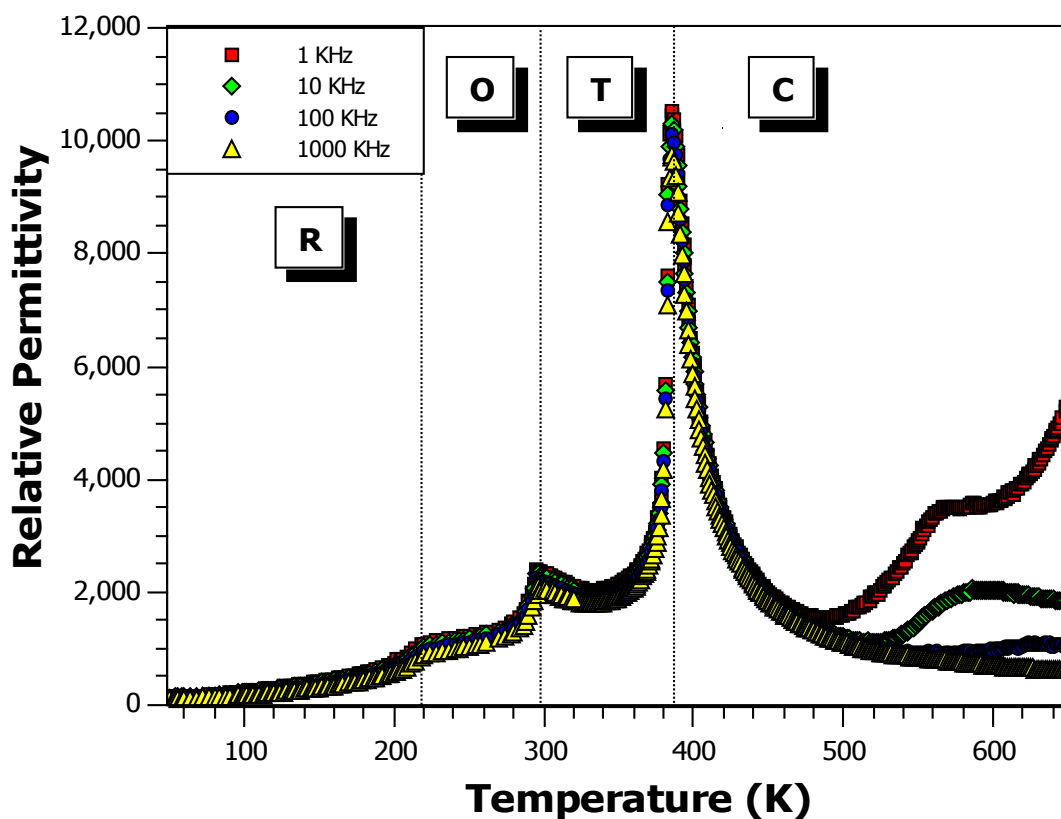


Figure 5.5: Dielectric spectroscopy data collected on a sample of 2 % CaZrO₃ –BaTiO₃ showing the presence of 3 peaks in the relative permittivity, all of which are frequency independent w.r.t. the temperature of the transition

The data shows no frequency dependency of the temperature of the peak positions and very little frequency dependency with regards to the magnitude of the relative permittivity, with the exception of at very high temperatures where electrode and grain boundary polarisations start to have an effect, particularly at low frequency.

Comparison of relative permittivity and loss data shows that each peak in the relative permittivity has an associated event in the loss data, figure 5.6. This indicates that the dipoles are more pliable by the electric field, \vec{E} , as the material is at a point of instability between phases. This can be compared to the point of instability between phases observed at an MPB, such as in PZT.

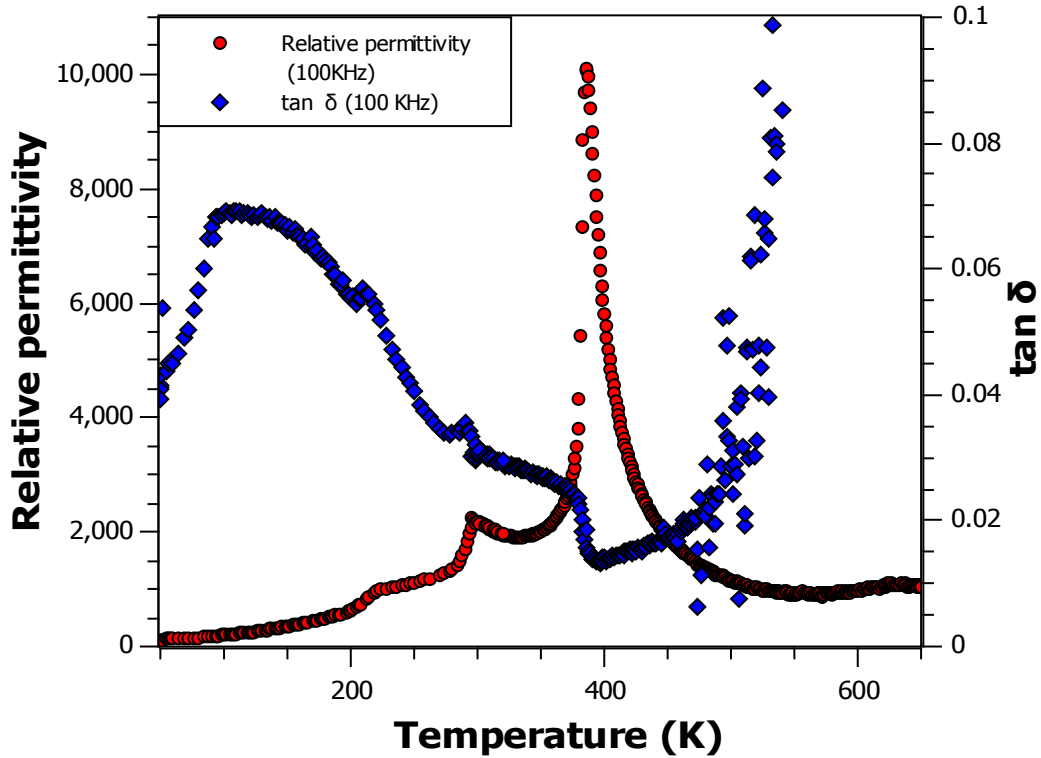


Figure 5.6: Dielectric spectroscopy data collected from a sample of 2 % $\text{CaZrO}_3\text{-BaTiO}_3$, showing the relative permittivity and loss as a function of temperature

The similarity between this data and that of un-doped barium titanate, figure 5.1, allows for the speculative assignment of each of the three peaks in the dielectric data as the rhombohedral/orthorhombic phase boundary ($T_{R/O}$): lowest temperature peak, orthorhombic/tetragonal phase boundary ($T_{O/T}$): middle temperature peak and the tetragonal/cubic phase boundary (T_C): highest temperature peak.

Similar responses were observed for BaTiO_3 pellets containing 5, 8 and 12 % CaZrO_3 . In each instance any peaks in the relative permittivity were accompanied by corresponding changes in the loss data, consistent with the relative permittivity peaks arising as a result of a change in the polymorphic phase of the material occurring at the temperature of the peak, (see appendix A5.1-A5.3).

The dielectric spectroscopy data for each of the compositions is shown below in figure 5.7, along with data collected from a sample of un-doped BaTiO₃.

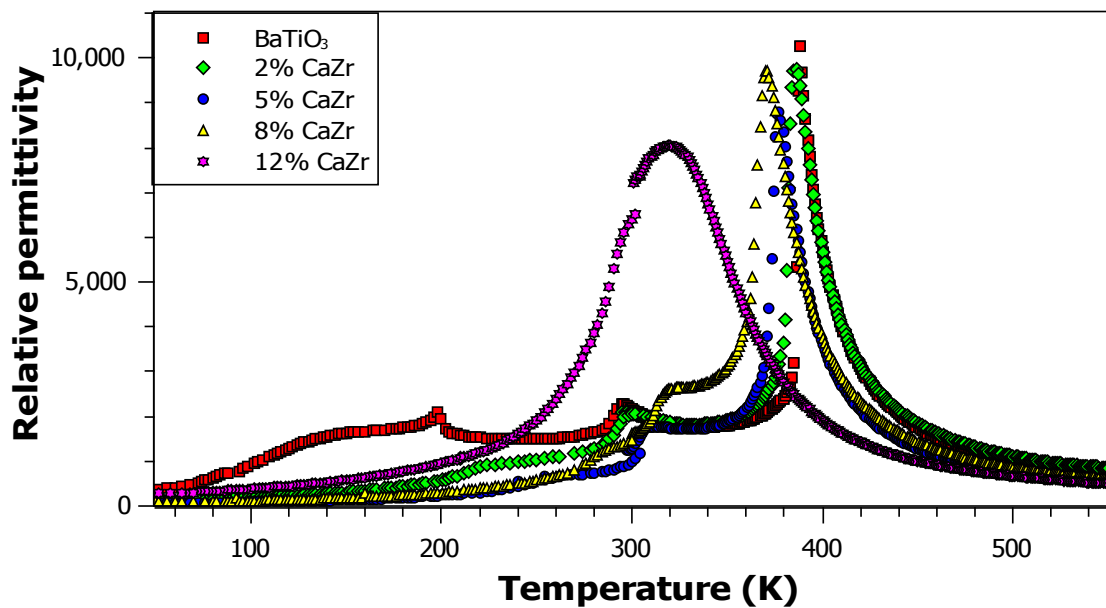


Figure 5.7: Dielectric data showing a trend of decreasing T_C with increasing CaZrO₃ dopant concentration and a coalescence of the peaks with 12 % CaZrO₃

The data shows that as the dopant concentration is increased, the phase boundaries start to come together, before fully coalescing into one broad peak, which is observed in the data set collected on the 12 % CaZrO₃ – 88 % BaTiO₃ sample.

Though the broader phase changes made accurate transition temperatures difficult to determine for some transitions shown in this data, especially the two lower temperature transitions, ($T_{R/O}$ and $T_{O/T}$), approximate temperatures for each transition, based on the dielectric data, are displayed below in table 5.2, along with the peak magnitudes. The temperature data is represented graphically in figure 5.8.

Table 5.2: Relative permittivity peak maxima and transition temperatures of CaZrO₃-doped BaTiO₃

Composition		T _C	T _{O/T}	T _{R/O}
BaTiO₃	Temperature (K)	389	295	197
	Magnitude	10216	2237	2088
2% CaZrO₃- 98% BaTiO₃	Temperature (K)	386	298	226
	Magnitude	9713	2013	969
5% CaZrO₃- 95% BaTiO₃	Temperature (K)	377	310	254
	Magnitude	8818	1790	633
8% CaZrO₃- 92% BaTiO₃	Temperature (K)	371	319	285
	Magnitude	9694	2606	1193
12% CaZrO₃- 88% BaTiO₃	Temperature (K)	320	320	320
	Magnitude	8034	8034	8034

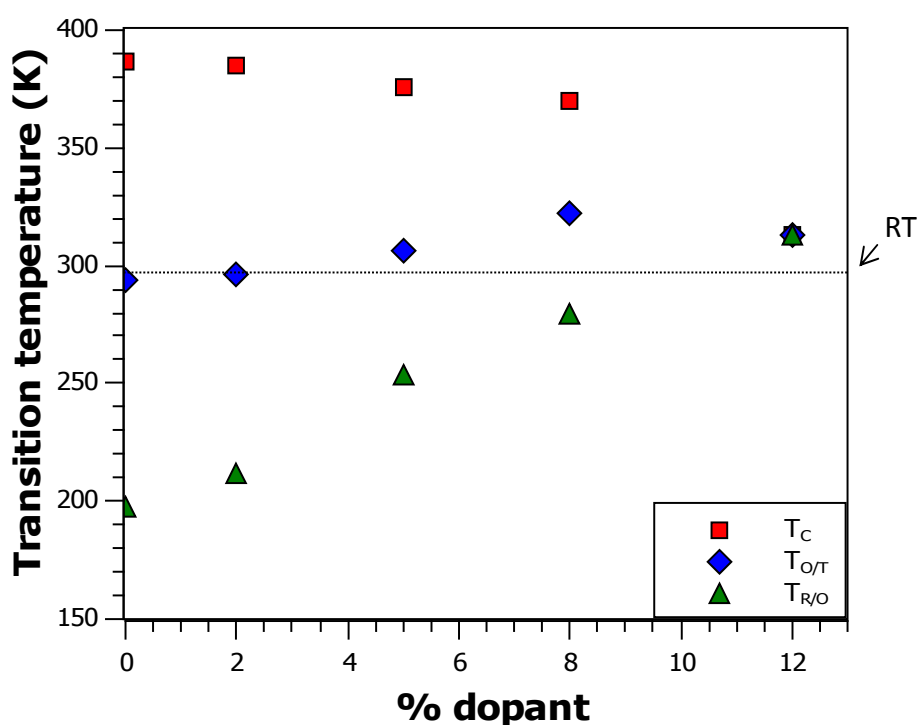


Figure 5.8: Variation in phase transition temperatures as a function of CaZrO₃ doping in BaTiO₃, with room temperature marked by a dashed line

This shows a clear trend of decreasing T_C with increasing dopant concentration, accompanied by an increase in the temperatures of the two lower temperature phase transitions. As a result of T_C decreasing and the other two phase transitions

increasing in temperature, a point of coalescence is reached. At dopant concentrations above the coalescence level only one broad peak is observed in the dielectric data, a scenario which has been reached by a dopant concentration of 12 %.

5.2.3: Synchrotron powder X-ray diffraction data analysis

The Diamond III beamline at the Rutherford Appleton Laboratory was used to collect high resolution powder X-ray diffraction data on each of the compositions at room temperature, with various compositions then selected for variable temperature X-ray analysis. This was carried out in order to determine whether the peaks in the relative permittivity correspond to the same polymorphic phase changes as observed in BaTiO_3 , and also to study the phase and/or phase changes of the coalesced peak in the 12 % CaZrO_3 -doped sample, data for which will be discussed in section 5.6.3.

Of the samples showing distinct phase transitions, the 5 % CaZrO_3 – 95 % BaTiO_3 composition was chosen for variable temperature X-ray analysis. Data were collected from 220 K to 400 K in 10 K intervals for a period of 900 s per data set, with time allowed for the sample to reach thermal equilibrium with the cryostream at each temperature. Two additional data sets were collected on the sample at 150 K and 470 K, considerably removed from the lowest and highest phase transitions as predicted using the dielectric data, in order to ensure that no other structural phase changes were occurring which were unobserved in the dielectric data.

The data was refined in one of four low temperature space groups associated with BaTiO_3 , $Pm\bar{3}m$, (cubic), $P4mm$, (tetragonal), $Amm2$, (orthorhombic) and $R3m$, (rhombohedral), with multiphase refinements being required at some of the phase boundaries, which is indicative of first order transitions. The lattice parameters were then plotted as a function of temperature in order to see whether the crystallographically determined phase transitions matched the temperatures of maxima in the dielectric data. It was also used to study the order of the phase transitions.

Despite the data having clearly defined crystal classes, which varied with temperature, the relative intensities of the peaks did not always match the model pattern for the assigned space group. This suggests that although it was clear that the sample had a cubic crystal class at high temperature, shifting to tetragonal, orthorhombic and rhombohedral crystal classes as the temperature was decreased, the space groups were not necessarily $Pm\bar{3}m$, (cubic), $P4mm$, (tetragonal), $Amm2$, (orthorhombic) and $R3m$, (rhombohedral) which are the most commonly reported space groups for $BaTiO_3$ ^[2, 3]. The process of grinding the sintered pellets has also been shown to increase strain in ferroelectric perovskite titanates, which leads to peak broadening and can mask peaks leading to mis-interpretation of the data^[21].

Generally it was observed that the low 2θ peaks were of relatively lower intensity than expected, whilst the higher 2θ peaks were of relatively higher intensity than predicted. An example of this is shown in figure 5.9, a refinement of 5 % $CaZrO_3$ -doped $BaTiO_3$ data collected at 340 K and refined in the $P4mm$ space group.

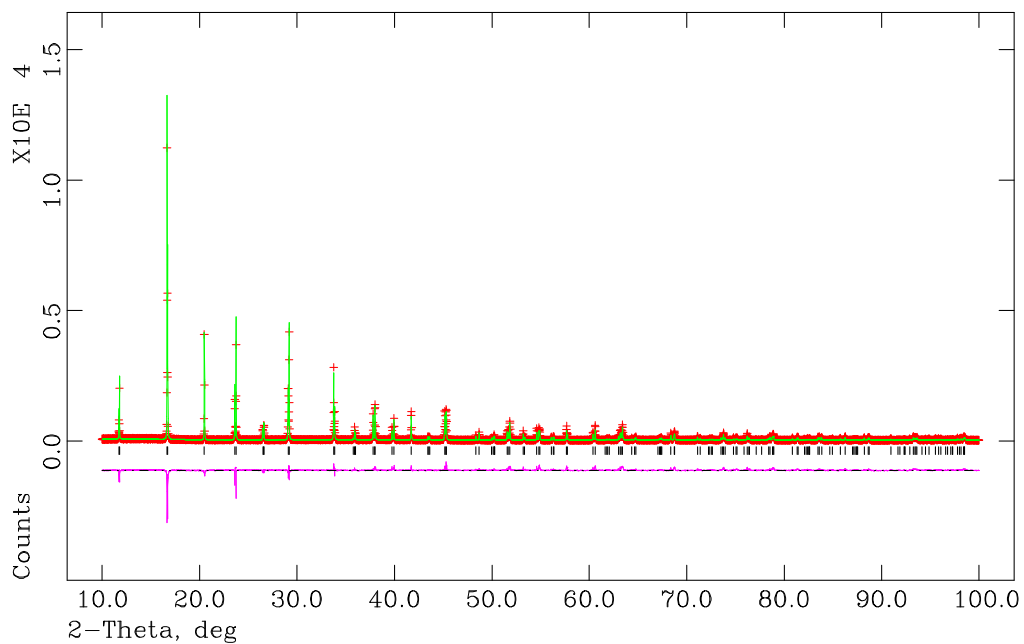


Figure 5.9: Refinement of synchrotron, powder X-ray diffraction data collected on a sample of 5 % $CaZrO_3$ -doped $BaTiO_3$ at 340 K using a $P4mm$ model

Despite the low angle peaks having an unexpectedly lower intensity compared to the high angle peaks, the relative ratios of the peaks were found to be generally of good agreement in to the $P4mm$ tetragonal model, figure 5.10.

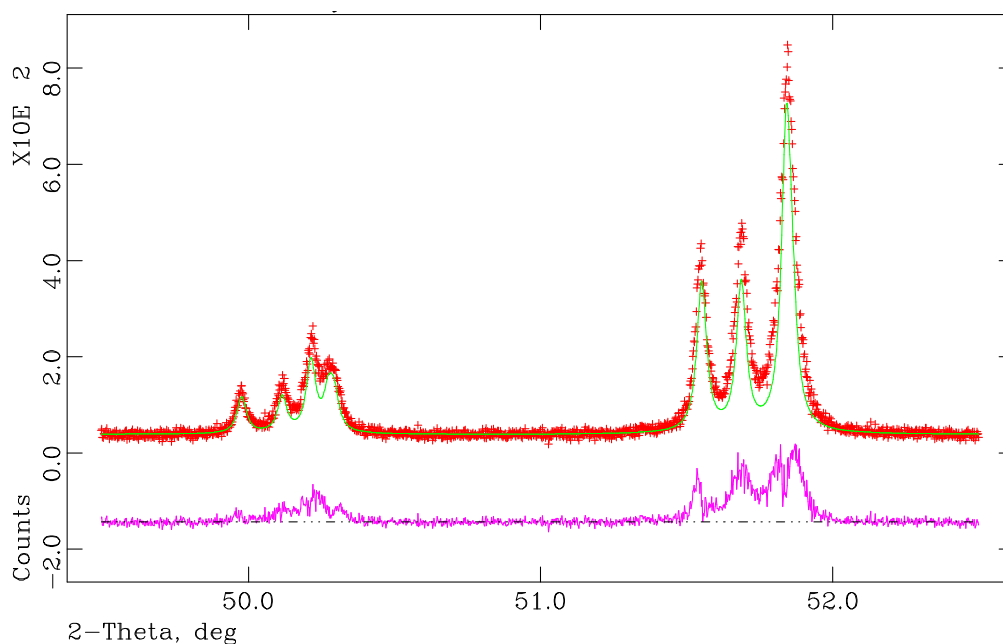


Figure 5.10: Relative ratios of the peaks shown to match the model ratios, despite all the peaks (at high angle) being higher than predicted

Many other space groups have been suggested for both un-doped BaTiO_3 and doped versions including $Pmn21$ ^[4] (orthorhombic), $P4/mmm$ (tetragonal)^[1, 4], $I4cm$ (tetragonal)^[4], $I-43m$ ^[4] (cubic). Refinements in space groups such as $I4cm$ as opposed to $P4mm$ tended to give better fits, figure 5.11, with lower χ^2 values (1.4 vs. 2.8) for the $P4mm$ model as shown in figure 5.9.

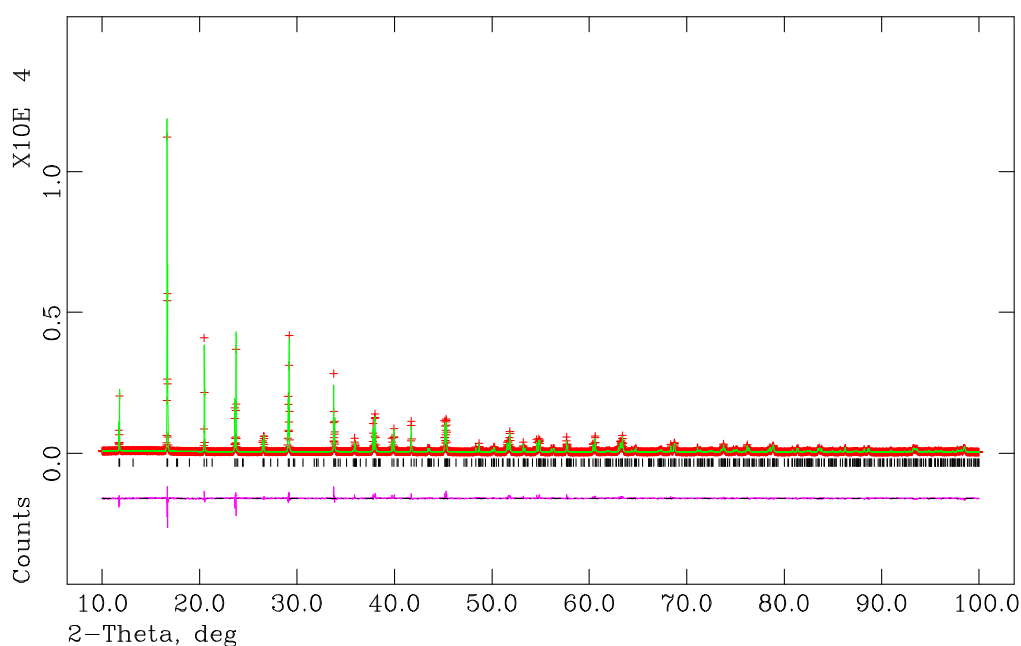


Figure 5.11: Refinement of synchrotron, powder X-ray diffraction data collected on a sample of 5 % CaZrO_3 -doped BaTiO_3 at 340 K using an $I4cm$ model

However, this was found to have some split peaks where the relative ratios of the peaks were not correctly predicted by the model, figure 5.12.

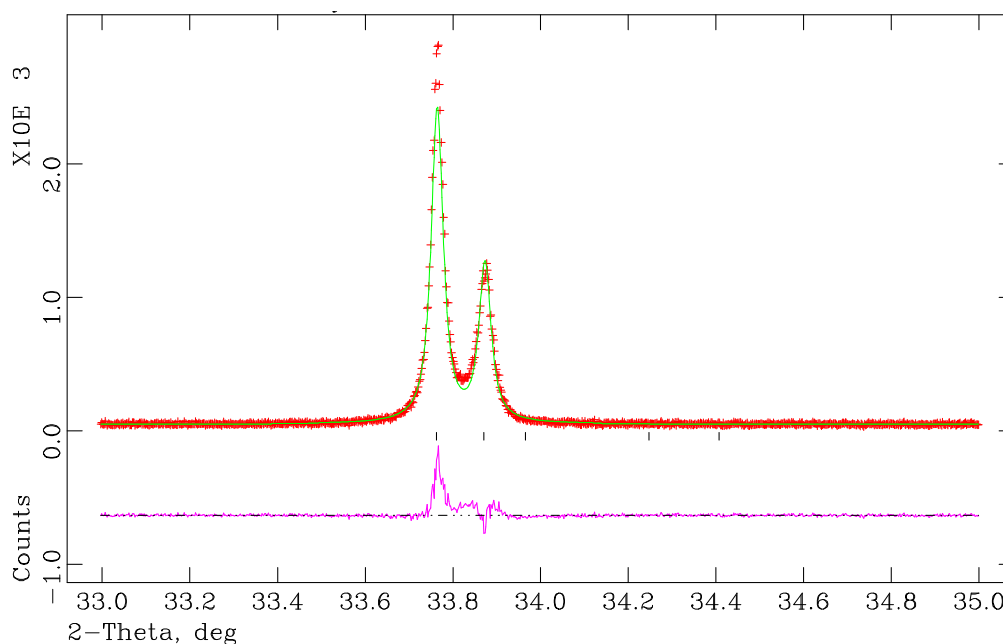


Figure 5.12: Differences between model intensities and actually intensities for certain peaks

However, regardless of which model was used, all the peaks were indexed, with no missing or extra peaks, and the lattice parameters, when corrected to the basic perovskite cell where required, were found to be in agreement to four decimal places. As such, subsequent refinements were done using models built in the $Pm\bar{3}m$, $P4mm$, $Amm2$, and $R3m$ space groups.

The lattice parameters were found to vary smoothly within a polymorphic phase, but have a discontinuity at each phase boundary, most noticeably in the c lattice parameter (figure 5.13). With the exception of small disjunctions at each phase boundary, the volume of the unit cell was found to be linearly dependant with temperature across the whole temperature range studied. At each of the phase transitions a two phase refinement was required, suggesting some co-existence of phases. This suggests that the phase changes between the different crystallographic polymorphs are first order.

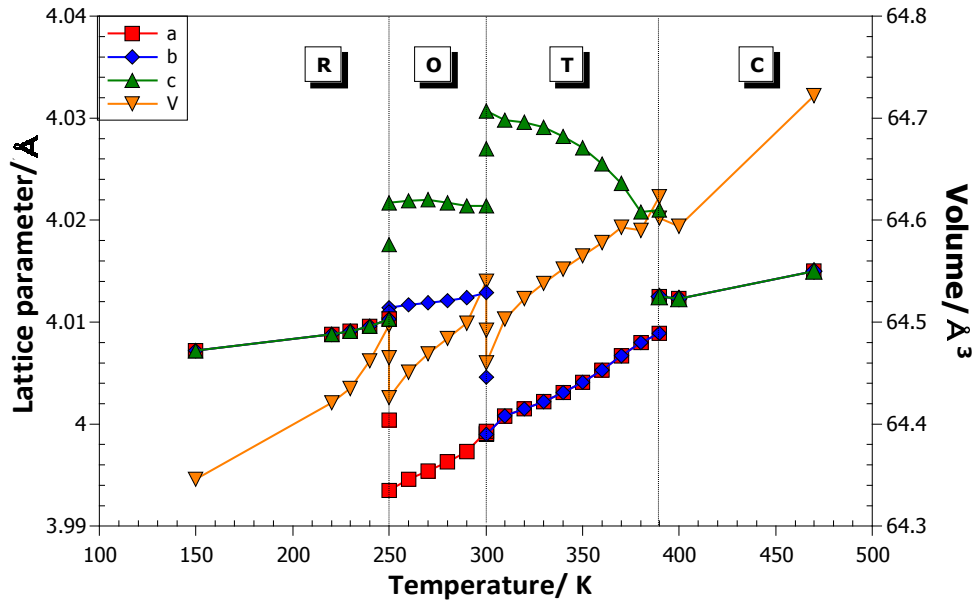


Figure 5.13: Changes in the lattice parameters and volume of 5% CaZrO_3 – BaTiO_3 as a function of temperature undergoing phase transitions between rhombohedral, R, orthorhombic, O, tetragonal, T and cubic, C, phases

The polymorphic phase boundaries as determined by variable temperature, synchrotron, powder X-ray diffraction data analysis were found to be in good agreement with the phase boundary temperatures suggested by the dielectric data, and confirmed that the peaks in the relative permittivity, along with corresponding events in the loss, were as a result of polymorphic phase changes occurring in the ceramic.

5.2.4: CaZrO_3 – BaTiO_3 Phase diagram

By combining the accurate profiles of the dielectric data as a function of temperature, along with evidence of the peaks in the relative permittivity being resultant of a change in the polymorphic phase of the material, it has been possible to build a phase diagram for barium titanate doped with CaZrO_3 , figure 5.14.

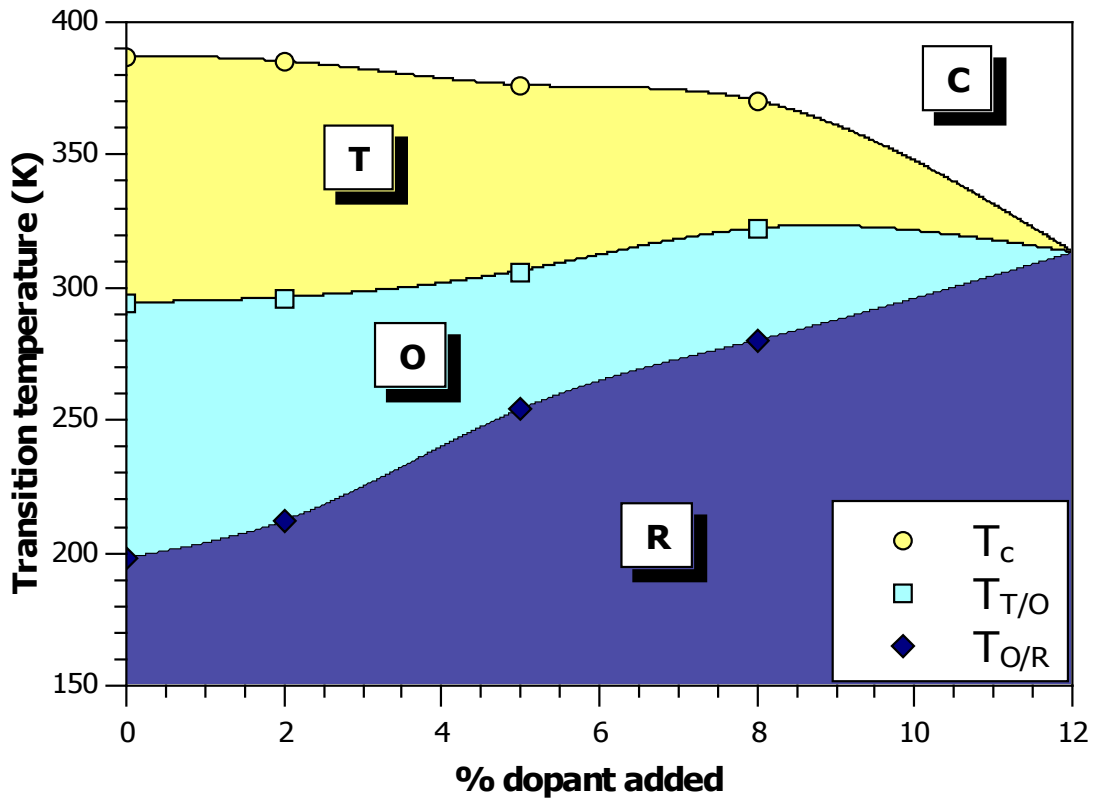


Figure 5.14: Phase diagram of CaZrO_3 -doped BaTiO_3 , showing T_C (Curie temperature), $T_{T/O}$ (tetragonal / orthorhombic phase boundary) and $T_{O/R}$ (orthorhombic / rhombohedral phase boundary)

This diagram clearly shows the decreasing T_C with increasing dopant addition, accompanied by an increase in the temperature of the other two phase boundaries, before reaching a coalesced state. T_C is observed to decrease relatively slowly from 0-8 % dopant before falling much more rapidly. This fits with the known behaviour of calcium doping where T_C is observed to increase^[14] with increasing dopant concentration, up to a maximum at 8 %, before falling. When doping with calcium alone, the rhombohedral/orthorhombic and orthorhombic/tetragonal phase transitions are found to fall with increasing dopant concentration, as seen in chapter 1 section 5, which is not observed; however the addition of zirconium is known to stabilise both of these transitions^[20], causing them to increase with dopant concentration.

5.3: The effects of SrZrO_3 dopant addition to BaTiO_3

As discussed in chapter 1 section 2, the variance in size between the parent and dopant cation can cause significant strain in the material, with increased strain

resulting in increased T_C 's. Substitution with an A-site species much more similar in size to barium would result in a lower variance which should cause T_C to fall more sharply. To see if this could be observed, strontium was added in the place of calcium.

5.3.1: Synthesis

A series of 2, 5, 8 and 12 % SrZrO_3 -doped BaTiO_3 compositions were synthesised in the same manner as those containing CaZrO_3 , (section 5.2), using the same starting materials and additionally SrCO_3 , (>98 %). Optimal synthesis conditions are shown in table 5.3.

Table 5.3: Optimal synthesis conditions for SrZrO_3 -doped BaTiO_3

Composition	Furnace temperature (°C)	Heating time (hours)
2% SrZrO_3 – 98% BaTiO_3	1400	36
5% SrZrO_3 – 95% BaTiO_3	1400	30
8% SrZrO_3 – 92% BaTiO_3	1400	16 x 2
12% SrZrO_3 – 88% BaTiO_3	1400	30

As before, in-house powder X-ray diffraction data were collected on each of the samples and used to confirm phase purity as well as a perovskite structure.

5.3.2: Dielectric spectroscopy

Dielectric spectroscopy measurements were collected on each of the four compositions as described in chapter 3, section 6 and chapter 5 section 2.3. As with the addition of CaZrO_3 , T_C is observed to fall as the dopant level is increased, figure 5.15, whilst the transition temperatures of the other phase transitions increases with increasing dopant concentration.

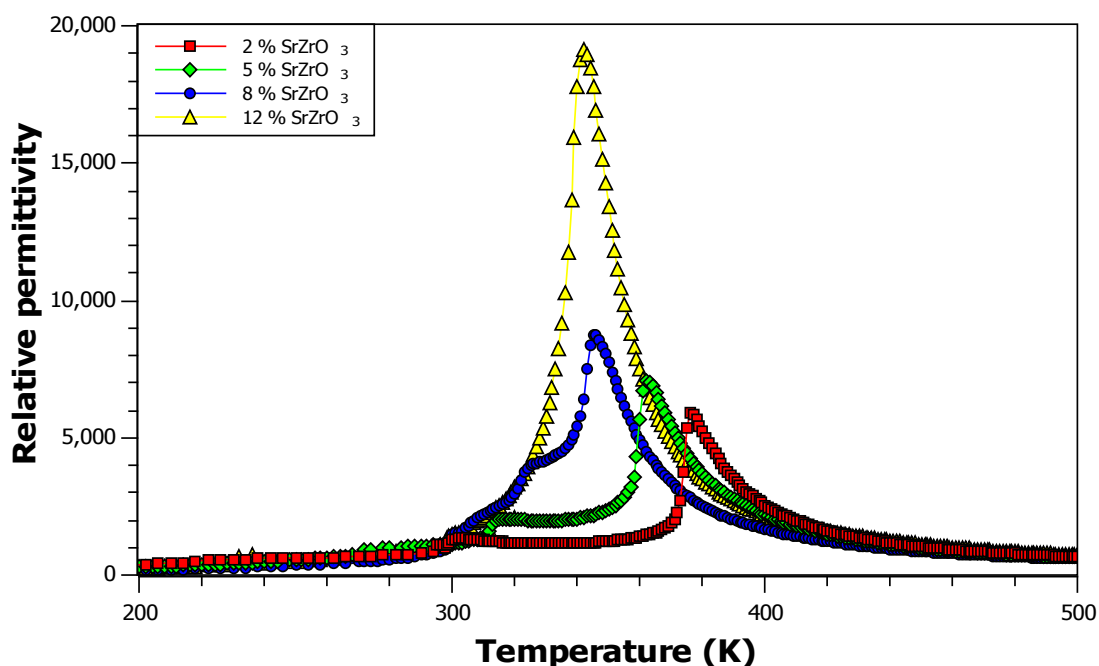


Figure 5.15: Dielectric data for 2, 5, 8 and 12 % SrZrO₃-doped BaTiO₃ showing a decrease in T_c and increase in the magnitude of the maximum in the relative permittivity with increasing dopant concentration

In each case an event in the loss data was found to accompany each peak in the relative permittivity, a feature which is to be expected when a composition undergoes a crystallographic change to a different polymorph. A graphical representation of this data for each composition can be found in appendix A5.4-A5.7

As with the CaZrO₃-doped BaTiO₃, it was observed that 12 % dopant concentration was required in order to bring about a coalescence of phases. However, the steeper increase in the phase transition temperatures of the two lower temperature phase transitions suggests that it is likely that the actual dopant concentration required for coalescence, though still between 8 -12 %, is somewhat lower for SrZrO₃ doping than for CaZrO₃. A plot of the transition temperatures is shown in figure 5.16.

As well as causing T_c to fall and the phases to coalesce, it is observed that as the dopant concentration is increased, the magnitude of the maximum in the relative permittivity increases, (figure 5.15, table 5.4). This increase in the maximum value is most stark as the phase coalescence is achieved at 12 % SrZrO₃-doped BaTiO₃.

Table 5.4: Relative permittivity peak maximums and transition temperatures of SrZrO₃-doped BaTiO₃

Composition		Peak 1	Peak 2	Peak 3
BaTiO₃	Temperature (K)	389	295	197
	Magnitude	10216	2237	2088
2% SrZrO₃- 98% BaTiO₃	Temperature (K)	376	295	226
	Magnitude	5900	1300	500
5% SrZrO₃- 95% BaTiO₃	Temperature (K)	362	318	272
	Magnitude	7000	2000	900
8% SrZrO₃- 92% BaTiO₃	Temperature (K)	345	323	306
	Magnitude	8700	3900	2050
12% SrZrO₃- 88% BaTiO₃	Temperature (K)	342	342	342
	Magnitude	19050	19050	19050

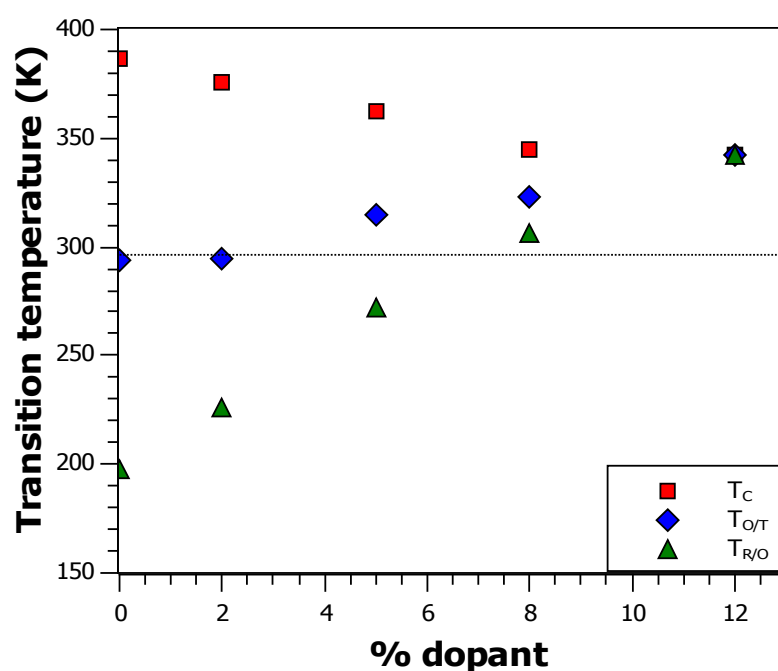


Figure 5.16: Variation in phase transition temperatures as a function of SrZrO₃ doping in BaTiO₃

The presence of three phase transitions in the compositions with distinct peaks in the relative permittivity suggests that, like the CaZrO₃-doped BaTiO₃, the compositions are undergoing a series of phase transitions with temperature, which mirror that of un-doped BaTiO₃.

5.3.3: Synchrotron powder X-ray diffraction data analysis

Powder X-ray diffraction data were collected on each sample at room temperature using the Diamond III beamline at the Rutherford Appleton laboratory. Although no variable temperature powder X-ray diffraction data was collected on these samples, the room temperature diffraction data did show the different compositions to have different crystallographic phases, figure 5.17.

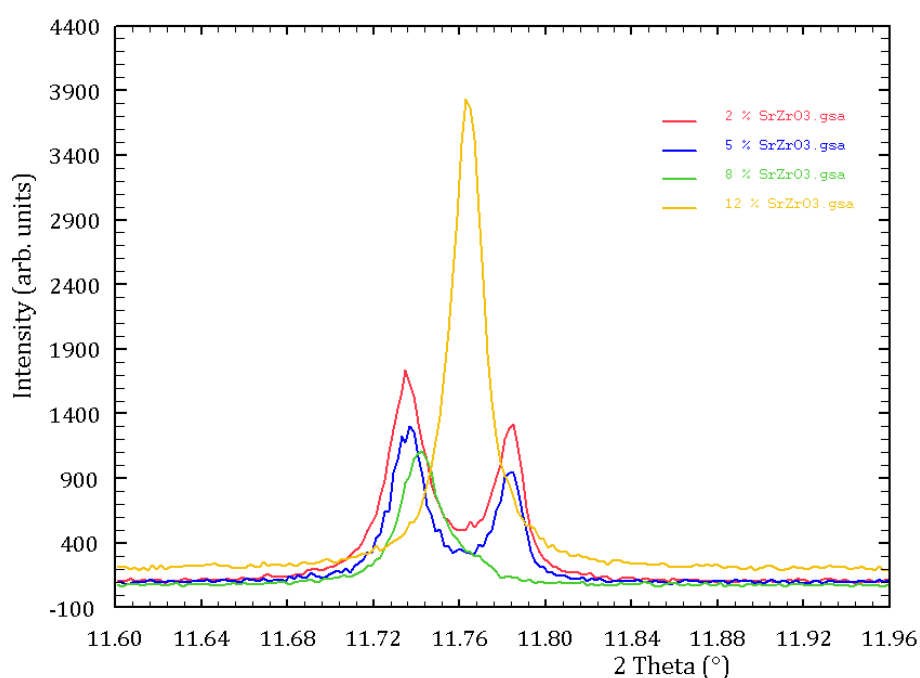


Figure 5.17: Room temperature powder X-ray diffraction data of 2, 5, 8 and 12 % SrZrO₃-doped BaTiO₃ showing a change in polymorphic phase with composition

Analysis of this data shows that each of the pellets was free from starting materials and other crystalline impurities. It also shows that both the 2 % and 5 % SrZrO₃-doped BaTiO₃ are orthorhombic at room temperature. This is in agreement with the dielectric data obtained from both these compositions.

It appears that both the 8 % and 12 % SrZrO₃-doped BaTiO₃ have a rhombohedral phase at room temperature. For the 12 % SrZrO₃ composition, the X-ray peaks are found to be sharp and give a good fit to a rhombohedral model using GSAS, suggesting a single phase rhombohedral composition. The peaks observed in the 8 % SrZrO₃ data are found to be slightly broader. The fact that unlike 12 % CaZrO₃-doped BaTiO₃, it is possible to clearly identify a major crystallographic phase further

suggests that the amount of dopant required to achieve coalescence using SrZrO_3 as opposed to CaZrO_3 is lower. The data suggests that 12 % CaZrO_3 doping results in a composition where the phases have only just coalesced, and thus all the phases are present, whereas by 12 % SrZrO_3 dopant addition the rhombohedral phase is considerably more stable than that of the other phases and so makes up the majority phase. This possibility is investigated further in section 6.4.

5.3.4: SrZrO_3 – BaTiO_3 phase diagram

With XRD evidence consistent with the peaks in the relative permittivity arises due to polymorphic phase changes, the following phase diagram can be plotted, figure 5.18.

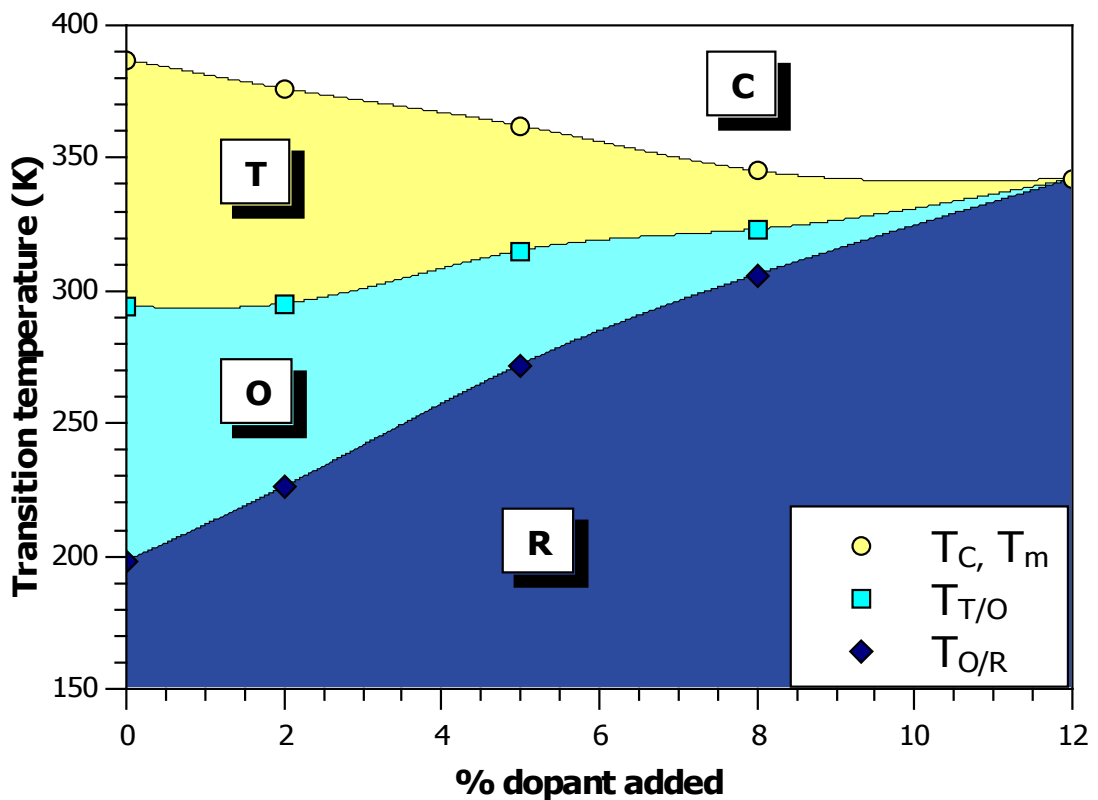


Figure 5.18: Phase diagram of SrZrO_3 -doped BaTiO_3 , showing T_C (Curie temperature), $T_{T/O}$, (tetragonal / orthorhombic phase boundary) and $T_{O/R}$ (orthorhombic / rhombohedral phase boundary)

This shows T_C falling more rapidly than that of the CaZrO_3 analogue and the phase transitions rising more rapidly. With the same B-site species in each, this is as a result of exchanging Ca^{2+} for the large Sr^{2+} species, resulting in less stabilisation as a result of strain.

5.4: The effects of LaScO₃ dopant addition to BaTiO₃

La³⁺ has a very similar size to Ca²⁺, and thus similar tolerance factor and variance. LaScO₃ was therefore chosen to be studied in order to see the effect of B-site charge dilution.

5.4.1: Synthesis

The synthesis of LaScO₃-doped BaTiO₃ proved to be significantly more complex than the synthesis of either CaZrO₃- or SrZrO₃-doped BaTiO₃, with pellets being formed with low densities and non-reproducible electrical properties, especially at high dopant concentrations. The synthesis of a pellet of 50 % LaScO₃-doped BaTiO₃ was attempted in order to try and understand the cause of the problems. It was observed that pellets pressed from powder after calcining, but before sintering, when left exposed at room temperature would gradually expand, suggesting that the material be air or moisture sensitive. In order to combat this, a series of pellets of varying compositions were synthesised using a variety of starting reagents and techniques. These included

- Solid state synthesis techniques described in section 3.1 using oxide starting materials: BaCO₃ (>99%), TiO₂ (>99%), La₂O₃ (>99.99%) and Sc₂O₃ (>99.995%)
- Solid state synthesis techniques described in section 3.1 using a mixture of nitrate and oxide starting materials
- Sol-gel techniques^[22, 23] using Sc₂O₃ (>99.995 %), BaCO₃ (>99 %), La(NO₃)₃·6H₂O (>99 %) and C₁₂H₂₈O₄Ti (>97 %) all dissolved in hot HNO₃
- Pre-reacting La₂O₃ and Sc₂O₃ to form LaScO₃, which was then used in a standard solid state synthesis as described in section 2.3
- Sintering pellets in an oxygen enriched atmosphere

It was found that the best synthesis route varied depending on the amount of LaScO₃ being added. For the lowest dopant concentration, 2 % LaScO₃, pellets could be reproducibly formed, with good electrical properties and of single phase by the standard solid state synthesis techniques used for CaZrO₃- and SrZrO₃-doped BaTiO₃. However this was not the case for the higher dopant concentrations. For each of the

other compositions the use of pre-reacted LaScO_3 yielded the best results, with the addition of an oxygen enriched atmosphere being required for good synthesis of 5% LaScO_3 -doped BaTiO_3 . In every instance heating the loose powder or loosely (< 1000 psi) pressed pellets before re-grinding, pressing isostatically to 30000 psi and sintering was found to yield better pellets than pellets that were pressed isostatically using 30000 psi and sintered directly after calcining. The optimised synthesis conditions for each composition are given in table 5.5.

The synthesis of LaScO_3 was completed by ball milling La_2O_3 (> 99.99 %) and Sc_2O_3 (> 99.995 %) and then reacting the ground power at 1500 °C for a period of 10 hours. The resultant powder was then re-milled and pressed uniaxially to loose pellets (< 1000 psi) before being reheated at 1525 °C for 24 hours.

Table 5.5: Synthesis conditions for 2, 5, 8 and 12 % LaScO_3 -doped BaTiO_3

Composition	Furnace temperature (°C)	Heating time (hours)	Atmosphere	Reagents
2% LaScO_3 – 98% BaTiO_3	1450 (< 1000 psi) 1450 (30000 psi)	30 24	air	BaCO_3 (>99 %) TiO_2 (>99.9 %) La_2O_3 (>99.99 %) Sc_2O_3 (>99.995 %)
5% LaScO_3 – 95% BaTiO_3	1475 (loose) 1475 (30000 psi)	24 24	O_2 enriched air	BaCO_3 (>99 %) TiO_2 (>99.9 %) LaScO_3
8% LaScO_3 – 92% BaTiO_3	1450 (loose) 1500 (30000 psi)	15 36	air	BaCO_3 (>99 %) TiO_2 (>99.9 %) LaScO_3
12% LaScO_3 – 88% BaTiO_3	1350 (loose) 1350 (30000 psi)	12 24	air	BaCO_3 (>99 %) TiO_2 (>99.9 %) LaScO_3

5.4.2: Dielectric spectroscopy

Dielectric spectroscopy was carried out initially on the 2 % LaScO_3 - 98% BaTiO_3 composition. This showed three phase transitions in the relative permittivity as with the un-doped BaTiO_3 and <12 % CaZrO_3 - and SrZrO_3 -doped BaTiO_3 , however, the peaks were found to be much closer together, with T_C significantly depressed compared to either un-doped BaTiO_3 or (Ca,Sr) ZrO_3 -doped BaTiO_3 figure 5.19.

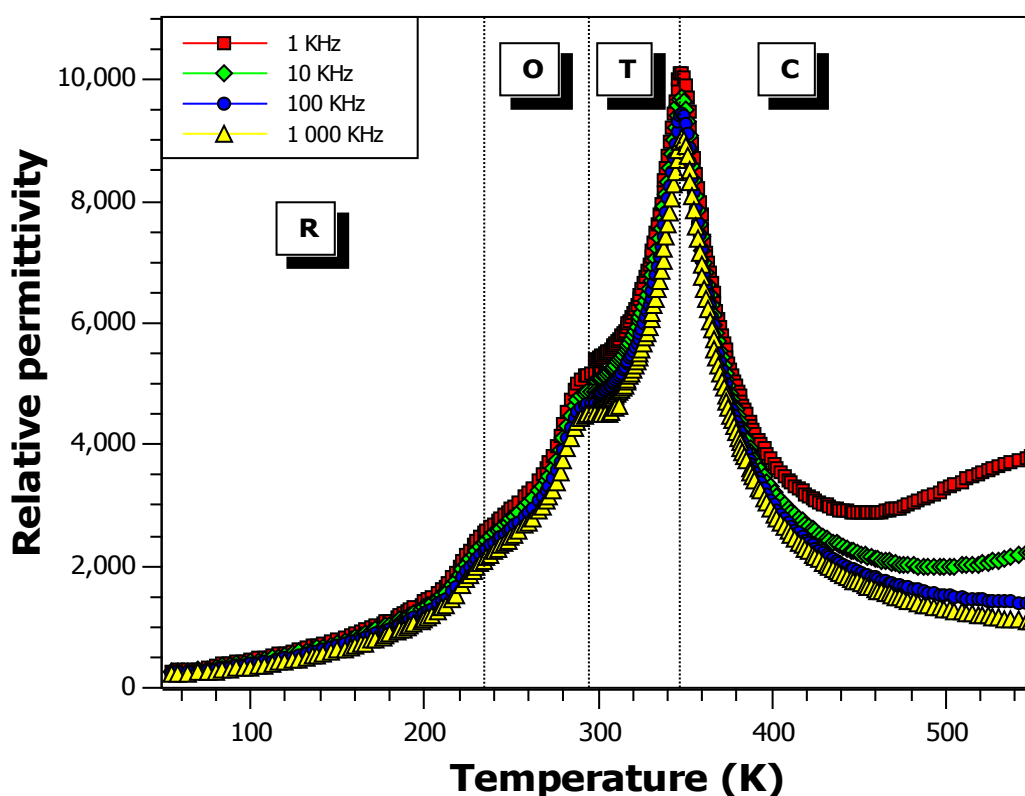


Figure 5.19: Dielectric spectroscopy data collected on a sample of 2 % $\text{LaScO}_3 - \text{BaTiO}_3$ showing the presence of three peaks in the relative permittivity, all of which are frequency independent w.r.t. the temperature of the transition

As with the other samples studied, there is a slight frequency dependence of the magnitude of the relative permittivity, but no frequency dependency of T_C . This was also true of each of the other compositions studied (appendix A5.8-A5.10)

The suppression of T_C as a result of the addition of dopant species is much greater than seen with either CaZrO_3 or SrZrO_3 doping. Whilst this would be the expected result of having a lower charged species being off-centred, and thus creating a lower polarisation as a result of displacement, the effect of dopant addition on the 2 lower temperature phase transitions is generally much less understood. This data shows that the LaScO_3 dopant addition greatly stabilises the rhombohedral and tetragonal phases compared to the CaZrO_3 and SrZrO_3 compositions. By 5 % dopant addition, full coalescence was achieved, which was maintained with higher dopant concentrations, figure 5.20.

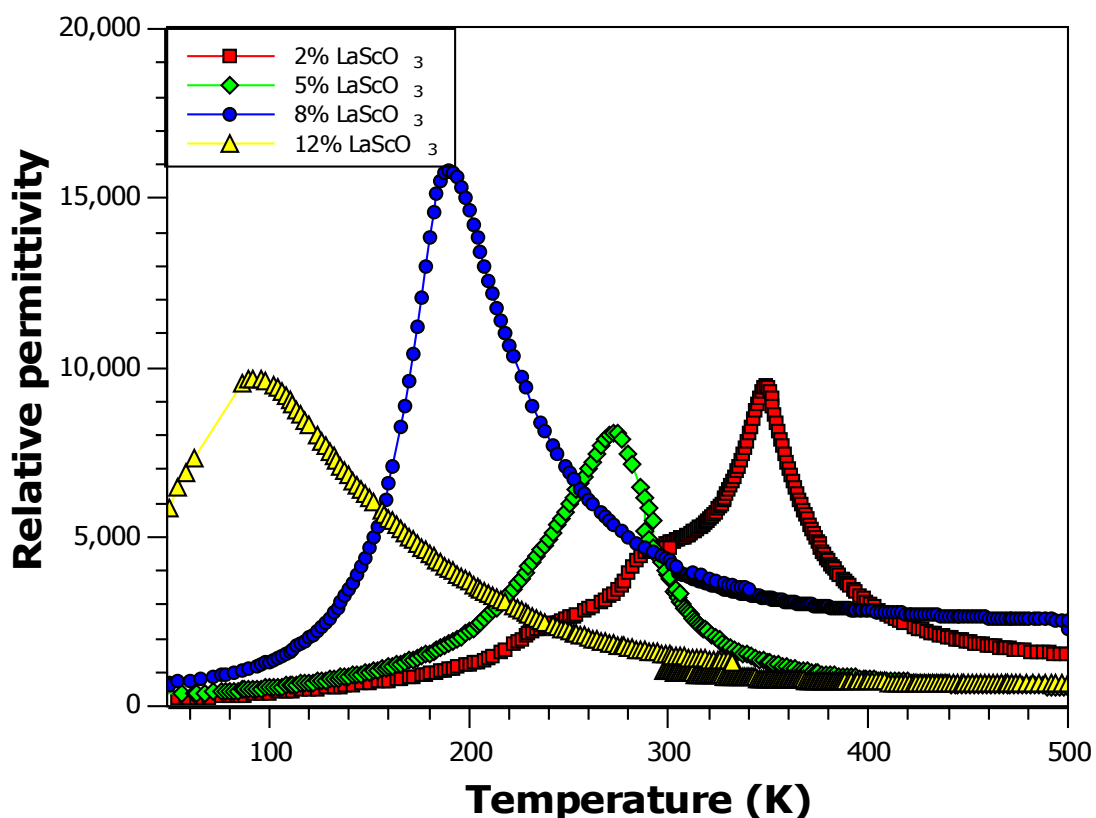


Figure 5.20: Dielectric spectroscopy data for 2, 5, 8 and 12 % LaScO_3 -doped BaTiO_3 showing a coalescence of peaks with increasing dopant concentration

5.4.3: Synchrotron powder X-ray diffraction analysis

The Diamond facility in Oxford was again used to collect high resolution room temperature powder X-ray diffraction data on each sample with variable temperature diffraction data also being collected on a samples of 2 and 5 % LaScO_3 -doped BaTiO_3 . The 2 % LaScO_3 composition was found to have four distinct crystallographic phases, as observed in the 5 % CaZrO_3 composition, however, the phases were found to exist over narrow temperature ranges with some phase mixture at the boundaries, leading to two phase refinement being required for many of the data sets. Again, this is consistent with the phase transitions being first order, figure 5.21. Despite the coexistence of phases, particularly between 220 -320 K, the volume was still observed to vary linearly with temperature.

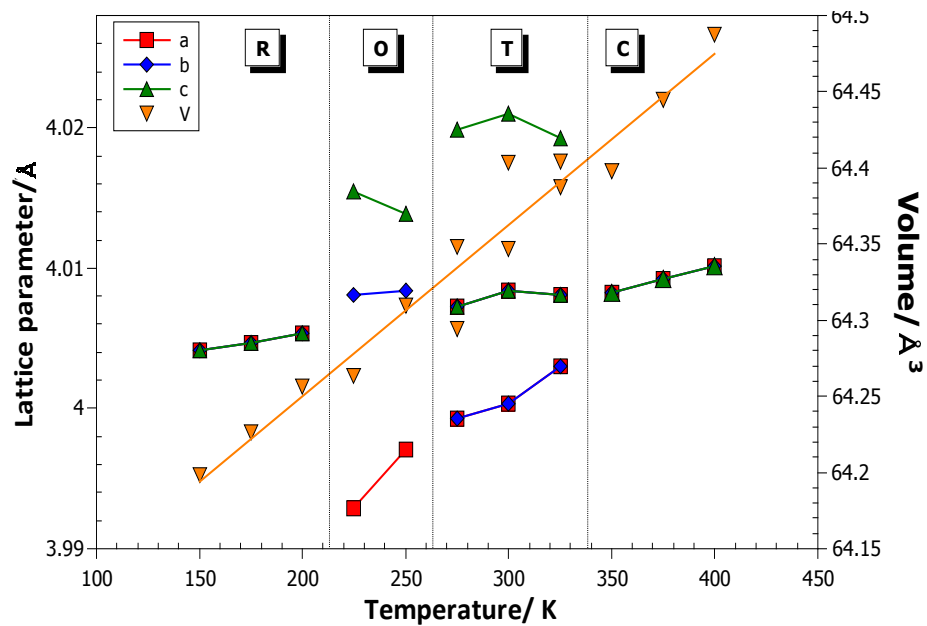


Figure 5.21: Changes in the lattice parameters and volume of 2 % LaScO_3 -doped BaTiO_3 as a function of temperature

5.4.4: LaScO_3 – BaTiO_3 Phase diagram

Using transition temperatures obtained from dielectric spectroscopy data alongside the variable temperature, powder X-ray diffraction data evidence of the associated phase changes, a phase diagram was formed for LaScO_3 -doped BaTiO_3 , figure 5.22.

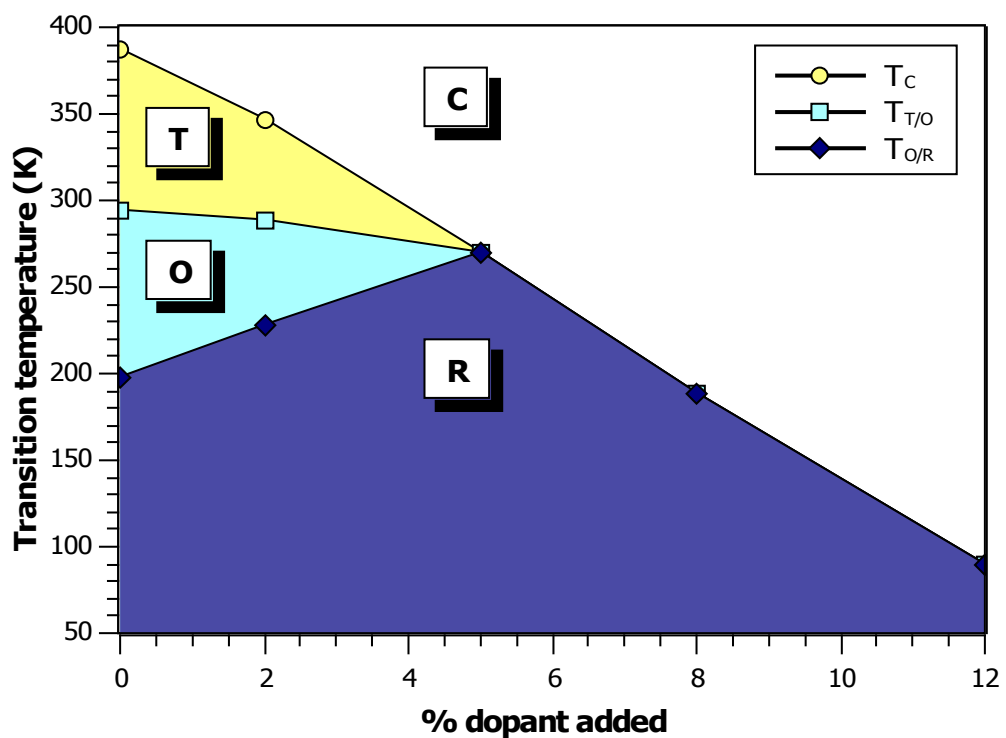


Figure 5.22: Phase diagram of LaScO_3 -doped BaTiO_3 , showing T_C (Curie temperature), $T_{T/O}$ (tetragonal / orthorhombic phase boundary) and $T_{O/R}$ (orthorhombic / rhombohedral phase boundary)

This clearly shows a dramatic drop in T_C accompanied by a rapid increase in $T_{O/T}$ and $T_{R/O}$ resulting coalescence on the peaks being achieved by 5 % LaScO_3 addition, a much lower concentration than required for coalescence in the CaZrO_3 - and SrZrO_3 -doped BaTiO_3 compositions.

5.5: The effects of GdScO_3 dopant addition to BaTiO_3

5.5.1: Synthesis

As with the other dopants studied, a series of 2, 5, 8 and 12 % GdScO_3 -doped BaTiO_3 were synthesised, using the same techniques and reagents as stated previously, along with the addition of Gd_2O_3 , (> 99.9 %). Due to time constraints of the project and equipment limitations, synthesis conditions for 8 and 12 % GdScO_3 have not been fully optimised, with the conditions listed in table 5.6 for these compositions resulting in pellets with small grain sizes, < 5 μm . However, the synthesis conditions for both the 2 and 5 % GdScO_3 were optimised and can be found below in table 5.6.

Table 5.6: Synthesis conditions for GdScO_3 -doped BaTiO_3

Composition	Furnace temperature (°C)	Heating time (hours)
2% GdScO_3 – 98% BaTiO_3	1350 (loose)	15
	1350 (loose)	15
	1350 (30000 psi)	24
5% GdScO_3 – 95% BaTiO_3	1400 (loose)	30
	1475 (loose)	15
	1500 (30000 psi)	15
8% GdScO_3 – 92% BaTiO_3	1500 (30000 psi)	30
	1500 (30000 psi)	30
12% GdScO_3 – 88% BaTiO_3	1450 (loose)	30
	1500 (loose)	15
	1500 (30000 psi)	15

In-house power X-ray diffraction data collected from all four compositions show each of them to be a single phase perovskite material, regardless of whether the material has been synthesised in a manner conducive to yielding good electrical properties.

5.5.2: Dielectric spectroscopy

Dielectric spectroscopy data collected were collected from pellets of each composition, figure 5.23. Whilst the data collected from both the 2 % and 5 % GdScO_3 -doped BaTiO_3 show clear transitions with sharp peaks of large magnitudes in the relative permittivity data, this was not the case for the higher dopant concentration samples. For both the 8 % and 12 % GdScO_3 -doped BaTiO_3 compositions the peaks were found to be coalesced but broad, irregularly shaped and having much lower relative permittivity magnitudes than would be expected compared to both the 2 and 5 % GdScO_3 -doped BaTiO_3 and also the coalesced peaks of BaTiO_3 with different dopants. This is likely to be due to incomplete optimisation of the processing conditions for these two compositions, although the highly suppressed and broadened peaks may also be a sign of having reached the solid solution limit^[24]. Each of the transition temperatures for the studies compositions are given in table 5.7.

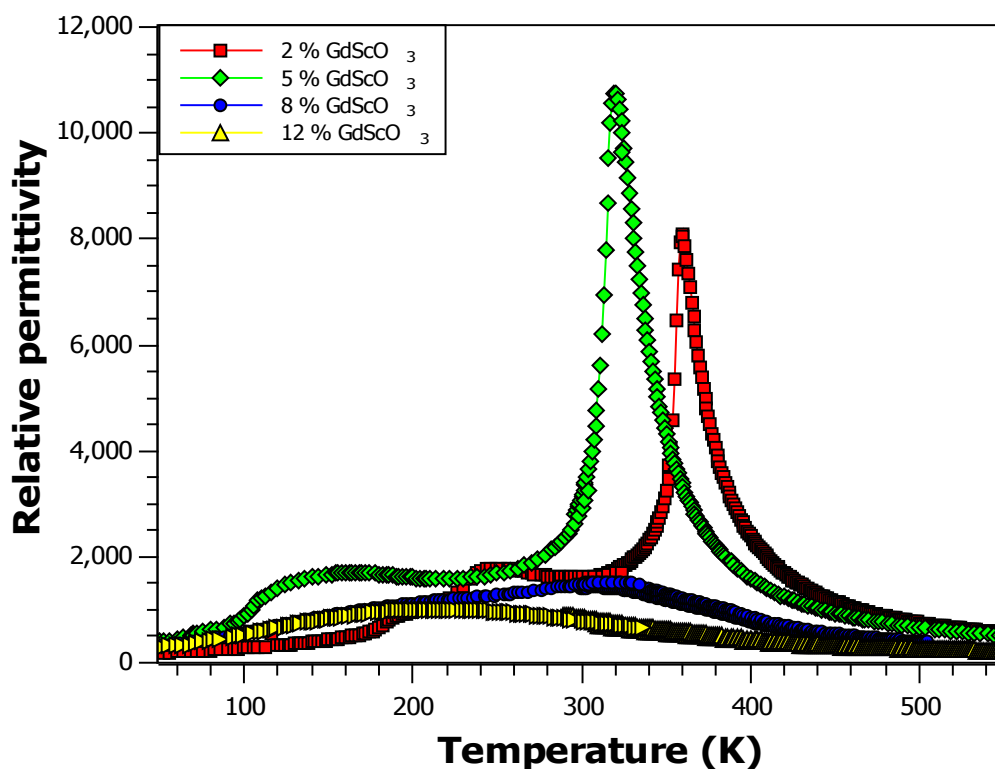


Figure 5.23: Dielectric spectroscopy data collected on samples of 2, 5, 8 and 12 % GdScO_3 – doped BaTiO_3

Table 5.7: Relative permittivity peak maxima and transition temperatures of SrZrO₃-doped BaTiO₃

Composition		Peak 1	Peak 2	Peak 3
BaTiO₃	Temperature (K)	389	295	197
	Magnitude	10216	2237	2088
2% GdScO₃- 98% BaTiO₃	Temperature (K)	364	238	184
	Magnitude	10500	1600	900
5% GdScO₃- 95% BaTiO₃	Temperature (K)	328	108	-
	Magnitude	11400	1150	-
8% GdScO₃- 92% BaTiO₃	Temperature (K)	304	-	-
	Magnitude	1500	-	-
12% GdScO₃- 88% BaTiO₃	Temperature (K)	206	-	-
	Magnitude	975	-	-

Of particular interest was the dielectric spectroscopy data collected on the 5 % GdScO₃-doped BaTiO₃ sample. This showed a decrease in T_C as expected, however, the lower temperature peaks have also been suppressed to lower temperatures, with only one further transition remaining observable down to a temperature of 50 K, the lowest operating temperature of the cryostat, figures 5.23 and 5.24. A corresponding event in the loss data is observed for both of the observed transitions, T_C and the remaining low temperature transition, suggesting that both are resultant of polymorphic phase changes occurring, this is shown in figure 5.24.

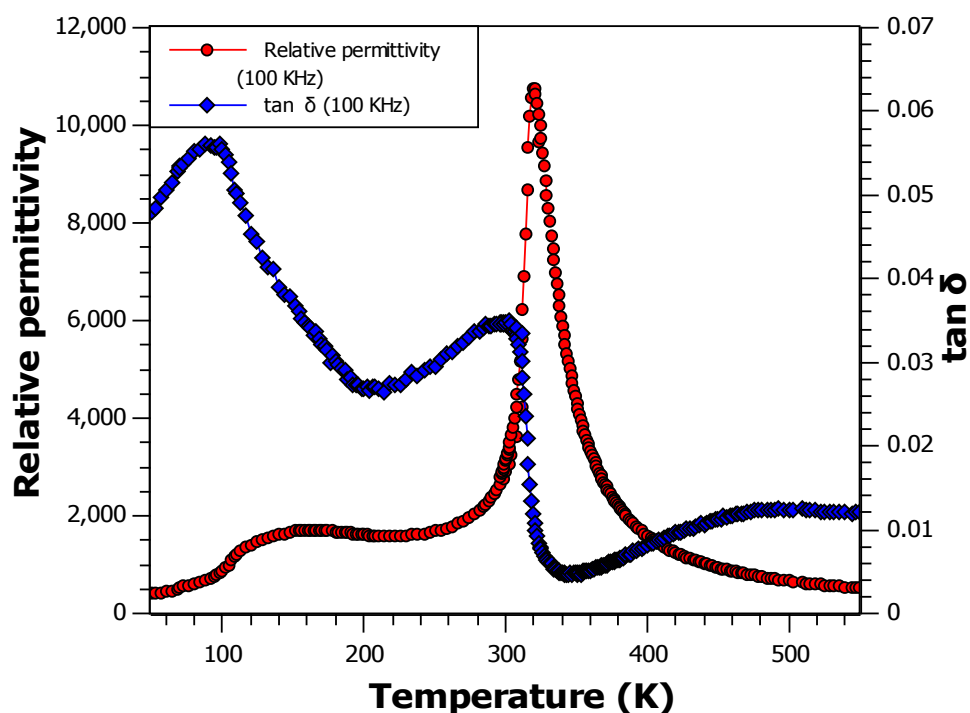


Figure 5.24: Dielectric spectroscopy and loss data collected at 100 KHz on a sample of 5% GdScO₃ – doped BaTiO₃ showing a large suppression of the expected low temperature peak in the relative permittivity

It is not clear from this data whether both the rhombohedral / orthorhombic and orthorhombic / tetragonal phase transitions have been suppressed with regards to temperature, with the rhombohedral / orthorhombic suppressed by such as extent that it is now outside the operating range of the cryostat, or whether the two low temperature phase transitions have coalesced, but are still distinct from the main tetragonal / cubic phase transition.

5.5.3: Synchrotron powder X-ray diffraction analysis

Room temperature synchrotron powder X-ray diffraction data were collected on each of the compositions in order to determine phase purity, with data collected on both the 8 and 12 % GdScO₃-doped BaTiO₃ samples consisting of a series of sharp, un-split peaks, consistence with a cubic or pseudo cubic space group, figures 5.25.

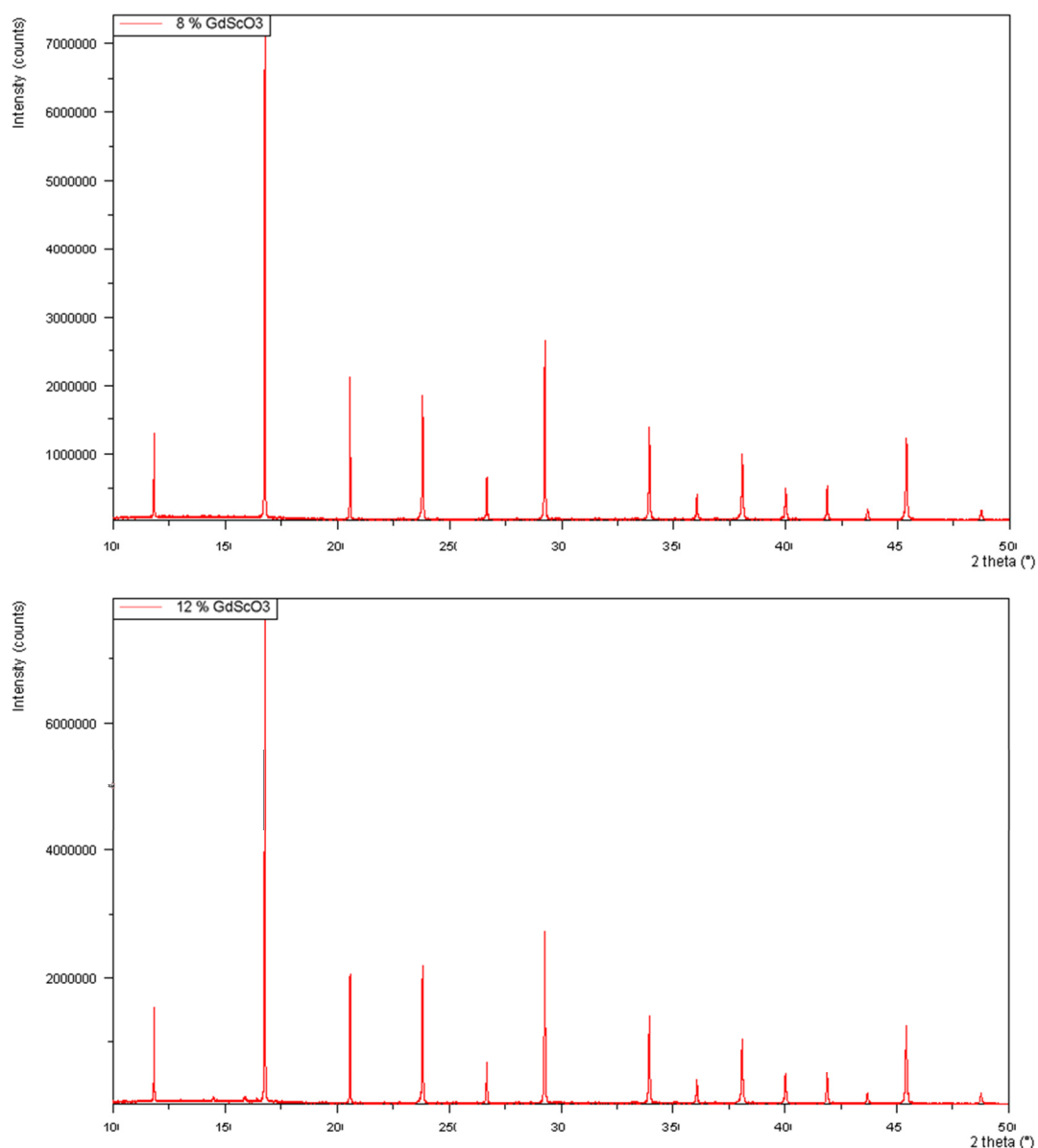


Figure 5.25: Power X-ray diffraction data collected from a sample of 8 % GdScO₃-doped BaTiO₃ (top) and 12 % GdScO₃-doped BaTiO₃ (bottom), showing the presence of a single phase “pseudo cubic” perovskite, despite the samples being non-optimised for electrical properties

Variable temperature powder X-ray diffraction data were collected on a sample of 2 % GdScO₃, with data collected at 20 K intervals between 100 – 380 K with additional data sets collected at 350, 370 and 430 K. Data were collected using the same conditions as for 5 % CaZrO₃-doped BaTiO₃. This data was found to be refinable in one of the four space groups associated with the different polymorphs of BaTiO₃ depending on the temperature at which the data were collected, figure 5.26. This showed that, despite the unusual suppression of the

temperature of the lower temperature phase boundaries, addition of GdScO_3 to BaTiO_3 does not significantly alter the structure of the crystallographic phases of the material. Again the volume change as a function of temperature was found to be linear, with small perturbations at phase boundaries.

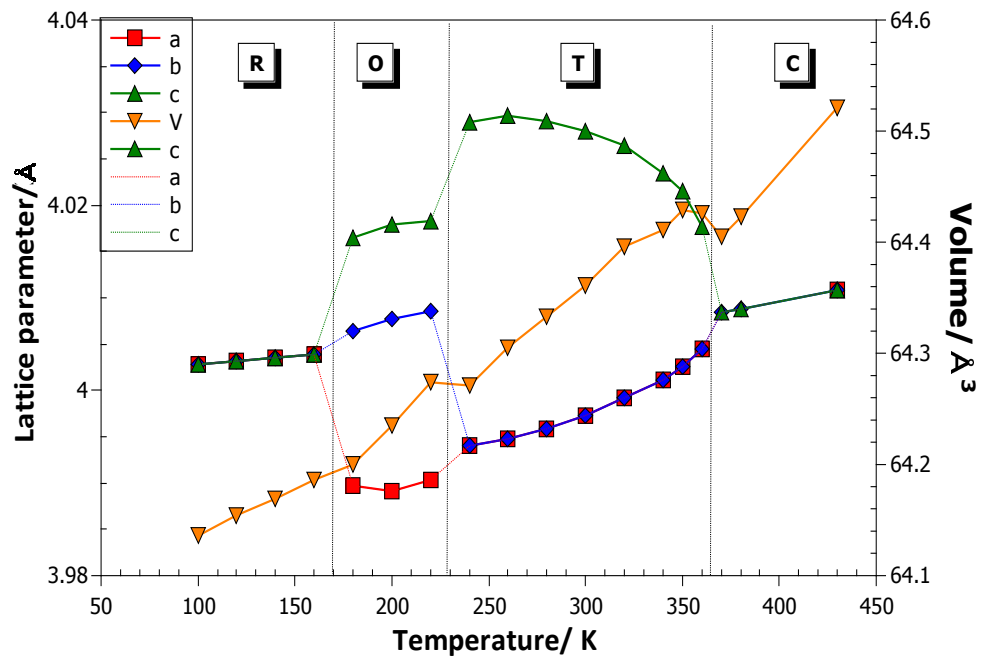


Figure 5.26: Changes in the lattice parameters and volume of 2 % GdScO_3 – BaTiO_3 as a function of temperature undergoing phase transitions between rhombohedral, (R), orthorhombic, (O), tetragonal, (T) and cubic, (C), phases

Variable temperature powder X-ray diffraction data was also collected on a sample of 5 % GdScO_3 -doped BaTiO_3 in order to determine how the crystallographic structure of the composition changed as a function of temperature in order that the peaks in the relative permittivity dielectric spectroscopy data might be better understood. Data was collected between 100 and 400 K in 25 K intervals with an additional data set collected at 95 K. Each data set was collected for a period of 900 s with the sample left to equilibrate for a period of 300 s at each temperature.

Analysis of the data showed that the data set collected at 325 K, along with all data sets collected above this temperature, were able to be refined fully in the $Pm\bar{3}m$ space group associated with cubic BaTiO_3 . Below this temperature, data sets collected between 300 and 125 K were all found to have tetragonal symmetry and could be refined in the $P4mm$ space group associated with tetragonal BaTiO_3 . The

data set collected at 100 K was inconclusive with regards to assigning a space group and looked to be a mixture of tetragonal and at least one other phase, figure 5.27. Having reached the temperature limit of the Cryostream Plus, it was not possible to determine whether the composition tended to an orthorhombic structure below the ~ 100 K event observed in the dielectric spectroscopy data, or whether it went straight to a rhombohedral or mixed orthorhombic / rhombohedral phase. A data set was recorded at 95 K, but this was as low as the Cryostream Plus could achieve, and the data set was little changed from that of the data set collected at 100 K and could not be fully resolved.

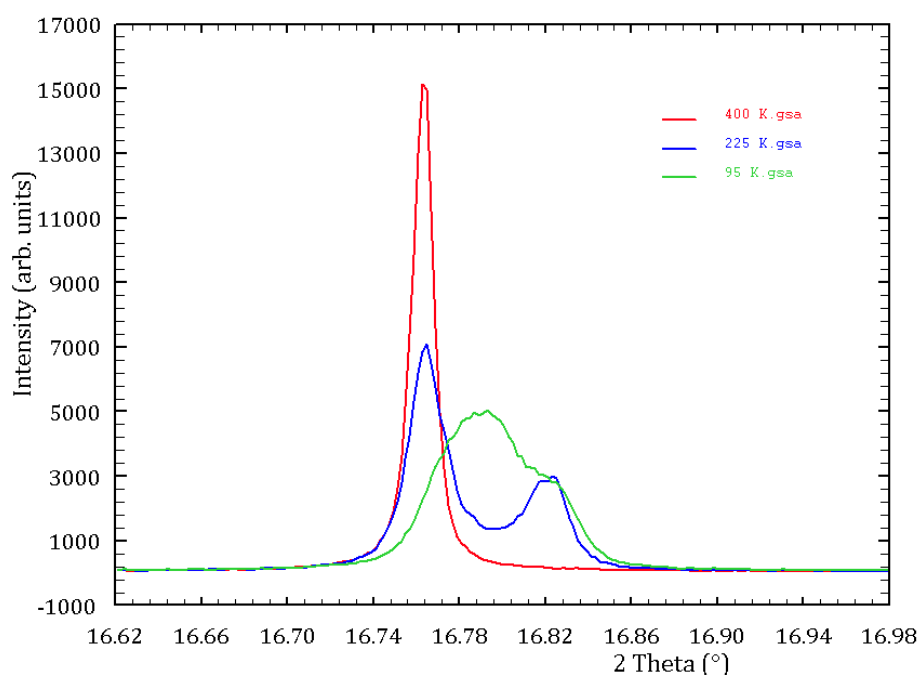


Figure 5.27: Variable temperature powder X-ray diffraction data collected on 5 % GdScO₃-doped BaTiO₃ at 400 K (cubic), 225 K (tetragonal) and 95 K (unresolved)

Though it was not possible to refine either the 100 K or 95 K data set in a single space group, this is possibly due to the fact that both data sets were collected around the transition temperature, as shown in the dielectric spectroscopy data, which shows the transition to be relatively broad compared to the much sharper tetragonal to cubic transition. This could suggest a coalescence of the lower temperature phases, explaining the inability for the data to be refined in a single space group. However, when looking at the lower temperature transitions for other doped BaTiO₃ compositions with non-coalesced peaks, it is observed that these peaks are often considerably broader than the tetragonal to cubic peak, and that in

many cases, such as that of the 5 % SrZrO₃-doped BaTiO₃ discussed earlier, do return to a single crystallographic phase after the transition.

The use of the Cryostream Plus to get variable temperature powder X-ray diffraction data, did allow for determination of the polymorphic phase of the material at temperatures between the temperatures of the two peaks in the relative permittivity, with a clear tetragonality being observed throughout this temperature range, figure 5.28. This proves that the addition of 5 % GdScO₃ to BaTiO₃ does result in an expansion of the tetragonal region of the phase diagram, something not seen in any of the other dopants studied.

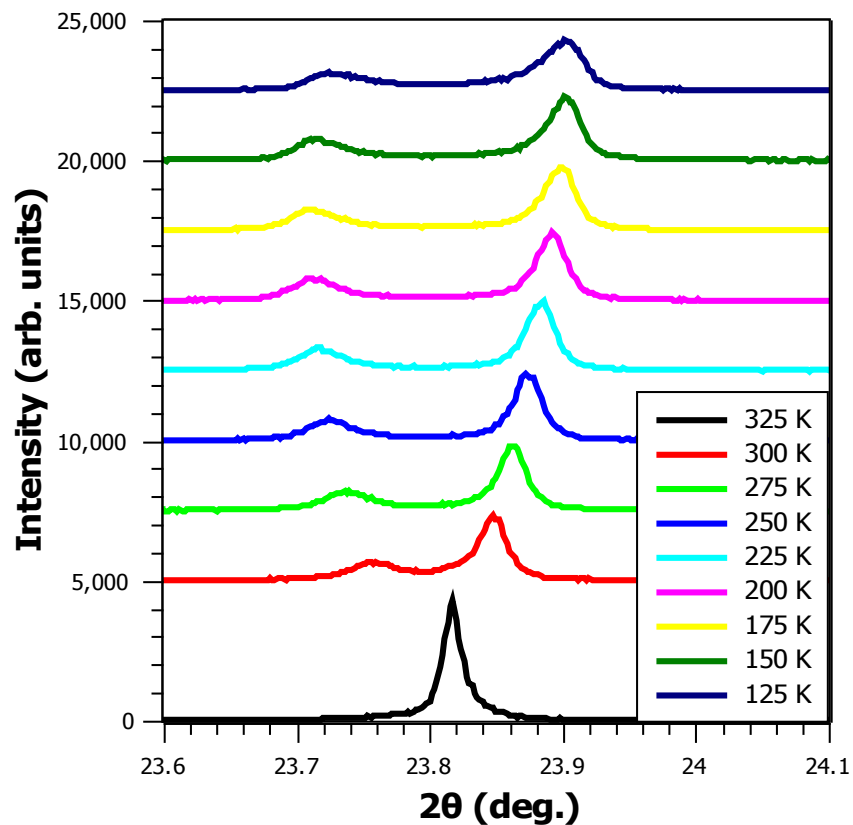


Figure 5.28: Variable temperature synchrotron, powder X-ray diffraction data showing a tetragonal splitting of the [200]/[002] peak of 5 % GdScO₃-doped BaTiO₃ maintained over a 200 K temperature range

Analysis of the lattice parameter and volume changes with temperature show a linear change in the volume, maintained, albeit with a slight perturbation, across the phase boundary, figure 5.29. As the composition reaches T_C the volume of the unit cell appears depressed. A similar depression is observed at the low temperature phase transition, with both being similar in magnitude to the phase

transition depressions in the unit cell volume observed in variable temperature powder X-ray diffraction data collected on other doped BaTiO_3 samples, such as 5 % $\text{CaZrO}_3 - \text{BaTiO}_3$, figure 5.13.

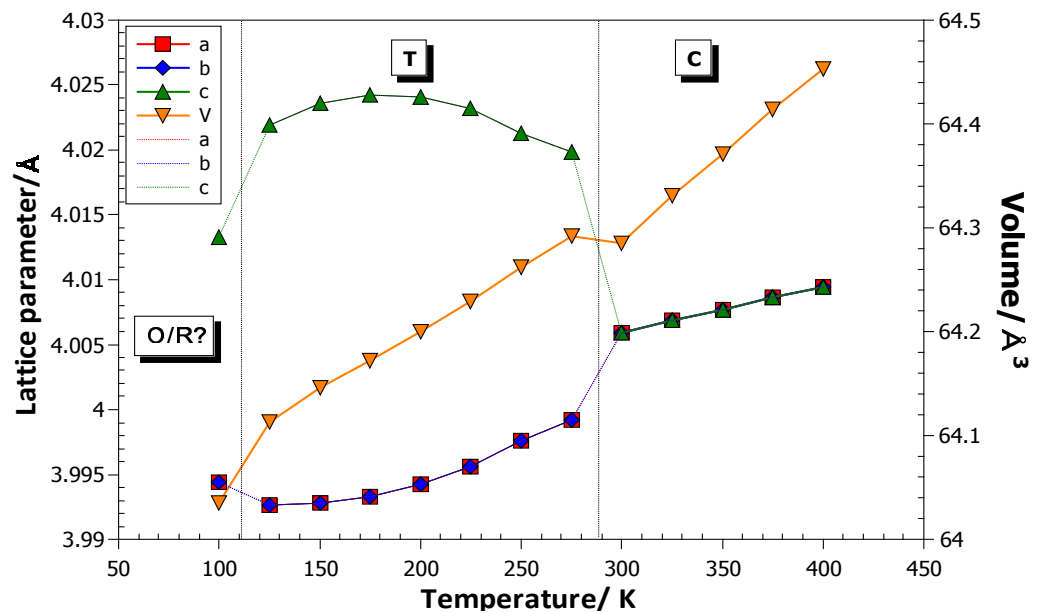


Figure 5.29: Changes in the lattice parameters and volume of 5 % $\text{GdScO}_3 - \text{BaTiO}_3$ as a function of temperature undergoing phase transitions at 300 and 100 K

5.5.4: $\text{GdScO}_3 - \text{BaTiO}_3$ Phase diagram

Combining knowledge gleaned from the variable temperature powder X-ray diffraction and dielectric spectroscopy data, enabled the production of a phase diagram for the addition of GdScO_3 to BaTiO_3 , figure 5.30.

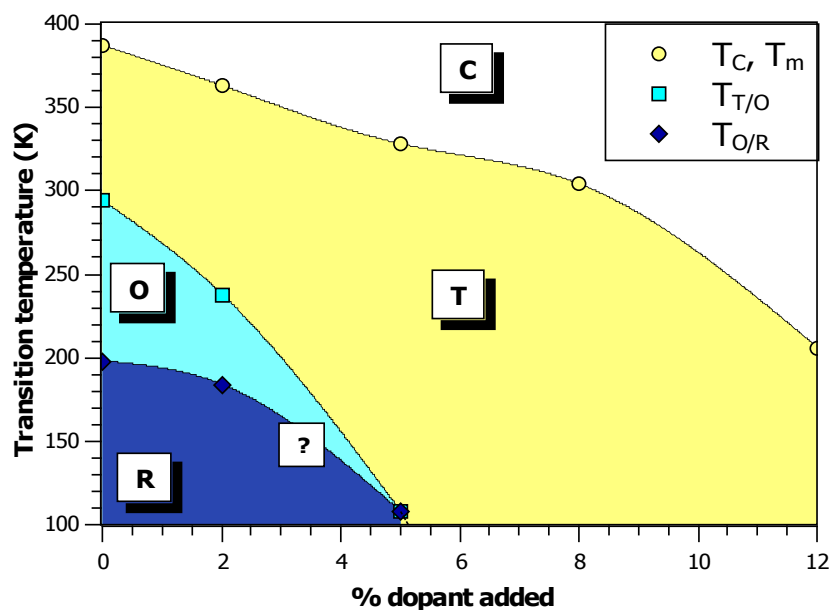


Figure 5.30: Phase diagram of GdScO_3 -doped BaTiO_3 , showing T_C , (Curie temperature), $T_{T/O}$, (tetragonal / orthorhombic phase boundary) and $T_{O/R}$, (orthorhombic / rhombohedral phase boundary)

This phase diagram shows a completely different profile to any of the other dopants studied. Though T_C clearly falls with increasing dopant concentration, the temperature of both the other phase transitions also fall with increasing dopant concentration, unlike the other phase diagrams, where these transitions are observed to shift to higher temperatures as the dopant level was increased. As a result the tetragonal phase is stabilised and no coalescence resulting in a PPB occurs.

5.6: Trends as a result of dopant addition to BaTiO₃

5.6.1: Trends in T_C

Phase boundary maps constructed from dielectric spectroscopy data and variable temperature X-ray data analysis for each of the four compositions $(\text{BaTiO}_3)_{1-x}(\text{CaZrO}_3)_x$, $(\text{BaTiO}_3)_{1-x}(\text{SrZrO}_3)_x$, $(\text{BaTiO}_3)_{1-x}(\text{LaScO}_3)_x$ and $(\text{BaTiO}_3)_{1-x}(\text{GdScO}_3)_x$, figure 5.31, show how the polymorphic phases of each material varies with the percentage of dopant added.

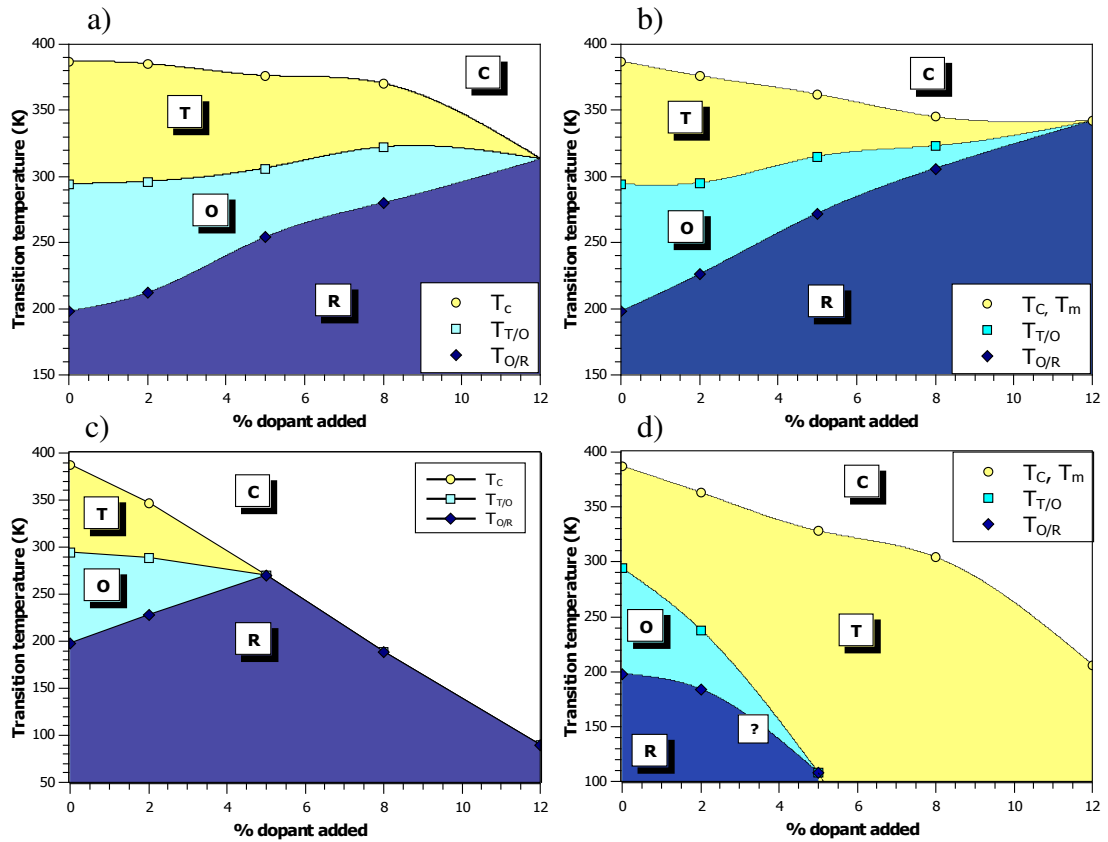


Figure 5.31: Phase boundary maps for a) $(\text{BaTiO}_3)_{1-x}(\text{CaZrO}_3)_x$, b) $(\text{BaTiO}_3)_{1-x}(\text{SrZrO}_3)_x$, c) $(\text{BaTiO}_3)_{1-x}(\text{LaScO}_3)_x$ and d) $(\text{BaTiO}_3)_{1-x}(\text{GdScO}_3)_x$

A general trend observed for all of these materials is for T_C to decrease with increasing dopant concentration. Standard size arguments predict that when a smaller A-site species or larger B-site species is doped into a perovskite lattice, T_C will fall. This argument is based on tolerance factors, where the tolerance factor, t , is given by equation 1.4 (chapter 1, section 2). Un-doped BaTiO_3 has a tolerance factor of ~ 1.06 . Tolerance factors greater than 1 tend to result in a tetragonal unit cell which allows for relief of stresses caused by non-ideal ratios between the ion sizes in the lattice. Substitution with dopants to lower t brings the value closer to the ideal value of 1 which would give rise to a cubic phase. Thus the amount of thermal energy required to go from the tetragonal to cubic phase falls as $t \rightarrow 1$.

For the dopants studied at the dopant concentrations synthesised, all the dopant additions would have caused a reduction in t , but with none giving a t so small as to be below a value of 1 which would favour a rhombohedral polymorphic phase, figure 5.32. Thus, based on a tolerance factor argument, T_C would be expected to fall with the addition of all the dopants studied, as is observed.

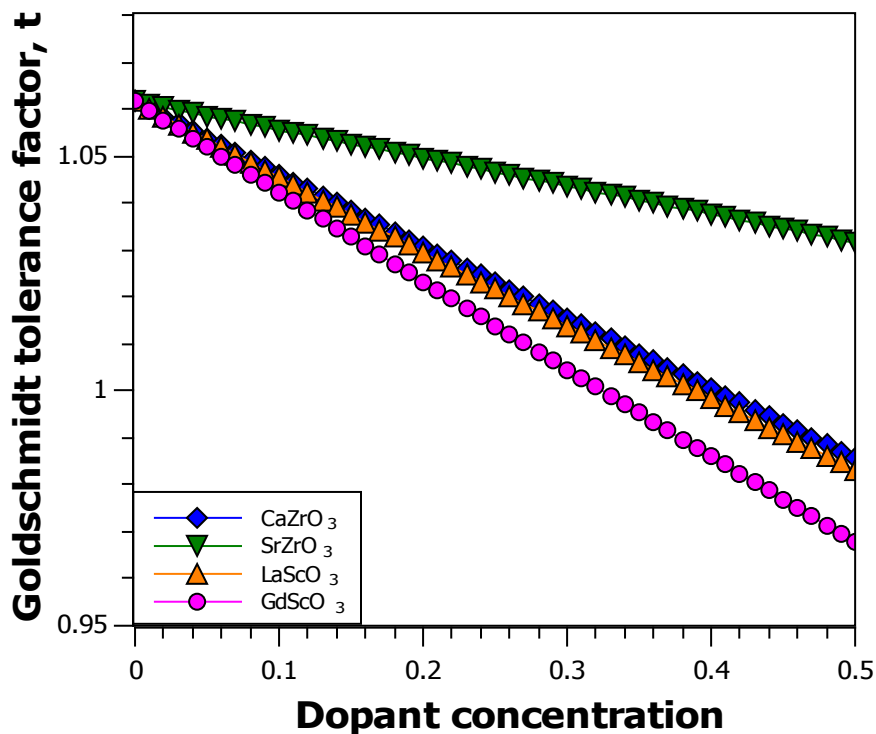


Figure 5.32: Tolerance factor as a function of dopant concentration where 0.5 = 50 % dopant and 0 is pure BaTiO_3

Based on tolerance factor arguments alone, T_C would be expected to fall most sharply with the addition of GdScO_3 as a dopant and least sharply with SrZrO_3 . However When T_C is plotted as a function of dopant addition, figure 5.33, this is not the case.

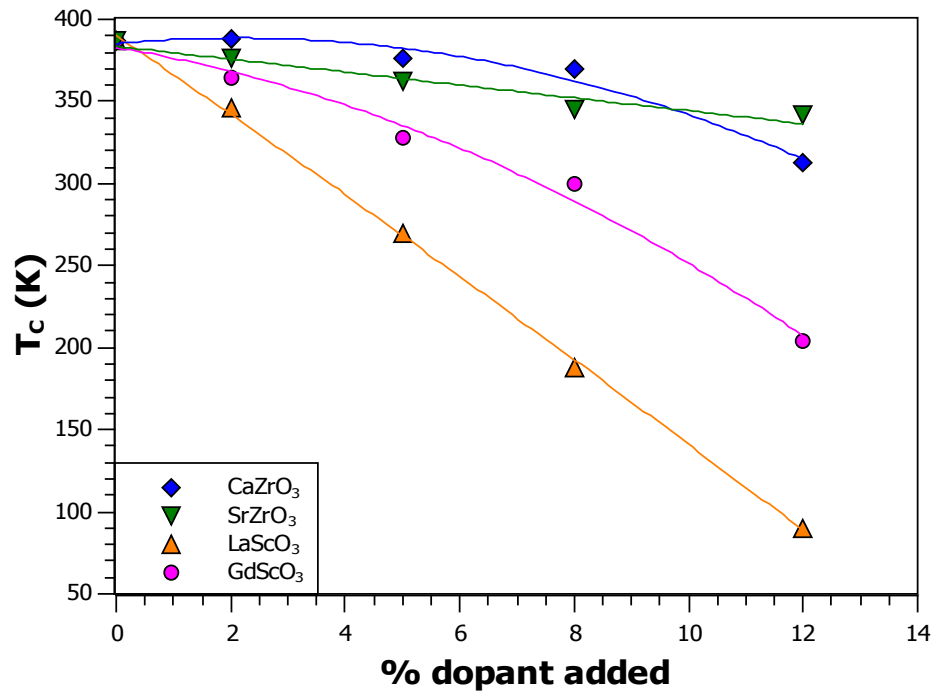


Figure 5.33: Rate of change of T_C as a function of dopant addition for CaZrO_3 , SrZrO_3 , LaScO_3 and GdScO_3

The fact that T_C does not fall fastest with GdScO_3 addition and slowest with SrZrO_3 addition suggests that something other than long range size effects must be having an effect on T_C . Whilst both LaScO_3 and SrZrO_3 dopants seem to result in approximately linear reductions in T_C with increasing dopant concentration, both CaZrO_3 and GdScO_3 show non-linear decreases. Instead T_C is observed to be somewhat less de-stabilised, especially at low dopant concentrations, than would be expected based on tolerance factor arguments.

It is well established that the large size mis-match between Ca^{2+} and Ba^{2+} results in a high degree of localised strain in Ca-doped BaTiO_3 , causing the ferroelectric, tetragonal phase to be stabilised to higher temperatures at low dopant concentrations^[18]. This strain is able to dominate over the general size effect at low dopant concentrations promoting an increase in T_C . Size mis-match can be quantified

mathematically as a statistical variance, σ . Previous work relating variance to an increased T_c has looked only at the A-site variance^[17] which can be calculated by equation 5.1.

$$\sigma_{(r_A)}^2 = \langle r_A^2 \rangle - \langle r_A \rangle^2 \quad \text{Equation 5.1}$$

Thus for $\text{Ba}_{1-x}\text{M}_x(\text{BO}_3)$ the A-site variance can be calculated by equation 5.2^[25].

$$\sigma_{(r_A)}^2 = x \cdot (1 - x)(r_{Ba} - r_M)^2 \quad \text{Equation 5.2}$$

A large statistical variance increases strain within the lattice. Distortions to the lattice in order to relieve this strain destabilise the cubic polymorphic state, as a result T_c is generally seen to increase. The effects of having a co-dopant are less well studied at a fundamental level and bring an added complexity to understanding the causes of any changes to the electronic and structural phase transition temperatures. However B-site variance is generally considered to be of negligible importance due to its much smaller magnitude, giving it a very limited role in distorting the lattice in order to relieve strain, thus the effect is likely to be dominated by the larger A-site species.

Calculated values for the A-site variance as a function of dopant addition are shown below in figure 5.34.

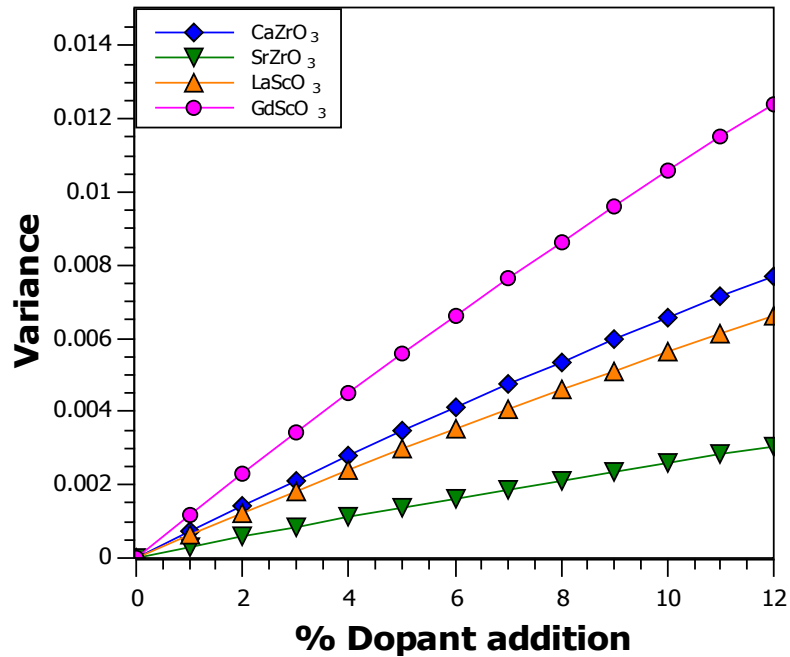


Figure 5.34: Rate of change of A-site variance as a function of dopant addition for CaZrO_3 , SrZrO_3 , LaScO_3 and GdScO_3

The addition of a variance component, caused by localised strain, to the long-range size argument (tolerance factor) could account for the fall in T_C with increasing dopant concentration being less rapid for GdScO_3 than LaScO_3 , and also for CaZrO_3 dopant addition resulting in a less rapid decrease in T_C than SrZrO_3 ^[5].

With the ionic radius of La^{3+} only 0.02 Å larger than that of Ca^{2+} , the calculated variance for LaScO_3 is very similar to that arising from the same amount of doping with CaZrO_3 , as is its tolerance factor. Thus, based on a combination of long range size effects, tolerance factors, and short range strain effects (variance) the T_C values for equally doped BaTiO_3 compositions would be expected to be very similar. However T_C is observed to be reduced in LaScO_3 -doped compositions by a considerably greater extent than with any of the other dopant pairs, with the same extent of dopant addition, figure 5.35.

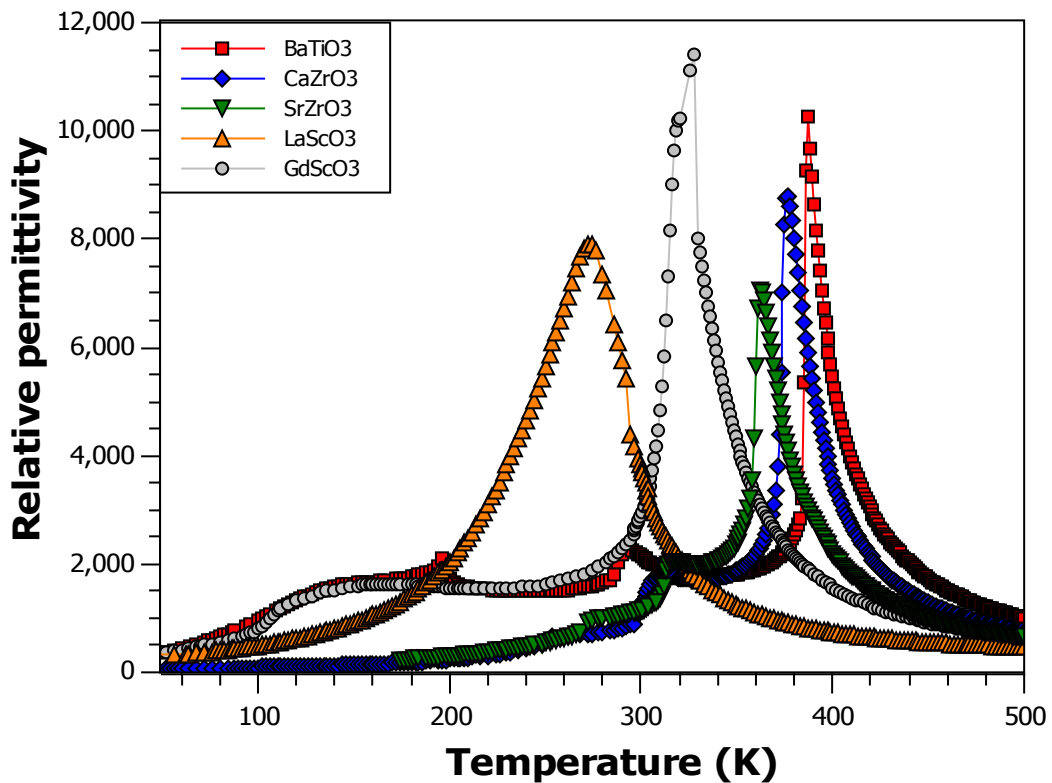


Figure 5.35: Relative permittivity as a function of temperature of BaTiO_3 and 5 % CaZrO_3 , 5 % SrZrO_3 , 5 % LaScO_3 and 5 % GdScO_3 -doped BaTiO_3

The rationalisation of this observation can be made when considering the charge of the B-site species and its role in the properties of the material. If the B-site dopant is not off-centred like Ti^{4+} , doping would cause a reduction in the number of dipoles, reducing the polarisation. This dipole dilution would therefore result in a decrease in T_C . Given the similarities in Zr^{4+} and Sc^{3+} compared to Ti^{4+} , it would be expected that should dipole dilution be occurring with Sc^{3+} addition, a similar dilution effect, reducing T_C , would be observed with Zr^{4+} addition. If the B-site dopant does displace, it would produce a dipole moment, however if the B-site species is of a lower charge than the Ti^{4+} cation it replaces, the polarisation caused by the displacement of the dopant species would be considerably lower. This would result in a more rapid reduction in T_C with an M^{3+} dopant compared to a M^{4+} dopant due to charge dilution.

As the introduction of both LaScO_3 and GdScO_3 results in a more rapid decline in T_C than doping with CaZrO_3 or SrZrO_3 , charge dilution is most likely occurring. Thus, despite having virtually the same tolerance factor and variance, LaScO_3 dopant addition is seen to result in a more rapid decrease in T_C than the analogous CaZrO_3 -doped sample. The greater variance of Gd^{3+} allows for some stabilisation of T_C compared to the larger La^{3+} cation.

5.6.2: Trends in $T_{R/O}$ and $T_{O/T}$

With the exception of GdScO_3 doping, the addition of each of the dopants causes an increase in the transition temperature for the both the lower temperature phase boundaries, $T_{R/O}$ and $T_{O/T}$. Whilst this is expected behaviour for Zr doping, and has been shown to occur in CaZrO_3 doping, no explanation has been offered of the cause of this behaviour^[15, 26-28].

The effect of adding A-site dopants generally causes a reduction in $T_{R/O}$ and $T_{O/T}$, regardless of the effect (stabilising or destabilising) on T_C , e.g. Ca^{2+} , Sr^{2+} , Pb^{2+} ^[20], La^{3+} ^[6]. However the addition of B-site species generally results in a decrease in T_C , but an increase in both the $T_{R/O}$ and $T_{O/T}$ transition temperatures, e.g. Zr, Sn,^[20] Ce^[29], Hf^[20, 30], with Sc^{3+} being one of the few exceptions where $T_{R/O}$ and $T_{O/T}$ decrease^[5]. The combination of Zr and Ca/Sr doping has shown that the stabilisation of the $T_{R/O}$ and

$T_{O/T}$ phase transitions expected from Zr doping dominates over the expected destabilisation of these phases caused by the A-site dopant^[31].

This is also the case for LaScO_3 doping, unlike in DyScO_3 ^[5] where $T_{R/O}$ and $T_{O/T}$ are destabilised. The rhombohedral and orthorhombic phases are stabilised, despite La^{3+} A-site substitution, which would normally be expected to destabilise these phases. The extent of stabilisation of the $T_{R/O}$ and $T_{O/T}$ phases, however, is considerably greater for LaScO_3 doping than either CaZrO_3 or SrZrO_3 doping.

However, this is not observed in GdScO_3 doping. Instead the tetragonal phase is observed to be stabilised to low temperatures. This will be discussed further in section 5.6.3.

5.6.3: Tetragonal stabilisation in GdScO_3 -doped BaTiO_3

It is observed that the tetragonal phase in GdScO_3 -doped compositions is stabilised to low temperatures. One mechanism by which this may be occurring could be an off-centring of gadolinium ions, made possible by the much smaller size of the gadolinium cation in relation to the A-site volume it occupies in the perovskite lattice.

Studies by Lifерович et al.^[32] into the structures of ternary lanthanide orthoscamdate perovskites, including GdScO_3 , have shown that the pure Ln -scandates, from lanthanum to holmium, form orthorhombic perovskites in the space group $Pbnm$. The orthorhombic distortion was found to generally increase across the series as unit cell size decreased with increasing Ln atomic number. The $Pbnm$ symmetry results from rotation of the ScO_6 octahedron denoted by an $a^-a^-c^+$ tilt in Glazer's notation^[33] and an antipolar displacement of the Ln species, figure 5.36, resulting in an 8-coordinate, four-fold anti-prism A-site as opposed to the more conventional 12-coordinate cube-octahedra. This effect has been attributed to the relative enlargement of the ScO_6 octahedra and reduction in the first coordination sphere of Ln^{3+} along with the expansion of the lanthanides second coordination sphere and complex orbital mixing, allowing for increased covalency. The orthorhombic distortion maximises the A-O bonds covalent character by creating several shorter A-

O bonds^[34]. This effect increases across the lanthanide series due to the lanthanide contraction causing a decrease in the ionic radii of the Ln^{3+} species resulting in an increasing relative enlargement of the ScO_6 octahedra compared with the Ln^{3+} polyhedron.

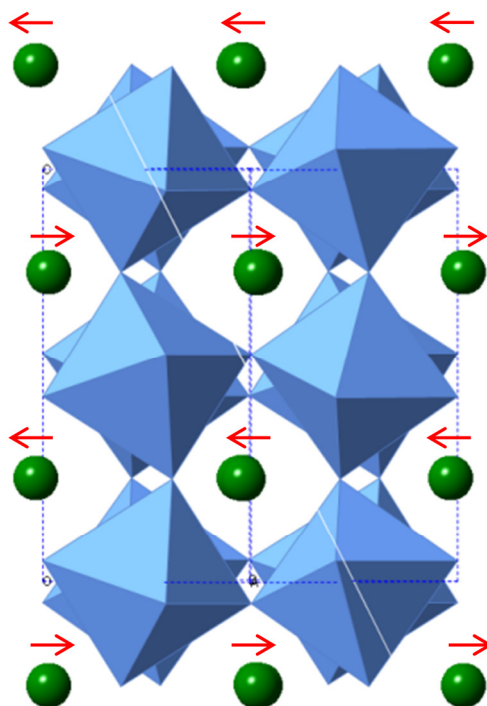
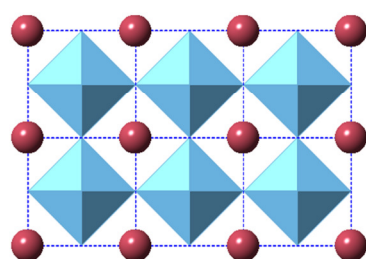
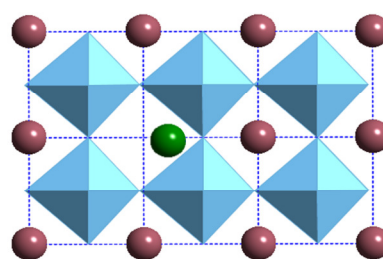


Figure 5.36: Antipolar displacement of A-site cations in $LnScO_3$ accompanied by ScO_6 polyhedra rotation, resulting in an orthorhombic distortion. Model adapted from^[32]

When a lanthanide scandate is doped into the barium titanate lattice there is a conflict as to the space group which the structure should adopt. Barium titanate generally adopts $P6_3/mmc$ (hexagonal), $Pm\bar{3}m$ (cubic), $P4mm$ (tetragonal), $Amm2$ (orthorhombic) or $R3mr$ (rhombohedral) spacegroups depending on temperature and pressure, whilst $LnScO_3$ favours a $Pbnm$ distortion with a corresponding $\bar{a}\bar{a}^+c^+$ tilt and A-site cation anti-polar displacement. At low dopant concentrations the barium titanate polymorphs are dominant. This prevents a rotation of the B-site octahedral which would require a break in symmetry and would cause a reduction in the A-site volume. However, the small size of the Gd^{3+} species relative to the Ba^{2+} and the A-site volume means that the species is able to displace from the centre of the cube-octahedron, figure 5.37. The anti-polar displacement of the A-site species observed in lanthanide scandates is possible in the tetragonal phase of barium titanate, stabilising this phase relative to each of the other phases, when this distortion would be lost.



Cubic BaTiO₃ lattice



A-site cation displacement promoting a tetragonal lattice distortion

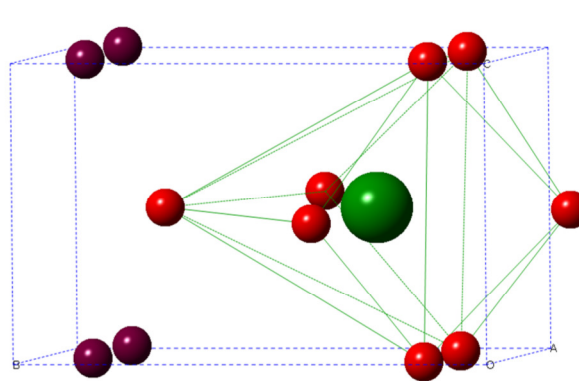
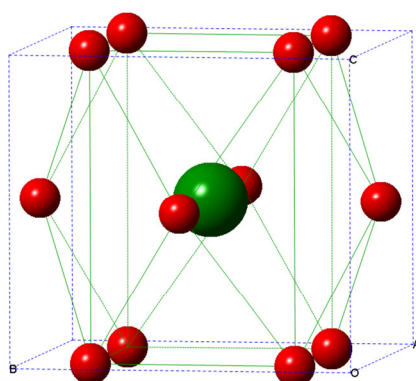


Figure 5.37: Displacement of Gd³⁺ cation, forming a 8-coordinate polyhedron and driving a tetragonal distortion to the unit cell

Though this effect may be expected to occur in the LaScO₃-doped BaTiO₃, stabilisation of the tetragonal phase to low temperatures is not observed. This is likely to be due to the effective 12-coordinate ionic radii for La³⁺ not being small enough at 1.36 Å to be able to undergo enough of a displacement from its central equilibrium position to result in a large enough polarisation to compensate for the disruption to the BaTiO₃ lattice. However, with Gd³⁺ the radius is much smaller at 1.28 Å, figure 5.38. This is small enough to allow for a large enough anti-polar displacement of the A-site to compensate for the energy cost of destabilising the BaTiO₃ cubic lattice and hence stabilises the tetragonal phase.

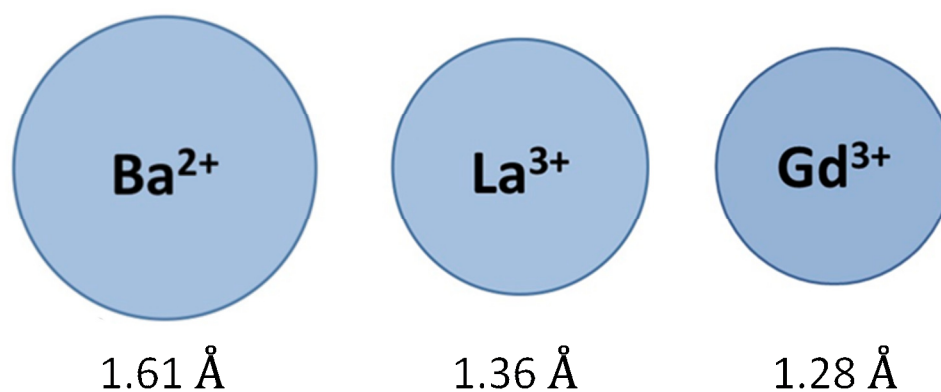


Figure 5.38: Ionic radii showing La³⁺ to be 84.5 % the radius of Ba²⁺, compared to Gd³⁺ which is 79.5 % the radius of Ba²⁺

5.6.4: Variable temperature X-ray data of coalesced peaks

The reduction of T_C accompanied by a stabilisation of the rhombohedral and orthorhombic phases brings about a coalescence of the phases resulting in one broad peak in the dielectric data. Often broad peaks are associated with diffuse phase transitions. The nature of such peaks has been greatly discussed, with peaks generally being considered as having one of two characteristic natures: either a diffuse phase transition (DPT), or a relaxor ferroelectric (RFE).

Diffuse phase transitions, DPT's, were first observed by Smolenski et al.^[35] in Sn-doped BaTiO₃ perovskites. They observed that unlike simple ferroelectric perovskites which became cubic at temperatures above T_C , some materials still exhibited piezoelectric properties at temperatures above the permittivity maximum, T_m . This phenomenon was found to be common in disordered perovskites, where the phase transition between the non-centrosymmetric and cubic structures is not an abrupt structural transition, but a gradual one which occurs over an extended temperature range with T_m generally having some frequency dependency and not coinciding with the peak in the loss data. Ferroelectrics with diffuse phase transitions are now generally termed relaxor ferroelectrics, RFE's, which have a distinctive dielectric relaxation which is frequency dependant, but behave like typical or classical ferroelectrics at low temperature^[36]. The term DPT now is now more commonly applied to ferroelectrics with broad maxima in the relative permittivity, often

exhibiting significant variation in the magnitude of the peak with frequency, but without a variation in T_C with frequency^[37].

5.6.4.1: 12% CaZrO_3

Variable temperature powder synchrotron X-ray diffraction studies were carried out on a sample of 12 % CaZrO_3 – doped BaTiO_3 , with data collected at 20 K intervals between 200 – 320 K, with additional data sets collected at 150 and 380 K. At all temperatures a series of broad peaks was observed suggesting a cubic or pseudo-cubic unit cell, figure 5.39. The shapes of the peaks were found to vary with temperature, giving rise to the possibility of some coexistence of polymorphic phases, the relative percentages of which might alter with temperature.

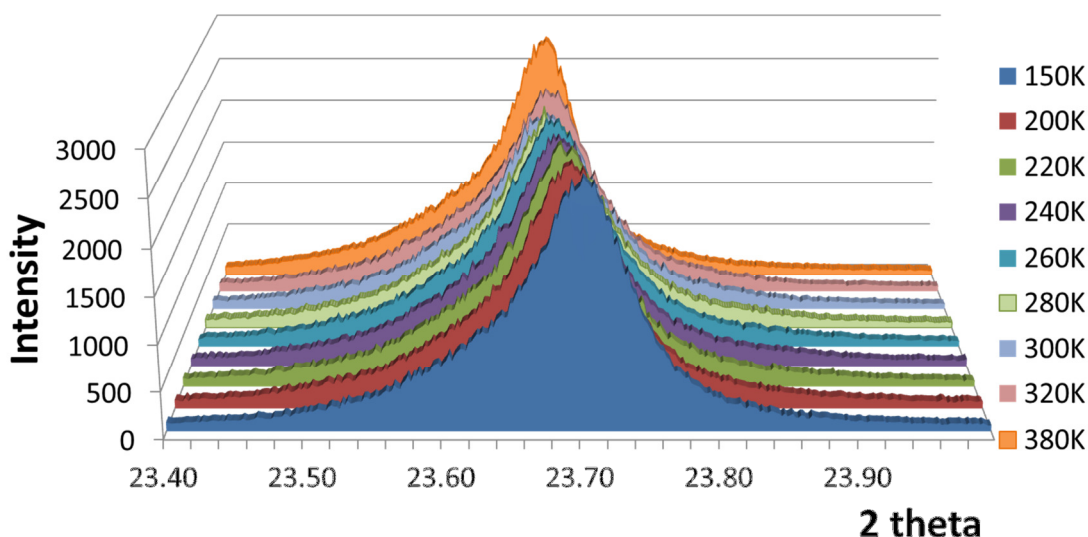


Figure 5.39: Variable temperature, synchrotron, powder X-ray diffraction data collected on a sample of 12 % CaZrO_3 -doped BaTiO_3

Models of the composition in pure cubic, tetragonal, orthorhombic and rhombohedral phases were created, with the “splitting” of each of the peak regions for the first 7 peaks noted, table 5.8 and figure 5.40. It was predicted that if the “splitting” were to increase from one phase to the next, then the composite peak seen in the experimental data should broaden, however if the “splitting” were to decrease from one phase to the next, then the peak in the experimental data should narrow.

In order for the experimental data to be considered to be a conglomerate of (up to) 4 different phases, each slightly more preferential over a particular temperature range, then the broadening and narrowing of the peaks should be harmonious, such that all the peaks width changes at a particular temperature corresponding to the same phase transition. If, however, the peaks change widths rather more arbitrarily, it would suggest that this was not the case. Effects on the peak width caused by changes in strain due to variation in the of the domain structure were not taken into account.

Table 5.8: Expected peak “splitting” for powder X-ray diffraction data for pure phase rhombohedral, orthorhombic, tetragonal and cubic perovskites taken from model X-ray data shown in appendix A5.11-A5.14

Peak angle (2θ)	Phase				
	Rhombohedral	Orthorhombic	Tetragonal	Cubic	[hkl]
11.75	1	2	2	1	[100]
16.7	2	2	2	1	[110]
20.5	2	2	1	1	[111]
23.7	1	2	2	1	[200]
26.5	2	3	3	1	[210]
29.0	3	3	2	1	[211]
33.8	2	3	2	1	[220]

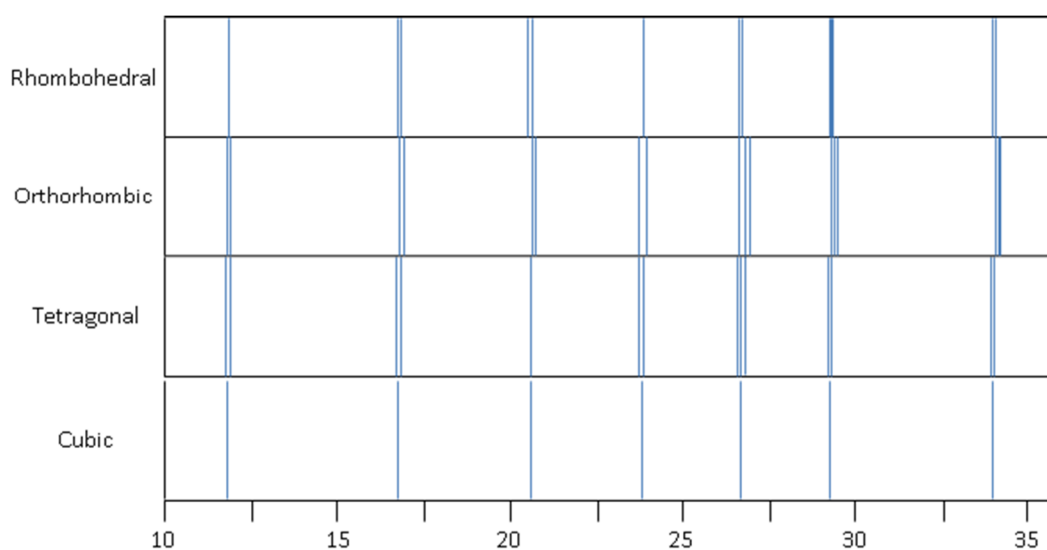


Figure 5.40: Graphical representation of varying peak splitting with crystal class

Analysis was carried out by recording the full width at half maxima (FWHM) for each of the first 7 peaks at each temperature. It was expected that the peaks would broaden with increasing 2θ due to instrumental and sample broadening, and in general this is what was observed, figure 5.40. However, it was noted that this effect was not linear, as would be expected for a material with a cubic or “pseudo- cubic” crystal class, and that some peaks were instead getting narrower with increasing 2θ . The peaks that this occurred for, and the temperature range over which this occurred, was also found to vary.

From the dependence of the FWHM on 2θ , figure 5.41, it becomes clear that at the highest and lowest temperatures of data collection, the FWHM was found to vary approximately linearly with 2θ . At intermediate temperatures, although a general trend of increasing peak width with increasing θ was observed, a significant non-linearity was observed. A gradual, but consistent change to the plot profile, in the form of a “hump” was observed with increasing temperature, where several peaks were found to be broader than would otherwise be expected. This suggests that at these intermediate temperatures there may be changes in the polymorphic phase of the material. As the polymorphic phase of the material changes, the pattern of peak splitting would be expected to change as shown in figure 5.40. This could account for the unexpected peak broadening/narrowing. The FWHM is also shown for the first seven peaks as a function of temperature in figure 5.42, with the expected peak splitting shown alongside the data for each of the four crystallographic phases.

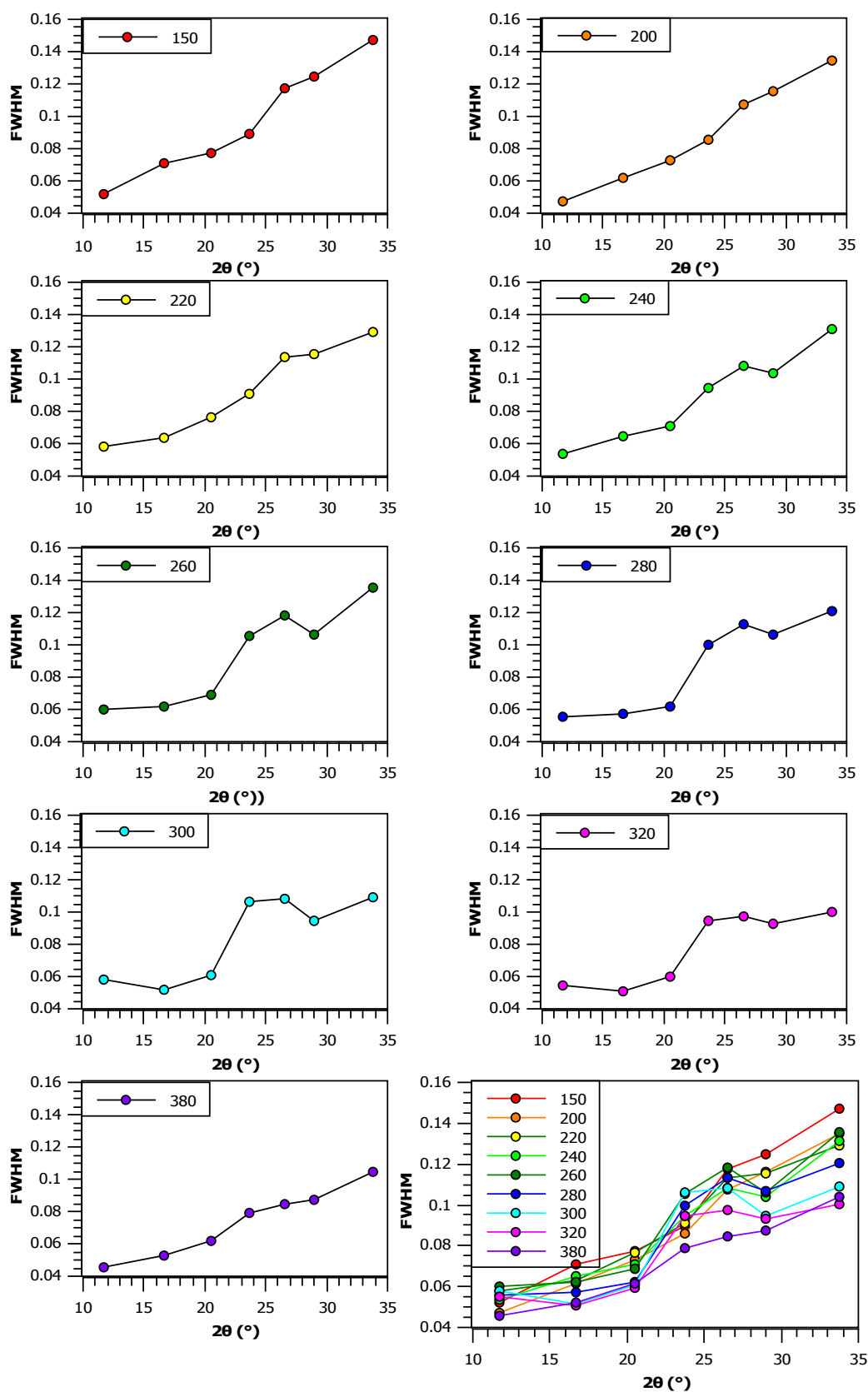


Figure 5.41: Full width at half maxima as a function of 2θ for 12 % CaZrO_3 -doped BaTiO_3 , collected at 150, 200, 220, 240, 260, 280, 300, 320 and 380K (left to right) and combined

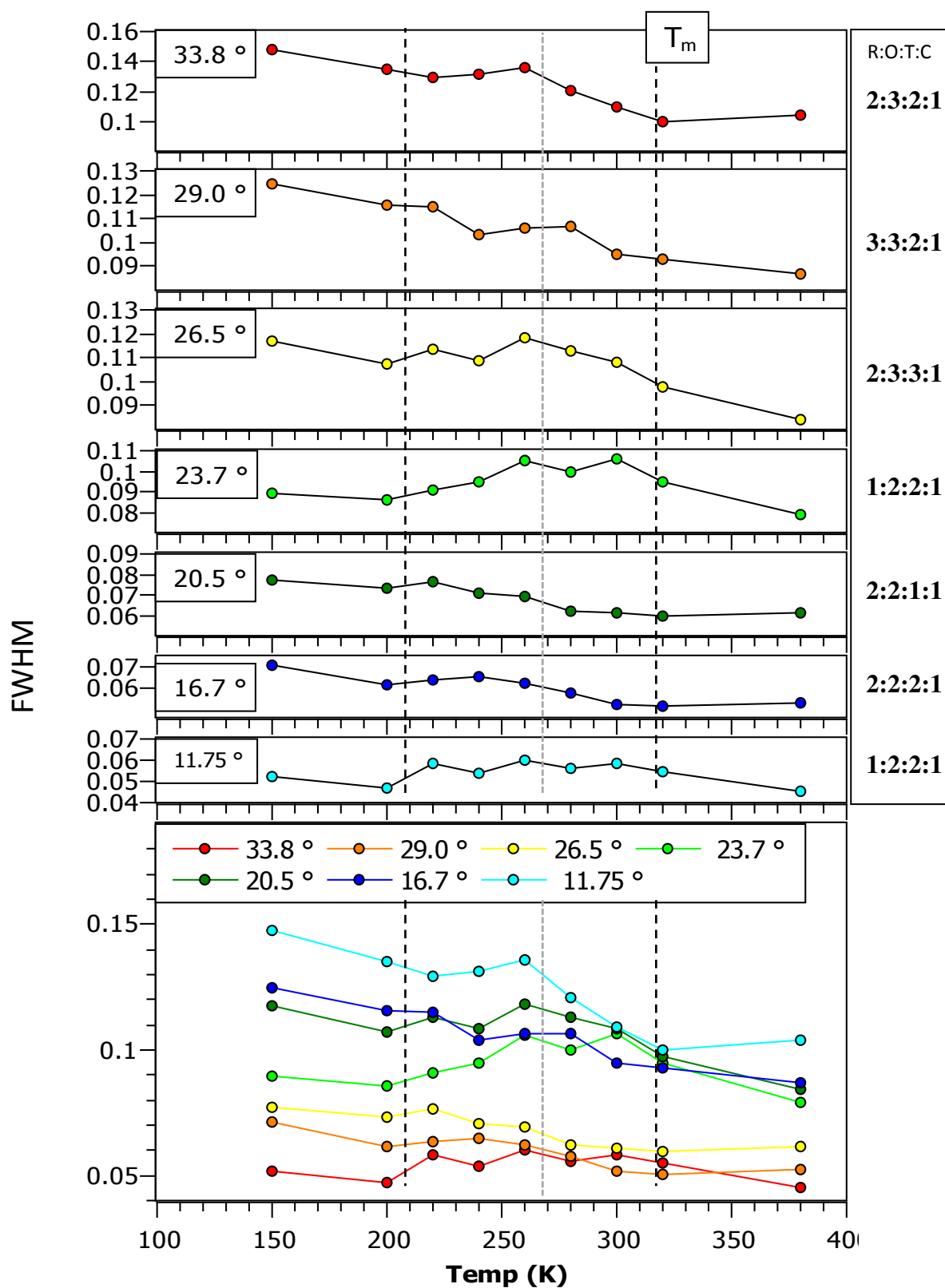


Figure 5.42: Full width at half maxima as a function of temperature for 12 % CaZrO_3 -doped BaTiO_3 , for peaks at 33.8, 29.0, 26.5, 23.7, 20.5, 16.7 and 11.75 ° 2θ , and combined (from top to bottom). R:O:T:C represents the number of reflections expected in each polymorphic phase

Regardless of whatever phases may be in existence below T_m , above this temperature it would be expected that the system has a cubic crystal class. All of the peaks would then be expected to be sharp, single peaks. Thus above T_m the FWHM would be expected to be low. If, on cooling a phase change does occur at T_m to either one, or a mixture of, non-cubic phase(s), an increase in the FWHM would be expected. The presence of a broad, asymmetric peak suggests that the composition is not of a single polymorphic phase at any point. If, however, more of the sample adopts a tetragonal crystal class as it is cooled through T_m , it would be expected that all the peaks would markedly broaden, except the peak at 20.5° , which is a single peak in both the cubic and tetragonal phases. When studying the data shown in figure 5.42, it is observed that apart from the 20.5° peak, which doesn't start to significantly broaden until it gets to 260 K and below, all the peaks start to broaden at temperatures below 320 K, allowing for this to be defined as the T_m of the material (table 5.2). This is consistent with $T_m = 320$ K as determined from dielectric data, figure 5.7.

Although more difficult to discern, the precise point at which the composition appears to be more orthorhombic than tetragonal, it does appear that a phase change may be occurring at ~ 260 K. This is most clearly observed in the 20.5° peak, which undergoes a splitting change from 1 \rightarrow 2 through the tetragonal to orthorhombic transition and hence should have a peak broadening.

A reduction in the FWHM would be expected to be observed in most of the peaks as the system shifts from an orthorhombic to rhombohedral crystal class, either due to a reduction in the number of reflections contributing to the peak, or due to a narrowing of the degree of splitting, figure 5.40. This can clearly be observed between the 200 and 220 K data sets.

It can therefore be suggested that, at the coalescence of the polymorphic phases shown in the dielectric data, figure 5.7, it is probable that the relative energies of each of the phases is similar and that all of the phases are in co-existence. However, though similar, there is likely to be some finite difference in the stabilities of each phase leading to non-equivalent amounts of each phase being present. As the

temperature is altered, the relative stabilities of each phase are likely to change resulting in a varying amount of each polymorphic phase; cubic, tetragonal, orthorhombic and rhombohedral. This is consistent with the first order nature of each of the associated phase transitions.

5.6.4.2: 5% LaScO₃

The 5 % LaScO₃-doped BaTiO₃ composition was found to have a coalesced peak in the dielectric spectroscopy data. However, analysis of the variable temperature powder synchrotron X-ray diffraction data showed it has distinct, different crystallographic classes at certain temperatures; namely it was found to have a cubic space group at high temperatures and a rhombohedral space group at low temperature, figure 5.43.

This suggests that this composition is more akin to the 12 % SrZrO₃ having gone past the triple point composition, which must exist for the LaScO₃-doped BaTiO₃ somewhere between 2-5 % dopant concentration. Data collected at 250 and 275 K were refined as a two phase cubic/tetragonal or rhombohedral/tetragonal mixture respectively. However, the data were very noisy and the fits were far from ideal, suggesting that some mixture of cubic, tetragonal, orthorhombic and/or rhombohedral existed in this region, but could not be fully identified.

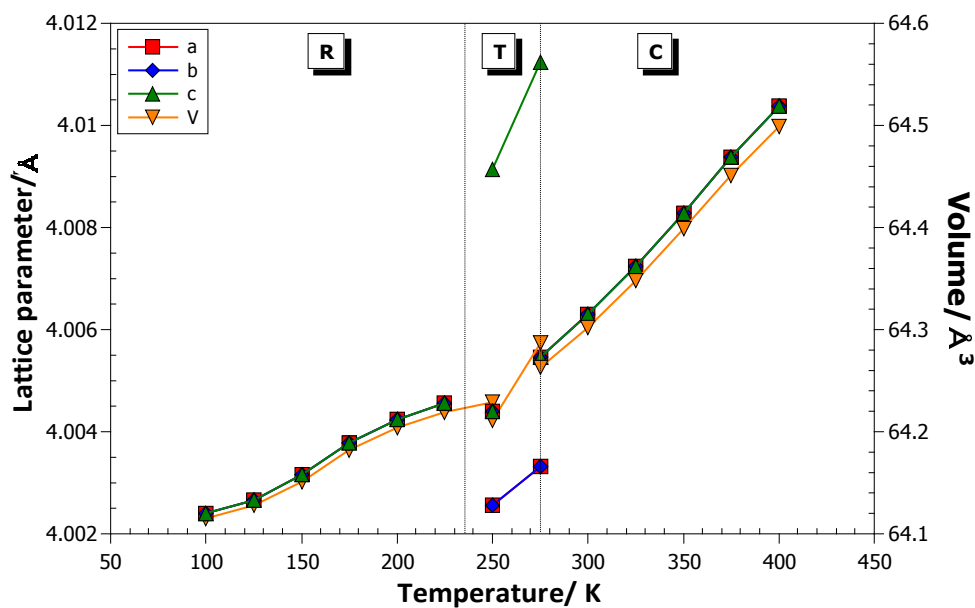


Figure 5.43: Lattice parameters as volume of 5 % LaScO₃ – BaTiO₃ as a function of temperature as determined by analysis of variable temperature powder X-ray diffraction data

There has been much debate over the years as to the polymorphic phase changes that occur at the MPBs and PPBs in perovskite ferroelectrics. Whilst some papers claim that the orthorhombic phase is simply omitted, others claim that this phase is present, but over very narrow temperature ranges^[38]. Other work shows the presence of a monoclinic phase which has also been shown to exist at the MPB in PZT^[39, 40]. Due to the narrow temperature ranges over which these phases exist, it is common for discrepancies to exist in the literature, where they have been missed by some experiments. The fact that the transitions tend to be first order, resulting in some phase co-existence, also hinders the observation of intermediate phases. There is also evidence to suggest that the grinding process required for converting the sintered pellets into a fine powder for powder X-ray or neutron diffraction increases the strain in the material, which can lead to significant peak broadening, which masks peak splitting which might otherwise show the presence of other phases^[21].

5.7: Hysteresis

Ferroelectric, polarisation-field (P-E), hysteresis measurements were carried out on each sample at room temperature. In each case the presence of a P-E hysteresis loop (chapter 1, section 1 and chapter 2, section 5) confirmed the ferroelectric nature of each composition. This data is collated in appendix 5, figures A5.15-A5.20 and tables A5.1-A5.6.

A more in-depth variable temperature analysis was carried out on selected pellets to study the effects of dopant addition on the ferroelectric properties. These measurements allowed for the maximum polarisation of each material to be established, was able to probe the hard-soft nature of the materials and how different dopants, as well as the level of doping, affected these characteristics. It was not possible to carry out an in-depth temperature dependant analysis of each of the materials due to temperature constraints of the apparatus, which was limited to measurements taken at room temperature and above. Compositions which had T_C at, or below, room temperature were therefore not suitable for this form of analysis.

Temperature dependent data are presented for the CaZrO_3 -doped BaTiO_3 series of compositions, all of which had T_C above room temperature.

Hysteresis data was collected as a function of temperature for each of the CaZrO_3 -doped materials. Room temperature data collected on the 2% CaZrO_3 - BaTiO_3 sample are shown in figure 5.44. The loop is observed to be fairly square in shape with a low degree of canting, suggesting a fairly hard response similar to that of BaTiO_3 , a room temperature hysteresis loop of which is also shown in figure 5.44.

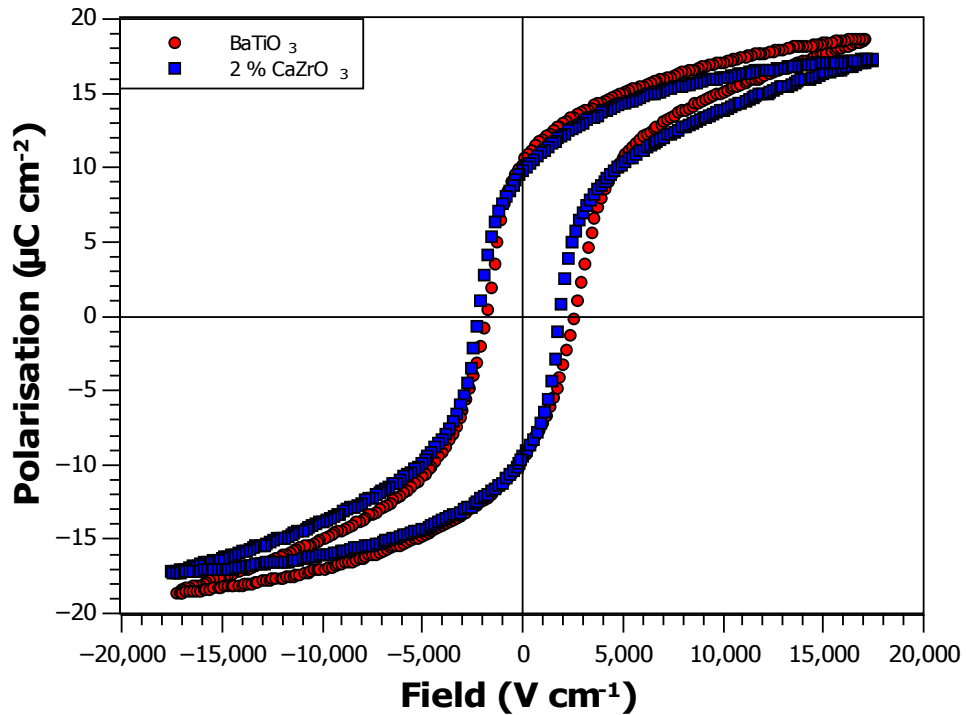


Figure 5.44: Room temperature hysteresis loops of BaTiO_3 and 2 % CaZrO_3 -doped BaTiO_3 collected at 1 Hz

Doping BaTiO_3 with 2 % CaZrO_3 is seen to cause a slight reduction in the maximum polarisation of the material for a given field, but there is little change in the hard-soft nature of the material, or the average coercive field, (V_{C+} and V_{C-} as defined in chapter 3.8)

At high temperatures a softer nature was observed, figure 5.45, along with a lower maximum polarisation which is to be expected due to the high degree of fluxionality of the structure of the material above T_C . A clear change in the form of the loop is observed between 120-134 °C, as the loop changes from an almost linear loop when in the high temperature fluxional state to that of a more typical ferroelectric

hysteresis loop below 120 °C. T_C for this composition is known to be ~ 113 °C, as given in table 5.2. The fact that ferroelectric hysteresis behaviour is observed slightly above this temperature is likely to be due to the large fields being applied. When close to T_C a large field can be made to induce ferroelectric-like behaviour, overcoming the thermally-induced randomisation of the dipoles.

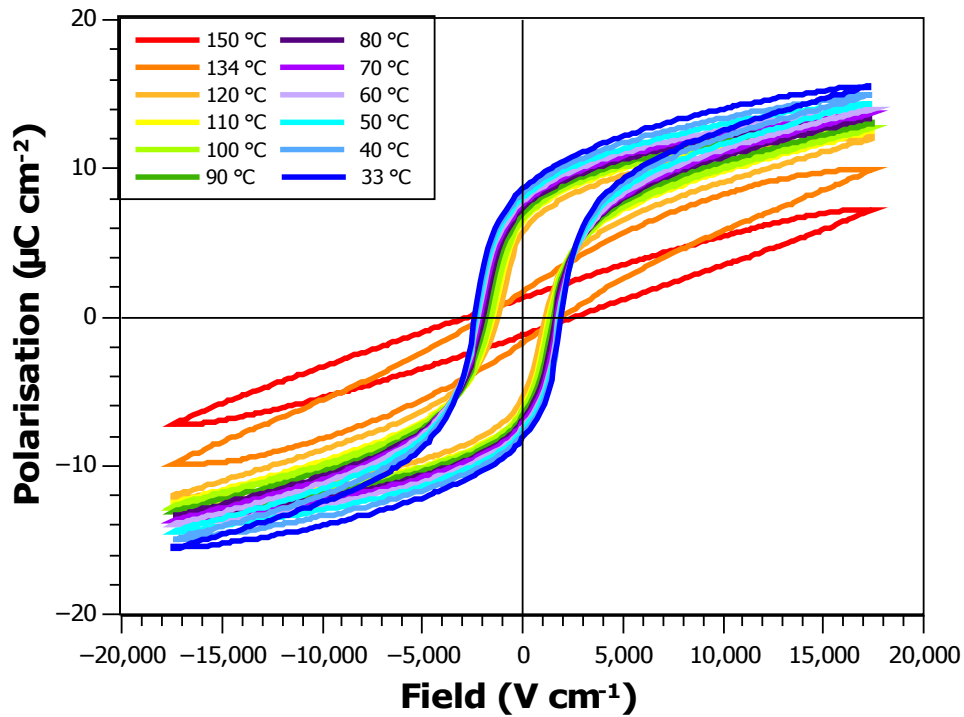


Figure 5.45: Hysteresis loops of 2 % CaZrO_3 -doped BaTiO_3 as a function of temperature, with the data collected at 1 Hz on cooling

It should be noted that the above data was collected by heating the material and collecting measurements during the cooling process. It is observed that $P_{\text{max+}}$ is increased slightly as a result of the poling process, by around $1 \mu\text{C cm}^{-2}$. This is due to the fact that the measurements require the use of large fields to be applied to the sample. As the process is repeated it can cause a partial poling of the material, increasing the number of domains aligned with the field, especially when the field is applied at temperatures above the Curie temperature, when the material is in a more fluxional (paraelectric) state.

As the dopant concentration was increased it was observed that the materials became softer, with a lower maximum polarisation per square centimetre, figure 5.46.

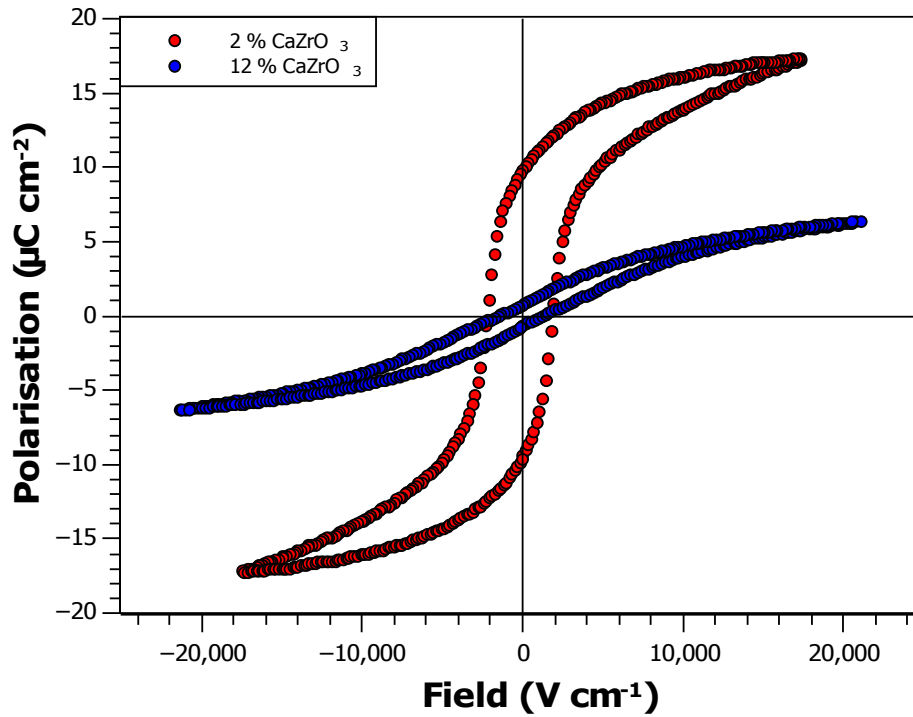


Figure 5.46: Increase in canting of the loop observed in more high doped compositions, along with a reduction in P_{\max} . Data collected at 1 Hz

The increase from 2 % CaZrO_3 doping to 12 % CaZrO_3 doping caused a reduction in $P_{\max+}$ from $17.23 \mu\text{C cm}^{-2}$ in the 2 % doped sample, to $6.31 \mu\text{C cm}^{-2}$ in the 12 % doped sample. The loop is also noted to be considerably slimmer and more canted. Given that the area of the loop is proportional to the hysteresis loss^[41], this shows that as the dopant level increases the power dissipated as thermal loss is decreased. The fact that the hysteresis loop arising from the more heavily doped sample is less “square” implies that there is a less abrupt change from one dipole direction to the other as the electric field is reversed^[20]. Some increase in the canting observed in the 12 % CaZrO_3 -doped composition may also be due to the material being closer to T_m at room temperature.

Heating the 12 % CaZrO_3 -doped composition and studying how the hysteresis loop changed on cooling, figure 5.47, showed the present of a “lossy” loop at high temperatures, becoming more a more typical ferroelectric hysteresis loop at lower temperatures.

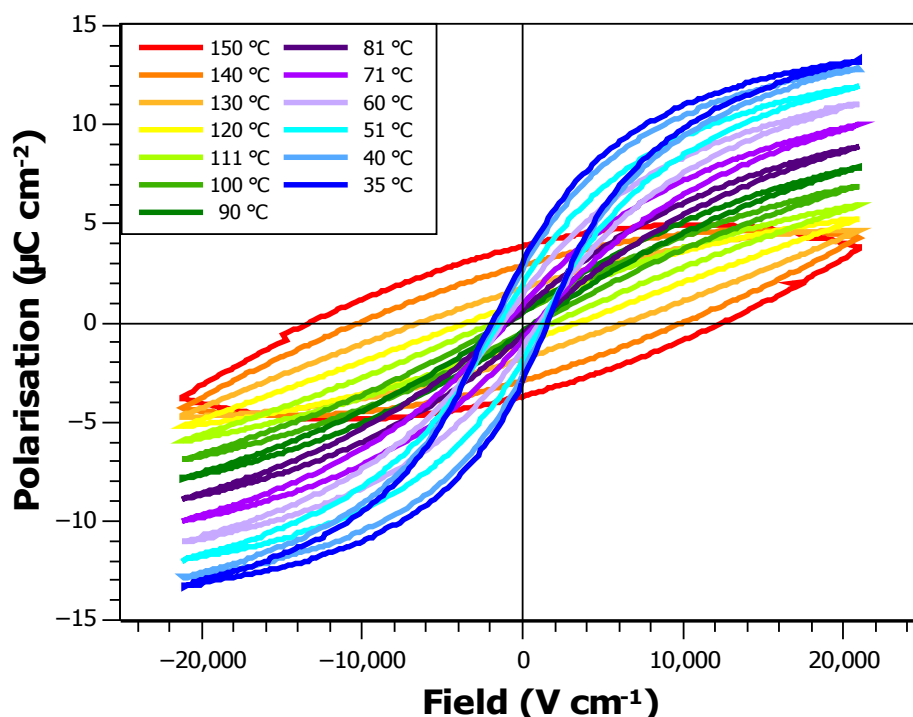


Figure 5.47: Hysteresis loops of 12 % CaZrO_3 -doped BaTiO_3 as a function of temperature, with the data collected on cooling at 1 Hz

A typical hysteresis loop was present above the known Curie temperature of the material, 47°C , with the loop being observable from about 110°C . The fact that the loop was observed at a temperature further above T_c than in the 2 % CaZrO_3 -doped composition, suggests that the addition of the dopant has made the system more pliant. There is also a significant increase in P_{max} between the initial room temperature hysteresis loop and the loop observed upon cooling. This suggests that the material was partially poled to a greater extent than the 2 % sample during data collection. This is likely to be partially due to the fact the T_c for this sample is lower, meaning that the field was more often applied when the system was in a fluxional state and is also consistent with the material being more pliant. However, even taking this into account, the composition is still found to have a lower hysteresis loss and be somewhat softer than the lower doped compositions.

Similar effects as a result of dopant addition were observed for BaTiO_3 -doped with SrZrO_3 , LaScO_3 and GdScO_3 (see appendix 5, figures A5.15-A5.20 and tables A5.1-A5.6), where such data could be obtained.

5.8: Conclusions

The doping of barium titanate with CaZrO_3 , SrZrO_3 , LaScO_3 and GdScO_3 causes a reduction in T_C , but this reduction is considerably less than the reduction expected due to size effects based on tolerance factor arguments alone. The degree of decrease in T_C can be suppressed due to high strain caused by size mis-match between the A-site species. This strain can be quantified by the statistical size variance of the A-site cations, and can be a dominant factor in determining T_C , particularly in instances where the size mis-match is large, such as in CaZrO_3 and GdScO_3 doping. The CaZrO_3 and LaScO_3 -doped samples have very similar cation sizes and, therefore, similar tolerance factors and A-site variance, *i.e.* long range (average) size effects and short range strain. Comparing these samples showed that aliovalent doping with a +3 B-site cation resulted in a significant lowering of T_C . This can be rationalised by a dilution of the polarisation at the B-site caused by off-centring of the lower charged Sc^{3+} cation compared to the Ti^{4+} (charge dilution). An alternate theory for the reduction in T_C caused by dopant addition is that of dipole dilution. This assumes that the dopant B-site species is not off-centred at all, reducing the total number of B-site species involved in creating the polarisation. Given the similarity between the size of Zr^{4+} and Sc^{3+} it would be expected that either both species would be unable to move off-centre and contribute to the dipole moment or neither. Thus, as T_C fall substantially quicker with the Sc^{3+} species than Zr^{4+} , the effect of doping onto the B-site can be described as charge dilution as opposed to dipole dilution, in which a similar reduction would be expected for an equal percentage of dopant, regardless of charge.

In the case of GdScO_3 doping, the tetragonal phase is found to be stabilised to low temperature as a result of anti-polar displacement of the A-site favouring the tetragonal phase. This behaviour is also seen in the pure LnScO_3 compounds where it is accompanied by an $a^-a^-c^+$ tilt, resulting in $Pbnm$ orthorhombic symmetry; however this tilt is inhibited by the surrounding barium titanate lattice in lightly doped compositions and thus it is the tetragonal and not orthorhombic phase that is observed to be stabilised in the GdScO_3 -doped BaTiO_3 compositions.

The presence of polymorphic phase coexistence at phase boundaries as seen in variable temperature powder synchrotron X-ray diffraction data confirms the phase transitions as being first order. This is further corroborated by data collected on coalesced peaks which show that having just reached the point of coalescence in the 12 % CaZrO_3 -doped BaTiO_3 , all four phases coexist, with their ratios being temperature dependant. As the level of doping increases beyond this initial point of phase coalescence, clear cubic and rhombohedral phases are observed as would be expected, but the change from cubic to rhombohedral crystal class still progresses through some intermediate state, as seen in the 5 % LaScO_3 –95 % BaTiO_3 data sets, with this intermediate state unable to be fully identified due to peak broadening and the presence of multiple phases at the boundary^[21].

Ferroelectric properties were observed in each of the materials, regardless of dopant species or dopant concentration. However, it was generally found that the addition of dopant species resulted in a lowering of the maximum polarisation, and a canting of the hysteresis loops. This suggests that the materials become softer ferroelectrics as the dopant level is increased. Soft ferroelectric hysteresis loops imply a more gradual re-orientation of the domains by reversing the direction of the applied electric field.

In each case a clear distinction was observed between the hysteresis loops obtained from the materials above and below T_c with the high temperature measurements showing that the material is no longer truly ferroelectric, *i.e.* it doesn't have a spontaneous polarisation, which can be made to switch direction by the application of an appropriate electric field. Instead the polarisation is field induced. Though not truly ferroelectric, the application of a large electric field was able to result in an open loop with a non-negligible polarisation. This is consistent with a slight distortion of the cation lattice away from the non-ferroelectric cubic lattice equilibrium positions resulting in a polarisation. At temperatures slightly above T_c this effect was great enough to produce more classical ferroelectric ceramic hysteresis loops. Induced hysteresis loops above T_c was first noted in single crystal BaTiO_3 by Merz in 1953^[42], however he noted the presence of a "pinched" or double hysteresis loop. Differing models have ascribed this behaviour to a change in the order of the

tetragonal/cubic transition, aging, or due to some acceptor impurities^[42, 43]. It is not clear why the loops obtained above T_C in this study do not exhibit the pinched behaviour observed by Merz and others^[42].

References

1. Kwei, G.H., A.C. Lawson, and S.J.L. Billinge, *Structures of the Ferroelectric Phases of Barium Titanate*. J. Phys. Chem-US, 1993. **97**: p. 2368-2377.
2. Shirane, G., H. Danner, and R. Pepinsky, *Neutron Diffraction Study of Orthorhombic BaTiO₃*. Phys. Rev., 1957. **105**(3): p. 856-860.
3. Evans, H.T., *The crystal structure of tetragonal barium titanate*. Acta Cryst. , 1951. **4**: p. 377.
4. Zhang, Q., T. Cagin, and W.A. Goddard III, *The ferroelectric and cubic phases in BaTiO₃ ferroelectrics are also antiferroelectric*. P. Natl. Acad. Sci. USA, 2006. **103**(40): p. 14695-14700.
5. Ferrarelli, M.C., C.C. Tan, and D.C. Sinclair, *Ferroelectric, electrical, and structural properties of Dy and Sc co-doped BaTiO₃*. J. Mater. Chem., 2011. **21**(17): p. 6292-6299.
6. Morrison, F.D., D.C. Sinclair, and A.R. West, *Doping mechanisms and electrical properties of La-doped BaTiO₃ ceramics*. Int. J. Inorg. Mater., 2001. **3**(8): p. 1205-1210.
7. Li, W., et al., *Enhancement of the temperature stabilities in yttrium doped (Ba_{0.99}Ca_{0.01})(Ti_{0.98}Zr_{0.02})O₃ ceramics*. J. Alloy. Comp., 2012. **531**: p. 46-49.
8. Ramam, K. and M. Lopez, *Barium modified lead lanthanum strontium zirconium niobium titanate for dielectric and piezoelectric properties*. J. Eur. Ceram. Soc., 2007. **27**(10): p. 3141-3147.
9. Yun, S.N., et al., *Dielectric properties Ca-substituted barium strontium titanate ferroelectric ceramics*. Solid State Communications, 2007. **143**(10): p. 461-465.
10. Freeman, C.L., et al., *The Influence of A-Site Rare Earth Ion Size in Controlling the Curie Temperature of Ba_{1-x}RE_xTi_{1-x/4}O₃*. Adv. Funct. Mater., 2013. **23**(4): p. 491-495.
11. Simon, A., J. Ravez, and M. Maglione, *The crossover from a ferroelectric to a relaxor state in lead-free solid solutions*. J. Phys-Condens. Mat., 2004. **16**(6): p. 963-970.
12. Unruan, M., et al., *Changes in dielectric and ferroelectric properties of Fe³⁺/Nb⁵⁺ hybrid-doped barium titanate ceramics under compressive stress*. J. Appl. Phys., 2008. **104**(12).

13. Gillot, C., et al., *Microscopic origin of the PTC effect in niobium-doped barium titanate*. J. Am. Ceram. Soc., 1997. **80**(4): p. 1043-1046.
14. Mitsui, T. and W.B. Westphal, *Dielectric and X-ray studies of $\text{Ca}_x\text{Ba}_{1-x}\text{TiO}_3$ and $\text{Ca}_x\text{Sr}_{1-x}\text{TiO}_3$* . Phys. Rev., 1961. **124**(5): p. 1354.
15. Ren, X. and W. Lui, *Non-Lead-Type piezoelectric Material*, N.I.f.M.S. [JP], Editor. 2009: Japan: 054540.
16. Kumar, A., A.S. Verma, and S.R. Bhardwaj, *Prediction of Formability in Perovskite-Type oxides*. The Open Applied Physics Journal, 2008. **1**: p. 11-19.
17. Attfield, J.P., *A simple approach to lattice effects in conducting perovskite-type oxides*. Chem. Mater., 1998. **10**(11): p. 3239-3248.
18. Sinclair, D.C. and J.P. Attfield, *The influence of A-cation disorder on the Curie temperature of ferroelectric ATiO_3 perovskites*. Chem. Commun., 1999(16): p. 1497-1498.
19. Shannon, R.D., *Revised Effective Ionic Radii and Systematic Studies of Interatomic Distances in Halides and Chacogenides*. Acta Cryst. A, 1976. **32**(751).
20. Jaffe, B., W.R. Cook, and H. Jaffe, *Piezoelectric Ceramics*. 1971: Academic Press London.
21. Aksel, E., et al., *Monoclinic crystal structure of polycrystalline $\text{Na}_{0.5}\text{Bi}_{0.5}\text{TiO}_3$* . Appl. Phys. Lett., 2011. **98**.
22. Cernea, M., et al., *Structural and optical characterization of sol-gel derived Tm-doped BaTiO_3 nanopowders and ceramics*. Curr. Appl. Phys., 2013. **13**(1): p. 137-141.
23. Hench, L.L. and J.K. West, *The sol-gel process*. Chem. Rec., 1990. **90**(1): p. 33-72.
24. Jaffe, B. and W.R. Cook Jr, *Piezoelectric ceramics*, J.P. Roberts, Editor. 1971. p. 100.
25. Attfield, J.P., *'A' cation control of perovskite properties*. Cryst. Eng., 2002. **5**: p. 427-438.
26. Damjanovic, D., *Ferroelectric, dielectric and piezoelectric properties of ferroelectric thin films and ceramics*. Rep. Prog. Phys., 1998. **61**(9): p. 1267-1324.

27. Favarim, H.R., et al., *Phase-transition studies of $Ba_{0.90}Ca_{0.10}(Ti_{1-x}Zr_x)O_3$ ferroelectric ceramic compounds*. Phys. Status Solidi A, 2010. **207**(11): p. 2570-2577.
28. Wu, J., et al., *Sintering Temperature - Induced Electrical properties of $(Ba_{0.90}Ca_{0.10})(Ti_{0.85}Zr_{0.15})O_3$ Lead-free Ceramics*. Mater. Res. Bull., 2010.
29. Ang, C., Z. Jing, and Z. Yu, *$CaZrO_3$ or $SrZrO_3$* J. Phys-Condens. Mat., 2002. **14**: p. 8901-8912.
30. Avrahami, Y. and H.L. Tuller, *Improved electromechanical response in rhombohedral $BaTiO_3$* . J. Electroceram., 2004. **13**(1-3): p. 463-469.
31. Su-Wei Zhang, H.Z., Bo-Ping Zhang, Sui Yang, *Phase transition behavior and piezoelectric properties of lead-free $(Ba_{0.95}Ca_{0.05})(Ti_{1-x}Zr_x)O_3$ ceramics*. 2010.
32. Liferovich, R.P. and R.H. Mitchell, *A structural study of ternary lanthanide orthoscandate perovskites*. J. Solid State Chem., 2004. **177**(6): p. 2188-2197.
33. Glazer, A.M., *Classification of tilted octahedra in perovskites*. Acta Cryst. B, 1972. **B 28**(NOV15): p. 3384-&.
34. Woodward, P.M., *Octahedral tilting in perovskites .2. Structure stabilizing forces*. Acta Cryst. B, 1997. **53**: p. 44-66.
35. Smolensky, G.A., *Physical Phenomena in Ferroelectrics with Diffused Phase Transition*. J. Phys. Soc. Jpn., 1970. **28**: p. 26-37.
36. Cross, L.E., *Piezoelectricity*, in Springer Series Mate. 2008. p. 131-155.
37. Fundora, A., et al., *Diffuse phase transitions in ferroelectric ceramics*. J. Non-Cryst. Solids, 1998: p. 567-569.
38. Keeble, D.S., et al., *Revised structural phase diagram of $(Ba_{0.7}Ca_{0.3}TiO_3)$ - $(BaZr_{0.2}Ti_{0.8}O_3)$* Appl. Phys. Lett., 2013. **102**(092903).
39. Noheda, B., et al., *The monoclinic phase in PZT: New light on morphotropic phase boundaries*, in AIP Conf. Proc. 2000. p. 304-313.
40. Noheda, B., et al., *A monoclinic ferroelectric phase in the $Pb(Zr_{1-x}Ti_x)O_3$ solid solution*. Appl. Phys. Lett., 1999. **74**(14): p. 2059-2061.
41. Moulson, A.J. and J.M. Herbert, *Electroceramics*. 1997: Chapman & Hall.
42. Merz, W.J., *Double Hysteresis Loop of $BaTiO_3$ at the Curie Point*. Phys. Rev., 1953. **91**(3): p. 513-517.
43. Kliem, H., A. Leschhorn, and T. Edtbauer, *A model for the double loop of ferroelectric polarization close to T_C* . J. Appl. Phys., 2013. **113**.

Chapter 6: Microstructural analysis and high temperature immittance spectroscopy

As discussed in chapter 4, the microstructure of a composition plays a significant role in the properties of the material. By the use of high temperature immittance and scanning electron microscopy (SEM) data analysis it is possible to probe the microstructure of the materials studied in chapter 5 in order to better understand their properties. Whilst chapter 5 presented information on the systematic variation in low temperature dielectric properties, this chapter will present the effects of doping on the high temperature conduction processes.

6.1: High temperature immittance spectroscopy

As explained in chapter 2, immittance data can be analysed by modelling the data as a series of parallel RC elements, each of which corresponds to a distinct electro-active region in the material, the most common components being bulk and grain boundary.

The bulk response, being transgranular, is expected to have a lower capacitance than the grain boundary response, which is modelled as a thin layer, intergranular region. Thus it is often possible to separate out the components of each using high temperature immittance data due to the differing time constants associated with each region.

At low temperatures the resistances of the materials studied are too high to be measured using the apparatus available, such that whilst it is possible to study the total capacitance as a function of frequency, it is not possible to discern any useful information from the complex plane or spectroscopic plots, meaning that it is not possible to extract bulk and grain boundary data. At high temperatures the resistance falls resulting in lower time constants and consequently the relaxation frequency increases, shifting it into the observable frequency range of the apparatus.

This means that it generally becomes possible to extract resistance and capacitance data from immittance data collected at high temperature^[1].

6.1.1: SrZrO₃ -doped BaTiO₃

Immittance data was collected on each of the SrZrO₃-doped BaTiO₃ compositions studied in chapter 5, with example complex plane plots depicting both modulus and impedance data shown below.

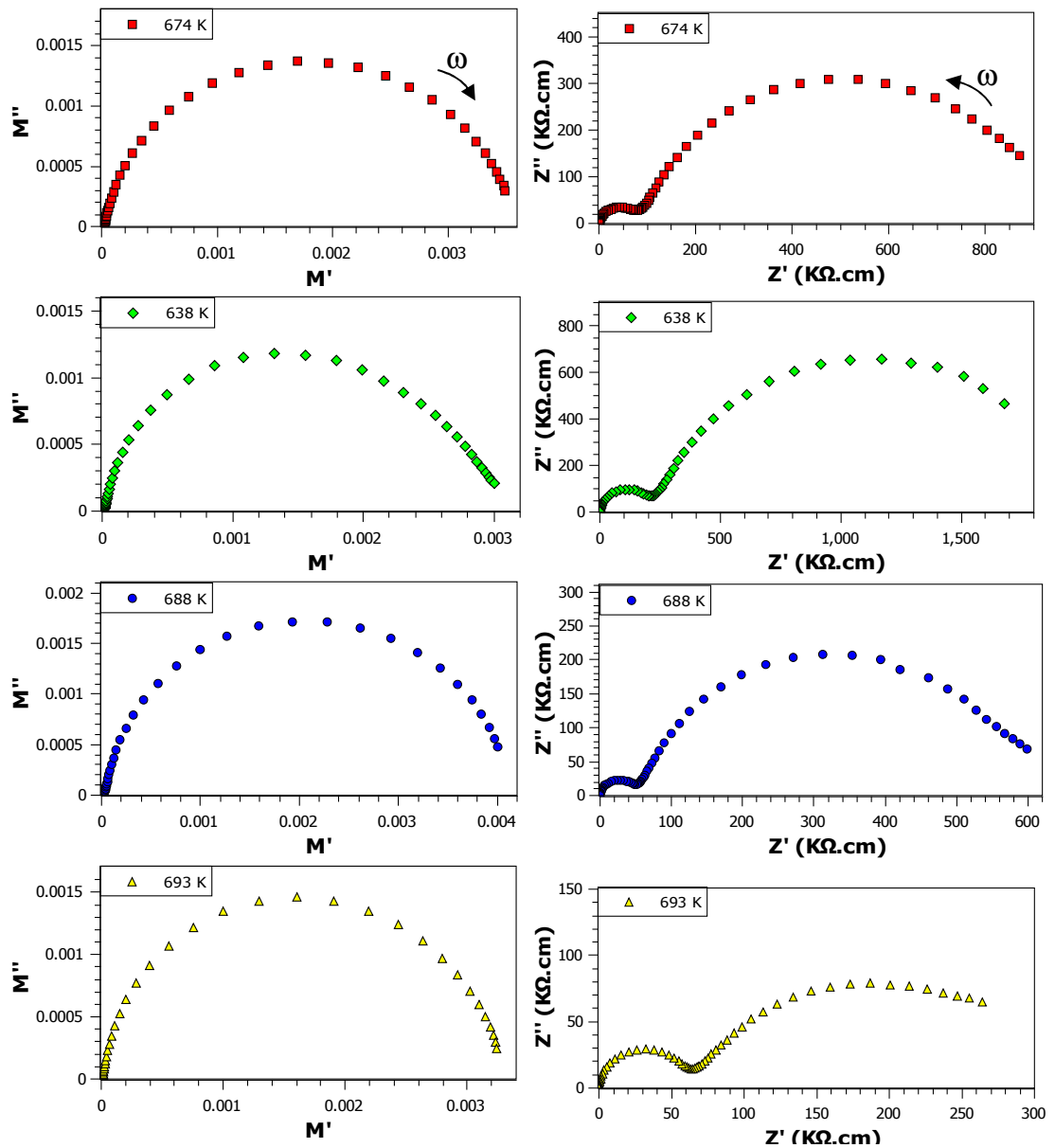


Figure 6.1: Sample complex modulus and impedance plane plots for 2, 5, 8 and 12 % SrZrO₃-doped BaTiO₃ (from top to bottom) showing the presence of one dominating semi-circular arc in each of the M' plots and two features in each of the Z' plots

In each instance one clear semi-circular arc is observed in the complex plane modulus plot. However, upon close inspection of the low frequency data, a slight deviation is observed in the profile of the semi-circular arc, figure 6.2. This deviation can be modelled as a second, smaller semi-circular arc overlapping onto the larger main arc.

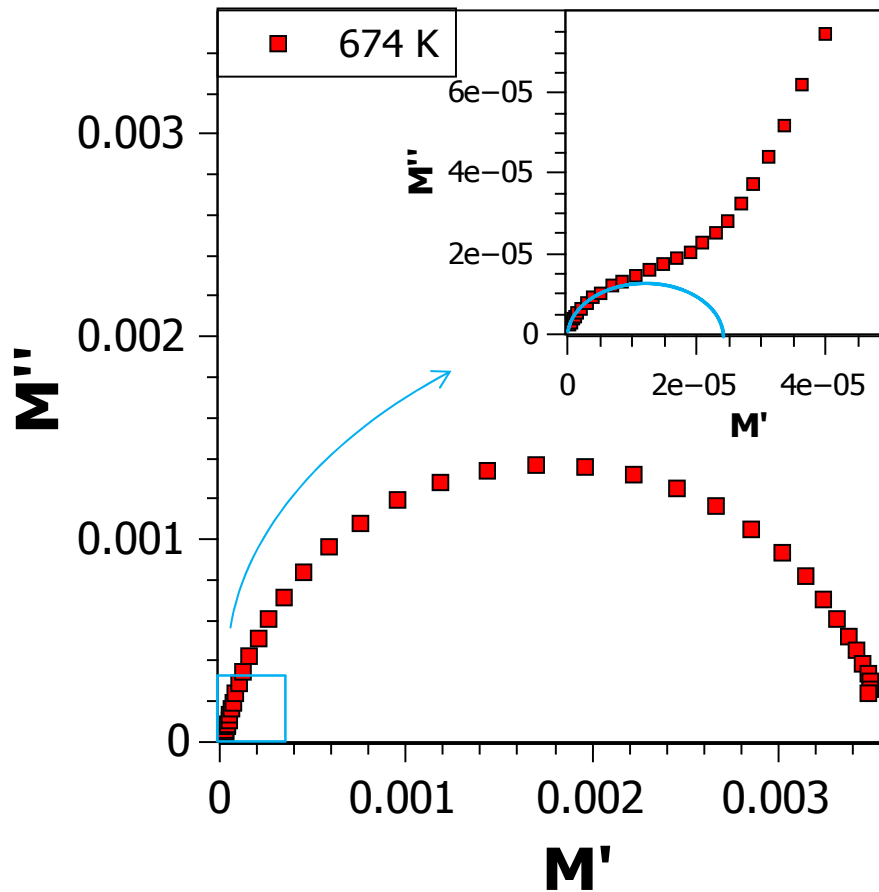


Figure 6.2: Complex modulus data collected from a sample of 2 % SrZrO₃ doped BaTiO₃ showing (inset) the presence of a smaller semi-circular arc at low frequency overlapping on to the dominant arc and contributing to the total capacitance

The complex plane Z^* plot also shows the presence of two semi-circular arcs, with both being clearly visible. The frequency of the semi-circle maxima of the larger of the two arcs in the Z^* plot is found at low frequency and corresponds with the frequency maximum of the smallest arc in the M^* data, whilst the smaller semi-circular arc in the Z^* plot is found at high frequency, and coincides with the dominant arc of the M^* plot.

The intercepts of each arc with the real Z' or M' axis allows for the calculation of the resistance and capacitance respectively, which, when combined with f_{\max} , the

frequency value at the semi-circle maximum, allows for the calculation of both R and C for each of the two components, equation 6.1. By using both complex plane plots, focusing on the dominant arc in each plot, it was possible to determine R and C of both components more accurately.

$$\omega_{max} = 2\pi f_{max} = (RC)^{-1} = \tau^{-1} \quad \text{Equation 6.1}$$

The magnitudes of the calculated resistances and capacitances allow for the assignment of each of the arcs as either bulk or grain boundary electro-active regions. For each of the plots shown in figure 6.1 the large semi-circular feature in the modulus data was found to have a capacitance of the order of magnitude of $\sim 10^{-11}$ F. This is consistent with values expected for the bulk electro-active region of BaTiO₃ and doped BaTiO₃ ceramics^[2] at such elevated temperatures. Similar values were also calculated for the high frequency, smaller feature in the impedance plots, confirming their being resultant of the same electro-active bulk region. The larger, low frequency response in the impedance plot was found to have a significantly larger capacitance, $\sim 10^{-9}$ F, which is consistent with it being a grain boundary response^[1, 2].

As described in chapter 2 each of the parallel RC elements also gives rise to a Debye peak in the Z'' and M'' spectroscopic plots, described mathematically by equations 6.2 and 6.3 respectively.

$$Z'' = R \left[\frac{\omega RC}{1 + (\omega RC)^2} \right] \quad \text{Equation 6.2}$$

$$M'' = \frac{\varepsilon_0}{C} \left[\frac{\omega RC}{1 + (\omega RC)^2} \right] \quad \text{Equation 6.3}$$

As explained in more detail in chapter 2, the frequency at the Debye peak maximum corresponding to each RC element is equal to the inverse of its time constant,

equation 6.1. Where there is good frequency separation between the Debye peaks in the spectroscopic plots and well defined, symmetric semi-circular arcs in the complex plane plots, there should be little difference in the R and C values that can be calculated from each data set. As the frequency separation between the Debye peaks decreases some mixing of the peaks starts to occur. This makes it more accurate to obtain R and C data from the fitting of the semi-circular arcs in the M^* and Z^* plots. If there is very significant overlap of the arcs, especially where several bulk and grain boundary phases are present simple analysis of either plots, complex plane or spectroscopic, will not result in exact R and C values for the different electro-active regions, however it may still be possible to determine f_{\max} , Z''_{\max} and M''_{\max} from the Debye plot which can be used to give some information as to whether the electro-active region is bulk or grain boundary.

The positions of the Debye peaks can also confirm that the time constants of the smallest arc in the Z^* plot and the largest arc in the M^* plot are the same. It also shows that the largest arc in the Z^* plot and the smallest arc in the M^* plot are coincident. Thus the materials can be shown to comprise of two electro-active regions, each having a contribution to both plots, and not due to four different electro-active regions.

Example spectroscopic plots of the imaginary component of the modulus and impedance for each of the four SrZrO_3 doped BaTiO_3 compositions studied are shown below in figure 6.3. In each case it is clear that the main feature in the modulus data coincides with the frequency of the minor feature in the impedance data, confirming that the two responses are resultant of the same electro-active region, in this case the bulk. Upon close inspection, the same is true of the major feature in the impedance data and minor feature of the modulus data; however this is hard to observe due to the relatively small magnitude of the minor peak in the modulus data associated with the grain boundary response, figure 6.4.

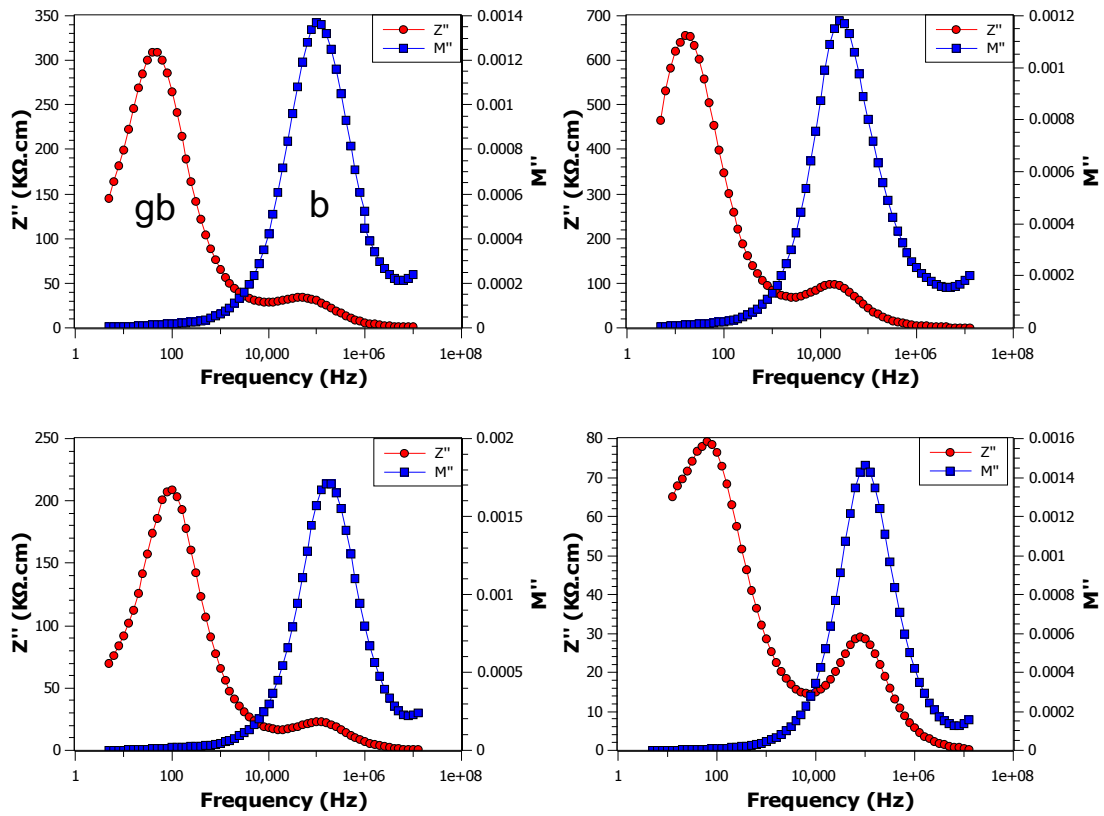


Figure 6.3: Spectroscopic plots showing Z'' and M'' data collected on samples of SrZrO_3 doped BaTiO_3 ; 2 % top left (674 K), 5 % top right (638 K), 8 % bottom left (688 K), 12 % bottom right (693 K), depicting the grain boundary (gb) and bulk (b) responses

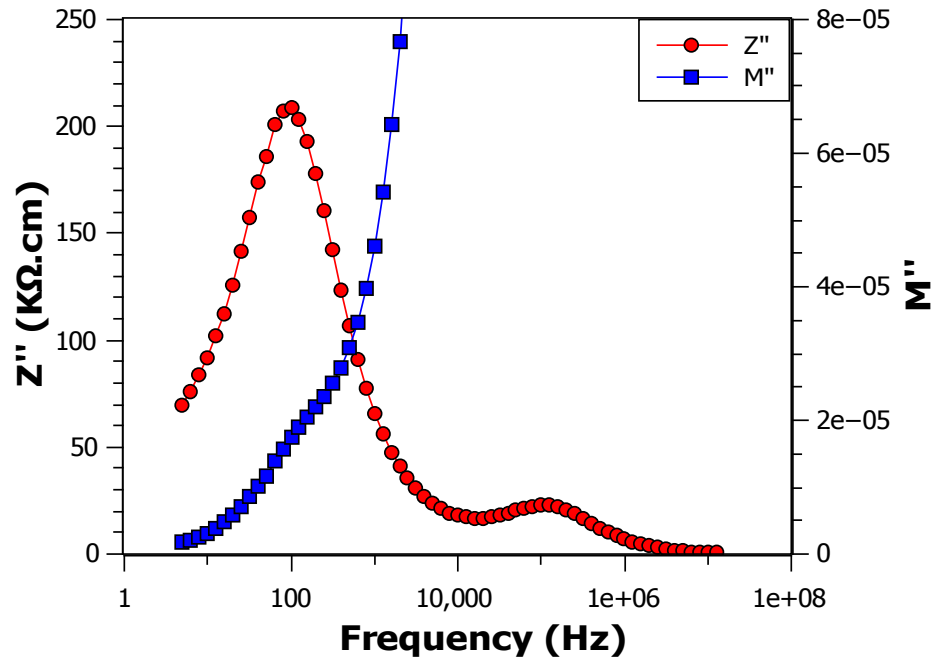


Figure 6.4: Grain boundary feature in the modulus data is shown to be coincident with the grain boundary peak in the impedance data. *n.b.* data shown was collected on a sample of 8 % SrZrO_3 at 688 K (see figure 6.3)

The presence of only a very small contribution to the complex modulus plot from the grain boundary suggests that the volume fraction of the grain boundaries is low and that the grain boundaries are well defined (*i.e.* thin) in these samples. SEM images of each of the pellets show the presence of large well sintered grains with narrow grain boundaries, consistent with the impedance spectroscopy data analysis.

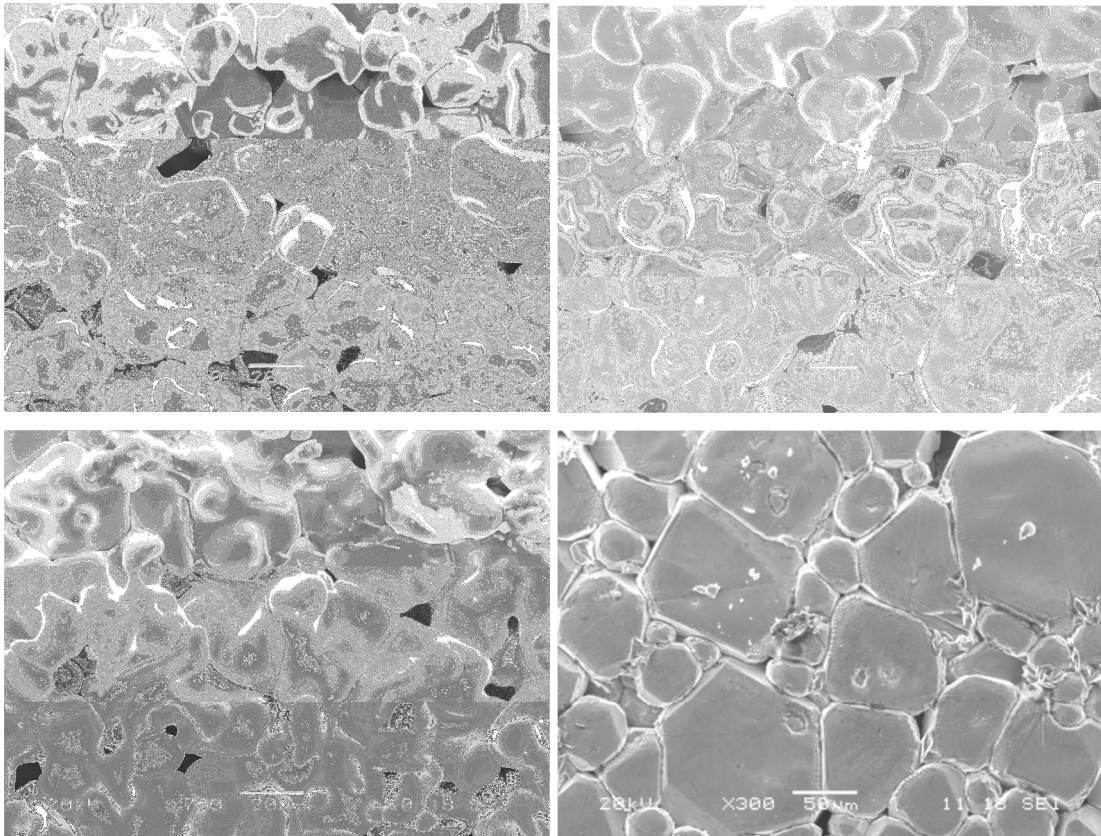


Figure 6.5: SEM images of x % SrZrO₃ doped BaTiO₃ samples; 2 %: top left, 5 %: top right, 8%: bottom left, 12 %: bottom right

Using the 2 % SrZrO₃ pellet as an example composition, it can be shown that the highly symmetric shape of the arcs in the complex plane plots, along with a relatively small degree of overlap between the arcs leads to very similar R values obtained by both spectroscopic and complex plane plot analysis. The data in figure 6.6 shows clearly that the resistance of the materials decreases with temperature and also that there is clear separation in the resistivities of the grain boundary and bulk responses. In addition it is clear that there is a high degree of agreement in the values calculated from both impedance and spectroscopic plots.

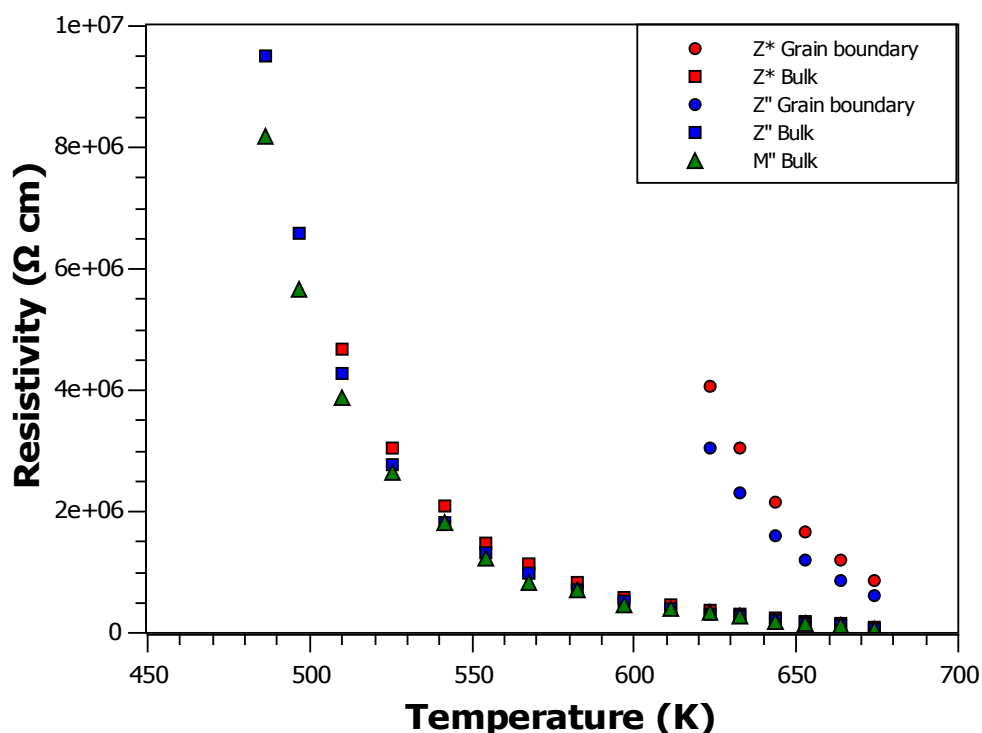


Figure 6.6: Two distinct electro-active regions present in a sample of 2 % SrZrO₃ – doped BaTiO₃, the resistivities of which can be calculated in various ways showing good agreement in values calculated by different methods

By contrast, the analysis of capacitance data calculated using both complex plane plots and spectroscopic plots shows that, although there is a clear distinction between the magnitudes of the grain boundary and bulk capacitance, there is not always good agreement between the values calculated by each route. Whilst the bulk capacitances calculated from each of the complex plane impedance and modulus plots give rise to very similar values, the values calculated using the spectroscopic plots are somewhat more scattered, although of the same order of magnitude. Similarly, whilst the grain boundary capacitance data calculated from the complex plane impedance plot shows a smooth trend, the values calculated using the spectroscopic data, although of the same order or magnitude as those calculated from the Z^* plot, do not show a smooth trend and instead are much more varied. This is likely to be due to the fact that the values calculated using the spectroscopic plots assume that the Debye peaks are symmetric and un-broadened. By contrast, the complex plane plot analysis allows for depression and asymmetry of the semi-circular arcs, from which the R and C values are calculated, by focusing on the intercepts (diameter) rather than the height (vertical radius). In addition, the data

calculated using the spectroscopic plots uses the Debye peak maxima. This is limited to one of 65 discrete frequencies, thus the resolution of the peak is fairly low. Both factors are especially noticeable in the grain boundary capacitance, due the fact that it is observed towards the limit of the frequency operating range of the equipment which results in greater noise in the data.

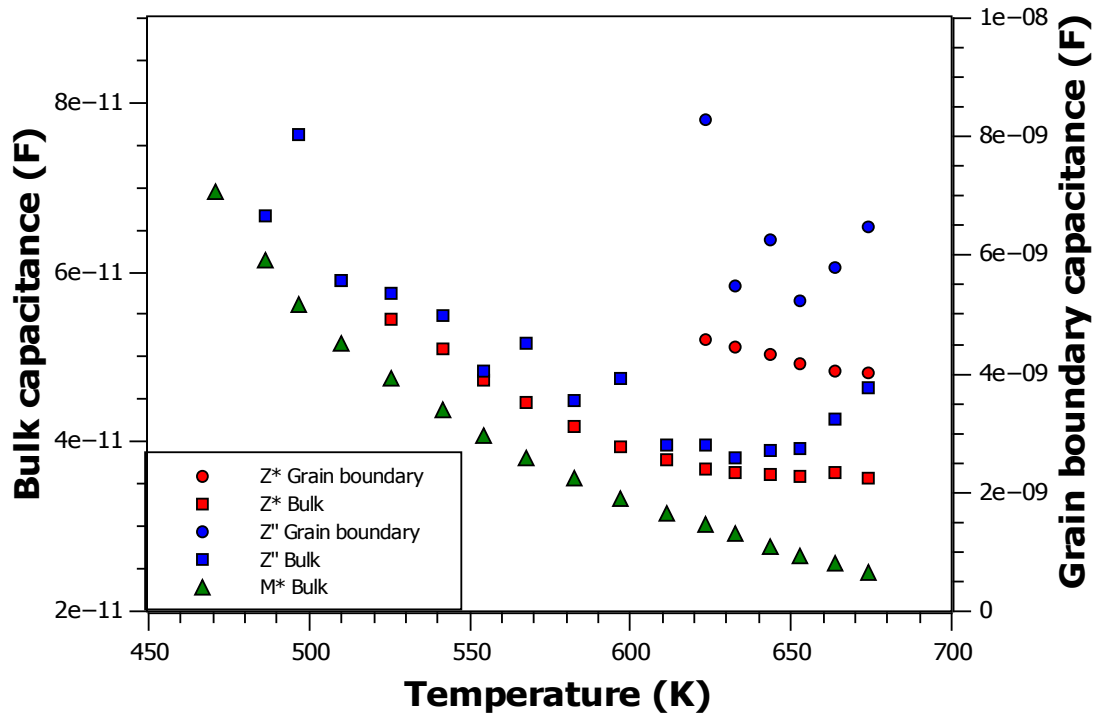


Figure 6.7: Two distinct electro-active regions present in the sample, however, the capacitance of these components cannot be as accurately established from the spectroscopic impedance plot.

Bulk and grain boundary log conductivities were plotted as a function of $1000/T$ for each of the compositions, figure 6.8, with activation energies calculated as described in chapter 3, section 6. The calculated values are displayed in table 6.1. In each case both the grain boundaries and bulk response from each composition was found to exhibit Arrhenius behaviour, with the activation energy of the bulk being lower than that of the grain boundary, but with the σ values calculated by each analysis method being very similar.

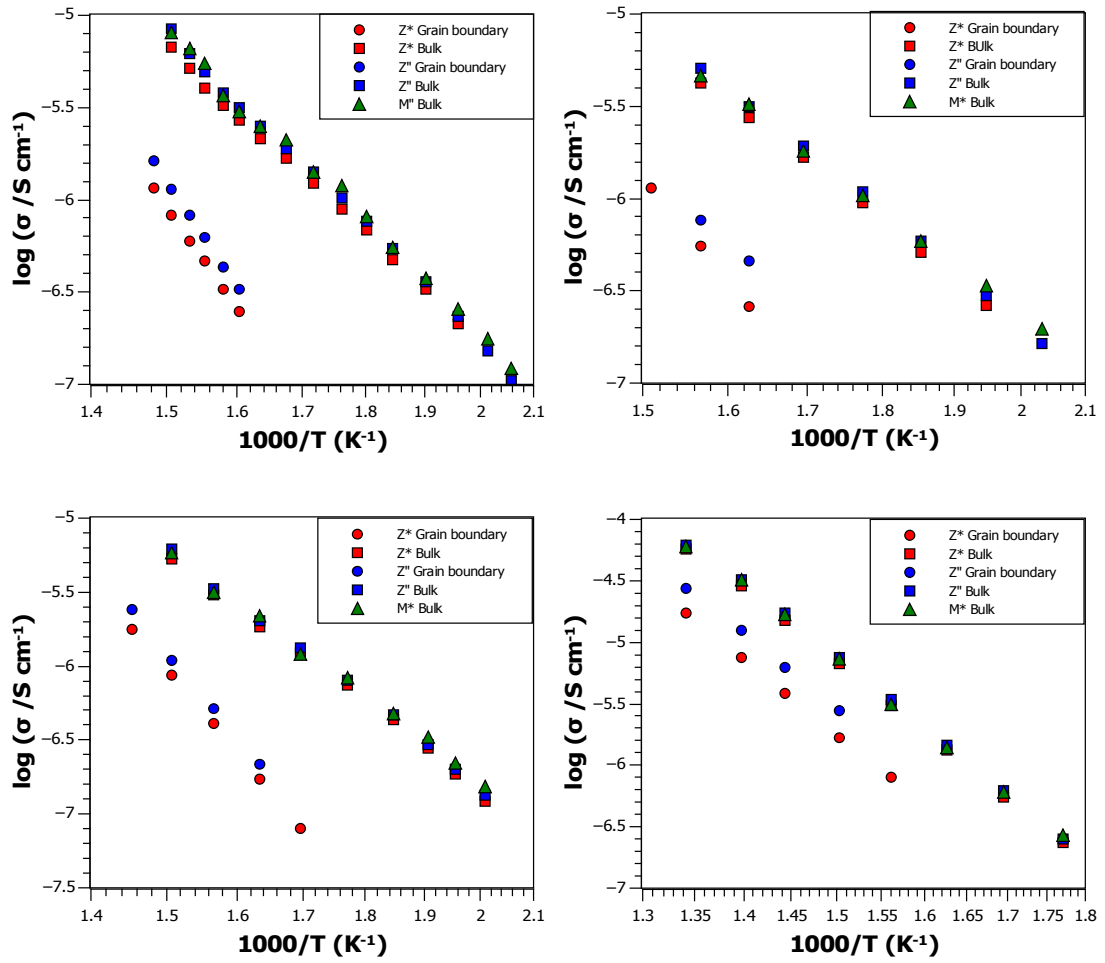


Figure 6.8: Conductivity plots of data collected on samples of x % SrZrO₃ doped BaTiO₃, showing Arrhenius behaviour; 2 %: top left, 5 %: top right, 8%: bottom left, 12 %: bottom right

Log conductivity plots calculated using data taken from the M'' plots shows that the activation energies for the 2, 5 and 8 % SrZrO₃ doped BaTiO₃ samples are very similar, although there is a significant increase in the activation energy of the 12% SrZrO₃ doped sample, figure 6.9. In this composition, where the polymorphic phases are known to have coalesced, it was found that the activation energy of the bulk was more akin to that of the grain boundary region of the lower doped compositions. The activation energies of both the bulk and grain boundary regions for each of the materials are of the order of 1 eV, with the grain boundaries shown to be slightly more resistive than the bulk. This is consistent with conductivity arising as a result of the presence of anion vacancies^[3, 4].

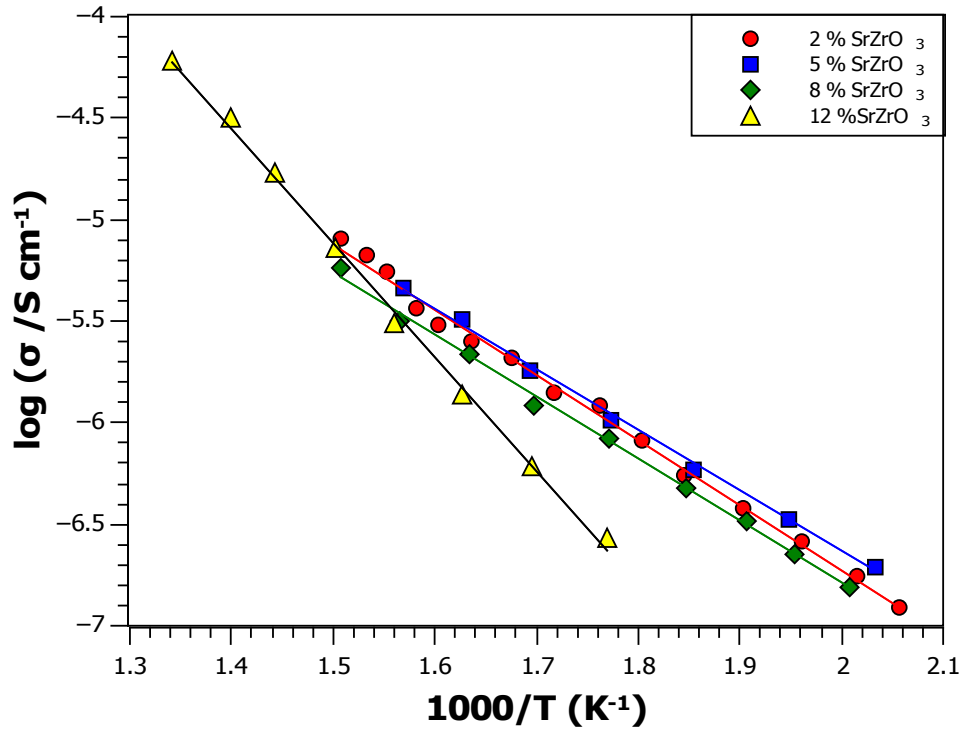


Figure 6.9: Activation energies calculated from M'' data for each of 2, 5, 8 and 12 % SrZrO_3 doped BaTiO_3

Table 6.1: Activation energies for x% SrZrO_3 doped BaTiO_3

Composition	E_a (eV) (M'' bulk)	E_a (eV) (grain boundary)
2 % SrZrO_3	0.64 ± 0.01	1.12 ± 0.01
5 % SrZrO_3	0.59 ± 0.02	1.10 ± 0.01
8 % SrZrO_3	0.61 ± 0.01	1.12 ± 0.02
12 % SrZrO_3	1.11 ± 0.02	1.23 ± 0.03

Plotting reciprocal capacitance ($1/C$) data as a function of T also shows that the capacitance of each of the materials follows Curie-Weiss behaviour above T_C , figure 6.10. In each case the total capacitance of the materials are shown to be non-capped, with good agreement between the bulk and total capacitance and little contribution from the grain boundary region. The Curie Weiss values for each of the materials are shown in table 6.2, and are found to be of similar magnitude to that of un-doped BaTiO_3 , which has a Curie constant of $\sim 1.05 \times 10^5 - 1.2 \times 10^5$ ^[5, 6]. All the values are consistent with “Group 1”; displacive ferroelectrics^[7], where the polarisation arises due to ion movement from their thermal equilibrium position, as

discussed in chapter 3, section 6. When compared to the T_C values of these materials established in chapter 5, each is found to be within 2 % of the experimental data, with the exception of the 2 % SrZrO₃ sample which is within 5 %. Where T_0 is larger than T_C , this would normally indicate capping caused by the microstructure^[8], which is evident in the 5 % SrZrO₃ doped sample, however the extent of capping is low, figure 6.10.

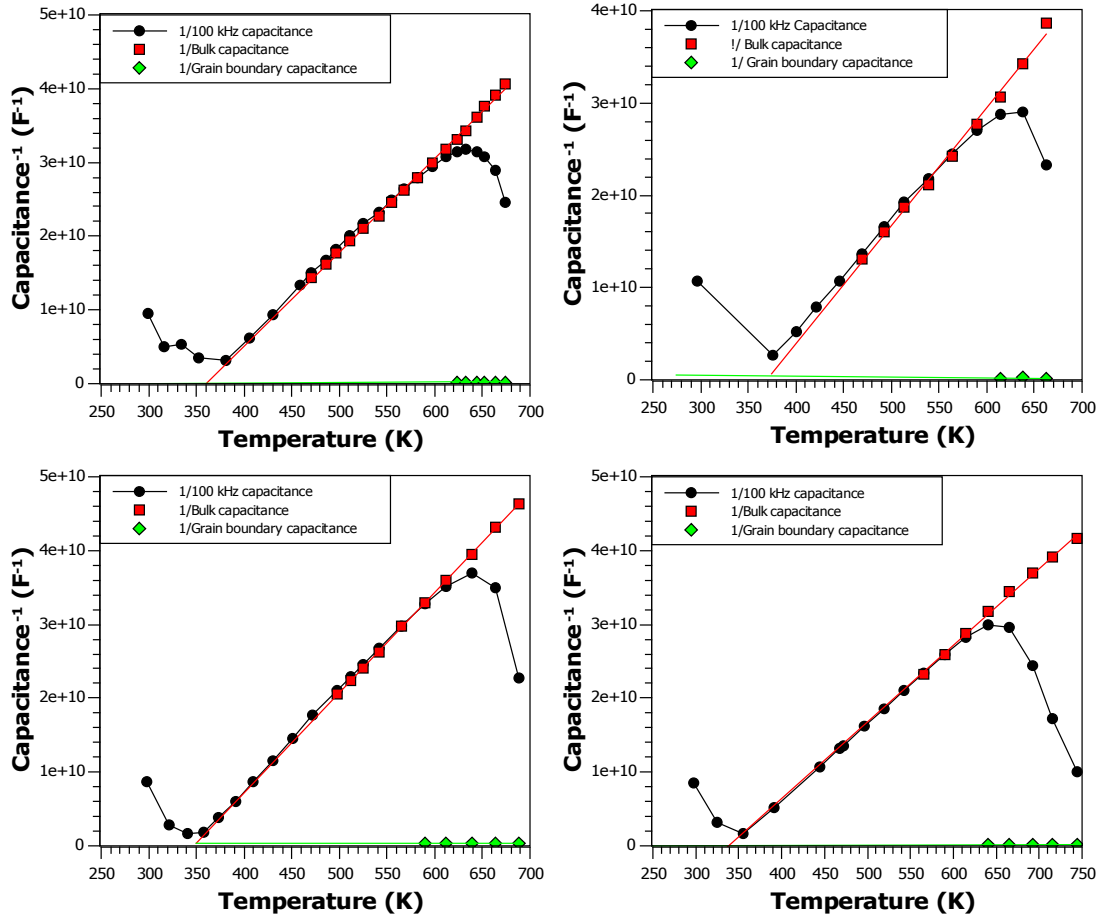


Figure 6.10: Reciprocal capacitance as a function of temperature for 2, 5, 8 and 12 % SrZrO₃ doped BaTiO₃ showing that the pellets are non-capped and obey the Curie-Weiss law. 2 %: top left, 5 %: top right, 8 %: bottom left, 12 %: bottom right

Table 6.2: Curie constant and Curie-Weiss constants calculated from the Curie-Weiss plots shown in figure 6.9

Temperature	Curie constant, C_w , (K)	θ (K)
2% SrZrO₃	$8.87 \times 10^4 \pm 9.67 \times 10^2$	359.91 ± 7.46
5 % SrZrO₃	$8.86 \times 10^4 \pm 2.47 \times 10^3$	369.05 ± 18.89
8 % SrZrO₃	$8.27 \times 10^4 \pm 3.37 \times 10^2$	348.08 ± 2.78
12 % SrZrO₃	$1.09 \times 10^5 \pm 2.49 \times 10^3$	337.23 ± 16.83

6.1.2: CaZrO₃-doped BaTiO₃

Spectroscopic data were plotted for each of the 2, 5, 8 and 12 % CaZrO₃ doped BaTiO₃ compositions. Data was collected at elevated temperatures, where the resistances of the materials were low enough that the electronic microstructure could be studied, figure 6.11.

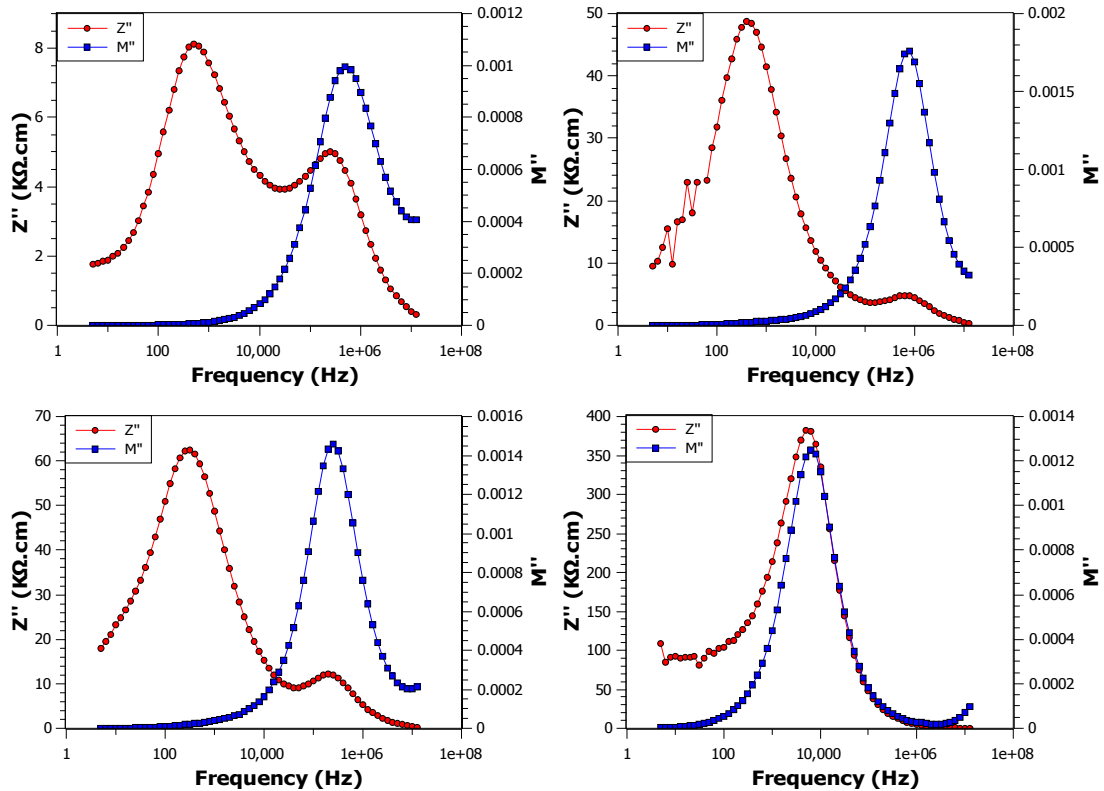


Figure 6.11: Spectroscopic plots showing Z'' and M'' data collected on samples of CaZrO₃ doped BaTiO₃; 2 %: top left (765 K), 5 % top right (745 K), 8 % bottom left (724 K), 12 % bottom right (547 K)

These plots show the presence of two electro-active regions in each sample with the exception of the 12 % CaZrO₃ doped BaTiO₃ which shows the presence of only one electro-active region, although a poorly resolved “tail” is evident in low frequency in the Z'' data. In each case where two peaks are present in the impedance data, one of the peaks is found at approximately the same frequency as the peak in the modulus data. These peaks can then be confirmed as being resultant of the same electro-active region of the pellet. The fact that the peak is clearly present in the modulus plot, along with the fact that the capacitances of these peaks are of the order of magnitude $\sim 1 \times 10^{-11}$ F leads to their being assigned as the bulk component. The

capacitance of the single peak in the 12 % CaZrO_3 sample can be calculated by equation 6.3 and gives a value of 7.074×10^{-11} F at 547 K. This value is consistent with the peak arising due to a bulk region, suggesting that this ceramic has no distinct grain boundary response.

SEM images of the surfaces of these materials show the presence of large grained ceramics for each of the 2, 5 and 8 % CaZrO_3 doped samples. However this is not the case for the 12% CaZrO_3 , which instead shows minimal grain growth ($\sim 1\text{-}5 \mu\text{m}$ grain size) figure 6.11.

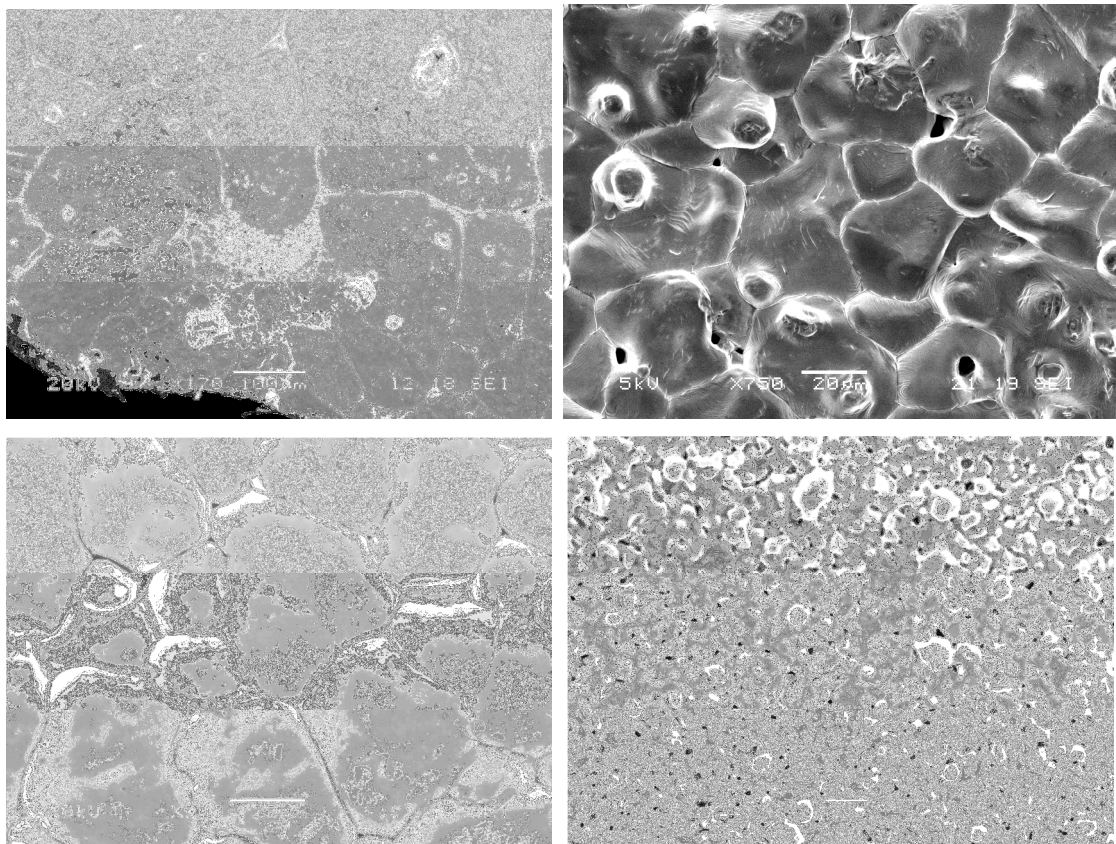


Figure 6.12: SEM images of x % CaZrO_3 doped BaTiO_3 samples; 2 %: top left, 5 %: top right, 8%: bottom left, 12 %: bottom right

The difference in grain sizes means that whereas in the large grained ceramics, a difference can exist between the internal grain structure and the interfaces between grains (grain boundary), resulting in bulk and grain boundary contributions, the grains in 12 % CaZrO_3 appear to be “necked”, i.e. the powder particles have not fully coalesced into well defined grains with grain boundaries, as described in chapter 1, section 5. As a result of not having two distinct, well defined regions, grain boundary

and bulk, only one electroactive region is observed in the high temperature immittance spectroscopy^[8].

Activation energies for each of the compositions were calculated based on data extracted from the Z^* plots and are shown in figure 6.13.

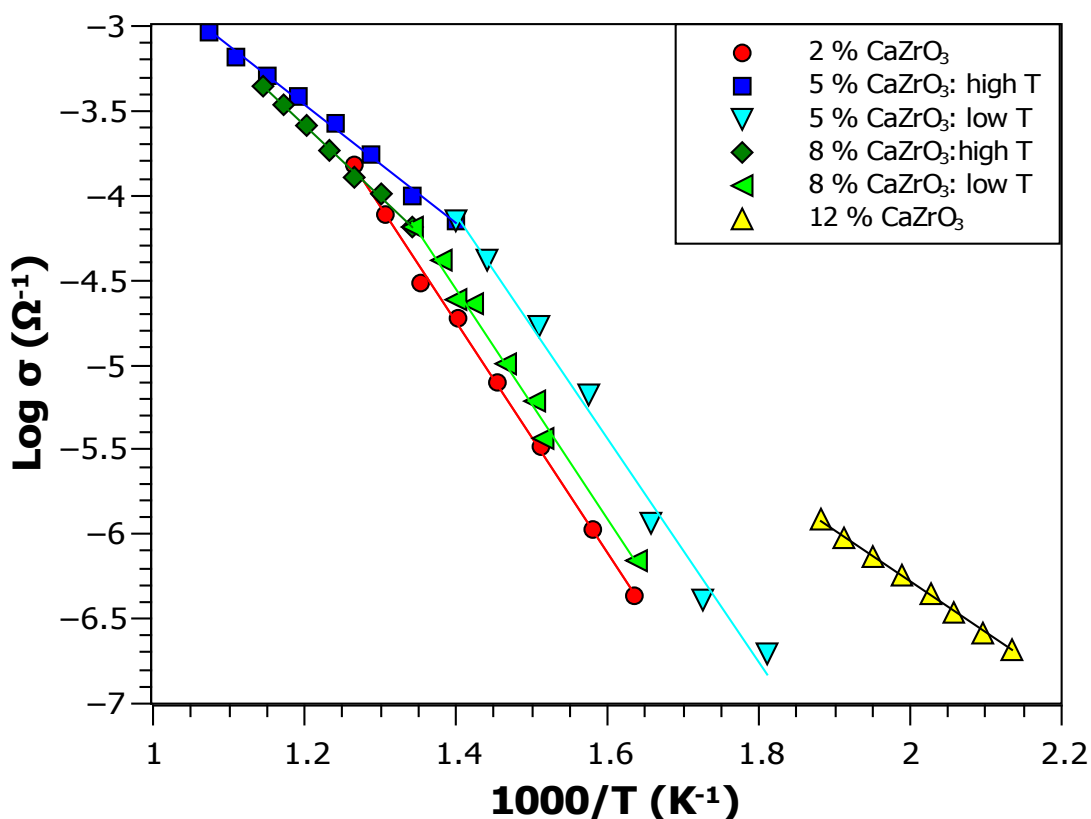


Figure 6.13: Activation energies calculated from Z^* plot for each of 2, 5, 8 and 12 % CaZrO_3 doped BaTiO_3

This data shows the presence of two different gradients. However, unlike in the SrZrO_3 doped compositions where each data set was linear, in two of the compositions, 5 and 8 % CaZrO_3 doped BaTiO_3 , there is a change in gradient observed. The gradients calculated from each section of the 5 and 8 % data sets (high and low T) are consistent with either the gradients obtained from 2 % CaZrO_3 and 12 % SrZrO_3 or, 12 % CaZrO_3 , 2,5 and 8 % SrZrO_3 doped compositions. The calculated activation energies are shown in table 6.3

Table 6.3: Activation energies for x% CaZrO₃ doped BaTiO₃ based on Z* data

Composition	E _a (eV) (bulk)	E _a (eV) (grain boundary)
2% CaZrO₃	1.35 ± 0.02	1.61 ± 0.07
5 % CaZrO₃ low T	1.31 ± 0.06	1.86 ± 0.02
5 % CaZrO₃ high T	0.69 ± 0.02	1.86 ± 0.02
8 % CaZrO₃ low T	1.34 ± 0.05	1.32 ± 0.01
8 % CaZrO₃ high T	0.84 ± 0.02	1.32 ± 0.01
12 % CaZrO₃	0.60 ± 0.01	-

As with the SrZrO₃ doped materials, there is a significant difference between the 2-8 % doped compositions (low T data from 5 and 8 % CaZrO₃ doped samples) and the 12 % doped composition. In this case, the activation energies of the lower doped compositions are considerably higher than that of the 12 % CaZrO₃ doped composition, which has an activation energy similar to that of the lower doped SrZrO₃ compositions, at around ~0.6 eV.

When the 5 % and 8 % CaZrO₃ compositions are closely studied, it appears that the gradient of the line changes between the high T and low T regions. When calculated, the values of these two regions correspond well with the values obtained for either the 2 % CaZrO₃ doped sample or the 12 % CaZrO₃ sample, table 6.3. This suggests that there are two conduction processes which are dominant at different temperatures. Given the similarity of the two magnitudes of activation energies observed in the CaZrO₃ doped materials and the SrZrO₃ doped materials, it is likely that there are the same two possible conductivity processes available in both systems, with either the dopant species or pellet microstructure causing a change as to which conduction route is active at any given temperature. This will be discussed in more detail later in this chapter.

6.1.3: GdScO₃-doped BaTiO₃

High temperature immittance data were collected on each of the four GdScO₃ - doped BaTiO₃ compositions studied in chapter 5 with spectroscopic plots of the M''

and Z'' data shown in figure 6.14. These show the presence of two electro-active regions in each of the compositions; however, the frequencies of the two regions are generally found to be much more similar than was observed for CaZrO_3 or SrZrO_3 doped compositions, thus it is likely that there may be some degree of mixing of the responses. This can be observed by a slight asymmetry in many of the peaks.

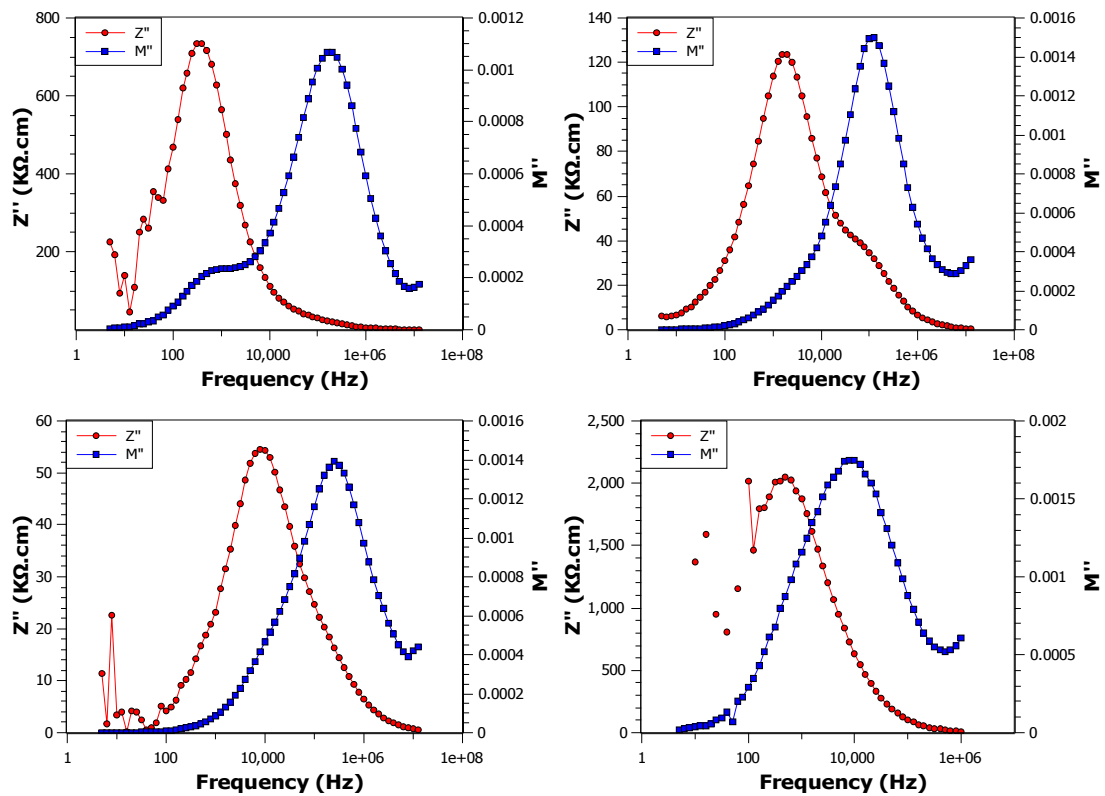


Figure 6.14: Spectroscopic plots showing Z'' and M'' data collected on samples of GdScO_3 doped BaTiO_3 ; 2 % top left (586 K), 5 % top right (758 K), 8 % bottom left (744 K), 12 % bottom right (657 K)

Activation energies were calculated for the bulk response of each composition as before. This data shows distinct changes in the gradients of the different compositions, with the 2 % GdScO_3 doped material giving rise to a considerably lower activation energy than the other materials. The 8 % GdScO_3 composition is shown to have a noticeably higher activation energy, as shown by the presence of a steeper line in the Arrhenius plot, figure 6.15. It is likely that the mixing of the grain boundary and bulk response is causing some increase in the calculated bulk E_a , with this not observed in the 2 % GdScO_3 – BaTiO_3 data which has a much greater frequency separation of the modulus and impedance peaks.

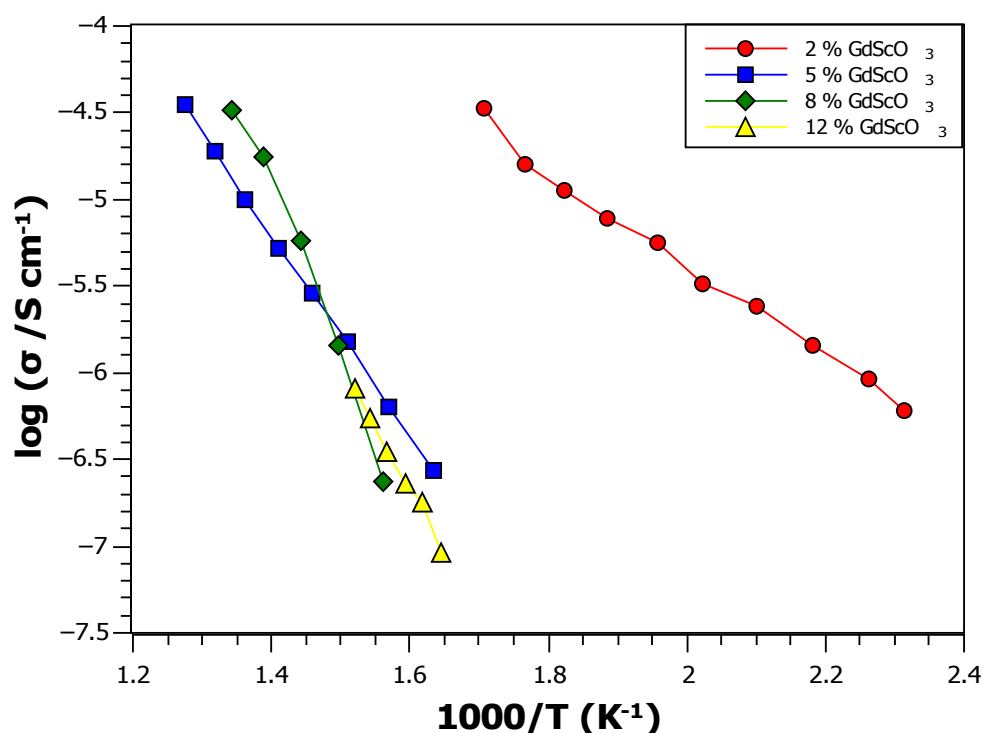


Figure 6.15: Activation energies calculated using M'' data for each of 2, 5, 8 and 12 % GdScO_3 doped BaTiO_3

Table 6.4: Activation energies for x% GdScO_3 doped BaTiO_3 based on M'' data

Composition	E_a (eV) (bulk)	E_a (eV) (grain boundary)
2% GdScO_3	0.53 ± 0.02	0.90 ± 0.03
5 % GdScO_3	1.16 ± 0.01	1.14 ± 0.03
8 % GdScO_3	1.99 ± 0.14	-
12 % GdScO_3	1.45 ± 0.07	-

Unfortunately it is not possible to collect higher temperature data on these samples to see if a change in the gradient is observed with the 5-12 % GdScO_3 doped samples as with the CaZrO_3 doped materials. This was because the peaks have already progressed to the maximum operating frequency of the apparatus and thus no more useful data can be obtain by collecting data at higher temperatures.

6.1.4: LaScO₃-doped BaTiO₃

When high temperature immittance data were collected on each of the four samples of LaScO₃ doped BaTiO₃ an unusual feature was observed in the modulus data. A representation of this in the spectroscopic plots for each sample is shown in figure 6.16.

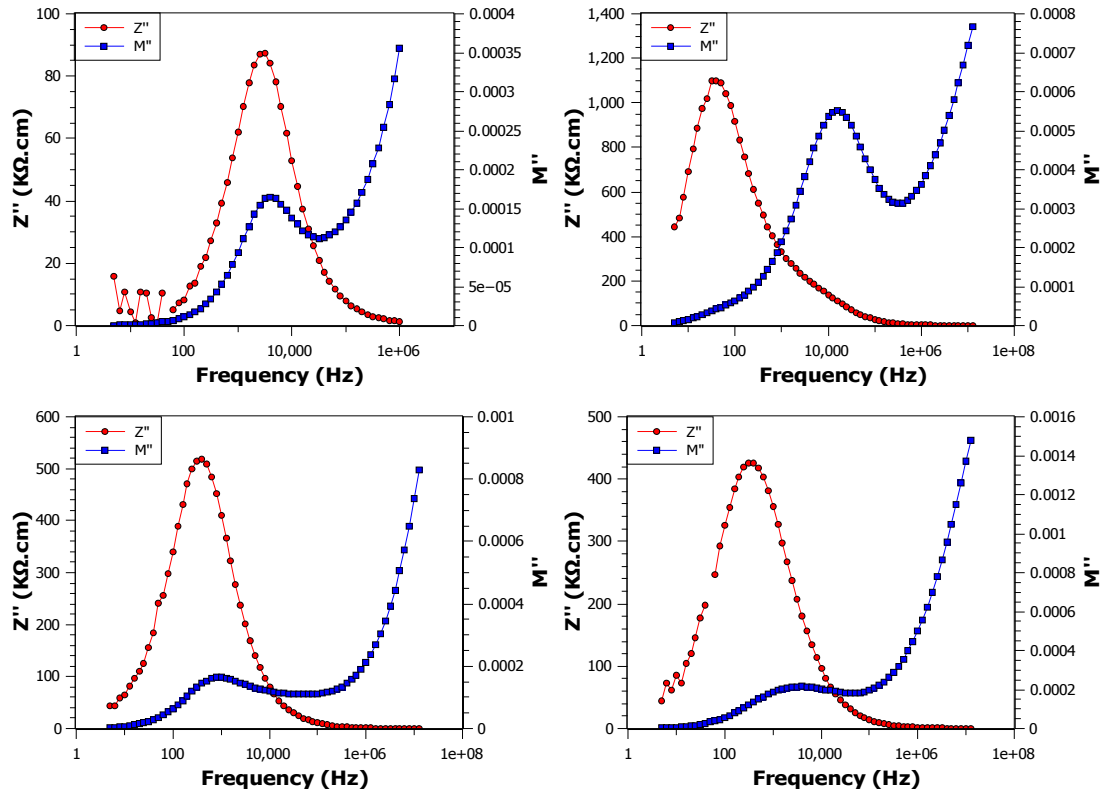


Figure 6.16: Spectroscopic plots showing Z'' and M'' data collected on samples of LaScO₃ doped BaTiO₃; 2 %: top left (815 K), 5 % top right (687 K), 8 % bottom left (735 K), 12 % bottom right (734 K)

In each of these materials the presence of a high frequency “tail” feature is observed in the modulus data. Initially it was thought that this might be another electro-active region starting to come into the visible frequency range of the equipment, however looking at how the presence of this feature changes with increasing temperature suggests that this is not the case. Studies of the complex modulus data shows that the “tail” never resolves into anything resembling an arc, and that instead the feature becomes, if anything, more linear at higher temperatures, figure 6.17.

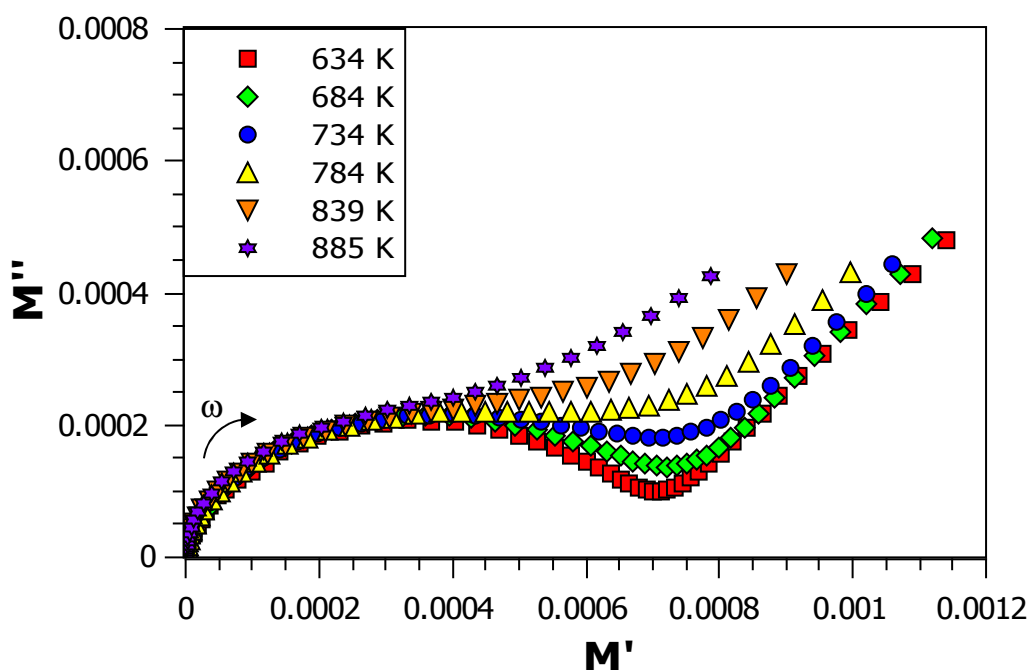


Figure 6.17: Presence of a "tail" feature in the M^* data collected on a sample of 12 % LaScO_3 doped BaTiO_3

As before, activation energies were calculated for each of the four compositions. The calculated values can be found in table 6.5, and show that the activation energies for each of the four compounds are fairly similar, all being around 1 eV.

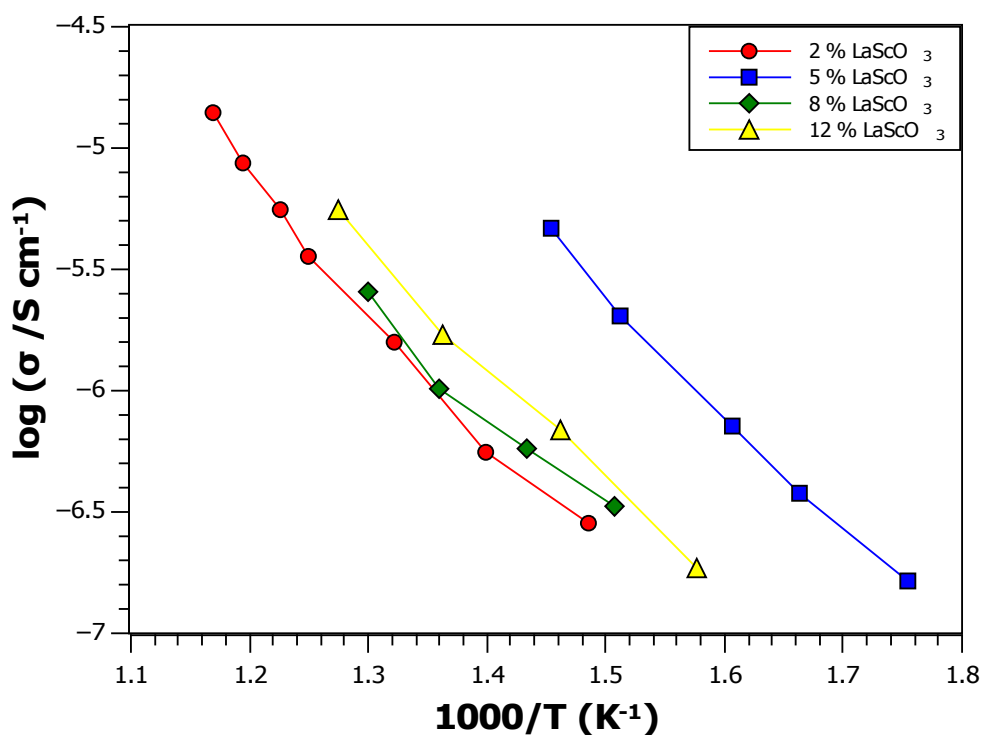


Figure 6.18: Activation energies calculated using M'' data for each of the 2, 5, 8 and 12 % LaScO_3 doped BaTiO_3 compositions

Table 6.5: Activation energies for x% GdScO₃ doped BaTiO₃ based on M'' data

Composition	E_a (eV) (bulk)	E_a (eV) (grain boundary)
2% LaScO ₃	1.06 ± 0.05	-
5 % LaScO ₃	0.96 ± 0.04	1.08 ± 0.04
8 % LaScO ₃	0.82 ± 0.10	-
12 % LaScO ₃	0.95 ± 0.04	-

6.2: Discussion

6.2.1: Changes in activation energies

All the materials were found to have very similar levels of conductivity as shown by the close grouping of most of the data, figure 6.19.

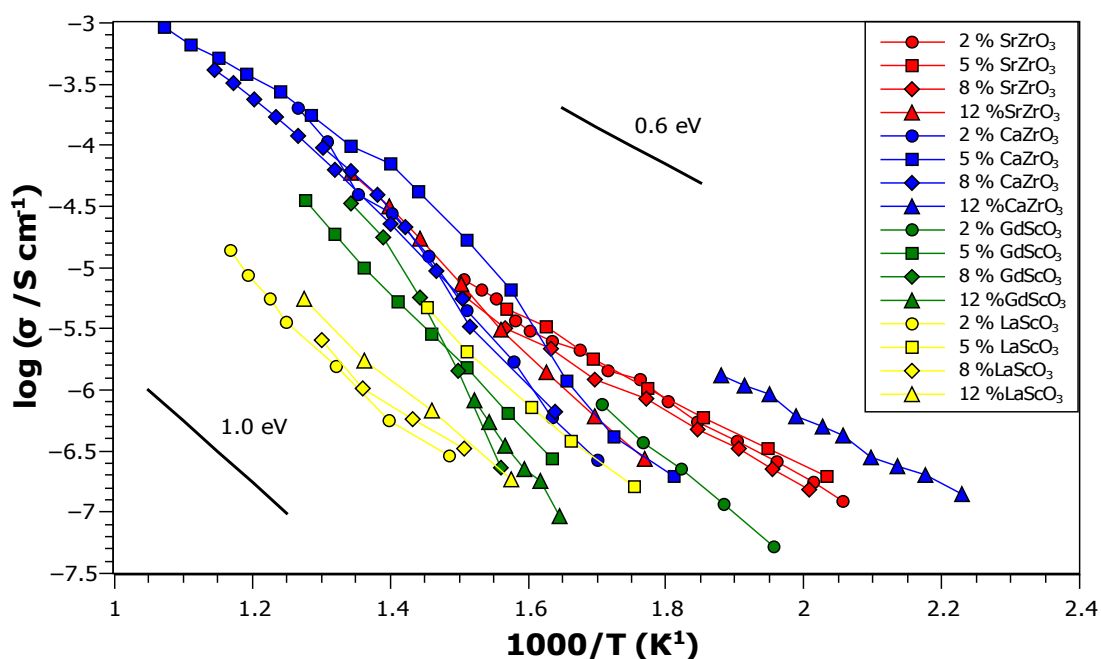


Figure 6.19: Arrhenius plots for each of the compositions studied. Gradients corresponding to 0.6 eV and 1.0 eV activation energies are shown as solid lines

In these materials it is found that the activation energies fall into one of two broad regimes, either ~ 0.6 eV or 1.0-1.3 eV. Both of these values are of the order of magnitude which is consistent with the conduction processes arising due to the

presence of anion vacancies^[3, 4, 9]. However, the presence of two groups of gradients, combined with the fact that both gradients can be observed within a single sample in the case of 2 and 5 % CaZrO₃ doped BaTiO₃, suggests that there are two distinct conduction regimes. Some explanation for the presence of two distinct activation energies can be given by an understanding of the defect chemistry of doped and un-doped BaTiO₃.

Un-doped barium titanate is known to have a conductivity which is dependent on the partial pressure of oxygen. At low P_{O_2} the conductivity varies linearly with oxygen concentration, decreasing as the pressure is increased, figure 6.20. This is expected behaviour for reduction-type semiconductors and can be rationalised by the partial reduction of Ti⁴⁺ ions to Ti³⁺, a process which results from the formation of anion vacancies, releasing electrons, equation 6.4. These electrons act as charge carriers in an n-type conduction mechanism.

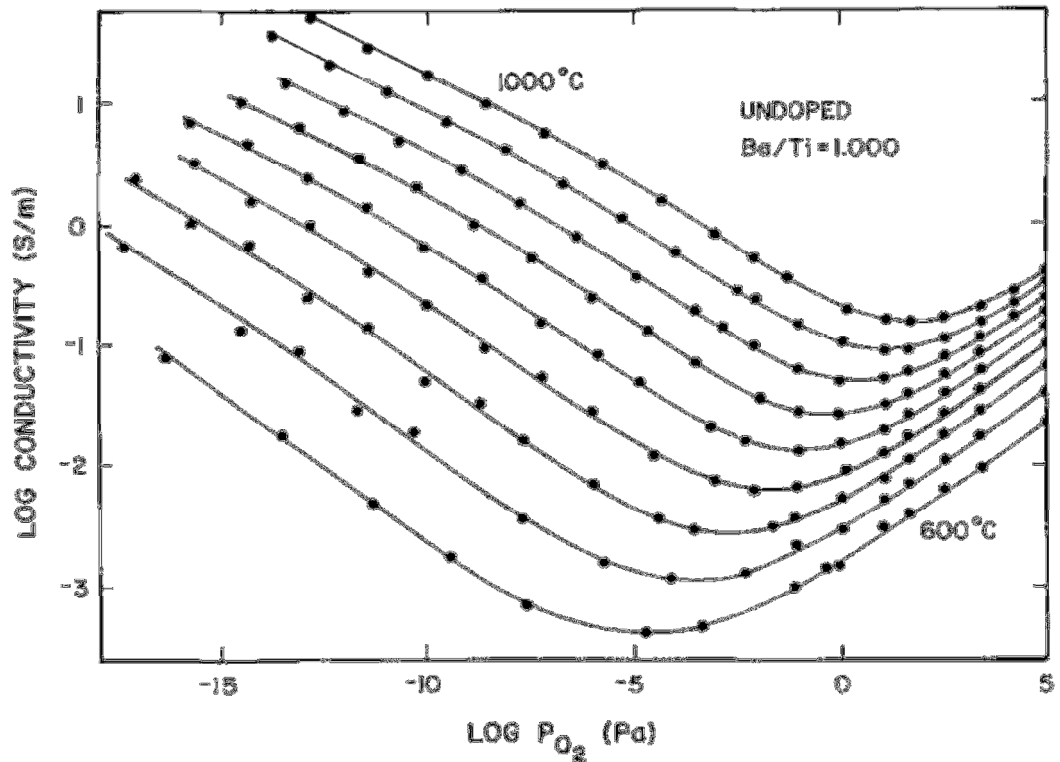
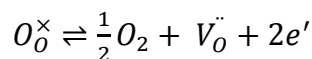


Figure 6.20: Equilibrium electrical conductivity of un-doped BaTiO₃ at 600 -1000 °C at 50 °C intervals, taken from^[10]



Equation 6.4

At higher P_{O_2} , conductivity increases with increasing P_{O_2} , figure 6.20. This is unexpected behaviour for perovskite materials such as $BaTiO_3$ as it would imply the presence of oxygen interstitials, O_i , being incorporated into the lattice at high P_{O_2} and acting as charge carriers. This is highly disfavoured in the cubic close-packed structure of $BaTiO_3$. Two mechanisms have been proposed which would instead create oxygen vacancies which can then be filled at high P_{O_2} creating electron holes, the movement of which through the lattice creates a conduction pathway. These two models are an intrinsic Schottky defect pair model and an extrinsic acceptor impurity model^[11].

The Schottky defect pair model for $BaTiO_3$ assumes the formation of 3 anion vacancies for each Ba/Ti vacancy pair, equation 6.5^[11]. The extrinsic acceptor impurity model instead assumes the presence of some amount of acceptor type impurities being incorporated into the lattice, resulting in the formation of anion vacancies in order to balance the higher charge of the acceptor species, equation 6.6^[10].

Schottky defect pair model:



Acceptor impurity model:



In each case anion vacancies are created which can be filled at high P_{O_2} , equation 6.7, resulting in the formation of electron holes. These holes can act as charge carriers in a p-type conduction mechanism^[10].



A minimum in the conductivity occurs when the number of n-types carriers, e^{\prime} , is equal to the number of p-type carriers, h^{\bullet} . At this point the material is an intrinsic

semi-conductor with an activation energy equal to half the band gap energy, E_g . This is generally reported as being between ~ 3.1 eV^[12, 13], resulting in an $E_a \sim 1.55$ eV.

The activation energy of each regime is given by the temperature dependence of the conductivity. Thus, the activation energy changes as the conduction mechanism switches from n-type to p-type as P_{O_2} increases or temperature decreases.

The presence of anion vacancies in both the n-type and p-type regime means that some ionic contribution to the conductivity is likely to occur. Though some models suggest that there may also be cation vacancies, these are unlikely to be involved in ionic conduction mechanisms as the migration enthalpy is so high that they are virtually immobile^[12]. Thus, E_a is likely to be a mixture of both electronic and ionic (anionic) conduction mechanisms, with the electronic conductivity being highly dependent on P_{O_2} , whilst the ionic partial conductivity is virtually independent of P_{O_2} ^[12].

Doped forms of $BaTiO_3$ can be made to exhibit either n-type or p-type conduction mechanisms by the addition of different dopants. Acceptor doping leads to the creation of more anion vacancies, equation 6.4. This expands the p-type region, effectively shifting the log conductivity curves shown in figure 6.20 to the left. Donor doping results in initially filling the anion vacancies, equation 6.6, before, once filled, resulting in the formation of B-site vacancies. Filling the anion vacancies extends the n-type conduction regime effectively shifting the log conductivity curves to the right.



Thus, the addition of dopant species can alter the conduction mechanism observed for a material at atmospheric P_{O_2} and within apparatus operating temperature ranges, with n-type, p-type, intrinsic semiconductor ($[h^{\bullet}] = [e^{\bullet}]$) and ionic conduction mechanisms all being possible and likely contributing to the measured E_a .

The donor-acceptor co-doped $BaTiO_3$ compositions studied in this project are likely to exhibit the same behaviour. Although the dopant species were chosen such that overall charge neutrality of the cation lattice was maintained, some net donor or

acceptor effect may be occurring. This could arise due to impurities in the starting reagents or inaccuracies in the weighing of both the parent and dopant species. By changing the temperature range over which the conductivity is measured, as well as changing the level of p-type/n-type conduction as a result of sample synthesis, the isotherms of the sort shown in figure 6.20 can be shifted both vertically and horizontally. This results in observing different sections of the curve over the data collection temperature range. Thus, it may be possible to observe the material in either conduction regime, or in the case of 2 and 5 % CaZrO_3 , both regimes over different temperature ranges, as well as the intrinsic semiconductor region where the number of p-type carriers is equal to the number of n-type carriers, *i.e.* $[\text{h}^\bullet] = [\text{e}^\bullet]$, as well as differing levels of ionic conduction contributions.

Activation energies for doped BaTiO_3 compositions have often been quoted as being either ~ 0.6 eV or ~ 1.3 eV^[9, 10, 14, 15], with Chan et al.^[10] observing a change in gradient at high temperatures, figure 6.23. These two values fit with the two sorts of values observed for the compounds studied in this project, and suggest that the different values found in the literature correspond either to compositions which exhibited either n-type (~ 0.6 eV) or p-type (~ 1.3 eV) conduction mechanisms, or to a change between electronic (p- or n-type) and ionic dominated conduction mechanisms.

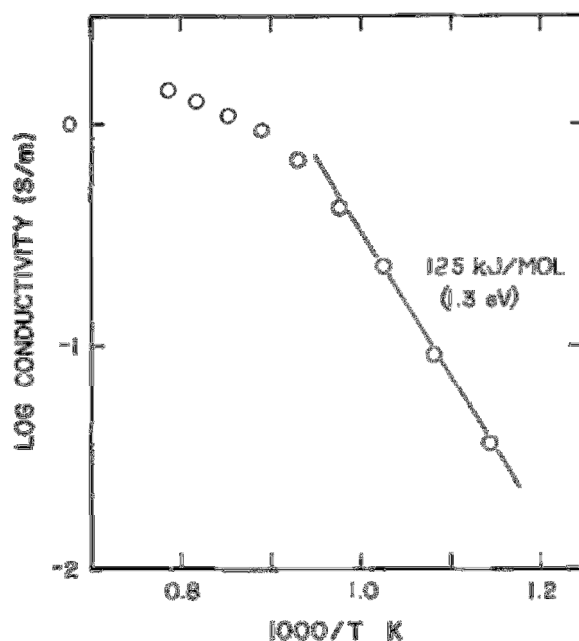


Figure 6.21: The activation energy of Nb-doped BaTiO_3 is found to change with temperature, with the low temperature activation energy being ~ 1.3 eV^[10]

6.2.2: Anomalous tail feature present in LaScO₃ doped BaTiO₃

The anomalous tail like feature observed in all of the LaScO₃ doped BaTiO₃ compositions is found at high frequency and with large magnitudes in the modulus data, although it is unobservable in the impedance data. This suggests that it corresponds to a region of low capacitance, low resistance which has a frequency maximum outside the operating range of the apparatus. The fact that it is present in each of the LaScO₃ samples, but none of the others, suggests that this region has formed due to some aspect of the lanthanum doping. It could be there is some inhomogeneity or La/Sc based impurity phase present which is unobserved in X-ray diffraction data.

Upon successive heating cyclings of the pellet the gradient of the tail was found to increase slightly, suggesting that were it to be the start of a large semi-circular arc, repeated heating of the pellet was causing the arc to either increase in diameter or become less depressed. Changing the synthesis conditions of the pellet from air to an O₂ enriched atmosphere caused little change in the gradient of the tail suggesting that the electro-active region it corresponds to does not exhibit an n-type conduction mechanism. Unfortunately the material was too resistive at low temperatures to ever determine whether this feature is the start of a semi-circular feature due to some low capacitance phase or some other unknown response.

6.3: Conclusions

For most of the samples studied two distinct electro-active regions were present which could be assigned as either bulk or grain boundary responses. In a few samples, generally those of higher dopant concentration including 12 % CaZrO₃ and 8 & 12 % GdScO₃ doped samples, only one clear region could be observed, which was found to have a capacitance characteristic of a bulk type response. As shown in chapter 5, the synthesis conditions 8 and 12 % GdScO₃ compositions were not fully optimised due to the time constraints of the project and were found to have relatively small grains with the 12 % sample in particular showing clear necking,

consistent with this having the most overlap of the Debye peaks in the modulus and impedance spectroscopic plots. The presence of necking was also observed in SEM images collected on 12 % CaZrO_3 despite the dielectric data on this sample appearing to be fully optimised when looking at the low temperature dielectric data.

The LaScO_3 doped compositions showed some of the most interesting behaviour with the presence of a high frequency tail in the modulus data. This is consistent with a region of low capacitance and resistance; however failure of the tail to resolve into an arc feature casts some doubt over its origin. Further work is required to understand what the significance of this feature is.

In each instance, doping with any of SrZrO_3 , CaZrO_3 , GdScO_3 or LaScO_3 gave rise to a bulk activation energy of either ~ 0.6 eV or $\sim 1-1.3$ eV, save where significant mixing in of the grain boundary responses in 8 & 12 % GdScO_3 doped occurred, which caused the activation energy to be artificially elevated. The fact that, despite the presence of necking, the activation energy of the 12 % CaZrO_3 doped composition was not artificially elevated by the grain boundary response suggests that the composition was much more homogeneous with no evidence of parasitic grain boundary influence on its activation energy, thus its synthesis can be deemed to be optimised.

The fact that two activation energies can be calculated for the bulk electro-active region of a single material (5 or 8 % CaZrO_3 -doped BaTiO_3) provides strong evidence that the two different magnitudes of activation energies observed for each of the other materials are not due to the same conduction process, occurring with slightly different magnitudes due to a difference on dopant species or impurities, but are due to different conduction mechanisms.

The two observed regions of activation energies are likely to be due to differences in the dominant conduction mechanisms, with the ~ 0.6 eV activation energies occurring where there are n-type conduction mechanisms and $\sim 1-1.3$ eV arising due to p-type conduction mechanisms. These mechanisms can be explained by the presence of “free electrons” and “electron holes” respectively, with the mechanism changing with both dopant and temperature. However, due to the presence of anion

vacancies, it is likely that there will also be some amount of ionic conductivity, thus it could be that the change in conductivity is not as a result of a change between n- and p-type conduction routes, but between ionic and electronic mechanisms, although literature suggests that the activation values observed are likely to be due to n- and p-type conduction routes. Analysis of the variation in conductivity as a function of P_{O_2} , as well as transport measurements would be required in order to attempt to separate out the possible ionic contribution to the conductivity from the electronic conduction mechanisms. The intrinsic semiconductor regime, where $[h^{\bullet}] = [e^{\bullet}]$, is likely to be occurring over a very narrow temperature range where the change in gradient between ~ 0.6 eV (n-type) regime and ~ 1.3 (p-type) eV regime is observed in the 5 and 8 % CaZrO_3 doped samples.

References

1. Sinclair, D.C. and A.R. West, *Impedance and modulus spectroscopy of semiconducting BaTiO₃ showing positive temperature coefficient of resistance*. J. Appl. Phys., 1989. **66**: p. 3850-3856.
2. Irvine, T.S., D.C. Sinclair, and A.R. West, *Electroceramics : Characterization by Impedance Spectroscopy*. Advanced Materials, 1990. **2**(3).
3. Islam, M.S., *Ionic transport in ABO₃ perovskite oxides: a computer modelling tour*. J. Mater. Chem., 2000. **10**(5): p. 1027-1038.
4. Cherry, M., M.S. Islam, and C.R.A. Catlow, *Oxygen-ion migration in perovskite-type oxides*. J. Solid State Chem., 1995. **118**(1): p. 125-132.
5. Flores-Ramirez, R., et al., *Curie-Weiss behavior in polycrystalline barium titanate from ac measurements*. Ferroelectrics, 1989. **99**: p. 195-201.
6. Rupprecht, G. and R.O. Bell, *Dielectric Constant in Paraelectric Perovskites*. Phys. Rev., 1964. **135**(3a): p. A748.
7. Nakamura, E., T. Mitsui, and J. Furuichi, *A Note on the Classification of Ferroelectrics*. J. Phys. Soc. Jpn., 1963. **18**(10): p. 1477-1481.
8. Hirose, N. and A.R. West, *Impedance spectroscopy of undoped BaTiO₃ ceramics*. J. Am. Ceram. Soc., 1996. **79**(6): p. 1633-1641.
9. Wu, T.B. and J.N. Lin, *Transition of compensating defect mode in niobium-doped barium-titanate*. J. Am. Ceram. Soc., 1994. **77**(3): p. 759-764.
10. Chan, N.H. and D.M. Smyth, *Defect Chemistry of Donor-Doped BaTiO₃*. J. Am. Ceram. Soc., 1984. **67**(4): p. 285-288.
11. Nowotny, J. and M. Rekas, *Defect chemistry of BaTiO₃*. Solid State Ionics, 1991. **49**: p. 135-154.
12. Yoo, H., C. Song, and D. Lee, *BaTiO_{3-δ}: Defect Structure, Electrical Conductivity, Chemical Diffusivity, Thermoelectric Power, and Oxygen Nonstoichiometry*. J. Electroceram., 2002. **8**: p. 5-36.
13. Bhuiyan, M.R.A., et al., *Synthesis and Characterization of Barium Titanate (BaTiO₃) Nanoparticle*. International Journal of Material and Mechanical Engineering, 2012. **1**: p. 21-24.
14. Morrison, F.D., D.C. Sinclair, and A.R. West, *Electrical and structural characteristics of lanthanum-doped barium titanate ceramics*. J. Appl. Phys., 1999. **86**(11): p. 6355-6366.

15. Song, H.W., et al., *Studies of shallow levels in undoped and rhodium-doped barium titanate*. J. Opt. Soc. Am. B., 1998. **15**(4): p. 1329-1334.

Chapter 7: Quantification of size, strain and charge effects

7.1: Separation of size, strain and charge effects on T_C

As discussed in chapter 5, the simple cation size explanation as to the changes in T_C as a result of dopant addition to BaTiO_3 is not able to fully explain the effects observed in experimental data. The inclusion of strain variance effects and B-site charge dilution is also required to qualitatively understand changes in the rate of reduction of T_C .

By selecting ions of appropriate sizes and charges, it should be possible to somewhat separate out the contributions of:

- long range size effects (based on tolerance factor)
- short range strain effects (based on variance)
- B-site charge dilution

In an ideal cubic perovskite, ions would be of the exact size required to give a tolerance factor of one. This would result in an unstrained structure. Due to the fact that ion choices of an appropriate charge and radius are limited, it is not possible to form a series of A-site/B-site co-doped barium titanate compositions with insignificant strain-variance and no B-site charge dilution in order to study size effects alone. Similarly it is not possible to study either strain variance or charge dilution effects without having a component to the change in T_C arising due to long-range size effects of the dopant species. However, it is possible to choose ions such that the contribution due to strain and charge are minimised, resulting in any changes to T_C arising largely as a result of size. Once an approximate effect of size is established, ions can be selected that have a considerable strain contribution to T_C , but no charge effect. This allows for calculations on the effect of strain-variance on T_C . Similarly ions can then be selected to calculate the effects on T_C as a result of

charge dilution. The doped systems studied for this work were chosen specifically with this in mind.

Although the calculations may not be exact as no system will truly have zero-strain, and assumptions will be required to approximate size-only effects in strained systems or charge diluted systems, it should be possible to look at the relative magnitudes of the effects to establish which factors have the greater effect on T_C . This could be useful in understanding and predicting the effects of on T_C caused by the addition of other dopants. Thus, in this chapter, attempts are made to more quantitatively deconvolute the effects on T_C caused by size, strain variance and charge dilution as introduced in chapter 5.

7.2: Quantifying size, strain and charge effects

SrTiO_3 is a well-studied material with a perovskite structure akin to that of BaTiO_3 . It has a tolerance factor of 1.00 and remains cubic down to a temperature of 105 K^[1]. It has very low strain, and is as close to an ideal titanate-based cubic perovskite as can be made, given the limitations of nature.

The addition of strontium to BaTiO_3 results in no charge dilution effects due to the dopant being isovalent. The A-site variance, shown in figure 7.1-left, is also considerably lower than the other dopants studied, especially at low dopant concentrations. Thus, the addition of strontium to BaTiO_3 results in a change in T_C that is mostly driven by long-range size effects. These size effects can be quantified by a change in the tolerance factor. As shown in chapter 5, the tolerance factor decreases linearly with varying average cation size as a result of doping. The use of tolerance factor is therefore a useful metric by which to compare size-only effects. Variance as a function of tolerance factor is shown in figure 7.1-right.

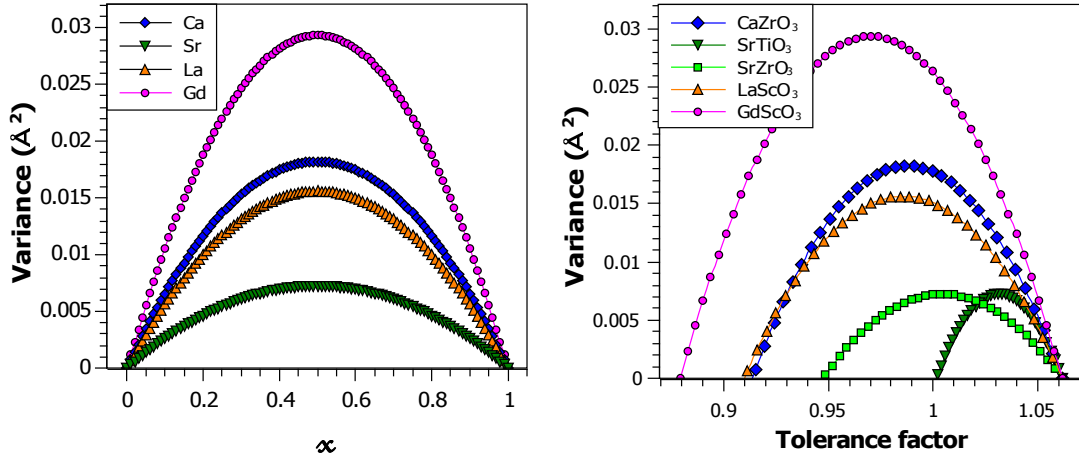


Figure 7.1: Dopant concentration dependence of A-site variance in doped BaTiO₃ as function of x in $(1-x)\text{BaTiO}_3 \cdot x\text{ABO}_3$ (left) and tolerance factor (right)

The addition of SrTiO₃ is known to result in a drop in T_C , equivalent to $-3.7 \text{ K } \%^{-1}$ [2] and is constant for all concentrations of strontium doping. As the isovalent A-site dopant closest in size, and hence of lowest variance, Sr is the most suitable choice to approximate the size-only effect on T_C . This can then be extrapolated for other dopant species.

The change in the average cation radius resulting from doping with SrTiO₃ changes the value of the tolerance factor. Thus, it is possible to calculate the change in the tolerance factor that occurs with 1 % SrTiO₃ doping, equations 7.1 and 7.2. As there is no charge dilution, and the variance is minimal, this change in tolerance factor, a measure of the long-range size effects, can be equated as resulting in a 3.7 K reduction in T_C .

$$t = \frac{r_A + r_O}{\sqrt{2} \cdot (r_B + r_O)} \quad \text{Equation 7.1}$$

$$r_A = (1 - x)r_{Ba} + x \cdot r_{Sr} \quad \text{Equation 7.2}$$

The tolerance factor of un-doped BaTiO₃ can be calculated as 1.0615, and is equal to 1.0609 for 1 % SrTiO₃-doped BaTiO₃. Thus, a change of 5.9954×10^{-4} of the tolerance factor can be said to result in change of -3.7 K in T_C .

Using cation radii values taken from Shannon et al.^[3], it is possible to calculate the change in the tolerance factor for each of the dopants studied at each composition,

based on the change to both the A-site and B-site average radii. By dividing the change in the tolerance factor, Δt , by 5.9954×10^{-4} and multiplying by -3.7, it is possible to calculate the size-only change to T_C , which shall be termed α . If this is then subtracted from T_C for un-doped BaTiO_3 , it is possible to calculate a predicted, size-only Curie temperature, T_α . This is shown for each sample in table 7.1, and depicted graphically in figure 7.2[†].

Table 7.1: Changes to the tolerance factor as a result of A-site and B-site cation doping, with calculated size-only effects on T_C

SrZrO_3	t	Δt	α (K)	T_α (K)	CaZrO_3	t	Δt	α (K)	T_α (K)
0	1.0615	0	0	387	0	1.0615	0	0	387
2	1.0591	0.002414	-14.90	372.10	2	1.0584	0.003119	-19.25	367.75
5	1.0555	0.006025	-37.18	349.82	5	1.0536	0.007783	-48.03	338.97
8	1.0519	0.009623	-59.39	327.61	8	1.0491	0.012432	-76.72	310.28
12	1.0471	0.014401	-88.87	298.13	12	1.0429	0.018605	-114.82	272.18
LaScO_3	t	Δt	α (K)	T_α (K)	GdScO_3	t	Δt	α (K)	T_α (K)
0	1.0615	0	0	387	0	1.0615	0	0	387
2	1.0583	0.003241	-20.00	367.00	2	1.0576	0.003894	-24.03	362.97
5	1.0535	0.008086	-49.90	337.10	5	1.0518	0.009715	-59.96	327.04
8	1.0486	0.012911	-79.68	307.32	8	1.0460	0.015512	-95.73	291.27
12	1.0422	0.019313	-119.19	267.81	12	1.0383	0.023204	-143.20	243.80

[†] In order to calculate changes to T_C a starting value for un-doped BaTiO_3 must be included. This value is often quoted as 392-400 K, however the values obtained in ceramic materials is often slightly lower, likely due to the presence of small amounts of impurities or defects. In order to allow for comparison with the experimentally observed values, the T_C used here for un-doped BaTiO_3 is 387 K, determined from ceramic samples sintered as described in chapter 4.

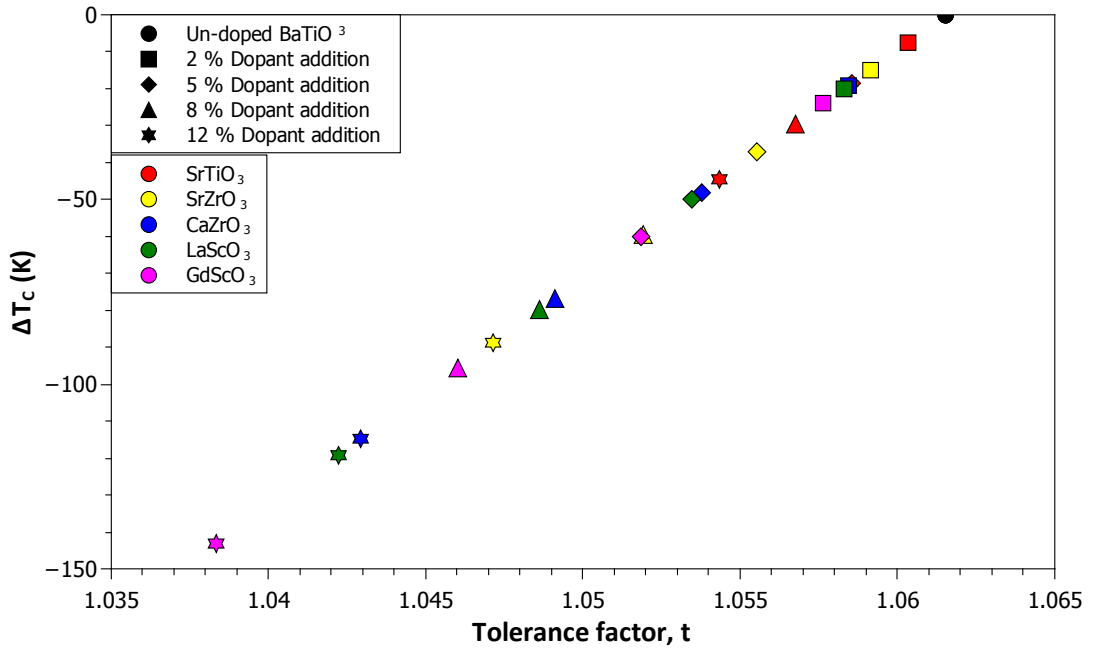


Figure 7.2: Predicted size-only Curie Temperatures, T_α for different dopants and dopant concentrations as a function of tolerance factor

As expected, the data in figure 7.2 shows a linear decrease in the predicted, size-only transition temperature, T_α , with increasing dopant concentration (decreasing tolerance factor, t). A tolerance factor of 1 would be expected for an ideal cubic system. For SrTiO_3 -doped BaTiO_3 to be considered a good system for a size-only model, it would be expected that the T_α would be equal to 0 K when the tolerance factor is unity. From extrapolation of a line of best fit in figure 7.2, $T_\alpha = 7.3$ K for $t = 1$. This suggests that SrTiO_3 -doped BaTiO_3 can be considered to be a good approximation for modelling size-only effects.

Figure 7.2 also shows that T_α for equivalently doped CaZrO_3 and LaScO_3 compositions are very similar, and that size only predictions would suggest that GdScO_3 doping should yield the lowest T_c values.

If the experimentally determined T_c values are superimposed on to the predicted T_α values, the effects of strain variance and charge dilution can start to be appreciated, table 7.2 and figure 7.3.

Table 7.2: Experimental T_c values and predicted size-only T_α values for CaZrO_3 , SrZrO_3 , LaScO_3 and GdScO_3 dopants at varying concentrations

Dopant (%)	SrZrO_3		CaZrO_3		LaScO_3		GdScO_3	
	T_α (K)	T_c (K)	T_α (K)	T_c (K)	T_α (K)	T_c (K)	T_α (K)	T_c (K)
2	372.10	376	367.75	385	367.00	347	362.97	363
5	349.82	362	338.97	376	337.10	270	327.04	328
8	327.61	345	310.28	370	307.32	188	291.27	300
12	298.13	342	272.18	313	267.81	90	243.80	204

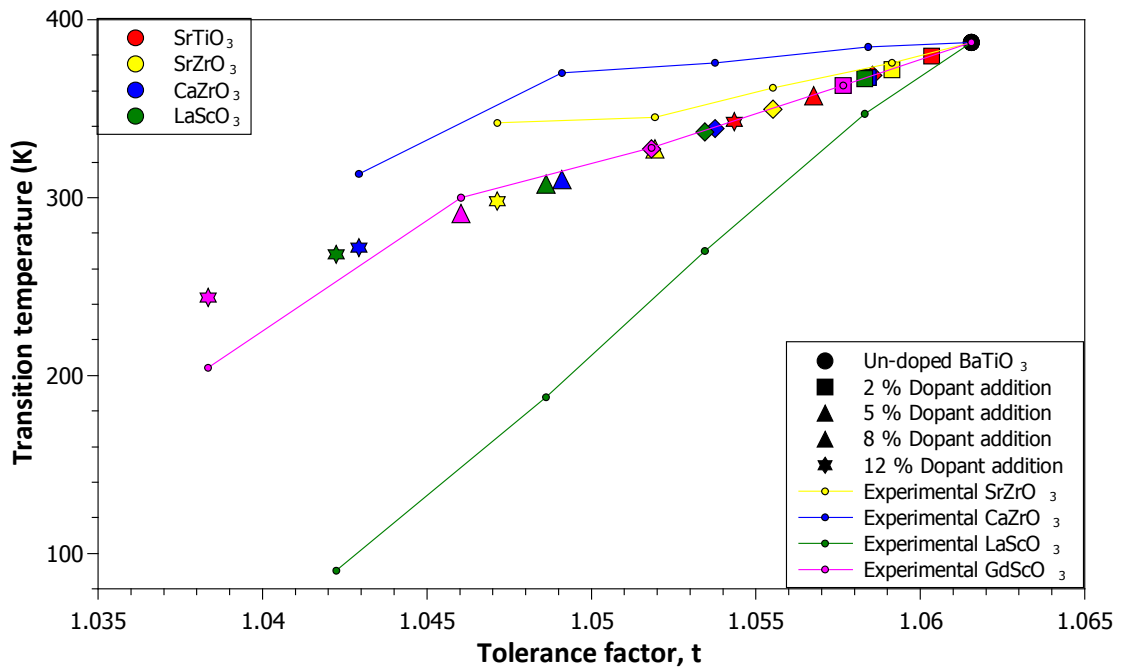


Figure 7.3: Comparison of predicted, size-only and experimentally determined Curie temperatures (T_α and T_c , respectively) as a function of tolerance factor

This data would suggest that LaScO_3 dopant addition causes a substantial reduction in T_c , at a much greater rate than is expected based on size arguments alone, but that CaZrO_3 -doping which has similar expected size-only effects to LaScO_3 (and thus, similar strain-variance), experimentally gives T_c values which are greater than T_α . This would suggest that there is a considerable difference due to the B-site charge dilution on LaScO_3 doping. However, GdScO_3 doping has the best fit to T_α , despite having the smallest A-site species, which should result in an significant decrease due

to size, and a +3 B-site which should further lower T_C due to charge dilution. Thus, it appears that the greater strain variance in this system might be off-setting these effects.

Calcium doping is known to have a significant A-site strain variance effect which initially raises T_C . When the experimentally observed T_C values are corrected for this to approximate a size-only effect, the corrected values show the expected linear decrease at a rate of $\sim 10 \text{ K } \%^{-1}$ Ca doping^[4]. Thus, having calculated T_α , the difference in predicted T_α and measured T_C should give an estimate of the contribution to T_C as a result of strain. This temperature off-set will hereafter be termed, $T_{\beta(\text{Ca})}$.

As introduced in chapter 1, and discussed in chapter 5, variance can be calculated by a parabolic expression as described by equation 7.3^[4, 5]. For a two cation system, however, this simplifies to equation 7.4.

$$\sigma^2 = \langle r_A^2 \rangle - \langle r_A \rangle^2 \quad \text{Equation 7.3}$$

$$\sigma^2 = x(1 - x)(r_{Ba} - r_M)^2 \quad \text{Equation 7.4}$$

where σ^2 is the size variance (a measure of the local strain), r_A is the average A-site cation radius r_{Ba} and r_M are the radii of barium and the A-site dopant, respectively.

At 0% and 100% doping the strain variance is necessarily zero, figure 7.1. Thus, by extrapolating the size-only effect to 100 % doping and comparing this with the transition temperature of un-doped BaTiO_3 (0 % doping) it is possible to fit a second order polynomial curve to the experimental data collected on doped BaTiO_3 compositions between these two points. The resulting fit gives the transition temperatures, T_{fit} . If the linear, size-only function for T_α is also calculated between 0 and 100 % doping, the difference between the size-only model, T_α , and the fit to experimental data, T_{fit} , as a function of tolerance factor should represent the contribution of the strain variance. This approach is shown for the CaZrO_3 -doped BaTiO_3 compositions in figure 7.4. The equations of the polynomial fit to the experimental data and the linear size-only effect are given by equations 7.5 and 7.6, respectively.

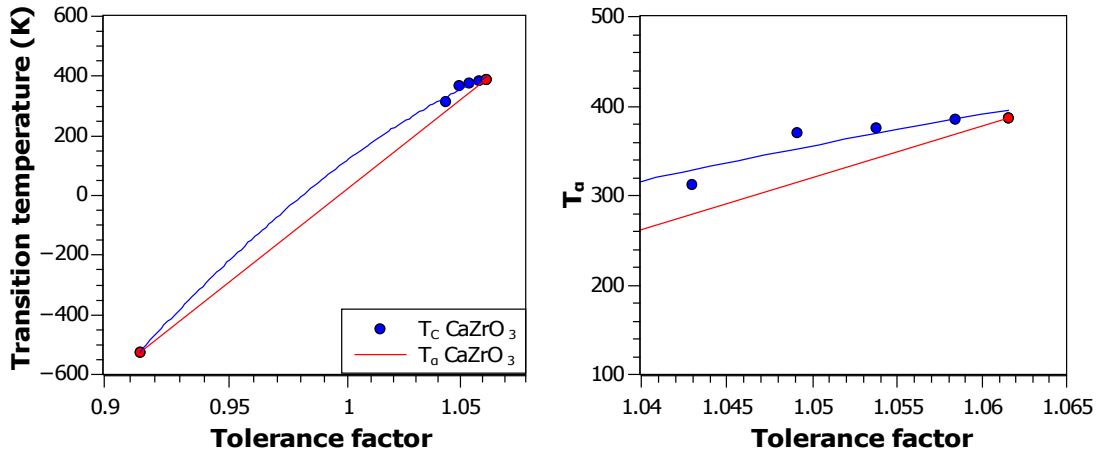


Figure 7.4: Predicted, size-only relationship between tolerance factor and transition temperature (red), and experimental data fitted to a second order polynomial, (blue) for CaZrO₃-doped BaTiO₃

$$\begin{aligned}
 T_{fit} = & (-2.022 \times 10^4 \pm 7.413 \times 10^3)x^2 \\
 & + (4.618 \times 10^4 \pm 1.461 \times 10^3)x \\
 & - (2.584 \times 10^4 \pm 7.156 \times 10^3)
 \end{aligned}
 \tag{Equation 7.5}$$

$$T_\alpha = 6.170 \times 10^3 x - 6.163 \times 10^3
 \tag{Equation 7.6}$$

When the linear function, T_α , is subtracted from the second order polynomial T_{fit} , the resultant arc is found to appear parabolic (figure 7.5-left), which is the response expected as a result of strain variance, figure 7.1. This strongly suggests that the deviation from linearity observed in the CaZrO₃-doped compositions is indeed related to a strain variance effect. In order to confirm this, $T_{fit} - T_\alpha$ was normalised and plotted alongside the normalised statistical variance parabola for CaZrO₃, figure 7.5-right).

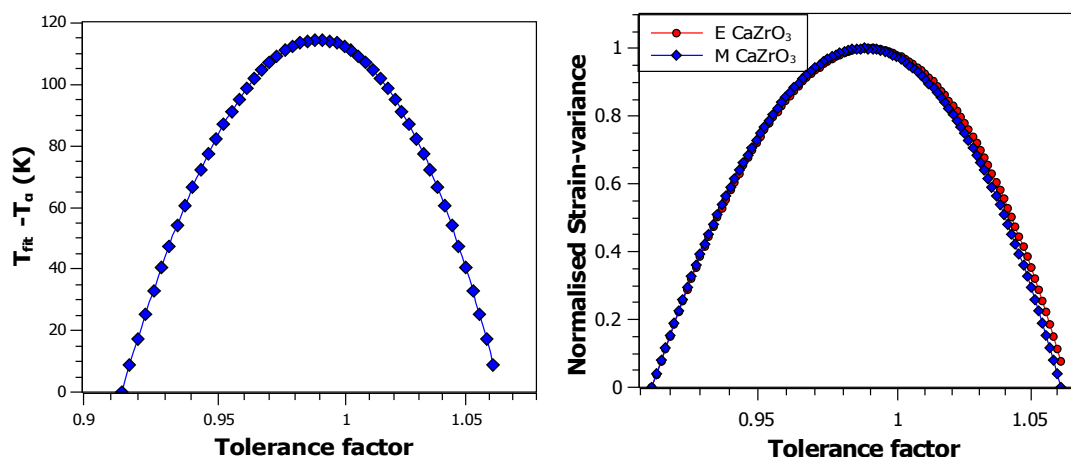


Figure 7.5: Left: Difference in transition temperatures predicted by size-only effects and fit of experimental data to a second order polynomial Right: Normalised (experimental) temperature difference, E (red), and (model) strain variance, M (blue), for CaZrO_3 -doped BaTiO_3

This figure shows a very good fit between the mathematical model for statistical variance and the fitted second order polynomial based on experimental data, with only a very slight asymmetry observed, suggesting that the approximation for size-only effects is appropriate and that the non-linearity is resultant of a strain variance effect, which will be termed β . Thus, the fitted polynomial can be considered to be a fit of the combined size-only and strain variance effects, $T_{\alpha\beta}$, and is able to effectively model the experimental effects on T_c caused by dopant addition.

Using equations 7.5 and 7.6, it is possible to work out the difference between the linear, size-only effects, α , and the parabolic strain effect, β . With these values listed for CaZrO_3 in table 7.3. (full derivation is shown in appendix 7.1).

Table 7.3: Calculated strain effects for CaZrO_3 -doped BaTiO_3

% CaZrO_3	$\beta_{(\text{Ca})}$ (K)	$\beta_{(\text{Ca})} \%^{-1}$ (K)
0	0	0
2	13.33	6.67
5	20.32	4.06
8	24.68	3.09
12	30.379	2.53

These values are seen to decrease with increasing dopant addition, suggesting that although the maxima in the strain variance should occur at 50 % dopant concentration, the effect of combining the linear decrease in T_C , due to size only effects, with the parabolic (polynomial) arc of strain-variance effects, causes the impact of the strain effects to be reduced with increasing cation doping.

The value of β should be very similar for the equivalent LaScO_3 -doped compositions due to the very similar sizes of the A-site dopant, 1.34 Å and 1.36 Å for calcium and lanthanum, respectively. Thus, if the same values are assumed for β as for the equivalent calcium composition, it is possible to establish a model size-only, α , and strain-variance only, β , term for each LaScO_3 composition. The difference between the sum of these two effects and the experimentally observed T_C should be equal to the effect on T_C due to the lower B-site charge. This charge-dilution factor shall be termed, γ .

The calculated values for $\gamma_{(\text{La})}$ are shown in table 7.4.

Table 7.4: Calculated charge displacement effects, γ , on T_C for LaScO_3 -doped BaTiO_3

% LaScO_3	T_C (K)	α (K)	$\beta_{(\text{Ca})}$ (K)	$\gamma_{(\text{La})}$ (K)	$\gamma_{(\text{La})}$ (K) % ⁻¹
0	387	0	0	0	0
2	347	-20	13.33	-33.33	-16.67
5	270	-49.9	20.32	-87.42	-17.48
8	188	-79.68	24.68	-144.00	-18.0
12	90	-119.19	30.379	-208.189	-17.35

This table shows the effects on T_C of 387 K for un-doped BaTiO_3 on doping. The expected size-only effect should reduce T_C by the predicted amount, α . The strain effect, β , is able to partially off-set this fall in T_C , but the charge dilution effect, γ , results in a catastrophic reduction in T_C . This results in the very low values of T_C

observed for LaScO_3 compositions. This data also shows that the γ -factor varies approximately linearly with dopant concentration, and is equal to $\sim -17.4 \text{ K } \%^{-1}$.

As GdScO_3 has exactly the same B-site species, the effect of T_C of charge dilution, γ , should be very similar for both LaScO_3 and GdScO_3 doping at equivalent concentrations. This allows an approximation of using the same γ values for equivalent GdScO_3 - and LaScO_3 -doped compositions to be made. Combining this with the calculated size-only, α , effect allows for the calculation of the strain variance component. This is combined by simply adding the size-only, α , and charge dilution, γ , effects and results in a steeper, but still linear, combined size and charge effect, which can be observed in figure 7.6. The parabolic strain effect, $\beta_{(\text{Gd})}$, can be then be superimposed onto this line by fitting to a second order polynomial, as with the CaZrO_3 plots. This is shown in figure 7.6, along with the CaZrO_3 data, shown as a reference to observe the scale of $\beta_{(\text{Gd})}$ compared to that of $\beta_{(\text{Ca})}$.

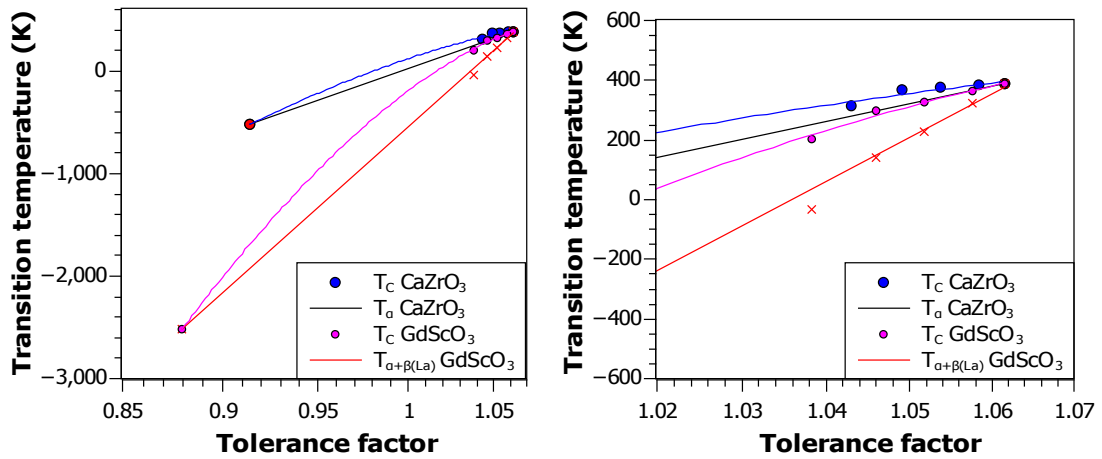


Figure 7.6: Predicted, size-only relationship between tolerance factor and transition temperature, and experimental data fitted to a second order polynomial representing the effects of strain variance for CaZrO_3 - and GdScO_3 -doped BaTiO_3

This shows the considerable reduction in T_C caused by the dipole dilution being offset by the strain factor, $\beta_{(\text{Gd})}$, which is required to be considerably greater than that of $\beta_{(\text{Ca})}$ in order to give the experimentally determined values. This is consistent with the considerably greater variance that arises as a result of having such a small A-site species in the GdScO_3 -doped compositions.

The equations corresponding to the second order polynomial fitting of the strain-variance, size and charge effects, $T_{\alpha\beta\gamma}$, and the linear, combined size and charge effects, $T_{\alpha\gamma}$, are given in equations 7.7 and 7.8 respectively.

$$T_{\alpha\beta\gamma} = (-5.311 \times 10^4 \pm 4.404 \times 10^3)x^2 + (1.190 \times 10^5 \pm 8.514 \times 10^3)x - (6.611 \times 10^5 \pm 4.083 \times 10^3) \quad \text{Equation 7.7}$$

$$T_{\alpha\gamma} = (1.588 \times 10^4 \pm 1.479 \times 10^2)x - (1.649 \times 10^4 \pm 1.479 \times 10^2) \quad \text{Equation 7.8}$$

The strain-variance effects, $\beta_{(\text{Gd})}$, calculated using equations 7.7 and 7.8 and are given in table 7.5, with full working shown in appendix chapter 7.

Table 7.5: Calculated strain effects for GdScO₃-doped BaTiO₃

% GdScO ₃	$\beta_{(\text{Gd})}$ (K)	$\beta_{(\text{Gd})} \%^{-1}$ (K)
0	0	0
2	52.15	26.08
5	103.92	20.78
8	151.89	18.99
12	210.14	17.50

As with the CaZrO₃, the difference between the fitted second order polynomial curve and the linear function can be calculated and normalised. This can then be plotted alongside the normalised parabolic curve expected for GdScO₃ strain-variance. This is shown in figure 7.7.

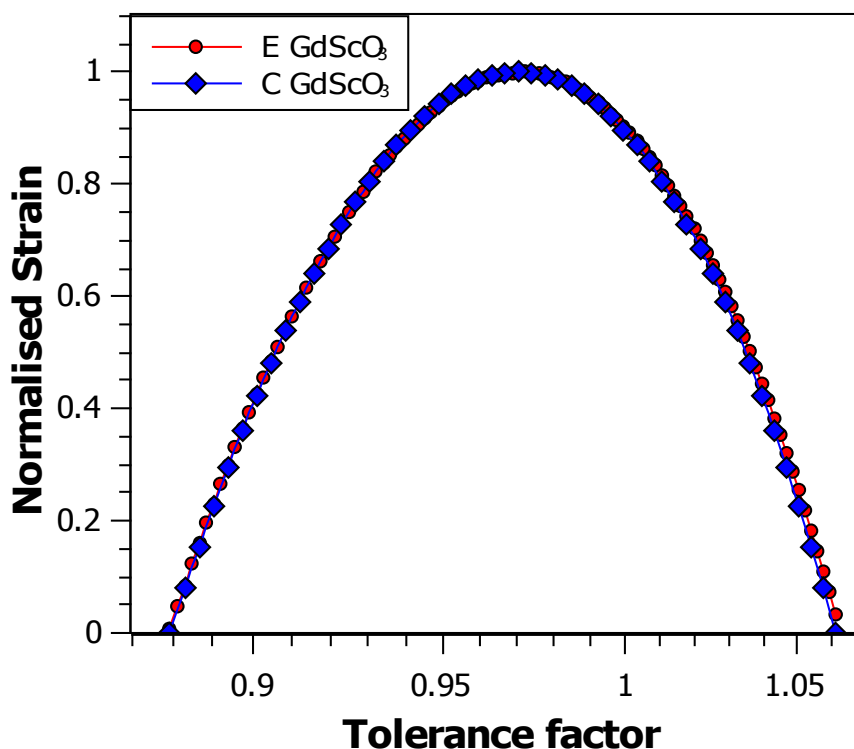


Figure 7.7: Normalised experimentally fitted second order polynomial function, E. (shown in red) (equ.7.4) and the normalised mathematical model parabola of statistical strain-variance in CaZrO_3 -doped BaTiO_3 , M, (blue)

As with the CaZrO_3 -doped compositions, there is excellent agreement with very little asymmetry, strongly suggesting that the strain variance model can be considered to be appropriate and result in good fits with the experimental data.

7.3: Discussion

The experimental data collected on these samples shows that while the LaScO_3 and SrZrO_3 compositions have approximately linear trends in T_C with dopant addition, CaZrO_3 and GdScO_3 doping show a distinct curvature, which cannot be rationalised by size-only effects. The incorporation of strain effects to account for the curvature observed in experimental T_C values for calcium doped BaTiO_3 is an established idea^[4, 5]. It is generally carried out quantitatively by extrapolating T_α to 100 % dopant addition, at which point the variance necessarily becomes zero, as shown in figure 7.1. Unlike previous studies which generally only involve A-site dopants, the size-only effects included the effect of B-site doping in calculations of the tolerance factor.

Fitting a second order polynomial expression to the data between 0 and 100% dopant addition allowed for the mathematical model for variance (a parabolic

function) to be scaled to the experimental data, incorporating the size-only, linear effect. This allowed for independent calculation of the variance (strain) effect, labelled as $\beta_{(\text{Ca})}$. Subtraction of the linear function from the polynomial fit, and normalisation of the residual arc, allowed for comparison with the normalised parabolic expression for the statistical strain variance. It was observed that in each case, the fitted CaZrO_3 and GdScO_3 arcs, had good agreement with the parabolic variance function, showing very little asymmetry. This suggests that the methodology and approximations used are applicable and able to predict ΔT_c with reasonable accuracy.

The impact on T_c of a size-only effect was approximated from SrTiO_3 -dopant addition to BaTiO_3 . LaScO_3 dopant addition was assumed to have the same magnitude of strain effects as the equivalently doped CaZrO_3 compositions, on account of similar A-site cation sizes. For aliovalent substitution, the effect of charge dilution, γ , was then estimated and was found to vary linearly with dopant concentration. This was not a requirement of the mathematical model, which could have yielded any trend in γ depending on the experimental data. The fact that the charge-dilution effect was found to be approximately linear suggests that the models used were able to effectively separate and account for the contributions to T_c due to size-only, strain-variance and charge-dilution effects, at least of the composition range studied. The polarisation should be linearly dependant on the percentage of Ti^{4+} cations replaced with Sc^{3+} cations. This is due to the charge dilution effect being resultant of the lower polarisation that arises when a B-site species of lower charge is displaced.

Like CaZrO_3 -doped compositions, the addition of GdScO_3 as a dopant was found to result in a distinctly non-linear trend in T_c . This is consistent with the small A-site Gd^{3+} species resulting in a high degree of strain which is able to off-set much of the size-only and charge-dilution effects which act to reduce T_c . The calculated strain variance values, $\alpha_{(\text{Gd})}$ were found to be considerably greater than the equivalent $\alpha_{(\text{Ca})}$ values, which is consistent with Gd^{3+} having a significantly smaller cation radius.

7.4: Conclusions

Whilst this data analysis is based on several approximations, and is somewhat limited due to the number of samples, this analysis route is able to account for size, strain and charge effects on T_C . Given that the highly strained compositions yield data that can be fitted well to second order polynomial function, and which show little asymmetry or deviation from the expected parabolic strain variance functions, and that charge displacement effects were found to vary approximately linearly with dopant addition, over the compositional range studied, it is suggested that this analysis methodology is appropriate for these systems. Thus, these approximations can be used to effectively predict ΔT_C due to size, strain and charge effects. However, data were only collected at dopant concentrations up to 12 %, thus the accuracy and applicability of the models beyond this dopant concentration cannot be verified and would require further research.

This data analysis shows that the effect on T_C due to B-site charge dilution and size only effects; where the A-site dopant species is of smaller ionic radii than Ba^{2+} or the B-site dopant is of greater ionic radii than Ti^{4+} , all result in a decrease in T_C . This is due to a reduction in the stabilisation energy of the system when an ion of lower charge displaces, and due to a reduction in the tolerance factor of the material, respectively. In contrast the effect of high strain stabilises the distorted polymorphs which has the effect of increasing T_C . *i.e.* α and γ are always found to be negative, whilst β is always found to be positive. These values are summarised in table 7.6.

Table 7.6: Effects of size, strain and charge dilution on T_C for each percentage of dopant added

Value per % of dopant	2 % dopant	5 % dopant	8 % dopant	12 % dopant
$T_{\alpha(\text{SrZrO}_3)}$	-7.45	-7.45	-7.45	-7.45
$T_{\alpha(\text{CaZrO}_3)}$	-9.63	-9.63	-9.63	-9.63
$T_{\alpha(\text{LaScO}_3)}$	-10.0	-10.0	-10.0	-10.0
$T_{\alpha(\text{GdScO}_3)}$	-12.01	-12.01	-12.01	-12.01
$T_{\beta(\text{Ca})}$	6.67	4.06	3.09	2.53
$T_{\beta(\text{Gd})}$	26.08	20.78	18.99	17.50
$T_{\gamma(\text{La})}$	-16.67	-17.48	-18.00	-17.35

The magnitude of the charge displacement effect is considerably bigger than that of the size-only effects. Thus, doping with a +3 B-site cation, rather than incorporating smaller A-site cations, more rapidly reduces T_C .

This data also shows that despite T_C falling rapidly with the incorporation of a lower charged B-site species, this reduction in T_C can be overcome by the addition of a suitably small A-site species. In this instance, GdScO_3 was not able to fully overcome the combined effect of size and charge, to give a higher T_C than the un-doped BaTiO_3 , but this work suggests that a slightly smaller A-site species might be able to produce an increase in T_C . However, previous studies with dopants including dysprosium and thulium have not yielded higher TC values^[6], one issue with working with such ions is that there is a tendency for the ions to dope onto both the A- and B-site^[7]. Despite its limitations, the sort of analysis presented here may be useful in suggesting future compositions which may have a particularly desired T_C .

References

1. Loetzsch R., et al., *The cubic to tetragonal phase transition in SrTiO₃ single crystals near its surface under internal and external strains*. Appl. Phys. Lett., 2010. **96**.
2. Jaffe, B., W.R. Cook, and H. Jaffe, *Piezoelectric Ceramics*. 1971: Academic Press London.
3. Shannon, R.D., *Revised Effective Ionic Radii and Systematic Studies of Interatomic Distances in Halides and Chalcogenides*. Acta Cryst. A, 1976. **32**(751).
4. Sinclair, D.C. and J.P. Attfield, *The influence of A-cation disorder on the Curie temperature of ferroelectric ATiO₃ perovskites*. Chem. Commun., 1999(16): p. 1497-1498.
5. Attfield, J.P., *A simple approach to lattice effects in conducting perovskite-type oxides*. Chem. Mater., 1998. **10**(11): p. 3239-3248.
6. Kim, J. and H. Lee, *Substitutional analysis of perovskite-type dysprosium and thulium co-doped barium titanate ceramics by a near edge X-ray absorption fine structure*. Mater. Lett., 2013. **92**(0): p. 39-41.
7. Tsur, Y., T.D. Dunbar, and C.A. Randall, *Crystal and defect chemistry of rare earth cations in BaTiO₃*. J. Electroceram., 2001. **7**(1): p. 25-34.

Chapter 8: Conclusions and future work

8.1: Conclusions

The objective of this work was to study the effects of dopant addition to BaTiO_3 , focusing on A-site/B-site co-dopant pairs. It was hoped that as well as understanding the effects caused by a single co-dopant pair of ions, it might be possible to compare different dopant pairs in order to better understand what properties of the ions correspond to which effects in the doped composition. In particular, the work aimed to look at the effect of changing the cation size, resulting in changes to both tolerance factor (size) and variance (strain), as well the effect of changing the charge of the B-site ion.

A key feature of this work was that the new materials synthesised were lead-free due to EU restrictions on the use of lead in new devices.

This work showed the importance of sintering conditions on the properties of the materials. While isolated pores were found to have negligible negative effects on either T_C or the relative permittivity, extended propagating cracks resulted in pellets unsuitable for electrical measurements, with the relative permittivity severely reduced. By altering the way that pressure was applied (from uniaxially to isostatically) to form the pellets prior to sintering it was found that the prevalence of propagating cracks could be greatly reduced. This was attributed to lower strain gradients in the isostatically pressed pellets.

Inhomogeneity of the pellets was shown to have significant impact on the pellet properties; these inhomogeneities arise either as a result of grain boundary and bulk regions or due to an uneven distribution of dopant ions throughout the material. Poorly defined grain boundary regions accounting for a significant volume fraction of the pellets were shown to result in a significant broadening of T_C , accompanied by a reduction in the maximum of the relative permittivity. Such materials are said to be

capped and are often accompanied by a slight, artificial increase in T_C . Uneven dopant ion distributions were also shown to suppress and broaden T_C as well as give rise to additional features in the relative permittivity as a result of minor phases.

For LaScO_3 doped compositions, relaxor ferroelectric type characteristics could be observed as a result of air or moisture sensitivity pre-sintering. In each case the effects of air/moisture sensitivity on pellet inhomogeneity could not be observed by powder X-ray diffraction analysis of the materials. Instead variable temperature, variable frequency impedance spectroscopy data analysis was required to determine the effect of the microstructure on the physical properties of each pellet. This information is of great significance when designing procedures for checking the properties of materials and their reproducibility, in order to be confident that a device which incorporates such materials has the desired properties.

It was also found that by carefully controlling the sintering conditions it was possible to minimise these effects, producing optimised pellets, the properties of which could be deemed to be characteristic of the composition as opposed to the microstructure. Thus, it was shown that by altering the synthesis route, the properties of materials could be considerably altered and improved.

A series of 2, 5, 8 and 12 % CaZrO_3 -, SrZrO_3 -, LaScO_3 - and GdScO_3 -doped BaTiO_3 compositions were synthesised, with these dopants chosen based on their cation size and charge. It was found that the addition of CaZrO_3 , SrZrO_3 or LaScO_3 each resulted in the formation of a PPB, while the addition of GdScO_3 was found to stabilise the tetragonal polymorph. This was attributed to the small size of Gd^{3+} compared to either BaTiO_3 or any of the other A-site dopants studied, enabling the off-centring of the A-site in an anti-polar displacement. This resulted in a stabilisation of the tetragonal polymorph.

Thus, by changing the dopant ions, it was possible to form materials with either heightened dielectric properties over a narrow temperature range due to the presence of a PPB, or to produce materials with stable dielectric properties over a wide range in temperature. Each of these features can be of use in various types of

devices depending on whether wide operating temperatures or maximum dielectric responses are the desired goal. Enhanced piezoelectric properties can also be expected to be present alongside the increased dielectric responses.

Varying the dopant type and concentration also affected the conductivity of the materials. Activation energies calculated for the bulk regions of each composition were found to be either ~ 0.6 eV or ~ 1.1 - 1.3 eV, with a change in gradient being observed in the both the 2 % and 5 % CaZrO_3 -doped BaTiO_3 compositions. For each of these two materials, the activation energies calculated from the gradient of each region corresponded to both ~ 0.6 eV and ~ 1.1 - 1.3 eV. Thus, it was determined that two conductivity mechanisms were being observed, corresponding to the two different activation energies. By altering the temperature of the material, it was possible, in both the 2 % and 5 % CaZrO_3 -doped BaTiO_3 compositions, to change between the two conduction mechanisms.

Based on activation energies quoted for similar materials in scientific literature^[1-3], it is suggested that these two conductivity mechanisms are due to n-type and p-type conduction mechanisms respectively, however it is also possible that ionic conduction mechanisms may be occurring. Thus, it is possible that the change in activation energy occurs due to a change between electronic and ionic conduction contributions. More work is required to discern the exact conduction mechanisms which dominate in each case. Though these conduction mechanisms exist above T_C and thus outside the temperature range over which dielectric properties are observed, understanding the conduction mechanism offers valuable insights into the types of defects present in the material.

The importance of strain and charge, as contributing factors to changes in T_C of perovskite based materials was highlighted. By understanding what causes T_C to alter when dopant species are added to BaTiO_3 it may become possible to predict dopant species and concentrations required to produce materials with suitable operating temperatures for particular applications. This has even wider significance for controlling or predicting the properties of other perovskite piezo-, pyro- or ferroelectric materials. This work found that lowering the charge of the B-site cation

was the dominating factor causing a dramatic decrease in T_C . T_C was further decreased by the effect of introducing smaller cations which reduced the tolerance factor. Although the combined reduction in T_C could be partially off-set by high strains, caused by small A-site species, it could not be overcome completely by these strain-variance effects. However, the effect of localised strain could be greater than the long range size effects, caused by introducing a A-site cation of considerable smaller ionic radii, where there was no change in the B-site valence.

This was demonstrated in LaScO_3 doping, which has a very similar A-cation radius to CaZrO_3 and thus very similar size and strain contributions to T_C . LaScO_3 doped BaTiO_3 has a significantly lower T_C than the corresponding CaZrO_3 -doped compositions. This was deemed to be resultant of the lower charged Sc^{3+} ion displacing compared to the Zr^{4+} ion. This would result in a lower polarisation and hence less stabilisation of the piezoelectric phases.

GdScO_3 -doping of BaTiO_3 introduces a much smaller A-site dopant than LaScO_3 and thus has a significantly greater strain-variance. Though T_C was still found to be lower than the correspondingly doped CaZrO_3 composition, it was considerably higher than the equivalent LaScO_3 composition. Thus, whilst B-site charge effects appear to be dominating T_C , this can be partially off-set by increasing strain in the material by the addition of a smaller A-site species.

Comparing the T_C 's of similarly doped CaZrO_3 and SrZrO_3 , which have the same ion charges, and accounting for long range size effects (described in chapter 7), showed that the CaZrO_3 compositions had higher T_C 's. This showed how the addition of a smaller A-site cation, resulting in a greater strain, could be the dominant factor effecting T_C . The increased variance has a greater impact than long range size effects, which would predict lower T_C 's for CaZrO_3 than the equivalently doped SrZrO_3 compositions.

Thus, this work would suggest that T_C might be maintained or improved by the addition of +5 B-site cations (with a +1 A-site co-dopant e.g. KNbO_3 - BaTiO_3), and/or the introduction of a considerable smaller A-site dopant resulting in large strain

gradients. Additionally, by varying the dopant concentration and the A-cation size it may be possible to form a material with either a PPB, with correspondingly enhanced piezoelectric properties over a narrow temperature range, or stabilise the tetragonal phase, resulting in lower but more stable relative permittivity, with a much wider temperature range.

8.2: Further Work

Further study into more dopant pairs is required to fully understand the implications of A-site/B-site self-compensating co-dopants on BaTiO₃. It would be interesting to study the effect of doping with other lanthanide scandates. This would result in a series of differently doped compositions with a constant B-site charge, but with increasingly strained systems. This would be able to show whether the effects of strain, caused by A-site variance, could ever dominate over the effect of having a lower charged (+3) cation on the B-site, and result in an increase in T_C . A mixture of different lanthanide species could also be used to create series of compositions with fixed average cation radii, $\langle r_A \rangle$, but varying variances, σ^2 . Such compositions would also be of great interest to study, with the aim of both better understanding the effects of strain-variance, and ideally forming compositions with higher T_C s.

It would also be interesting to study the series of REScO₃ doped BaTiO₃ compositions to see if any of the other dopants cause the tetragonal phase to stabilise over a wide temperature range. If the strain was increased due to an even smaller A-site dopant than Gd, the tetragonal phase may be further stabilised, resulting in wider operating ranges which may be suitable for a variety of piezoelectric devices.

The possibility of increasing T_C by doping with +1/+5 cations pairs would also be particularly interesting to study. A +1/+5 co-doped system would result in the higher charged +5 B-site species displacing, which should result in greater magnitudes of polarisation and stabilise the piezo-, pyro- or ferroelectric phases, yielding higher T_C 's. However, care would need to be taken to ensure that the more volatile +1 A-site cationic species were not lost during the material synthesis processes, which

could result in significant vacancies and other charge compensation routes which would impact of the properties of the materials.

Further work is required to fully understand the crystallographic phases of the materials, especially when phase coalescence has been achieved. This would require high resolution powder X-ray or neutron diffraction studies, perhaps focused on certain peaks, and with data collected at much more frequent temperature intervals so as to build up a full picture of the phase change. Work by Aksel et al.^[4] suggests that the process of grinding these sorts of materials from the sintered pellet into a powder suitable for powder X-ray diffraction increases the strain in the material, resulting in peak broadening which can mask the split nature of some of the peaks. This could account for the varying literature reports as to the space groups of each of the crystallographic phases. It would interesting to anneal some powders after grinding and see if this effect is observed, and if it might be possible to conclusively determine the space group of each phase.

Finally, it would also be interesting to incorporate some of these new materials into fully working devices, such as a transducer. This would make it possible to see how suitable these materials are for machining and to determine how easily the materials are depoled, either during device assembly or whilst in use, which would help to determine their suitability for use in various piezoelectric devices.

References

1. Morrison, F.D., D.C. Sinclair, and A.R. West, *Electrical and structural characteristics of lanthanum-doped barium titanate ceramics*. J. Appl. Phys., 1999. **86**(11): p. 6355-6366.
2. Song, H.W., et al., *Studies of shallow levels in undoped and rhodium-doped barium titanate*. J. Opt. Soc. Am. B., 1998. **15**(4): p. 1329-1334.
3. Wu, T.B. and J.N. Lin, *Transition of compensating defect mode in niobium-doped barium-titanate*. J. Am. Ceram. Soc., 1994. **77**(3): p. 759-764.
4. Aksel, E., et al., *Monoclinic crystal structure of polycrystalline $\text{Na}_{0.5}\text{Bi}_{0.5}\text{TiO}_3$* . Appl. Phys. Lett., 2011. **98**.

Appendix

Appendix chapter 2

In an A.C. field a resistor will follow Ohms law $|I| = V/R$. The current magnitude is directly related to the voltage, and the phase angle is zero.

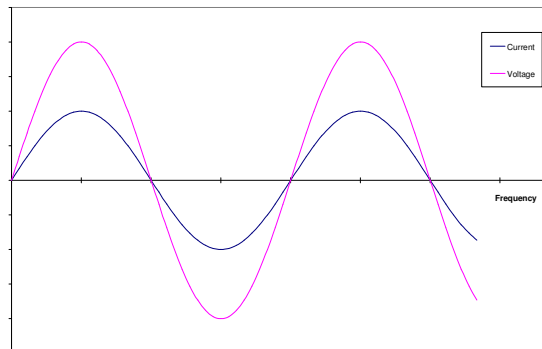


Figure A2.1: Current magnitude of a resistor with a varying frequency voltage.

For a capacitor, Ohms law is not obeyed and there is a -90° phase angle. This arises due to the application of voltage causing a polarisation by the movement of charge-carrying electrons. At the maximum voltage a stable state is reached where the system is already in its state of maximum polarisation, thus charge movement is zero and hence the current is also zero. At the point where the voltage changes sign, there is a maximum in the flow of electrons as the polarisation reverses, resulting in a maximum current.

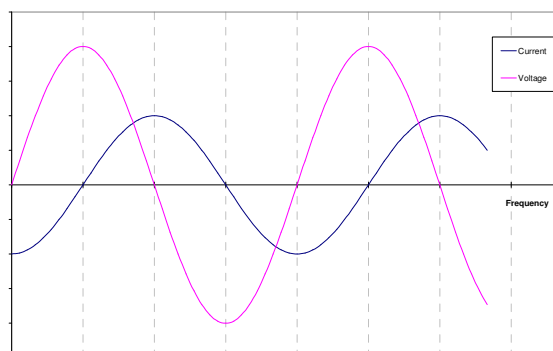


Figure A2.2: Current magnitude of a capacitor with a varying frequency voltage

Thus for a dielectric material we would expect to see a component of current in phase with the voltage and a component that is out of phase by -90° .

The resistive behaviour of a material arises due to the migration of electrons through the material. The speed at which these electrons are able to travel is dependent upon the material itself along with the temperature, but is independent of voltage and the frequency of that voltage in an A.C. supply, thus the magnitude of current observed for a given voltage is the same regardless of frequency.

The capacitance of a material is related to the amount of charge stored in the material as a result of polarisation of the ions and their resulting off-centring. This behaviour is frequency-dependant with a high capacitance being observed at low frequency.

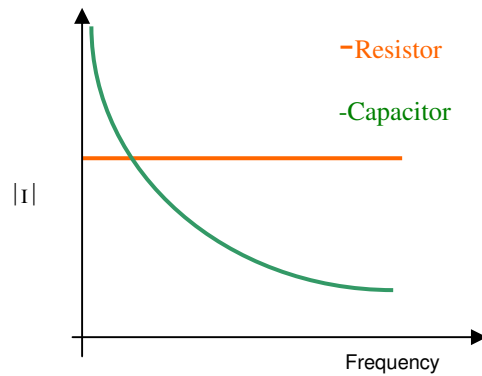


Figure A2.3: Current frequency dependences for resistors and capacitors.

When an oscillating voltage is applied to a dielectric material, a time dependent current response is observed with the magnitude of the impedance at any frequency being equal to the voltage divided by the current.

$$Z^*(\omega) = \frac{V(t)}{I(t)} = \frac{V_m \sin(\omega t + \varphi_v)}{I_m \sin(\omega t + \varphi_i)} = Z' + jZ'' = |Z| \cos \vartheta + j|Z| \sin \vartheta$$

φ_v and φ_i = Phase Angle

$V(t)$ = Voltage at time, t
 $I(t)$ = Current at time, t

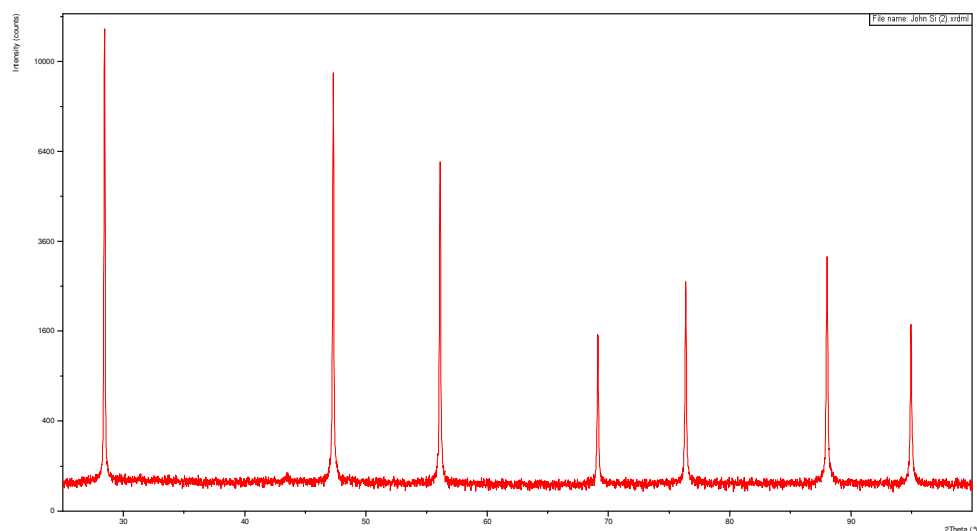
Equation A1

$$\vartheta = \varphi_v - \varphi_i$$

For a pure resistor $\theta = 0^\circ$, whilst θ for an ideal capacitor is -90° .

Appendix chapter 3

Powder X-ray diffraction data collected on a sample of silicon powder collected using an in-house PANalytical EMPYREAN X-ray diffractometer in reflection mode



Appendix chapter 4

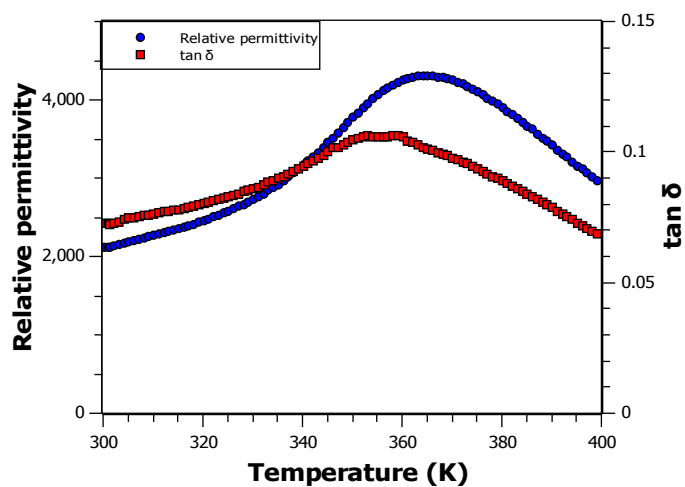


Figure A4.1. Relative permittivity and loss data collected on a sample of 50:50 BZT-BCT sintered at 1450 °C

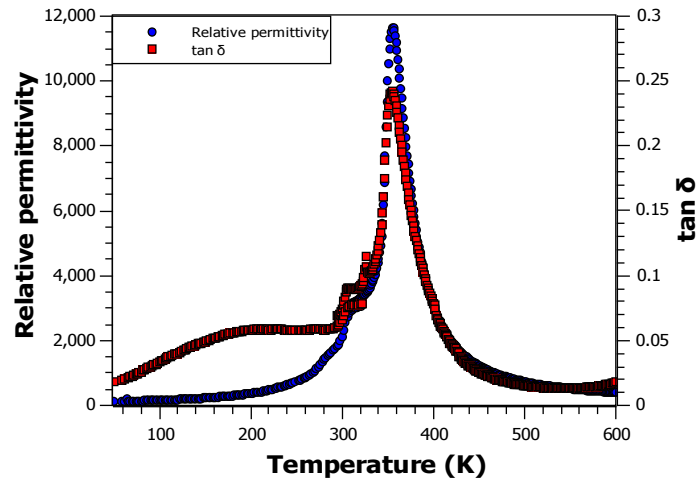


Figure A4.2. Relative permittivity and loss data collected on a sample of 50:50 BZT-BCT sintered at 1450 °C

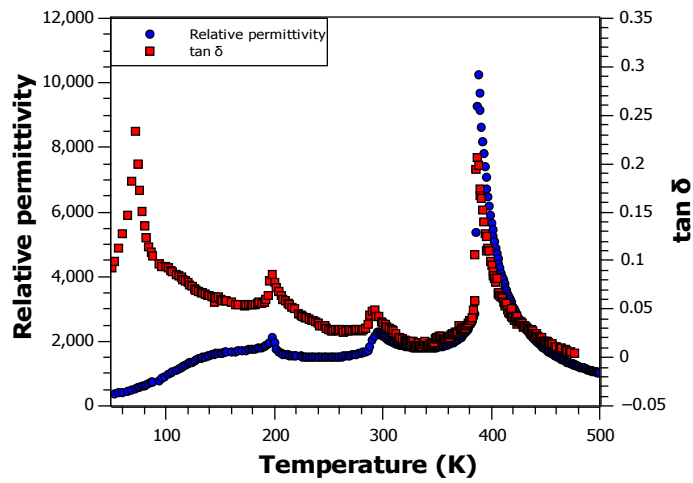


Figure A4.3. Relative permittivity and loss data collected on a sample of BaTiO₃

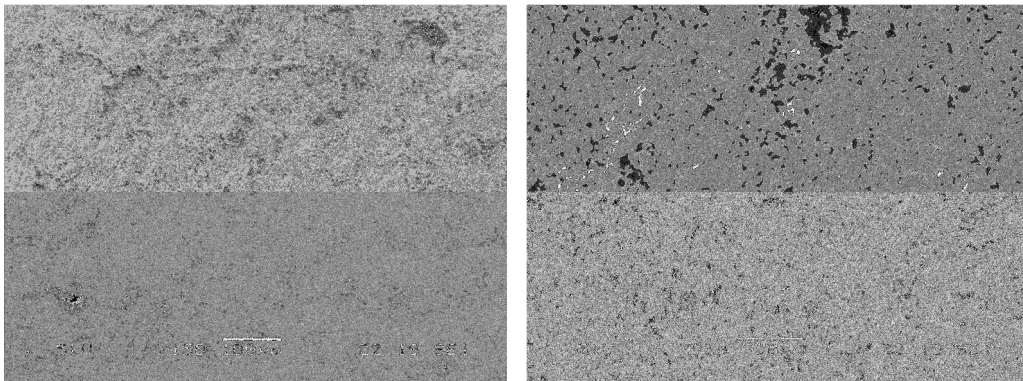


Figure A4.4. SEM images of 5% LaScO₃-doped BaTiO₃ sintered in air and composed from BaCO₃ (>99%), , TiO₂ (>99.9%), La₂O₃ (>99.99%) and Sc₂O₃ (>99.99%) starting reagents



Figure A4.5. Inhomogeneity observed in LaSO_3 doped BaTiO_3 compositions

Appendix chapter 5

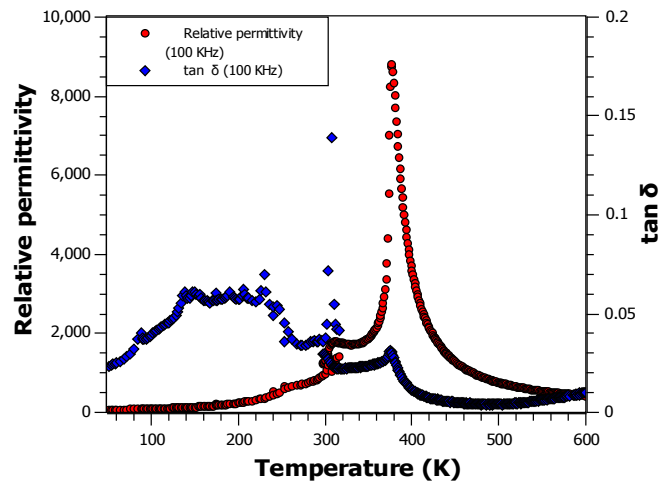


Figure A5.1. Relative permittivity and loss data collected on a sample of 5 % CaZrO_3 doped BaTiO_3

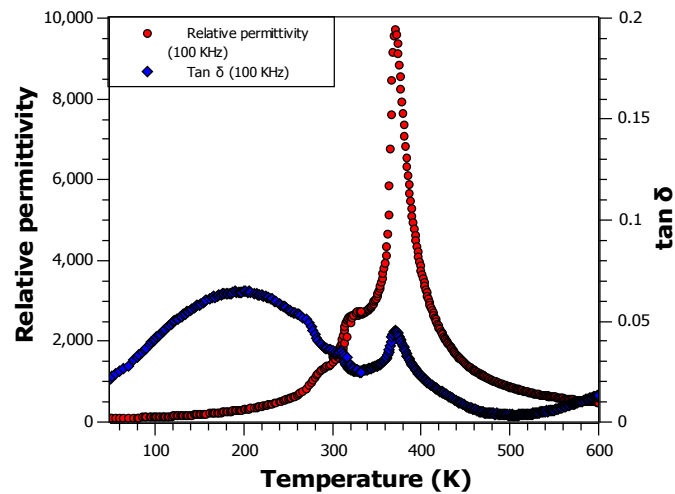


Figure A5.2. Relative permittivity and loss data collected on a sample of 8 % CaZrO_3 doped BaTiO_3

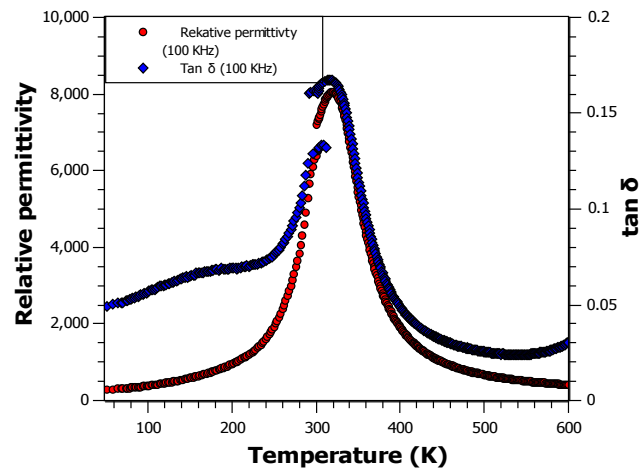


Figure A5.3. Relative permittivity and loss data collected on a sample of 12 % CaZrO_3 doped BaTiO_3

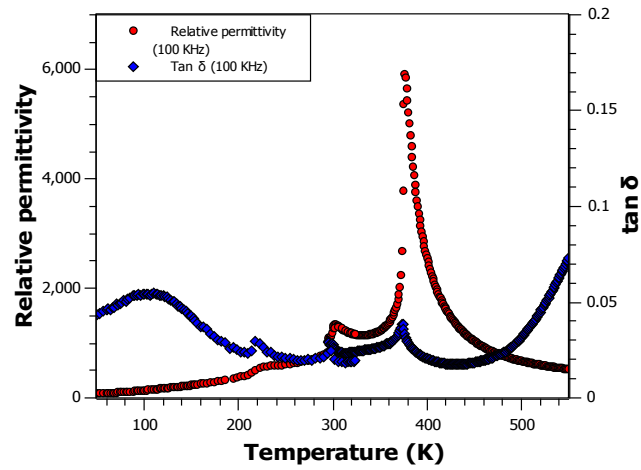


Figure A5.4. Relative permittivity and loss data collected on a sample of 2 % SrZrO_3 doped BaTiO_3

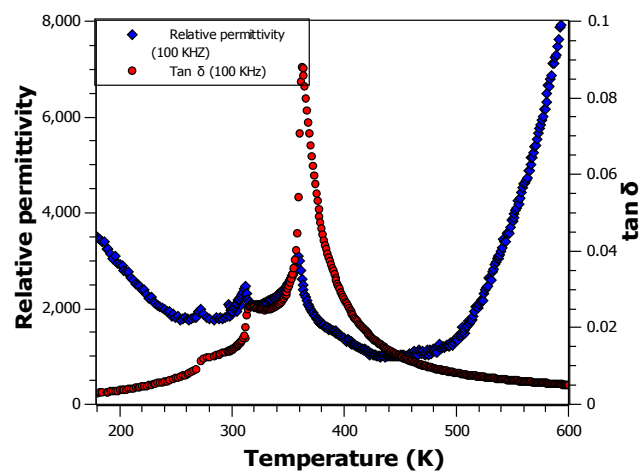


Figure A5.5. Relative permittivity and loss data collected on a sample of 5 % SrZrO_3 doped BaTiO_3

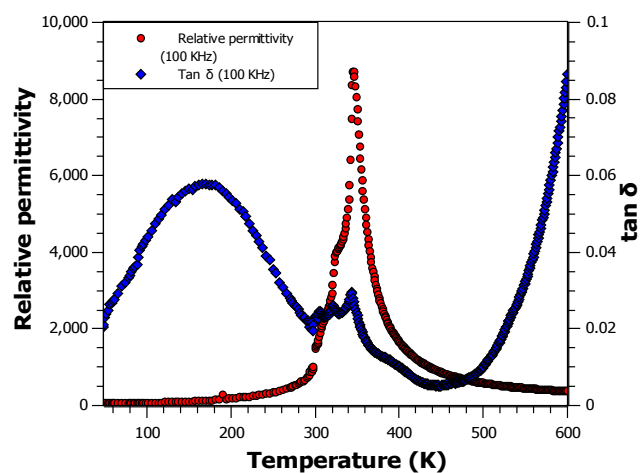


Figure A5.6. Relative permittivity and loss data collected on a sample of 8 % SrZrO₃ doped BaTiO₃

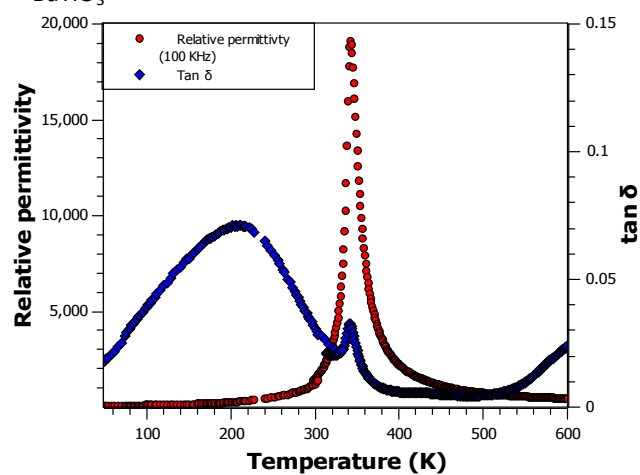


Figure A5.7. Relative permittivity and loss data collected on a sample of 12 % SrZrO₃ doped BaTiO₃

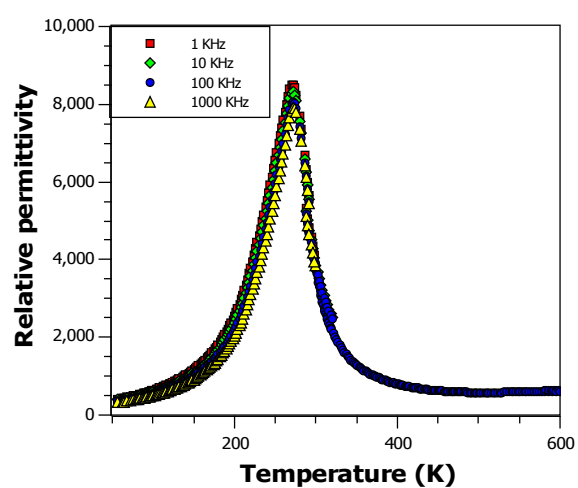


Figure A5.8. Relative permittivity as a function of frequency collected on a sample of 5 % LaScO₃ doped BaTiO₃

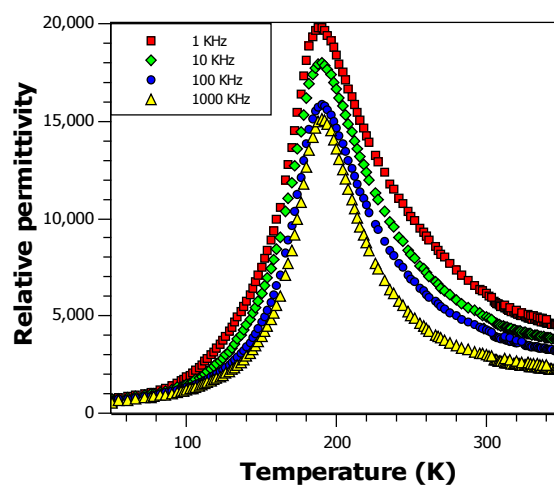


Figure A5.9. Relative permittivity as a function of frequency collected on a sample of 8 % LaScO₃ doped BaTiO₃

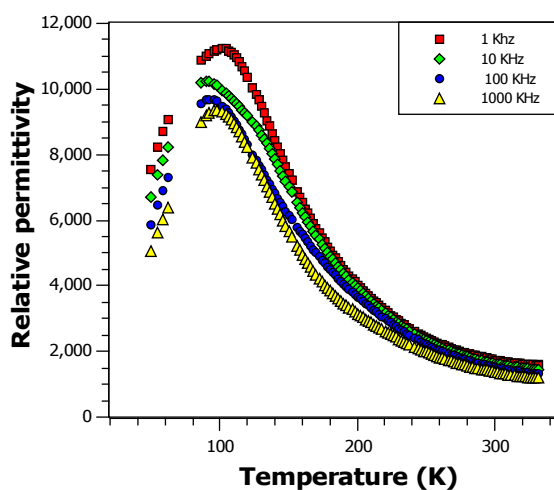


Figure A5.10. Relative permittivity as a function of frequency collected on a sample of 12 % LaScO₃ doped BaTiO₃

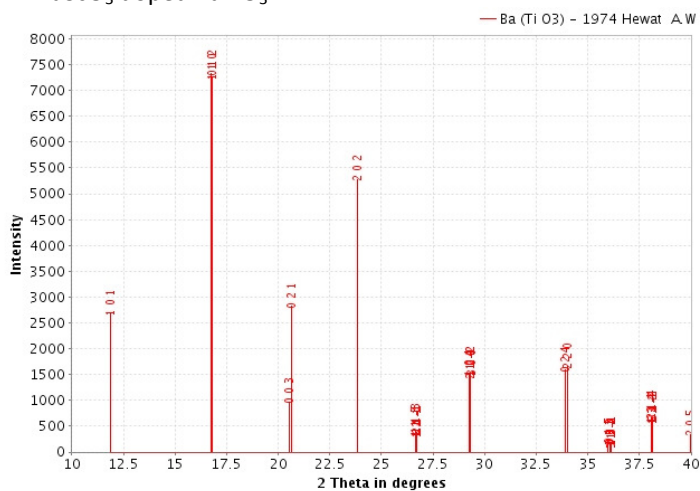
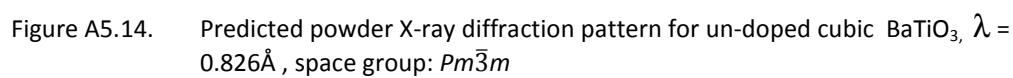
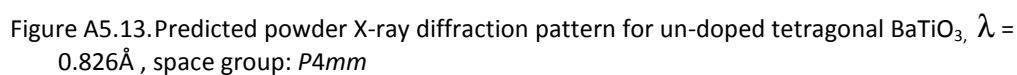
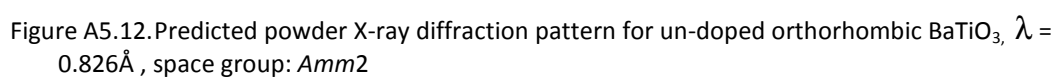


Figure A5.11. Predicted powder X-ray diffraction pattern for un-doped rhombohedral BaTiO₃, $\lambda = 0.826\text{\AA}$, space group: $R3mr$



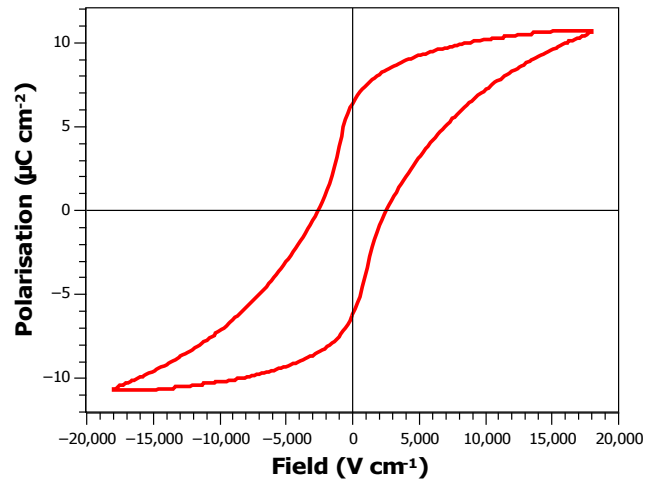


Figure A5.15. Room temperature hysteresis loop collected on a sample of 2 % SrZrO₃-doped BaTiO₃ at 1 Hz

Table A5.1: Hysteresis loop collection conditions and properties for 2% SrZrO₃-doped BaTiO₃

Frequency(Hz)	1	Voltage (V)	4000	Thickness (mm)	2.18
P_{\max} ($\mu\text{C cm}^{-2}$)	10.6203	V_{c+} (V)	550.402	V_{c-} (V)	-573.435
P_{r+} ($\mu\text{C cm}^{-2}$)	6.33628	P_{r-} ($\mu\text{C cm}^{-2}$)	-6.17822		
$P_{\text{rrel}+}$ ($\mu\text{C cm}^{-2}$)	5.48868	$P_{\text{rrel}-}$ ($\mu\text{C cm}^{-2}$)	-5.59258		

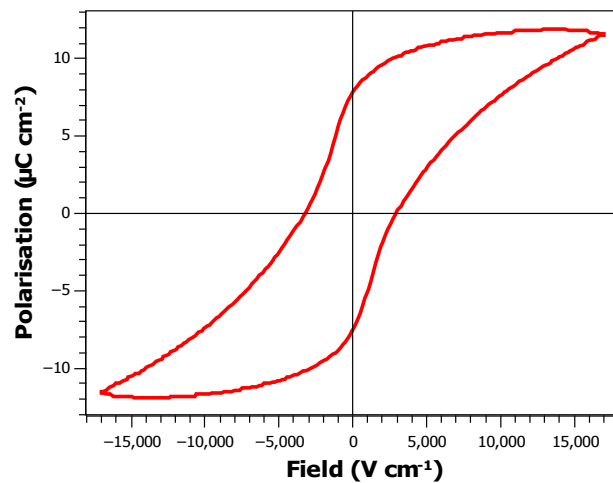


Figure A5.16. Room temperature hysteresis loop collected on a sample of 5 % SrZrO₃-doped BaTiO₃ at 10 Hz

Table A5.2: Hysteresis loop collection conditions and properties for 5 % SrZrO₃-doped BaTiO₃

Frequency(Hz)	10	Voltage (V)	3000	Thickness (mm)	1.73
P_{\max} ($\mu\text{C cm}^{-2}$)	11.609	V_{c+} (V)	511.78	V_{c-} (V)	-561.352
P_{r+} ($\mu\text{C cm}^{-2}$)	7.76987	P_{r-} ($\mu\text{C cm}^{-2}$)	-7.47838		
P_{rrel+} ($\mu\text{C cm}^{-2}$)	6.04859	P_{rrel-} ($\mu\text{C cm}^{-2}$)	-6.3456		

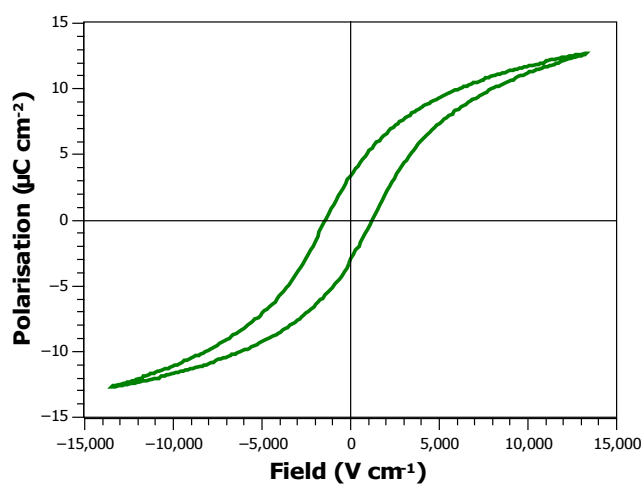


Figure A5.17. Room temperature hysteresis loop collected on a sample of 2 % LaScO₃-doped BaTiO₃ at 100 Hz

Table A5.3: Hysteresis loop collection conditions and properties for 2 % LaScO₃-doped BaTiO₃

Frequency(Hz)	100	Voltage (V)	1500	Thickness (mm)	1.10
P_{\max} ($\mu\text{C cm}^{-2}$)	12.6739	V_{c+} (V)	136.502	V_{c-} (V)	-157.232
P_{r+} ($\mu\text{C cm}^{-2}$)	3.32795	P_{r-} ($\mu\text{C cm}^{-2}$)	-3.16491		
P_{rrel+} ($\mu\text{C cm}^{-2}$)	1.86787	P_{rrel-} ($\mu\text{C cm}^{-2}$)	-1.95843		

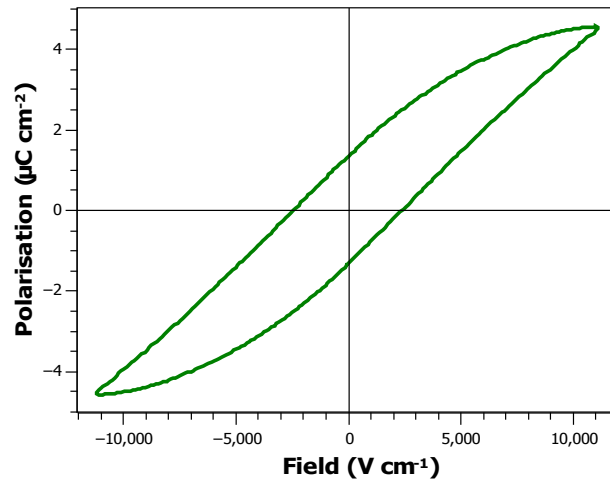


Figure A5.18. Room temperature hysteresis loop collected on a sample of 5 % LaScO₃-doped BaTiO₃ at 100 Hz

Table A5.4: Hysteresis loop collection conditions and properties for 5 % LaScO₃-doped BaTiO₃

Frequency(Hz)	100	Voltage (V)	1500	Thickness (mm)	1.33
P_{\max} ($\mu\text{C cm}^{-2}$)	4.55441	V_{c+} (V)	314.838	V_{c-} (V)	-327.81
P_{r+} ($\mu\text{C cm}^{-2}$)	1.36466	P_{r-} ($\mu\text{C cm}^{-2}$)	-1.32307		
$P_{\text{rrel}+}$ ($\mu\text{C cm}^{-2}$)	0.65552	$P_{\text{rrel}-}$ ($\mu\text{C cm}^{-2}$)	-0.69213		

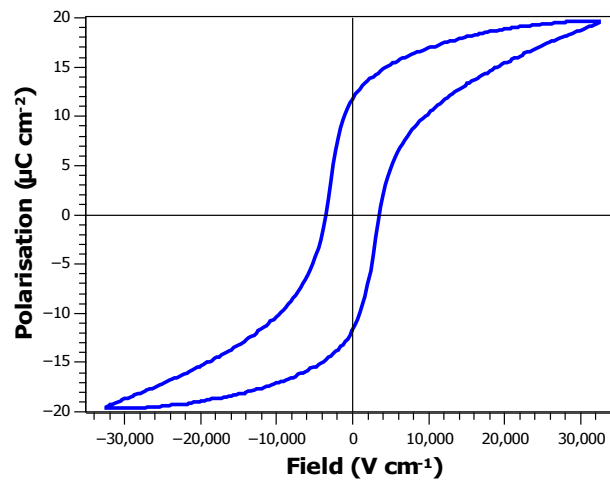


Figure A5.19. Room temperature hysteresis loop collected on a sample of 2 % GdScO₃-doped BaTiO₃ at 1 Hz

Table A5.5: Hysteresis loop collection conditions and properties for 2 % GdScO₃-doped BaTiO₃

Frequency(Hz)	1	Voltage (V)	4000	Thickness (mm)	1.20
P_{\max} ($\mu\text{C cm}^{-2}$)	19.4986	V_{c+} (V)	413.993	V_{c-} (V)	-427.693
P_{r+} ($\mu\text{C cm}^{-2}$)	11.7844	P_{r-} ($\mu\text{C cm}^{-2}$)	-11.5853		
$P_{\text{rrel}+}$ ($\mu\text{C cm}^{-2}$)	9.23181	$P_{\text{rrel}-}$ ($\mu\text{C cm}^{-2}$)	-9.63232		

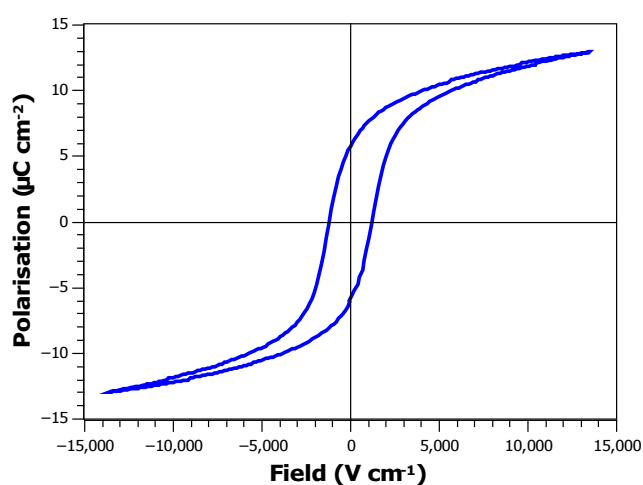


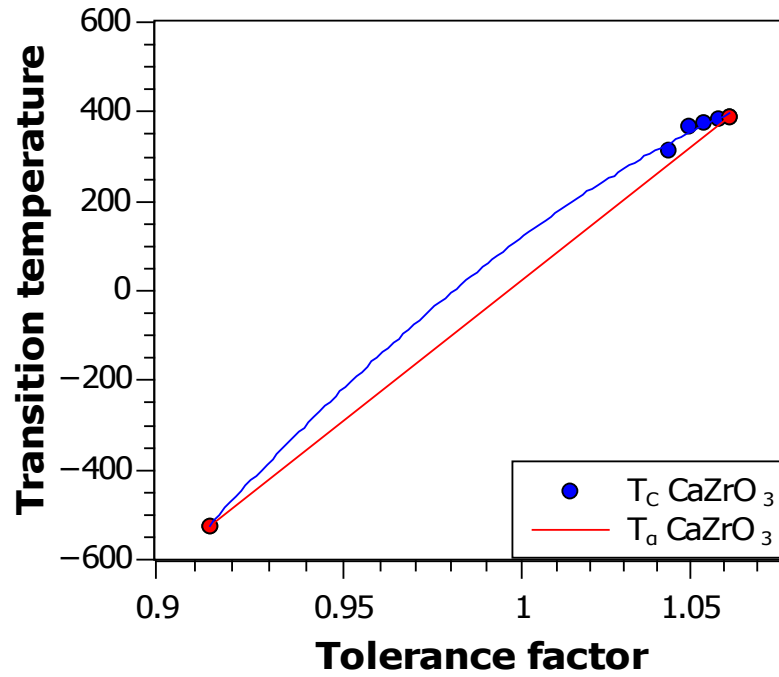
Figure A5.20. Room temperature hysteresis loop collected on a sample of 5 % GdScO₃-doped BaTiO₃ at 1 Hz

Table A5.6: Hysteresis loop collection conditions and properties for 5 % GdScO₃-doped BaTiO₃

Frequency(Hz)	1	Voltage (V)	2000	Thickness (mm)	1.45
P_{\max} ($\mu\text{C cm}^{-2}$)	12.9823	V_{c+} (V)	177.862	V_{c-} (V)	-180.321
P_{r+} ($\mu\text{C cm}^{-2}$)	5.88652	P_{r-} ($\mu\text{C cm}^{-2}$)	-5.94952		
$P_{\text{rrel}+}$ ($\mu\text{C cm}^{-2}$)	4.51138	$P_{\text{rrel}-}$ ($\mu\text{C cm}^{-2}$)	-5.05103		

Appendix chapter 7

7.1: CaZrO₃ – Doped BaTiO₃ size and strain fitting



Linear size-only equation: $(6.170427436 \times 10^3)x - 6.163166962$

Second order polynomial: $(-2.022250005 \times 10^4 \pm 7.4172867769 \times 10^3)x^2 + (4.617875119 \times 10^5 \pm 1.460663955 \times 10^3)x - (2.583678149 \times 10^4 \pm 7.156162928 \times 10^3)$

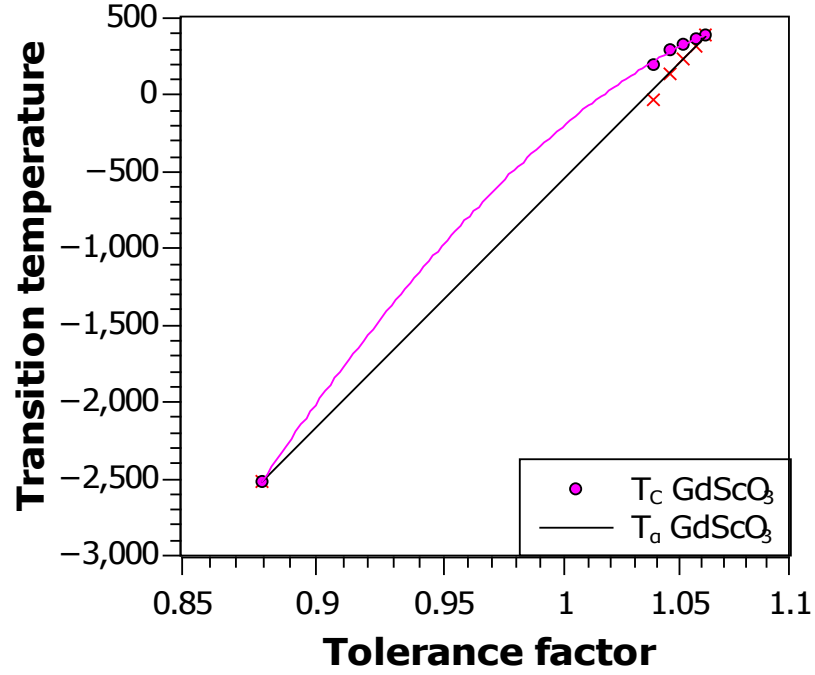
The y- values calculated form the linear size-only equation can be termed the size-only Curie temperature, T_α

The y-values calculated from the polynomial expression give the size & strain combined effect on T_C , which shall be termed $T_{\alpha\beta}$

$T_{\alpha\beta} - T_\alpha$ gives the effect on T_C due to strain, this shall be termed β

Composition	Tolerance factor	T_α (K)	$T_{\alpha\beta}$ (K)	β (K)	β % ⁻¹ (K)
2 % CaZrO ₃	1.058423	327.1	385.43	13.33	6.67
5 % CaZrO ₃	1.053759	349.8	370.11	20.32	4.06
8 % CaZrO ₃	1.049110	327.6	352.28	24.68	3.09
12 % CaZrO ₃	1.042937	298.1	328.38	30.38	2.53

7.2: GdScO₃ – Doped BaTiO₃ size and strain fitting



Linear size-only equation: $(1.587719236 \times 10^4 \pm 1.479079409 \times 10^2)x - (1.647843671 \times 10^4 \pm 1.515280031 \times 10^2)$

Second order polynomial: $(-5.311470666 \times 10^4 \pm 4.404064962 \times 10^3)x^2 + (1.190279663 \times 10^5 \pm 8.513814420 \times 10^3)x - (6.610836318 \times 10^4 \pm 4.083136101 \times 10^3)$

The y- values calculated from the linear size-only and charge dilution equation can be termed, $T_{\alpha\gamma}$

The y-values calculated from the polynomial expression give the size, strain and charge combined effect on T_c , which shall be termed $T_{\alpha\beta\gamma}$

$T_{\alpha\beta\gamma} - T_{\alpha\gamma}$ gives the effect on T_c due to strain, this shall be termed β

Composition	Tolerance factor	$T_{\alpha\gamma}$ (K)	$T_{\alpha\beta\gamma}$ (K)	β (K)	$\beta \text{ } ^\circ\text{-}^1$ (K)
2 % GdScO ₃	1.057647	314.04	366.19	52.15	26.08
5 % GdScO ₃	1.051827	221.32	325.54	103.92	20.78
8 % GdScO ₃	1.049603	129.58	281.48	151.89	18.99
12 % GdScO ₃	1.038338	7.46	217.50	210.04	17.50